Impacts of Channel Curvature on Drag, Mixing, and Stratification in Estuaries

by

Tong Bo

B.S., Peking University (2018)

Submitted to the Department of Civil and Environmental Engineering
in partial fulfillment of the requirements for the degree of

Doctor of Philosophy in Civil and Environmental and Oceanographic Engineering

at the

Massachusetts Institute of Technology

and the

Woods Hole Oceanographic Institution

June 2023

Authored by: Tong Bo
Joint Program in Oceanography/Applied Ocean Science & Engineering
Massachusetts Institute of Technology &
Woods Hole Oceanographic Institution
May 4, 2023

Certified by: David K. Ralston
Associate Scientist with Tenure, Applied Ocean Physics and Engineering
Woods Hole Oceanographic Institution
Thesis supervisor

Accepted by: Colette L. Heald
Professor of Civil and Environmental Engineering
Chair, Graduate Program Committee

Accepted by: David K. Ralston
Associate Scientist with Tenure, Applied Ocean Physics and Engineering
Woods Hole Oceanographic Institution
Chair, Joint Committee for Applied Ocean Science and Engineering

Impacts of Channel Curvature on Drag, Mixing, and Stratification in Estuaries

by

Tong Bo

Submitted to the Department of Civil and Environmental Engineering
on May 4, 2023, in partial fulfillment of the
requirements for the degree of
Doctor of Philosophy in Civil and Environmental and Oceanographic Engineering

Abstract

Estuaries often have sinuous planforms, and channel curvature can lead to distinct flow processes in bends, e.g., secondary circulation and flow separation. An integrated approach combining field observations, idealized modeling, and realistic modeling is used to understand how curvature-induced flow processes affect hydrodynamic drag, salinity mixing, and stratification in estuaries. In the North River (MA, USA), a sinuous, tidally-dominated estuary, drag is observed to be much greater than typically found in straight channel estuaries, and data analysis points to links between the high drag and curvature-induced processes. Idealized models and a realistic North River model are developed to investigate the mechanisms of drag increase in sinuous estuaries. Two key processes are found to dominate. First, flow separation leads to low-pressure eddies on the lee side of bends and thus creates bend-scale form drag. Second, curvature-induced secondary circulation transports higher momentum fluid from the surface toward the bed. Consequently, the near-bed shear and bottom stress are enhanced compared with a logarithmic velocity profile. The form drag due to flow separation and enhanced bed stress due to secondary circulation combine to increase the drag in the North River by a factor of 2-5 compared to the expected values. In addition to increasing the drag, channel curvature also affects the salinity distribution, mixing, and stratification. During ebb tides, secondary circulation in bends interacts with the salinity field to create bottom salinity fronts upstream of bend apexes. Intense mixing occurs at these curvature-induced fronts and leads to overall decreased stratification in sinuous estuaries compared to straight channels. In addition, flow separation in bends and at channel constrictions can create sharp lateral salinity gradients through differential advection during flood tides, and the resulting baroclinic forcing influences secondary circulation. Surface convergence fronts are generated at bends and constrictions as secondary circulation interacts with the laterally sheared flow, resulting in intensified mixing near the fronts. This thesis advances our understanding of how flow curvature affects the hydrodynamics, salinity, and mixing in estuaries with complex topographic features found in natural systems.

Thesis Supervisor: David K. Ralston
Title: Associate Scientist with Tenure, Applied Ocean Physics and Engineering
Woods Hole Oceanographic Institution

Acknowledgments

This thesis is based on work supported by NSF awards OCE-1634480, OCE-1634481, and OCE-2123002 and the Michael J. Kowalski Fellowship in Ocean Science and Engineering in the MIT-WHOI Joint Program.

Foremost, I would like to thank my advisor, Dave Ralston, for his guidance and support throughout my doctoral studies. He has always been patient in guiding me through every step of the way, especially during my initial year in the program when I had no prior experience with estuarine research. His expertise in research and commitment to rigor have been invaluable in fostering my academic skills and shaping my research. I also appreciate that he has given me a lot of freedom to explore my research projects while providing timely advice, without making me feel any extra stress. I feel really fortunate to have had Dave as my advisor. I also want to thank my other thesis committee members, Heidi Nepf, Rocky Geyer, Peter Traykovski, and Charles Harvey, Their insightful suggestions and discussions have been instrumental in broadening the scope of my research and improving this thesis.

The fieldwork would not have been possible without substantial assistance from many people. Thank Rocky Geyer for his expertise in the field and for all the exciting discussions on the North River. Thank Adrian Garcia for showing me how to prepare for fieldwork and providing the wonderful drone images. Thank Wouter Kranenburg for sharing his expertise in field data analysis, Peter Traykovski for collecting the bathymetric data, and Jay Sisson, Sean Whelan, and Salme Cook for helping with the fieldwork. Likewise, I am thankful to Suzi Clark and Adrian Garcia for their discussions about the ROMS model, and Gordon Zhang for his helpful suggestions. I would also like to thank the EFM group at MIT, especially Heidi Nepf for giving me the opportunity to gain laboratory and teaching experience and Autumn Deitrick for showing me how to process water samples, as well as the COFDL student group at WHOI.

Thanks to Kris Kipp, Tricia Nesti, Kevin Kirwin, and all the other administrative and technical people at MIT and WHOI, for providing support, resources, and assistance.

I also want to thank my friends, Yilang, Ruijiao, Jinshi, Zhaozhong, Weiguang, Zihua, Bofu, and many others in the WHOI community, and Yue, Tian, Xiaoyu, Jie, Yunpo, and many others in the MIT community. Most of all, thanks to my family, for their love and support.

Contents

List of Figures

List of Tables

Chapter 1

Introduction

Estuaries are unique environments at the interface of rivers and the ocean, serving as hosts for diverse ecosystems and large population and economic centers (Pritchard, 1952; Valle-Levinson, 2010). Rivers provide the dominant buoyancy source in most estuaries (Geyer and MacCready, 2014). The horizontal salinity gradient between a river and the ocean is a key characteristic of estuarine dynamics because the horizontal baroclinic pressure gradient drives the estuarine exchange flow. Moreover, stratification results from the influence of gravity tilting horizontal salinity gradients into the vertical direction, further affecting the vertical structure of turbulence and the mean flow, as well as the transport of salinity, sediment, chemicals, and biota (Simpson et al., 1990; Geyer and Ralston, 2011). Tides cause periodic water level fluctuations and bidirectional tidal currents, and strong turbulence generated by interaction with the boundary can cause decay in tidal energy with distance along an estuary due to the drag effect (Ippen, 1966). Tidal mixing occurs associated with this turbulence generation, which affects salinity stratification, estuarine exchange, and transport of other materials (Geyer and MacCready, 2014). The along-estuary propagation of tides, particularly in combination with sea level rise and storm surges, also influences the risk of flooding of surrounding uplands and along with risks to built infrastructure and natural habitat.

Channel morphology also plays a crucial role in estuarine dynamics, as it interacts with river and tidal flows to influence the tidal and salinity dynamics. One commonly observed morphological characteristic is channel curvature (Marani et al., 2002; Fagherazzi et al., 2004), similar to the curvature of fluvial rivers that have meander bends (Langbein and Leopold, 1966). The natural processes that shape the sinuous form of estuarine and river channels result from interactions between the fluid motion that carries sediment and the erosion and deposition at channel boundaries (Ahnert,

1960; Langbein and Leopold, 1970; Seminara, 2006). The curved channel geometry, in turn, leads to distinct flow processes in meanders, including secondary circulation (e.g., Thomson, 1877) and flow separation (e.g., Leopold, 1960).

Flow in a curved channel generates a water level setup near the outer bank and a setdown near the inner bank (Thomson, 1877). This lateral water level slope yields a barotropic pressure gradient that balances the centrifugal acceleration. Vertical shear in the streamwise flow causes a depth-dependent imbalance between these two forcing terms and, as a result, secondary circulation develops in the lateral plane perpendicular to the primary flow direction. Curvature-induced secondary circulation is predicted by the analytical solution presented by Rozovskii (1957) and Kalkwijk and Booij (1986), and it is observed in rivers (e.g. Apmann, 1964) and estuaries(e.g. Seim and Gregg, 1997; Chant, 2002; Buijsman and Ridderinkhof, 2008), typically with flow toward the outer bank near the surface and toward the inner bank in the lower layer. This secondary circulation can causes sediment transport across the channel and in turn provide feedback to meander morphology including erosion of the outer bank, evolution of the meander position, deposition at the inner bank, and growth of point bars.

In estuaries, salinity variations provide an additional factor that can influence the response of tidal flow to channel curvature. Stratification can enhance the shear of the streamwise flow and thereby strengthen the secondary circulation (Geyer, 1993b). Alternatively, lateral baroclinic pressure gradients can reverse the sense of secondary circulation or lead to multiple circulation cells and more complex structure than in homogeneous density flow (Chant and Wilson, 1997; Lacy and Monismith, 2001; Nidzieko et al., 2009; Scully et al., 2009; Kranenburg et al., 2019). The reversed circulation due to baroclinic forcing may contribute to the absence of point bars in some tidal meanders, and the lack of bedload transport in cohesive-bed tidal channels may also make it less likely for point bars to form (e.g. Jamieson et al., 2013).

In addition to generating secondary circulation, channel curvature can cause flow separation in the along-channel currents at the inside of bends. With flow separation, streamlines of the main flow detach from the inner bank, and recirculating eddies are generated in the "separation zone" in the lee of channel bends (Leopold, 1960). Flow with curvature creates a lateral water level slope in the bend (Thomson, 1877), and as the curvature effect weakens downstream from the bend apex, the lateral water level slope decreases toward the exit of the bend. As a result, an adverse pressure gradient occurs along the inner bank, and this adverse pressure gradient is a necessary condition for flow separation (Blanckaert, 2010; Vermeulen et al., 2015). Inner bank separation has been reported

in sharp-bend flume experiments including Blanckaert (2011), Constantinescu et al. (2013), and Blanckaert (2015). In field observations from intertidal channels in the Solway Firth (Scotland), Leeder and Bridges (1975) found that flow was separated from the inner bank and restricted to a narrower part of the cross-section, and they suggested that flow separation is to be expected in many natural systems. In the Satilla River estuary, Seim et al. (2006) reported the formation of counter-rotating eddies near the apex of bends, with similarities to flow around headlands as in Signell and Geyer (1991). Flow separation in the lee of a bend and recirculating eddies in the separation zone have also been observed in fluvial rivers, including the Embarras River (Frothingham and Rhoads, 2003), the River Dean (Ferguson et al., 2003), and the Tollense River (Schnauder and Sukhodolov, 2012).

Both the strength of curvature-induced secondary circulation and occurrence of flow separation have been noted to depend on the sharpness of channel bends. The bend sharpness is customarily quantified as R/W, the ratio of bend radius of curvature to channel width. Typical values of R/W are in the range of $1-5$ for both rivers (Leopold and Wolman, 1960) and tidal channels (Marani et al., 2002). Secondary circulation has been reported in a range of sharp and mild bends with R/W from 1 to 5 (e.g., Chant and Wilson, 1997; Lacy and Monismith, 2001; Ferguson et al., 2003; Kranenburg et al., 2019), and the magnitude of secondary flows is suggested to increase with stronger curvature (i.e., smaller R/W) (Kalkwijk and Booij, 1986; Geyer, 1993b; Blanckaert and De Vriend, 2010; Blanckaert, 2011). The bends where flow separation occurs tend to be sharper than average, e.g. $R/W < 1.5$ (e.g., Leeder and Bridges, 1975; Ferguson et al., 2003; Schnauder and Sukhodolov, 2012)

The goal of this thesis is to use numerical simulations and field observations to understand the importance of channel curvature for estuarine dynamics. The curvature-induced secondary circulation can interact with the streamwise flow and affect the distribution of momentum in the channel cross-section (Chang, 1983; Seim et al., 2002; Blanckaert and Graf, 2004), thus influencing the vertical shear of streamwise and lateral velocities as well as the drag force experienced by tidal currents. Likewise, secondary circulation can alter the salinity distribution through lateral and vertical advection, with impacts on stratification, turbulent mixing, and estuarine circulation (Lerczak and Geyer, 2004; Ralston and Stacey, 2005a; Becherer et al., 2015). Flow separation creates eddies and laterally restricts the main flow to a narrower part of the cross-section, which can therefore affect the bed shear stress, pressure field distribution, and the overall momentum budget (Leopold, 1960; Blanckaert, 2015). The lateral shear between the separation zone and main flow can also

lead to straining of the salinity gradient and thus affect frontogenesis and mixing (Wolanski and Hamner, 1988). This thesis investigates the influences of curvature-induced secondary circulation and flow separation on hydrodynamic drag, tidal decay, estuarine frontogenesis, and salinity mixing and stratification. The thesis is organized into five main body chapters, and each corresponds to a published or in-preparation paper.

This study of channel curvature effects has been inspired by the North River estuary, a sinuous tidal channel in Massachusetts, USA. The curvature ratio R/W of North River bends is generally in the range of $1-4$, representative of values typically found in river and tidal meanders (Leopold and Wolman, 1960; Marani et al., 2002). Chapter 2 presents an observational study of the high drag and increased tidal decay rate in the North River estuary. The magnitude and variability of drag are quantified, and the linkage between the high values of drag and curvature-induced processes is investigated. Inspired by the observed high drag from the North River estuary, numerical modeling studies are conducted in the following two chapters to examine the mechanisms of drag increase in estuaries with curvature. Chapter 3 uses idealized numerical models to study the increased drag in sinuous estuarine channels, and investigates the bend-scale form drag associated with flow separation. Form drag is the integrated pressure force normal to the channel boundaries, and is found to be the dominant source of drag in relatively sharp and deep bends. Chapter 4 uses a numerical model of the North River estuary to investigate sources of drag with realistic bathymetry. While form drag from flow separation is dominant in sharp idealized bends, both form drag and enhanced bottom friction due to secondary circulation are important in the realistic model because bends in the North River tend to be smoother and have complex bottom topography. The enhanced bottom friction results from secondary circulation transporting higher momentum fluid toward the bed and increasing the vertical shear of near-bed streamwise velocity.

The drag force is an important factor in the decay of tidal energy and the generation of turbulence in estuaries, and thus has significant implications for turbulent mixing and salinity dynamics as well. Therefore, the following two chapters focus on the impact of channel curvature on estuarine salinity mixing and stratification. Chapter 5 presents an idealized model study to understand how curvature-induced secondary circulation affects salinity mixing and stratification in estuarine channels with curvature. Bend-scale bottom salinity fronts are generated during ebb tides upstream of bend apexes as a result of interaction between the secondary flow and stratification. Intense mixing occurs at these bottom fronts, and this provides the dominant mechanism for the weaker stratification in sinuous channels. Chapter 6 studies surface convergence fronts and salinity mixing during

flood tides by combining model analysis with observations from the North River. Flow separation that occurs in bends and at channel constrictions leads to differential advection of salinity, and this provides a common mechanism for surface frontogenesis at the different topographic features. Intense turbulent mixing occurs at the surface fronts such that the near-surface mixing during flood tides is similar in magnitude to bottom boundary layer mixing during ebbs in this estuary. Chapter 7 presents conclusions and suggestions for future research.

Chapter 2

High and variable drag in a sinuous estuary with intermittent stratification

In field observations from a sinuous estuary, the drag coefficient C_D based on the momentum balance was in the range of $5 - 20 \times 10^{-3}$, much greater than expected from bottom friction alone. C_D also varied at tidal and seasonal time scales. C_D was greater during flood tides than ebbs, most notably during spring tides. The ebb tide C_D was negatively correlated with river discharge, while the flood tide C_D showed no dependence on discharge. The large values of C_D are explained by form drag from flow separation at sharp channel bends. Greater water depths during flood tides corresponded with increased values of C_D, consistent with the expected depth dependence for flow separation, as flow separation becomes stronger in deeper water. Additionally, the strength of the adverse pressure gradient downstream of the bend apex, which is indicative of flow separation, correlated with C_D during flood tides. While C_D generally increased with water depth, C_D decreased for the highest water levels that corresponded with overbank flow. The decrease in C_D may be due to inhibition of flow separation with flow over the vegetated marsh. The dependence of C_D during ebbs on discharge corresponds with inhibition of flow separation by a favoring baroclinic pressure gradient that is locally generated at the bend apex due to curvature-induced secondary circulation. This effect increases with stratification, which increases with discharge. Additional factors may contribute to the high drag, including secondary circulation, multiple-scales of bedforms, and shallow shoals, but the observations suggest that flow separation is the primary source.

The material in this chapter has been published as Bo et al. (2021) in *Journal of Geophysical Research: Oceans* and is included with permission.

2.1 Introduction

The drag force is an important part of the estuarine momentum balance, and it directly affects tidal propagation, flooding potential, and marsh inundation, as well as estuarine exchange, mixing processes and salinity intrusion (e.g., Geyer, 2010). Models to predict water level elevations and velocities in estuaries require appropriate parameterization of the drag (e.g., Lewis and Lewis, 1987). The drag coefficient C_D is one of the typical ways to quantify the drag and is defined as

$$C_D = \frac{\tau}{\rho U|U|}, \tag{2.1}$$

where τ is the total drag, ρ is density, and U is a reference velocity, usually taken at a fixed elevation (e.g., 1 m above the bed) or as the depth average.

Drag in shallow flows (e.g., estuaries, rivers, and the coastal ocean) is mainly attributed to bottom friction. A common value for C_D used in estuaries and tidal channels is around 3×10^{-3} (e.g., Dronkers, 1964; Sternberg, 1968; Soulsby, 1990; Geyer et al., 2000), but C_D can vary depending on the dominant sources of drag. C_D due to bottom roughness can be calculated directly by assuming a near-bed boundary layer velocity profile (e.g., Gross et al., 1999; Lentz et al., 2017). The bottom friction also depends on the size and structure of roughness elements like bed forms (Grant and Madsen, 1982; Fong et al., 2009) and can be enhanced by wind waves (Grant and Madsen, 1986; Bricker et al., 2005). Factors other than bottom friction can also contribute to the drag, e.g., stem drag from vegetation (e.g., Kadlec, 1990; Nepf, 1999) and form drag from large topographic features including headlands (McCabe et al., 2006) and channel bends (Seim et al., 2006).

A sinuous channel planform is a common feature of many estuaries (Marani et al., 2002) and the channel curvature influences the flow structure and the drag (e.g., Leeder and Bridges, 1975; Lacy and Monismith, 2001; Chant, 2002; Seim et al., 2006). Increased flow resistance due to channel curvature has been examined extensively in rivers and laboratory channels (e.g., Chow, 1959; Leopold, 1960; Chang, 1984; Arcement and Schneider, 1989). Several processes have been identified as contributing to increased drag in sinuous channels, including secondary circulation (e.g., Chang, 1984) and flow separation (e.g., Leopold, 1960).

Secondary circulation due to flow curvature interacts with the primary along-channel flow to increase drag. Flow around a bend generates a water level setup near the outer bank and a setdown near the inner bank (Thomson, 1877; Kalkwijk and Booij, 1986). This lateral water level slope yields a barotropic pressure gradient that balances the centrifugal acceleration. Vertical shear in

the streamwise flow causes a depth-dependent imbalance between these two forcing terms and, as a result, secondary circulation develops in the lateral plane perpendicular to the primary flow direction. In estuaries, lateral baroclinic pressure gradients caused by salinity variation can also affect the secondary circulation in bends (e.g., Nidzieko et al., 2009; Pein et al., 2018; Kranenburg et al., 2019). Laboratory experiments have shown that secondary circulation can increase drag by: 1. increasing the lateral velocity and creating an additional bed shear stress component; 2. vertically advecting high momentum toward the channel bed, compressing the bottom boundary layer, and increasing the bottom stress (Chang, 1983; Blanckaert and de Vriend, 2003; Blanckaert and Graf, 2004). In observations from estuaries, secondary circulation associated with channel curvature has been found to increase turbulent stresses and the drag (Seim et al., 2002; Fong et al., 2009).

In addition to secondary circulation, drag can be enhanced due to flow separation and the associated form drag at channel bends. Channel curvature creates a lateral water level slope in the bend, and as the curvature effect decreases downstream from the bend apex, the lateral water level slope decreases toward the exit of the bend. As a result, an adverse pressure gradient can occur along the inner bank, potentially causing flow separation (Blanckaert, 2010; Vermeulen et al., 2015). With flow separation, streamlines of the main flow detach from the inner bank and recirculating lee eddies are generated (Leopold, 1960; Leeder and Bridges, 1975). The separation zone has a lower water surface elevation than the main flow, and the resulting pressure difference around the bend creates form drag that can be a major contribution to the total drag (McCabe et al., 2006; Bo and Ralston, 2020). The drag associated with flow separation has been studied in laboratory experiments with unidirectional flow (e.g., Leopold, 1960; James et al., 2001), and Bo and Ralston (2020) conducted numerical model studies to investigate form drag and explain its parameter dependence in curved estuarine flows with idealized channels.

In this research we calculate from observations the drag coefficient in an estuary with channel curvature and intermittent stratification, and investigate factors potentially contributing to the observed drag coefficients that are greater than expected from bottom roughness alone. In sections 2.2 and 2.3, we introduce the field site, measurements, and data processing methods. The calculated drag coefficient and its dependence on tides and river discharge are shown in section 2.4. In section 2.5, we examine factors contributing to the increased drag, including evidence of flow separation and form drag at bends, dependence on overbank flow, and the influence of stratification. In section 2.6, we explain the increased drag and its variability, and discuss other potential contributors. Section 2.7 presents conclusions.

2.2 Observations

2.2.1 Field site

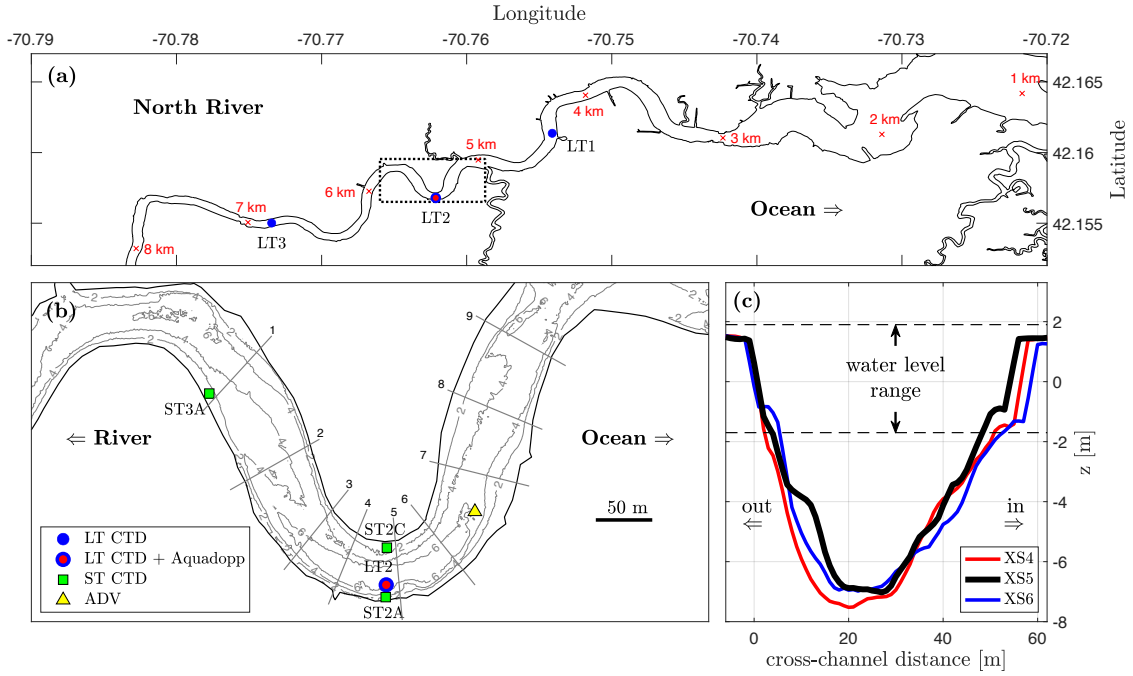

Figure 2-1: **(a)**: The North River estuary, with the intensive study area marked by the rectangle. Red crosses mark the along-channel distance from the mouth. **(b)**: The intensive study area with contours showing the bathymetry, with locations of long-term (LT) CTDs, short-term (ST) CTDs, Aquadopp profiler, and ADV measurements. Gray lines represent shipboard survey transects. **(c)**: Three cross-sectional profiles near the bend apex that correspond to transects 4, 5, 6 in **(b)**. The two dashed lines show the tidal water level range and $z = 0$ is the mean water level.

The field study was conducted in the North River estuary (Massachusetts, USA), a narrow, sinuous channel through a salt marsh (Figure 2-1 (a)). The tidal range of the North River varies between 2 m and 3.5 m. Intertidal marshes are widespread over the banks and are inundated during high spring tides. The North River has a modest discharge, based on USGS discharge measurements in a contributory stream upriver (station 01105730) that have been scaled up according to the total catchment area (Kranenburg et al., 2019). During the high-flow season of the spring, the discharge is typically $5 - 10$ m^3/s (corresponding to a mean velocity of $2 - 4$ cm/s in the mid-estuary) with increases of up to 30 m^3/s for rain-event peaks. In the low-flow season of summer, discharge is typically less than 5 m^3/s. The North River estuary is intermittently stratified, with seasonal variation that is examined in section 2.4.1.

The focus of this study is in the mid-estuary, centered around a sharp bend at about 5.4 km from

the mouth of the estuary. The mid-estuary channel has a typical width W of about 50 m and average depth H of about 5 m, i.e., an aspect ratio $W/H \approx 10$, which is common for salt marsh meanders (Marani et al., 2002). At the apex of the sharp bend that was the focus of the observations, the radius of curvature is $R \approx 60$ m, yielding a curvature ratio $R/W \approx 1.2$. Most other mid-estuary bends are less sharp, with a radius of curvature of around $100 - 200$ m and R/W of $2 - 4$. The range of R/W in the North River is representative of the bend sharpness generally found in sinuous rivers (Leopold and Wolman, 1960) and tidal channels (Marani et al., 2002), where R/W values are typically in the range of $1.5 - 5$ and sharp bends can have R/W of around 1 (e.g., Nanson, 2010; Schnauder and Sukhodolov, 2012; Marani et al., 2002). The cross-sectional profile at the sharp bend apex is approximately symmetric laterally, with relatively steep banks and no distinct point bar (Figure 2-1 (c)). Shallow shoals exist along the inner bank on the seaward side of the sharp bend, and also on the seaward side of the inner bank of the next bend landward.

Kranenburg et al. (2019) investigated the lateral circulation patterns at the apex of the sharp bend. The "normal" helical circulation for flow around a bend was observed during ebb tide, with inward flow near the bottom and outward flow near the surface. However, during flood tide, lateral circulation was reversed from the "normal" structure, with flow toward the inner bank near the surface and toward the outer bank in the lower layer. During both flood and ebb, streamwise velocity was greatest near the inner bank, which is consistent with potential flow due to curvature and indicates that friction does not play as big a role in shifting the velocity maximum toward the outer bank as is found in many river and laboratory meanders (e.g., Jamieson et al., 2013; Blanckaert, 2015). The lateral shear in the streamwise velocity creates lateral salinity differences through differential advection of the along-estuary salinity gradient. During ebbs the lateral baroclinic pressure gradient reinforces the "normal" lateral circulation, but during flood tides the lateral baroclinic forcing is outward and counteracts the inward barotropic pressure gradient (Kranenburg et al., 2019). Triggered by this lateral baroclinic forcing, the sense of secondary circulation can therefore be reversed during flood tide.

2.2.2 Measurements

The field measurements used in this study overlap with those from Kranenburg et al. (2019), including time series of velocity, pressure and salinity from April 4 to July 31 in 2017 (long-term (LT) moorings). While Kranenburg et al. (2019) investigated the lateral momentum balance and the resulting secondary circulation in the sharp bend, this study examines the drag that leads to along-

channel momentum loss in the sinuous North River estuary. Pressure and salinity were measured at three mooring locations by conductivity-temperature-depth (CTD) sensors sampled every 2 min: one mooring at the bend apex (LT2) and two at comparable distances down-estuary (LT1) and up-estuary (LT3) of the bend, i.e., 4.4, 5.4 and 6.9 km from the mouth respectively (Figure 2-1 **(a)**). Five CT/CTD sensors were deployed at LT2 with similar vertical spacing through the water column, and two CT/CTD sensors were deployed near the surface and bed at each of LT1 and LT3. The sensors nearest to the surface only measured conductivity and temperature. Velocity profile data were collected at the bend apex (same location as the LT2 CTD, about 15 m from the outer bank, Figure 2-1) by an upward-looking Aquadopp profiler (0.2-m vertical resolution, 10-min sample interval, 45-s averaging period) mounted on a bottom frame. The accuracy of water depth measurement is 0.01 m, and the accuracy of Aquadopp velocity measurement is 0.005 m/s. In addition, short-term (ST) CTD sensors were deployed at the inner (ST2C) and outer (ST2A) bank of the bend apex and at the south side of the up-estuary exit of the bend (ST3A) from April 18 to May 24 (Figure 2-1 (b)). Short-term CTDs were also deployed near the inner bank landward of the bend and near both banks seaward of the bend, but these deployments failed. Shipboard surveys were conducted on April 18, 19, and 27, May 17, and July 24, 25, 28, and 31 with an acoustic Doppler current profiler (ADCP, cell size 0.50 m, profile interval 0.25 s) over cross-sections $1-9$ through the bend and temperature-salinity profile measurements at lateral cross-sections 1, 3, 5, 7 and 9 (Figure 2-1 (b)). An acoustic Doppler velocimeter (ADV) was deployed near the bend apex (Figure 2-1 (b)) from July 24 to July 27 in 2017 for high-frequency velocity measurement (16-Hz sample rate, 12-min bursts) at about 0.5 m above the bed.

Bathymetric surveys of the study site were conducted using a Jetyak Unmanned Surface Vehicle (Kimball et al., 2014). The Jetyak was equipped with a bathymetric sidescan sonar, and a post-processing kinematic global navigation system sensor coupled to a inertial motion sensor for attitude heading reference and position measurements. The bathymetric sonar is optimized for shallow water surveys, and is capable of measuring seafloor topography with resolution and accuracy of better than 10 cm in both lateral and vertical dimensions in swath widths of up to 10 times the water depth. The final bathymetric output was gridded in 50-cm bins for overall bathymetry of the mid-estuary region (Figure 2-1), and selected areas were gridded at 20 cm for detailed analysis of bedform geometry.

2.3 Data processing methods

We calculated the drag in the North River estuary using multiple approaches. First, the drag coefficient C_D was calculated from the depth-averaged along-estuary momentum balance, and it represents the total momentum loss in the observation region. The along-estuary momentum balance includes the along-estuary time-mean water level gradient, which is not measured directly but is estimated from theory and forcing conditions. In addition, we estimated the drag coefficient $C_{D,energy}$ using the tidal energy flux balance since drag causes energy dissipation. In addition to these larger-scale estimates of the total drag, the bottom friction coefficient C_f was calculated from local high-frequency velocity measurements and reflects the near-bed shear stress.

2.3.1 Drag coefficient from the momentum balance

An approximate depth-averaged along-estuary momentum equation is

$$\frac{\partial U}{\partial t} = -g\frac{\partial \eta}{\partial s} - \frac{1}{2}\beta g\frac{\partial \langle S\rangle}{\partial s}H - \frac{C_D U|U|}{H}, \tag{2.2}$$

where we have neglected the advection and Coriolis terms. While advection can be a significant contributor to the local momentum balance in the bends, the advection term is less important when assessing the momentum budget at larger scales. η is the water level, $\langle S\rangle$ is the depth-averaged salinity and H is the water depth. s is the along-channel coordinate and β is the haline contraction coefficient. C_D is the drag coefficient used to represent the total flow resistance including bottom friction and other sources of drag. In this analysis, C_D is defined based on the depth averaged streamwise velocity U.

We can therefore calculate a drag coefficient that satisfies the momentum budget in the North River estuary using

$$C_D = \left(\frac{\partial U}{\partial t} + g\frac{\partial \eta}{\partial s} + \frac{1}{2}\beta g\frac{\partial \langle S\rangle}{\partial s}H\right) \Big/ \left(\frac{-U|U|}{H}\right). \tag{2.3}$$

U was measured by the Aquadopp profiler at the bend apex, and calculated as the vertical average of the velocity profile. The velocity has been extrapolated in the near-bed (0.4 m) and near-surface (~ 0.8 m) regions that are not covered by Aquadopp measurements due to the mount height, blanking distance, and surface interference. The tidal water level gradient and salinity gradient were calculated using LT1 and LT3 CTD measurements down- and up-estuary of the bend based on cen-

tered difference. In addition, the measured tidal water level gradient was adjusted to account for the time-mean along-estuary water level gradient that could not be assessed directly with the measurements (further explained in section 2.3.2). H is the laterally averaged water depth, with the time series of the single-location water depth recorded by the LT2 CTD at the apex and converted to a lateral average using data from shipboard cross-channel surveys. Average depth H is calculated for the channel width, and does not include the marsh extent for periods with overbank flow.

The drag term is quadratic with velocity and velocity is in the denominator of (2.3), and therefore we focus on the averaged C_D over 1-hr windows around maximum flood and ebb tide to reduce the sensitivity to low velocity periods. The calculated C_D applies to the total momentum loss at the scale of the spacing between the pressure sensors (~ 2.5 km) in the mid-estuary region that contains the sharp studied bend as well as several other bends that are less sharp.

2.3.2 Mean along-estuary barotropic pressure gradient

The measured instantaneous water level at each location is the free surface deviation from the local mean water level, i.e., $\eta' = h - \overline{h}$, where h is the instantaneous depth measured by CTD sensors and $\overline{h}$ is the time-mean depth. The time-mean depth is calculated using a low-pass filter over 33 hours to allow for longer term variation in the measurements that do not reflect the tidal dynamics (e.g., instrument drift or movement). The measured water levels are not referenced to an absolute vertical coordinate, and to obtain the absolute water level, the measured instantaneous water level η' must be corrected as

$$\eta = \eta' + \overline{\eta}, \tag{2.4}$$

where η is the absolute water level and $\overline{\eta}$ is the time-mean water level (varying at subtidal timescale) that was not directly resolved in the North River observations. The calculation of C_D was based on measurements of the instantaneous water level gradient in the along-estuary momentum balance, with the absolute water level gradient forcing being

$$g\frac{\partial \eta}{\partial s} = g\frac{\partial \eta'}{\partial s} + g\frac{\partial \overline{\eta}}{\partial s}. \tag{2.5}$$

The first term on the right side is the measured water level gradient forcing calculated between LT1 and LT3 CTDs. The second term is the unresolved time-varying mean (subtidal) water level gradient forcing that needs to be incorporated into the momentum balance.

A mean along-estuary water level gradient can be generated due to river inputs or by tidal

processes, and is typically a water level setup from seaward to landward. In the mean along-estuary momentum balance, the mean water level gradient forcing (barotropic pressure gradient, BTPG) is balanced with three forcing terms (Appendix A): the bottom friction from the mean flow, the tidal stress (e.g., Nihoul and Ronday, 1975), and the mean salinity gradient forcing (baroclinic pressure gradient, BCPG).

The bottom friction from the mean flow is estimated as (e.g., Nihoul and Ronday, 1975; Parker, 2007)

$$\tau_{b,\overline{u}} = -\frac{4}{\pi} C_f \rho \|U\| \overline{U}, \tag{2.6}$$

where C_f is the bottom friction coefficient, $\|U\|$ is the norm of tidal velocity, i.e., the amplitude of the periodic velocity, and $\overline{U}$ is the mean flow or residual current. $\overline{U}$ is typically seaward in the estuary, and is dominated by the freshwater discharge but also includes the Eulerian return flow of the landward Stokes drift of the tidal forcing (Zimmerman, 1979; Uncles and Jordan, 1980). $\overline{U}$ and $\|U\|$ were calculated from the depth averaged velocity measurements by the LT Aquadopp profiler at the bend apex (section 2.2.2). C_f was set as 3×10^{-3}, a typical value for bottom friction that is consistent with the ADV measurements (section 2.4.4).

The tidal stress is estimated as (e.g., Nihoul and Ronday, 1975; Zimmerman, 1978)

$$\tau_t = -\frac{1}{4} \rho g \frac{\partial}{\partial s} \left(\|\eta\|^2 \right), \tag{2.7}$$

where $\|\eta\|$ is the norm of tidal water level fluctuation, i.e., tidal amplitude. Details of the derivation are in Appendix A. τ_t is a manifestation of the radiation stress in a tidal wave (Zimmerman, 1978) and is in the direction of tidal amplitude decay. The tidal amplitude decay was calculated between the down-estuary (LT1) and up-estuary (LT3) moorings.

The mean depth-averaged BCPG (salinity gradient forcing) was calculated using

$$\text{mean BCPG} = -\overline{\frac{1}{2} \beta g \frac{\partial \langle S \rangle}{\partial s} H}, \tag{2.8}$$

where the salinity gradient was estimated between LT1 and LT3 CTDs and the overbar means time averaged (low-pass filtered results).

We can estimate the mean BTPG on the North River estuary from the mean momentum balance

by calculating the mean flow bottom friction, the tidal stress, and the mean BCPG, i.e.,

$$g\frac{\partial\overline{\eta}}{\partial s} = \frac{1}{\rho H}(\tau_{b,\overline{u}} + \tau_t) - \overline{\frac{1}{2}\beta g\frac{\partial\langle S\rangle}{\partial s}H}, \tag{2.9}$$

where $\overline{H}$ is the mean water depth (low-pass filtered H measured by the LT2 CTD). The absolute BTPG can therefore be calculated by substituting in (2.9) into (2.5)

$$g\frac{\partial\eta}{\partial s} = g\frac{\partial\eta'}{\partial s} + \frac{1}{\rho H}(\tau_{b,\overline{u}} + \tau_t) - \overline{\frac{1}{2}\beta g\frac{\partial\langle S\rangle}{\partial s}H}. \tag{2.10}$$

2.3.3 Drag coefficient from the energy flux balance

The second method to calculate the drag is based on the tidal energy budget. The energy flux balance for the depth-integrated tidal flow is (van Rijn, 2011)

$$\frac{\partial\|\eta\|}{\partial s} = 0.5(\gamma_w + \gamma_h)\|\eta\| - \frac{4C_D\|U\|^2}{3\pi g\overline{H}\cos(\Delta\phi)}, \tag{2.11}$$

where $\|\eta\|$ is tidal amplitude and $\|U\|$ is the amplitude of tidal velocity. $\Delta\phi$ is the phase difference between tidal water level and velocity. γ_w and γ_h are the convergence coefficients for channel width and depth.

$$\gamma_w = \frac{1}{L_w},\ \gamma_h = \frac{1}{L_h}, \tag{2.12}$$

with L_w and L_h being the e-folding scales for channel width and depth change. The channel depth convergence rate γ_h is set to be zero ($L_h = \infty$), because there is no clear trend in channel depth in the mid-estuary region. The channel width has an overall landward decreasing trend, although local variations exist with expansions and convergences of $O(100$ m). Exponential fitting to the channel width yields an $L_w \approx 20$ km.

We can calculate the drag coefficient by rearranging (2.11),

$$C_{D,energy} = \left(-\frac{\partial\|\eta\|}{\partial s} + 0.5(\gamma_w + \gamma_h)\|\eta\|\right)\frac{3\pi g\overline{H}\cos(\Delta\phi)}{4\|U\|^2}. \tag{2.13}$$

The tidal energy flux balance (2.13) provides a method to calculate the drag coefficient different from (2.3), as $C_{D,energy}$ represents the tidal energy loss due to drag. Tidal analysis was applied to the water level data collected by the three LT CTDs and the velocity U measured by the Aquadopp profiler at bend apex, with an analysis window length of 99 hours (eight M2 tidal cycles). Tidal amplitude $\|\eta\|$ was calculated from the LT2 CTD data, $\|U\|$ was from the Aquadopp profiler collocated

with the LT2 CTD, and $\Delta\phi$ is their phase difference. The tidal amplitude gradient was calculated between the LT1 and LT3 CTDs.

2.3.4 Bottom friction coefficient

The local near-bed shear stress was calculated from the high frequency ADV measurements near the bend apex. The bottom shear stress is quantified by the bottom friction coefficient C_f (similar to C_D, but only quantifies bottom stress), estimated using (e.g., Bowden and Fairbairn, 1956)

$$C_f = \frac{\overline{u'w'}}{\overline{u}^2} = \frac{\int S_{uw}\mathrm{d}k}{\overline{u}^2}. \tag{2.14}$$

$\overline{u}$ is the burst-averaged streamwise velocity. u' and w' are the temporal fluctuations of streamwise and vertical velocity around their means; $\overline{u'w'}$ is the Reynolds stress; S_{uw} is the wave number cospectrum of u' and w'.

Additionally, the C_f has been calculated from the near-bed dissipation rate ϵ (e.g., Kaimal et al., 1972) using law of the wall scaling

$$\epsilon = \frac{u_*^3}{\kappa z_a}, \tag{2.15}$$

where $u_* = \sqrt{\tau_b/\rho}$ is the shear velocity and τ_b is the bottom shear stress. $\kappa = 0.41$ is the von Kármán constant and $z_a = 0.5$ m is the height of ADV above the bed. Therefore,

$$C_f = \frac{u_*^2}{\overline{u}^2} = \frac{(\kappa z_a \epsilon)^{2/3}}{\overline{u}^2} \tag{2.16}$$

by substituting (2.15). ϵ is estimated from the wave number spectrum of w'

$$S_{ww}(k) = a_0 \epsilon^{2/3} k^{-5/3} \tag{2.17}$$

with $a_0 = 0.68$ (e.g., Tennekes et al., 1972).

2.4 Results

2.4.1 Estuarine conditions

The laterally averaged water depth at the bend apex in the North River estuary ranges between 2 m and 5.5 m as a result of tidal water level variation (Figure 2-2 **(a)**), with the tidal range varying

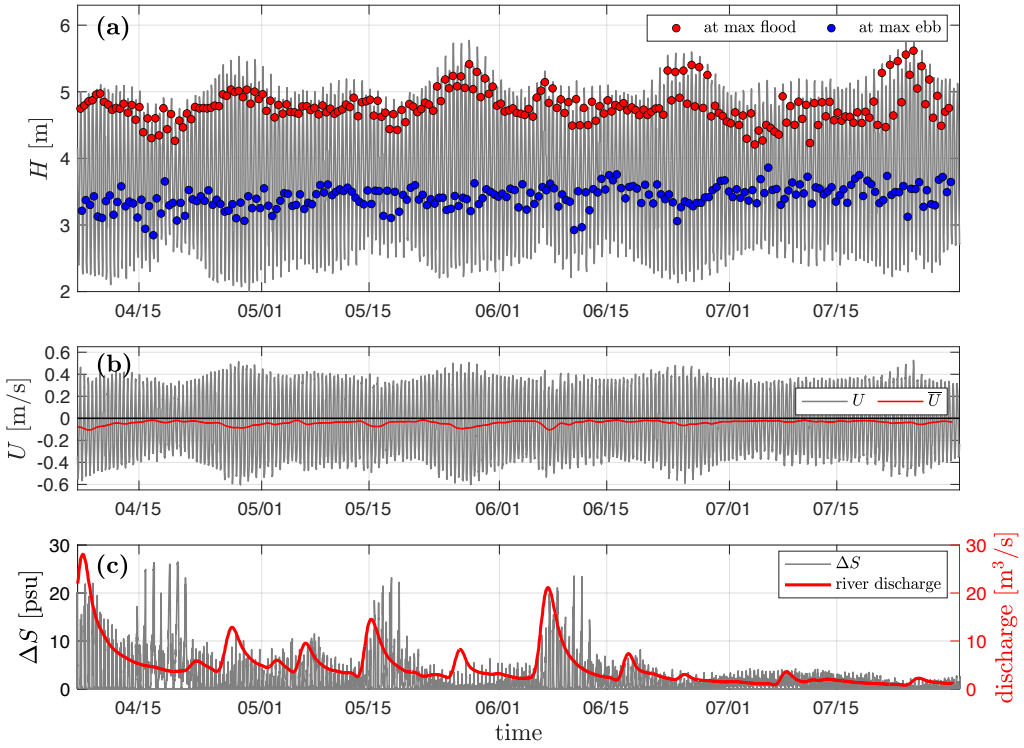

Figure 2-2: **(a)**: Water depth at the bend apex in the North River estuary. Red dots represent water depth at max flood tide; blue dots at max ebb tide. **(b)**: Black line: depth-averaged velocity at the bend apex; red line: low-pass filtered (33 hr) velocity. $U > 0$ is flood tide. **(c)**: Left axis: stratification (surface-to-bottom salinity difference) at the bend apex; right axis: river discharge.

between 2 m and 3.5 m from neap to spring tides . The water level is higher during flood tide than during ebb tide due to the phase difference between water level and velocity being less than 90 degrees (examined below). The tides are dominated by the semi-diurnal M2 tide (1.2-m amplitude), with contributions from the S2 constituent (0.1 m), N2 constituent (0.3 m), and the diurnal K1 constituent (0.1 m). Stronger and weaker spring-neap tides appear each lunar month due to the N2 tidal constituent. During the observation period, the stronger spring tides occur around the end of each month. At the mooring locations, the tidal amplitude ranges between 0.9 m and 1.5 m with increasing phase lag from LT1 to LT3 (Figure 2-3 **(a)**). The tidal amplitude is similar between LT1 and LT2, and decreases at LT3. Note that the analysis used a 99-hr low-pass filter window, so the calculated tidal amplitude may be slightly different from the range of fluctuations in the original water depth record. The tidal velocity amplitude varies between 0.35 m/s and 0.55 m/s and the velocity phase leads that of the water level by 45 (spring tides) to 55 (neap tides) degrees, so the tidal wave is partially progressive (Figure 2-3 **(b)**).

Stratification is calculated as the surface-to-bottom salinity difference ΔS (Figure 2-2 **(c)**). Stratification is stronger early in the observation period (before mid-June) due to the greater freshwater discharge. The greatest stratification (e.g., $\Delta S > 10$ psu) is found during high discharge events or neap tides. Tidally, stratification is most common from max flood tide through late flood and early ebb tide, and ΔS is less than 1 psu at max ebb tide except for during the weakest neap tides (less than 10% of the data record). Stratification is weaker in the summer (after mid-June) when freshwater discharge is less, with peaks of $\Delta S \sim 1 - 5$ psu during early flood and ebb tides and $\Delta S < 1$ psu most of the rest of the tidal cycle. Therefore we describe the North River estuary as intermittently stratified.

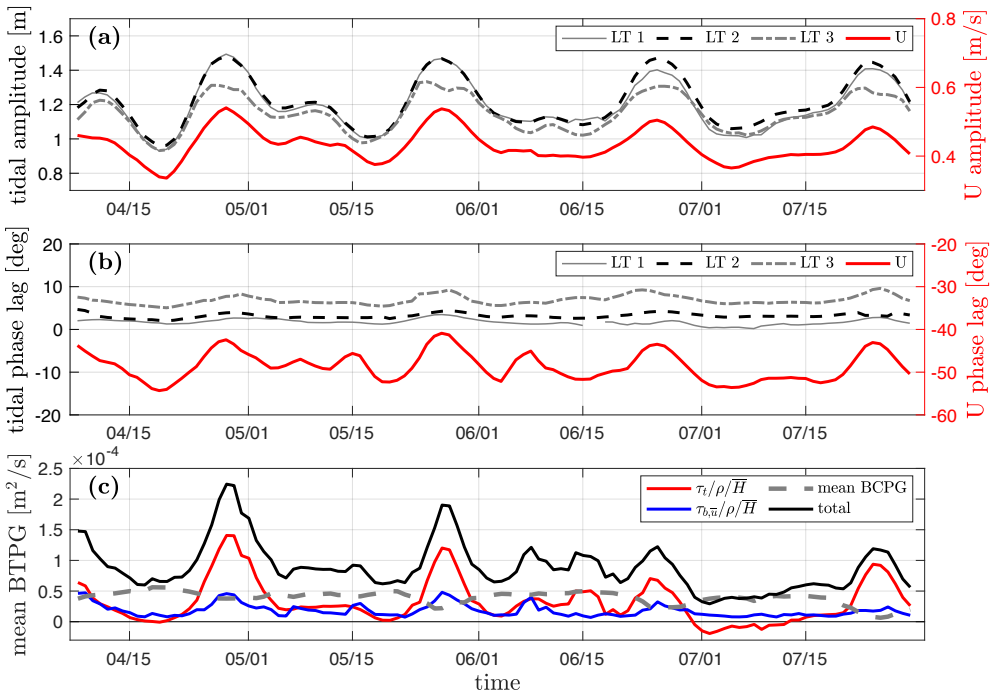

Figure 2-3: **(a)**: Left axis: tidal amplitude at LT1, LT2, and LT3; right axis: velocity amplitude at LT2. **(b)**: Left axis: tidal phase lag at LT1, LT2, and LT3, referenced to the tidal phase near the estuary mouth; right axis: velocity phase lag at LT2. Note the difference in vertical axis range. **(c)**: Terms that contribute to the mean along-channel BTPG. The red line represents the tidal stress; the blue line represents the mean bottom friction; the dashed gray line represents the mean BCPG; the black line is the total of the above three terms that is balanced by the mean BTPG.

The time-mean BTPG on the North River estuary was estimated using the mean momentum balance (2.9) by calculating the tidal stress, the mean flow bottom friction, and the mean BCPG (Figure 2-3 **(c)**). The mean flow friction increases during high discharge periods or high spring tides when a stronger mean current is generated due to greater Stokes drift (e.g., Uncles and Jordan,

1980); the tidal stress increases during high spring tides because tidal decay is more rapid when tidal forcing is stronger (Appendix A); the mean BCPG decreases during high spring tides because of the greater salinity intrusion length. The three terms have similar magnitudes, but the tidal stress is more sensitive to tidal forcing and can be dominant during high spring tides. The time-mean BTPG calculated from these three terms is large during large spring tides (e.g., in late April, May, June, and July) and during several high discharge events (e.g., in early April and early June). The seaward mean flow results in a landward bottom friction. The tidal stress is in the direction of decreasing tidal amplitude, so it is mostly landward in this shallow and weakly-converging estuary, except in early July when the tidal stress becomes seaward because the tidal amplitude is larger at mooring site LT3 than LT1 (Figure 2-3 **(a)**). The mean BCPG has a landward forcing because salinity decreases from seaward to landward. The mean BTPG balances these three terms, and always provides a seaward forcing during the observational period (Figure 2-3 **(c)**), i.e., a water level setup at the landward side.

2.4.2 Drag

The drag coefficient C_D is calculated using (2.3) (Figure 2-4 **(a)**) and it represents the total momentum loss between mooring sites LT1 and LT3. The total BTPG is the dominant term that balances the drag in the momentum budget, similar to other studies in the coastal regions (e.g., Lentz et al., 2017; Rogers et al., 2018; Monismith et al., 2019). The BCPG is about an order of magnitude smaller than the BTPG in most of the observational period, except during neap tides and high discharge events when the BCPG can be up to 30% of the BTPG for ebb tides and 50% for flood tides. The C_D values calculated from the mooring observations are generally in the range of $5 \times 10^{-3} - 20 \times 10^{-3}$ (Figure 2-4 **(a)**). C_D values during both flood and ebb tides are higher than the typical values of $\sim 3 \times 10^{-3}$ and show large temporal variability. Averaging over the observation period, C_D is greater during flood tide (12×10^{-3}) than ebb tide (10×10^{-3}) (Figure 2-4 **(c)**). The highest calculated values (up to 25×10^{-3}) correspond to flood tides, and flood tide C_D values are notably greater than ebb values during high spring tides, e.g., late April, late May and late July. Application of the two-sample t-test to the flood C_D and ebb C_D indicates that they have unequal means and the flood-ebb asymmetry is significant.

A seasonal difference can also be observed in ebb tide C_D (Figure 2-4 **(e)**). Most high values of C_D during ebb tide (e.g., $> 10 \times 10^{-3}$) are found in the low-flow season (starting from mid-June), resulting in a higher average C_D in the low-flow season (11×10^{-3}) than in the high-flow season

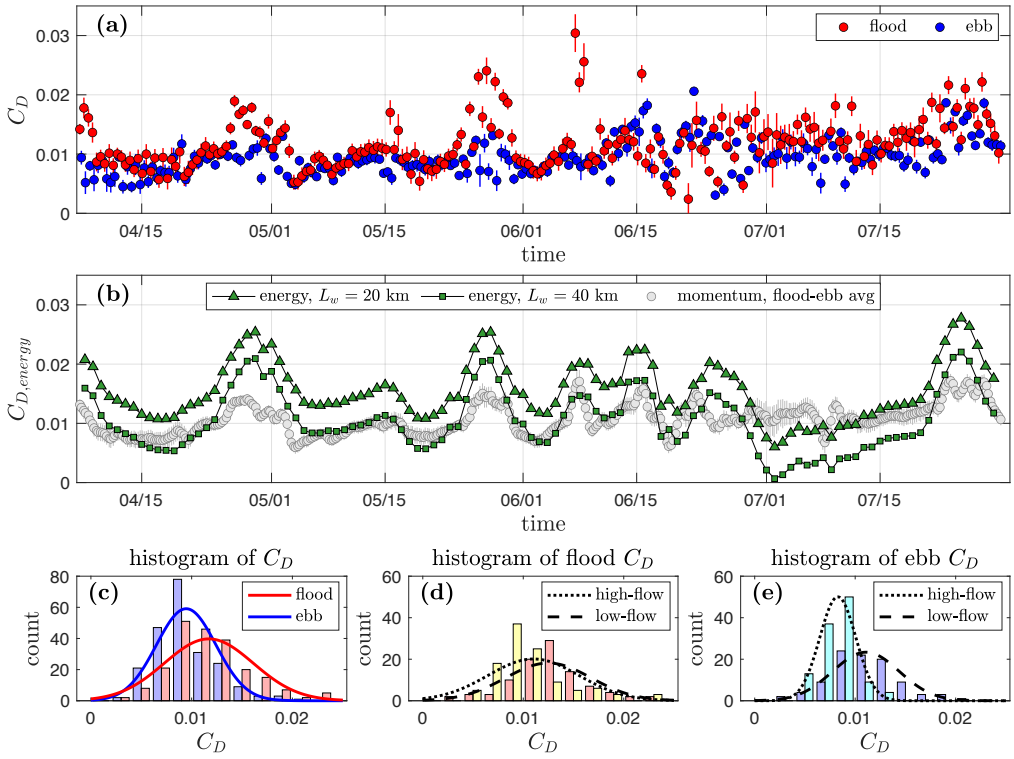

Figure 2-4: **(a)**: Drag coefficient C_D in the North River estuary calculated from the momentum balance. Red dots represent C_D at max flood tide; blue dots at max ebb tide. Vertical lines show the larger of the instrument error and the standard deviation within each 1-hr window around max flood and ebb tide. **(b)**: Drag coefficient $C_{D,energy}$ calculated by energy flux balance. Green triangles are based on a width convergence distance $L_w = 20$ km; green squares use $L_w = 40$ km; gray circles are the flood-ebb averaged C_D from momentum balance in **(a)**. **(c)**: Histograms of flood tide C_D and ebb tide C_D. **(d)**: Histograms of high-flow season flood C_D (before mid-June) and low-flow season flood C_D (after mid-June). **(e)**: Histograms of high-flow season ebb C_D and low-flow season ebb C_D. Lines show the Gaussian curve fits.

(8×10^{-3}). In contrast, flood tide C_D has a less clear seasonal difference (Figure 2-4 **(d)**), with average values of 12.5×10^{-3} in the low-flow season and 11×10^{-3} during high flow.

It is worthwhile to note that the calculation of C_D includes the estimation of the time-mean BTPG (section 2.4.1). The seaward mean BTPG opposes the tidal BTPG during floods, and it is additive to the tidal BTPG during ebbs. The mean BTPG on average corresponds with an adjustment of C_D of $2 - 3 \times 10^{-3}$ ($20 - 30\%$ of the total C_D), and including the mean BTPG reduces the tidal asymmetry in the calculated C_D.

$C_{D,energy}$ is calculated from the energy flux balance using (2.13) (Figure 2-4 **(b)**) and it reflects the tidal energy dissipation. Generally $C_{D,energy}$ is $5 \times 10^{-3} - 20 \times 10^{-3}$ with the largest values during high spring tides, in agreement with the C_D from the momentum balance. $C_{D,energy}$ calculated using $L_w = 20$ km, as suggested by the exponential fitting (section 2.3), is generally greater than the tidally averaged C_D from the momentum budget. Using $L_w = 40$ km instead results in $C_{D,energy}$ values that are more consistent with the momentum calculation. $C_{D,energy}$ has particularly low values around July 1 when the tidal amplitude increases from LT1 to LT3 (Figure 2-3 **(a)**). The overall high values of $C_{D,energy}$ indicate a high rate of tidal energy dissipation that is broadly consistent with the high C_D calculated from the momentum balance. Moreover, the calculation of $C_{D,energy}$ is independent of estimation of the mean BTPG since it is based on the tidal amplitude decay rate instead of the instantaneous water level gradient. The values of $C_{D,energy}$ that are comparable with momentum-balance estimates of C_D provide corroborating evidence for the high values of effective drag coefficient.

In the following analysis, we used the C_D from the momentum balance, since it can be assessed for each flood and ebb tide and because it does not require estimation of the channel convergence rate.

2.4.3 Uncertainty of the calculated drag coefficient

The uncertainty in the C_D calculated from the momentum balance is contributed by two categories of factors: instrument error and estimation of the momentum budget. Based on the accuracy of the pressure sensors and velocity measurements, we estimate that the instrument error leads to a relative uncertainty in C_D of less than 10%. The approximation of the momentum budget from observed quantities also introduces uncertainty in the calculated C_D, because estimation based on single-location measurements cannot fully represent the cross-channel and along-channel variability of the North River estuary, and because we have made simplifications to the momentum equation, e.g.,

neglecting the advection term and estimating the time-mean pressure gradient. The drag term is greatest and most insensitive to errors induced by different sources of uncertainty around maximum flood and ebb tide, so the reported values of C_D are for 1-hr windows around max tides.

The velocity data were collected by the LT2 Aquadopp near the outer bank, but the depth-averaged velocity also can have lateral variability. Therefore, the Aquadopp data were compared with the cross-sectional average velocity from ADCP surveys near the mooring. Based on comparison of ten tides, the Aquadopp measurements were nearly the same as the cross-channel average, with less than 5% deviation. Therefore, using the depth-averaged velocity from the mooring is not likely to cause significant bias or uncertainty in C_D. Cross-channel bathymetry is not uniform at the bend apex, and we have used the laterally-averaged depth H as being more representative than the single depth at the velocity measurement location.

The LT2 mooring site was near the bend apex, and the lateral structure of the depth and velocity also varies along the channel. To estimate the influence of the along-channel geometry on C_D, we integrated the momentum balance along the channel between LT1 and LT3 following a method as in Lentz et al. (2017). This approach uses bathymetric data and assumes mass flux conservation to estimate the velocity variability, and simplifies the momentum balance to a balance between the water level gradient and drag. Based on this along-channel integration, we estimate that along-channel variability in channel geometry may reduce the C_D calculated at the bend apex by up to 10% for flood tide and up to 30% for ebb tide. This is due to the width convergence and depth decrease landward of the bend, which in the along-channel integration corresponds with increased velocity and a reduction in C_D. Ebb tide C_D is more sensitive to along-channel depth variations than flood tide, because water is shallower during ebbs. The along-channel variability of bathymetry may contribute to larger values of C_D calculated at the bend, but it is not a sufficient explanation, particularly for flood tides when the highest drag was observed. Furthermore, the channel geometry factors alone suggest that ebb tide C_D would be larger than flood tide C_D, but the opposite flood-ebb asymmetry was observed. Incorporating more accurate estimates of the along-channel variability in the momentum budget could lead to lower values of C_D and enhance the observed flood-ebb asymmetry, but that would require much better spatial resolution of velocity and water level.

The advection and Coriolis terms were neglected when simplifying the momentum equation, and the resulting uncertainty is estimated to be small. The estimated time-mean pressure gradient is an order of magnitude smaller than the directly measured tidal pressure gradient, so the uncertainty in the estimation of time-mean pressure gradient represents a higher-order error for the tidal

momentum balance and calculation of C_D, and is thus negligible.

The standard deviation of C_D was reported for each 1-hr window around max flood and ebb tides to show the potential uncertainty caused by estimation of the momentum budget. The standard deviation of C_D is generally less than 10% of the drag value except from late June to early July (Figure 2-4 **(a)**), when it can be in the range of 10% to 40%. Note that the along-channel variability may introduce a bias that is not totally accounted for by the reported standard deviations, so C_D could be up to 10% - 30% lower than the plotted error bars, especially for ebb tides. Overall, the uncertainty estimates are modest compared to the magnitude and temporal variability of C_D in the observations, and the drag estimates from the momentum balance are considered to be robust based on the uncertainty analysis.

2.4.4 Local bottom shear stress

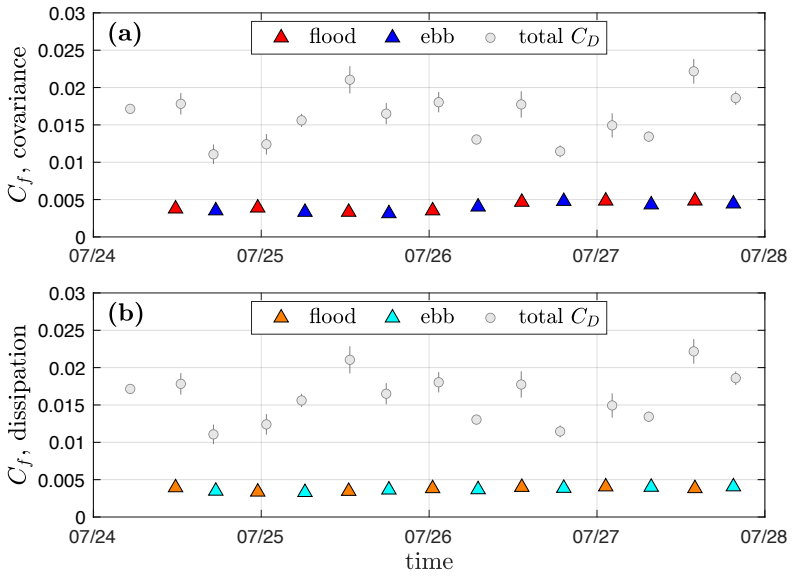

Figure 2-5: ADV measurement from July 24 to July 27. **(a)**: Bottom friction coefficient C_f calculated from the covariance method (2.14), (triangles, averaged over multiple ADV bursts in flood or ebb tides). Gray circles show the total C_D from momentum balance in Figure 2-4 **(a)** as a comparison. **(b)**: Bottom friction coefficient C_f calculated from the dissipation method (2.16).

The bottom friction coefficient C_f was estimated using both (2.14) and (2.16). The tidal-phase averaged values of C_f from the ADV measurements are consistent between the two methods, and range between 3×10^{-3} and 5×10^{-3} (Figure 2-5), which is similar to values for C_D due to bottom roughness in other estuaries (e.g., Heathershaw and Simpson, 1978; Seim et al., 2002). However,

C_D calculated from the momentum balance during the same time period ranges between 11×10^{-3} and 18×10^{-3} for ebb tides and $13 \times 10^{-3} - 22 \times 10^{-3}$ for flood tides. The total drag C_D is larger than the bottom stress C_f by a factor of $3 - 5$, indicating the existence of other sources of drag in addition to bottom friction. Form drag due to flow separation at sharp channel bends could contribute to this high total drag, as well as other potential factors including secondary circulation in bends, form drag from bedforms in the channel, and friction from flow through marsh vegetation.

2.4.5 Dependence on water depth and discharge

Tides and river discharge provide the dominant forcing in this estuary, and we investigate the dependence of C_D on these two factors. Tidal conditions could affect the drag through creating variation in water level, velocity amplitude, and flow structure. The calculated C_D does have a slightly increasing trend with water depth, with $R^2 = 0.1$ and p-value < 0.001 (Figure 2-6 **(a)**). C_D does not correlate with the tidal velocity ($R^2 = 0.0$, p-value > 0.05, not shown). The depth dependence primarily reflects the flood-ebb asymmetry in C_D noted previously. Water levels are higher during flood tides than ebb tides (Figure 2-2 **(a)**), and flood tide C_D has a greater average value than ebb tide C_D. The flood-ebb asymmetry in C_D is most apparent during high spring tides (Figure 2-4 **(a)**) when the flood-ebb difference in water level is also greatest (Figure 2-2 **(a)**). In addition, zooming in on the cases with overbank flow, C_D shows a decreasing trend with water depth for overbank flow conditions, opposite to the overall increasing trend. Possible reasons for the observed depth dependence of C_D will be investigated in the following analysis.

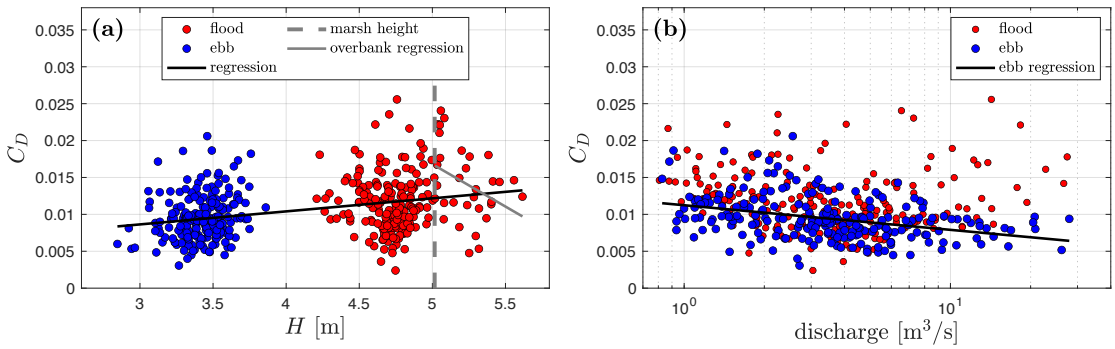

Figure 2-6: **(a)**: Drag coefficient vs. water depth at the bend apex. Linear regressions give $R^2 = 0.10$ (p-value < 0.001) for the overall data and $R^2 = 0.14$ (p-value $= 0.03$) for the overbank cases (water depth exceeds marsh height). **(b)**: Drag coefficient vs. river discharge. $R^2 = 0.13$ (p-value < 0.001) for ebb tides, and $R^2 = 0.00$ (p-value > 0.05) for flood tides.

River discharge creates a seaward mean flow that influences the salt balance in addition to mo-

mentum, and thus affects the salinity intrusion, along-estuary salinity gradient, and stratification (Geyer, 2010). The salinity field affects the momentum budget through the along-estuary BCPG, and stratification can also reduce drag by damping turbulence. In the observations, the ebb tide C_D has a negative correlation with river discharge (Figure 2-6 **(b)**). This negative correlation is reflected in the seasonal trend in ebb tide C_D, where lower ebb C_D values occur during the higher discharge season, and ebb C_D values increase in summer as river discharge decreases (Figure 2-4 **(e)**). In contrast, the flood tide C_D shows no significant dependence on river discharge, and this corresponds with the less apparent seasonal variation in flood C_D values (Figure 2-4 **(d)**). Factors that may be contributing to the observed discharge dependence will also be addressed in the analysis.

2.5 Analysis

2.5.1 Flow separation and adverse pressure gradient

The high C_D in the North River estuary suggests the existence of other sources of drag beyond bottom friction, and one source could be flow separation in the lee of bends (e.g., Leopold, 1960; Leeder and Bridges, 1975). An idealized modeling study by Bo and Ralston (2020) found that flow separation in sinuous estuarine channels results in significant form drag. In a sinuous channel with geometric parameters similar to the North River (e.g., bend sharpness, aspect ratio), the total C_D increased to around 12×10^{-3} due to flow separation and the resulting form drag. In the model results, C_D also increased with water depth in a manner consistent with the tidal differences in water level and C_D observed in the North River (section 2.4.5). The positive depth-dependence in the model study was because the flow separation and form drag became stronger in deeper water (Bo and Ralston, 2020).

In the cross-channel ADCP surveys in the North River, flow separation was observed in the velocity field downstream of the sharp bend (Figure 2-7). Depending on the tide, flow near the inner bank was decelerated relative to the main current, and in some cases flow reversal was observed in the lee of the bend. Similar patterns of flow separation and reversal were also found in field, laboratory, and modeling studies of curved channels, e.g., Ferguson et al. (2003), Finotello et al. (2020), Blanckaert (2015), and Bo and Ralston (2020). In many river bends, point bars form at the inner bank, and the shallower bathymetry there leads to topographic steering and contributes to the deceleration of flow at the inner bank (e.g, Dietrich and Smith, 1983). In the North River bend, the cross-channel bathymetry is relatively symmetric (section 2.2.1) so the deceleration and flow

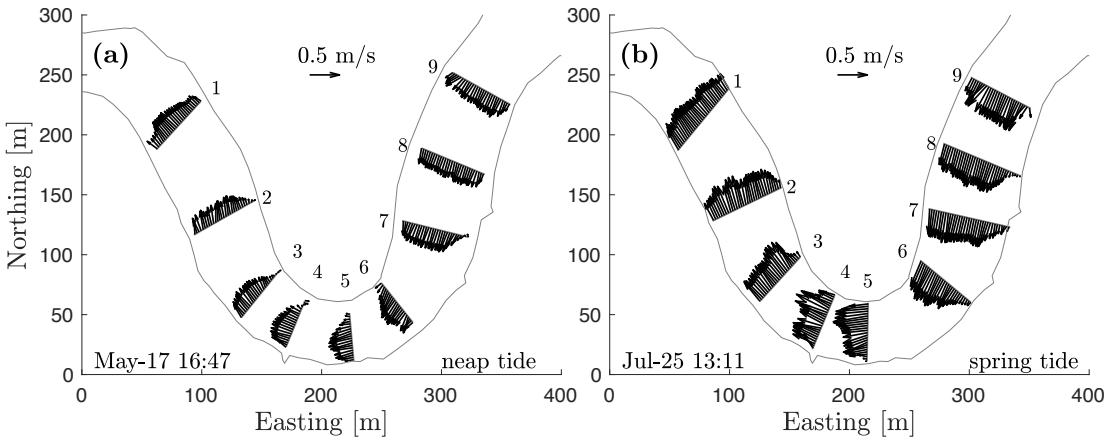

Figure 2-7: Depth-averaged velocity field during flood tides. **(a)**: Neap flood tide in mid-May. **(b)**: Spring flood tide in early July.

reversal near the inner bank is not primarily due to topographic steering (Kranenburg et al., 2019). Instead the curvature effect on the pressure field is likely the predominant mechanism for generating the observed flow separation.

The channel curvature results in a cross-channel water level slope at the apex of this bend (Kranenburg et al., 2019), while the lateral differences in water level upstream and downstream of the bend are nearly zero. As a result, the water level at the inner apex is lower than the downstream exit of the bend, and an adverse pressure gradient occurs along the inner bank downstream of the apex. This adverse pressure gradient can lead to convex bank flow separation and produce a low pressure "separation zone" in the lee of bends that thus creates the form drag (e.g., Ferguson et al., 2003; Blanckaert, 2010; Blanckaert et al., 2013; Bo and Ralston, 2020).

We examine the pressure gradient downstream of the bend apex to assess the potential for flow separation and form drag. We have focused on the flood tide in the adverse pressure gradient analysis because the short-term (ST) instrument array better resolved the local pressure gradient during the flood (section 2.2.2). The water level difference ($\Delta\eta$) between the CTD downstream of the bend (ST3A) and the CTD at the apex near the inner bank (ST2C) was calculated to estimate the along-inner-bank pressure difference (Figure 2-8). In doing so, we have assumed that the water level is laterally uniform at the downstream exit, and the ST3A measurement at the outer bank can represent the inner bank water level. This assumption is reasonable because channel curvature is weak there (Figure 2-8 **(d)**), and Kranenburg et al. (2019) reported negligible lateral water level differences at the exit of this bend. Note that we have focused on the barotropic pressure, i.e., the water level, be-

cause the baroclinic pressure gradient is usually much smaller. The measured $\Delta\eta$ is on the order of centimeters, comparable to the instrument accuracy and the high-frequency water surface variability due to capillary waves and boat wakes. Thus, the data have been averaged over 2-min intervals (360 samples) to reduce random noise and instrument error and increase measurement precision.

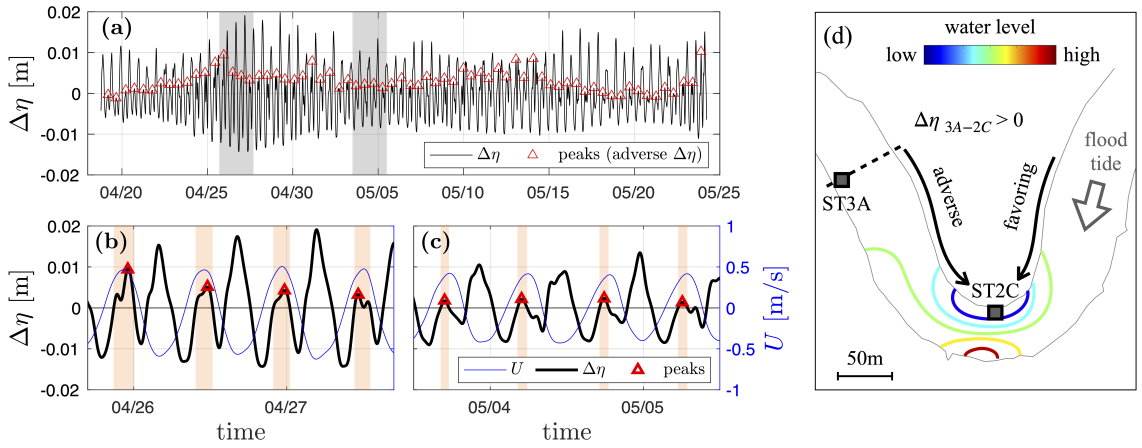

Figure 2-8: **(a)**: Water level difference ($\Delta\eta$) between CTDs ST3A and ST2C. Red triangles mark the peaks of adverse η_s. The gray bands represent the zoomed-in time periods shown in panels **(b)** and **(c)**. **(b)**, **(c)**: $\Delta\eta$ and adverse $\Delta\eta$ in late April (spring tide) and early May (neap tide). The left vertical axis shows $\Delta\eta$ (black line) and the right vertical axis shows U (blue line) – the depth-averaged velocity at the apex. Orange bands mark the periods when adverse pressure gradient appears. $U > 0$ is flood tide. **(d)**: A schematic of the adverse pressure gradient in the bend, with contours of the water level field.

The water level difference $\Delta\eta$ is positive during ebb tide (Figure 2-8), consistent with the downstream favoring pressure gradient that drives the seaward current. Entering flood tide, the flow direction turns and $\Delta\eta$ becomes negative, consistent with a favoring pressure gradient. However, as the landward tidal current keeps growing, the adverse pressure gradient associated with the curvature effect occurs and this can be seen in the upward peaks in $\Delta\eta$ during flood tides in Figure 2-8. This positive, or adverse, $\Delta\eta$ around max flood tide creates the adverse pressure gradient downstream of the bend along the inner bank that corresponds with flow separation.

To assess the potential influence of flow separation and form drag on the observed C_D, we examine the correlation between the drag and adverse pressure gradient along the inner bank. The adverse pressure gradient was calculated using the short-term measurements (in April and May), so only the corresponding part of the C_D record (calculated using the long-term moorings) is examined. The C_D calculated from the large-scale LT measurements is significantly correlated with the bend-scale adverse $\Delta\eta$ from ST measurements ($R^2 = 0.25$ and p-value < 0.001), with C_D increasing as

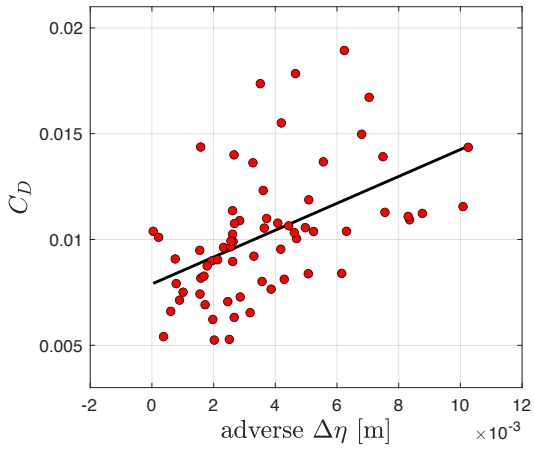

Figure 2-9: Correlation between the drag coefficient and adverse $\Delta\eta$ that appears at flood tide. $R^2 = 0.25$ (p-value < 0.001).

the adverse pressure gradient increases (Figure 2-9). While the spatial and temporal coverage of the observational data is limited, the trends in the available evidence are consistent with the explanation that flow separation, as reflected in the strength of the adverse pressure gradient measured at the sharp bend of the study, contributes to the high drag found in the North River estuary.

The adverse pressure gradient for ebb tide is not investigated due to the lack of pressure measurement at the down-estuary exit of the bend. Flow separation was also observed in the ebb tide velocity field with decelerated flow near the inner bank (not shown), although the velocity field during ebb is also affected by topographic steering associated with the relatively shallow shoal near the inner bank at the down-estuary side of the bend (Figure 2-1). According to the previous idealized modeling results, flow separation is expected to be weaker during ebb tide because of the shallower water depth and greater influence of friction (Bo and Ralston, 2020).

2.5.2 Overbank flow

During high spring tides, the water level exceeds channel bank height and marshes are inundated. The marsh height at the bend apex corresponds to a water depth of ~ 5 m. The high spring tides in late May and late July are plotted in Figure 2-10 as an example. Water level displays a diurnal variation due to the K1 tidal component and channel flow substantially goes onto the marsh at the higher flood tide, every other tidal cycle.

The drag coefficient also shows a diurnal variation, with C_D that is smaller during the flood tides that have overbank flow compared to the prior and subsequent tides. The marsh platform is

vegetated, and the overbank flow through the marsh vegetation might be expected to increase the total drag due to stem friction. Instead, the total drag is decreased with overbank flow. The reduced values of C_D during flood tides with overbank flow also is counter to the overall relationship of drag increasing with water depth (Figure 2-6 **(a)**), and is opposite to the depth dependence expected from flow separation (Bo and Ralston, 2020).

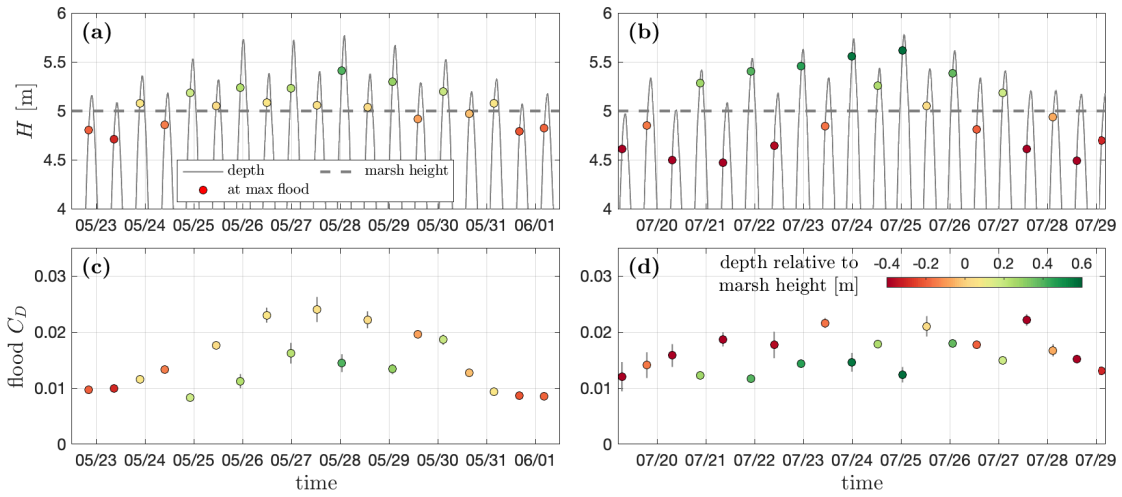

Figure 2-10: Water depth H and flood-tide drag coefficient C_D during high spring tides in late May and late July. **(a)**: Water depth in late May; **(b)**: water depth in late July; **(c)**: flood tide C_D in late May; **(d)**: flood tide C_D in late July.

A potential explanation for the decrease in C_D with overbank flow could relate to the inhibition of flow separation. While deeper water facilitates flow separation, increased bottom friction due to the shallow overbank flow and stem friction from flow through vegetation could inhibit flow separation. The frictional effect is illustrated by dimensionless numbers from theoretical models that predict flow separation, e.g., $H/(C_f W)$ in Blanckaert (2010) where H is water depth, C_f is the friction coefficient, and W is channel width, and $H/(C_f L)$ in Bo and Ralston (2020) with L being the bend length. The underlying mechanism of these theoretical models is that stronger bottom friction diminishes the local adverse pressure gradient along the inner bank and inhibits flow separation. The effective C_f increases for overbank flow because of both the shallower water depth over the marsh and the stem friction of vegetation. As a result, flow separation that creates form drag is inhibited when flow goes onto the marsh and the total drag is decreased, even though locally flow over the marsh has relatively large friction. The overbank flow effect is reflected in the depth dependence plot, where C_D shows a decreasing trend when water depth exceeds the marsh platform height (Figure 2-6 **(a)**). Similar results were reported for laboratory experiments by Marriott (1998)

where flow separation occurred in a sinuous channel but did not occur when flow was overbank. Similarly, James et al. (2001) found that vegetation can inhibit flow separation in sinuous laboratory channels and decrease the total drag, consistent with the decreased C_D for flow over the marsh in the North River estuary.

2.5.3 Stratification and baroclinic effects

The dependence of C_D on river discharge (Figure 2-6 **(b)**) suggests that baroclinic effects may play a role in flow separation and the drag. In this subsection, we describe an observed interaction between stratification and secondary circulation during ebb tides, and propose a baroclinic mechanism that can potentially reduce the adverse pressure gradient along the inner bank, and thereby inhibit flow separation and decrease the drag.

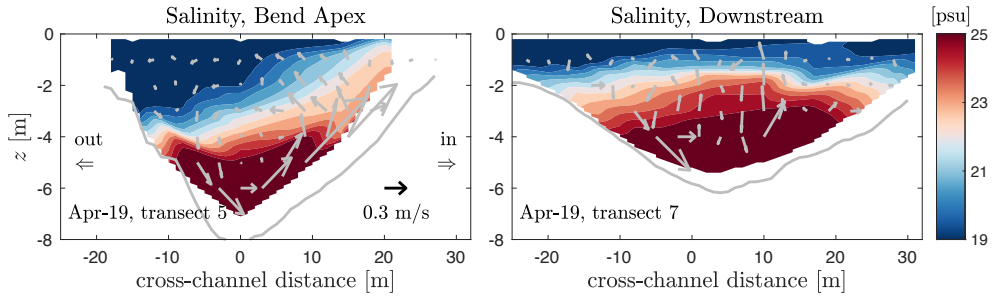

Figure 2-11: Salinity and secondary circulation in two cross-sections at the apex (transect 5) and downstream (transect 7) during an early ebb tide with strong stratification.

During ebb tides, a normal secondary circulation is observed in the cross-section at the apex (Figure 2-11). When the channel is stratified, this normal secondary circulation brings high salinity water to the inner bank and tilts the isohalines up near the bend apex. Downstream of the bend, the lateral circulation is weaker and has less effect on the lateral salinity distribution, so the isohalines are relatively flat. Similar isohaline tilting has been observed in, e.g., Seim and Gregg (1997); Chant (2002). The lateral circulation resulting from flow curvature creates a bulge of high salinity water near the inner bank at the bend apex. During the ebb, this high salinity at the inner bank of the apex exerts a favoring baroclinic pressure gradient downstream of the apex that counteracts the adverse barotropic pressure gradient downstream of the bend created by the flow curvature (section 2.5.1). Consequently, the interaction between the lateral circulation and stratification could inhibit flow separation, and reduce the form drag around bends.

The next question is whether the favoring baroclinic pressure gradient along the inner bank due

to the lateral circulation is large enough to balance the barotropic adverse pressure gradient created by the curved streamwise flow. The baroclinic pressure gradient can be directly calculated using $\beta g(\partial S_{in}/\partial s)H_{in}$, where S_{in} and H_{in} are the depth-averaged salinity and depth at the inner bank. The barotropic pressure gradient is estimated from the along-inner-bank momentum balance

$$g\frac{\partial \eta_{in}}{\partial s} = -U_{in}\frac{\partial U_{in}}{\partial s} - C_f\frac{U_{in}|U_{in}|}{H_{in}} = adv. + fricț., \tag{2.18}$$

where U_{in} is the depth-averaged velocity at the inner bank. On the right side of (2.18) are the advection and friction terms that determine adverse pressure gradient and flow separation in homogeneous fluids (Bo and Ralston, 2020). The barotropic and baroclinic pressure gradients are estimated using the cross-channel surveys during an early ebb tide on April 19 (transects 5 and 7, Figure 2-7). U_{in} and H_{in} are calculated from the cross-channel ADCP measurements and S_{in} is from the shipboard CTD measurements, each taken as the average over 10 m from the inner bank ($S_{in} = 22.6$ psu at transect 5 and $S_{in} = 20.9$ psu at transect 7, Figure 2-11). The advection term contributes to an adverse pressure gradient and the friction term contributes to a favoring pressure gradient, which is consistent with theoretical models that predict flow separation in Signell and Geyer (1991) and Bo and Ralston (2020). The barotropic pressure gradient that is the sum of the advection and friction terms is positive ($\sim$ 1 to 6 $\times$ 10^{-4} m/s^2), indicating an adverse pressure gradient that can cause flow separation downstream of the apex. In contrast, the baroclinic pressure gradient is negative ($\sim -2 \times 10^{-4}$ m/s^2) and can counteract the adverse pressure gradient. Downstream of the apex, the favoring baroclinic pressure gradient is of the same order of magnitude as the adverse barotropic pressure gradient, suggesting that the salinity effect has the potential to inhibit flow separation.

This baroclinic inhibition of flow separation may explain the variation in ebb tide C_D with the river discharge (Figure 2-6 **(b)**). The along-inner-bank baroclinic pressure gradient results from the interaction between the stratification and secondary circulation during the ebb tide. Stratification is stronger in the high-flow season, which can lead to stronger baroclinic pressure gradients and weaker flow separation, and thus reduce ebb tide C_D. Under low-flow conditions, stratification is weak, and while the lateral circulation is still present, the baroclinic pressure gradient due to tilting of isopyncals disappears.

The direct effects of stratification on damping turbulence and reducing the bottom friction could be another reason for the observed negative correlation between ebb tide C_D and discharge. Stratification becomes stronger during higher discharge periods and it can inhibit turbulence (Geyer,

1993a), alter vertical momentum distribution, and decrease the bottom shear stress. However, the bottom stress is not the dominant contributor to the total C_D (section 2.4.4), and the inhibition of bottom friction alone is insufficient to explain the discharge dependence of C_D. The variation in ebb tide C_D with river discharge is more than 5×10^{-3} (Figure 2-6 **(b)**), which is greater than the local estimates of C_f (Figure 2-5).

The ebb tide C_D is negatively correlated with ΔS, but the correlation only holds for ΔS during the early ebb ($R^2 = 0.2$ and p-value < 0.001) not for ΔS at max ebb tide ($R^2 = 0.0$ and p-value > 0.05) because stratification has typically mixed away by max ebb. C_D is calculated from the momentum balance around max ebb tide (section 2.3.1), suggesting that the inhibition of flow separation by stratification has a lagged effect. Stratification can impede the growth of adverse pressure gradient during early ebb tide so that flow separation is not fully developed at max ebb, even if stratification has disappeared at that time. In contrast, the inhibition of bottom shear stress by stratification happens instantaneously. Any inhibition of turbulence and bottom shear stress by stratification during early ebb is unlikely to affect bottom shear stress at max ebb, which further indicates that the discharge dependence of C_D is not due to the direct inhibition of turbulence by stratification.

The secondary circulation is more complex during flood tide, as the sense of secondary circulation can be reversed and multiple circulation cells are formed (Kranenburg et al., 2019). The interaction between stratification and the secondary circulation during flood tide, as well as any influence on flow separation and drag are still unknown.

2.5.4 Bed roughness

The bottom friction appears to contribute less than form drag to the increased total drag, given that the bottom friction coefficient C_f is around $3 \times 10^{-3} - 5 \times 10^{-3}$, much smaller than the total drag coefficient C_D (sections 2.4.2 and 2.4.4). The C_f calculation was based on the ADV measurements near the apex of bend, and the calculated C_f values correspond with a log-layer estimate for the bottom roughness of $z_0 = 0.002 - 0.005$ m (e.g., Lentz et al., 2017). However, the bathymetry survey of the North River (section 2.2.2) indicates that the bedforms vary in size along the estuary, and that in some areas the bed roughness elements may be much larger than this local estimate from the ADV would suggest.

We estimate the bottom roughness scales quantitatively by using the detrended bathymetry data following an approach as in Rogers et al. (2018). Mega ripples are found at several locations near

the sharp bend with roughness height h_b of $0.1-0.5$ m and wavelength λ_b of $1-10$ m, and bedform crests are generally oriented perpendicular to the along-channel flow. The bedform steepness h_b/λ_b is generally in the range of $0.05-0.1$. The bottom roughness z_0 due to these bedforms is estimated as

$$z_0 = a_1 h_b \frac{h_b}{\lambda_b}, \tag{2.19}$$

where a_1 is a linear roughness coefficient (e.g., Grant and Madsen, 1982; Rogers et al., 2018). a_1 is typically in the range of $0.3-3$ (Soulsby, 1997; Trowbridge and Lentz, 2018) and here we assume $a_1 = 1$ as an estimate. Based on this, the mega ripples in the North River correspond to a z_0 of $0.002-0.05$ m and a depth-averaged drag coefficient of up to 0.01 (Lentz et al., 2017). These higher values of z_0 apply only in parts of the estuary rather than everywhere, so bottom roughness alone does not explain the observed high drag. In addition, the C_f due to bottom roughness typically has a decreasing trend with increasing water depth (Lentz et al., 2017), opposite to the observed depth dependence, so bottom roughness does not explain the variability of the total C_D with water depth. However, these large scale bottom features could be an important factor locally, and the combined effects of the multiple scales of bottom roughness on the overall drag still requires further investigation.

2.6 Discussion

2.6.1 Explaining the high drag and its large variability

We observed that the effective drag coefficients were greater than expected from bottom friction alone in the North River estuary. Multiple lines of evidence suggest that form drag due to flow separation at channel bends is a leading factor in the high drag observed in the North River. The high values of C_D are consistent with modeling results in sinuous channels with similar geometric parameters in Bo and Ralston (2020) where C_D was dominated by form drag due to flow separation. The correlation between the observed adverse pressure gradients and C_D is also consistent with the explanation that the high C_D is associated with flow separation and form drag. The high C_D shows a flood-ebb asymmetry that is most apparent during high spring tides, which corresponds with a depth dependence of C_D due to higher water levels around max flood. This positive correlation with depth is consistent with the response expected for form drag due to flow separation based on idealized and theoretical models. This suggests that C_D values are higher during flood tides than

ebb tides because the deeper water during flood tides leads to stronger flow separation and greater form drag.

Diurnal variations in flood tide C_D appear to correspond with the diurnal inundation of the marsh platform during spring tides, and C_D is decreased when the marsh is inundated. As a result, C_D has the opposite trend with water depth when flow is above the channel banks compared with the rest of the data. A potential explanation for this trend is that the local increase in friction with overbank flow inhibits flow separation and reduces the form drag.

The ebb tide C_D has a decreasing trend with river discharge, while the flood tide C_D does not depend on discharge. Stratification increases with river discharge, and the correlation between discharge and ebb C_D may be due to interaction between the stratification and lateral circulation that results in a local baroclinic pressure gradient that inhibits flow separation. While direct field evidence is lacking, the observations are suggestive that baroclinicity can influence flow separation in estuarine channels. The direct influence of stratification on damping turbulence and reducing drag appears to be less important here, due to the relatively weak stratification during periods with the strongest tidal velocities.

We have focused on the impact of flow separation on the momentum budget, as it creates pressure differences around a bend and results in form drag, but the role of flow separation in the tidal energy flux is still unclear. Flow separation could increase energy loss by enhancing lateral shear dissipation and eddy loss (Chang, 1984), or by narrowing and accelerating the main flow and thereby enhancing bottom dissipation (Bo and Ralston, 2020). $C_{D,energy}$ generally has similar magnitudes to C_D, suggesting that the high energy dissipation is consistent with the high drag. However, the $C_{D,energy}$ calculated based on the channel convergence rate, i.e., $L_w = 20$ km, is higher than C_D during most of the observational period (Figure 2-4 **(b)**). While uncertainty in the channel geometry estimation could be an explanation, the discrepancy may also relate to differences in how form drag and bottom friction lead to energy loss. Typically the dissipation caused by bottom friction is scaled with the bottom stress times tidal velocity $\|U\|$ (e.g., van Rijn, 2011), but the appropriate velocity for scaling the dissipation associated with form drag is more uncertain (MacCready et al., 2003). The fact that $C_{D,energy}$ (based on $L_w = 20$ km) is higher than C_D from the momentum budget suggests that the effect of form drag in leading to energy dissipation may be overestimated by (2.13), i.e., the dissipation due to form drag needs to be scaled with a smaller velocity than $\|U\|$.

2.6.2 Other factors contributing to the high drag

While flow separation and form drag appear to play an important role in the high drag observed in the North River, other process may also contribute. Secondary circulation due to curvature and baroclinic forcing is strong in the North River (Kranenburg et al., 2019). Interactions between the secondary circulation and lateral salinity distribution may influence the form drag from flow separation (section 2.5.3), but secondary circulation can also directly increase the drag by creating stronger near-bed lateral velocity and by redistributing the streamwise momentum (e.g., Blanckaert and de Vriend, 2003). The near-bottom streamwise velocity ranges between 0.2 and 0.6 m/s at max flood and ebb and the near-bottom lateral velocity is $0 - 0.3$ m/s. The ratio of bottom lateral velocity to streamwise velocity is $0.4 - 0.5$ on average, so based on the quadratic dependence of drag we can estimate that the lateral velocity may increase the bottom shear stress by $20 - 30\%$. The effects of the redistribution of streamwise momentum by the lateral circulation are harder to estimate. The downward vertical velocity associated with secondary circulation advects greater streamwise velocity toward the bed and squeezes the boundary layer, and the increased velocity variance and thinner boundary layer enhance the local bottom friction. Consequently, secondary circulation can change the bottom stress distribution in channel bends and increase the overall drag.

In addition to flow separation and secondary circulation in channel bends, smaller-scale roughness elements can also influence the drag. The bed roughness features of the mid-estuary region have been analyzed in section 2.5.4, but the integrated effects of multiple scales of bedforms and features like point bars and shallow shoals that can affect the drag still need to be studied. The sharp studied bend does not have a distinct point bar at the apex, nor do other bends in the mid-estuary region. Shallow bathymetry near the inner bank can enhance local friction and inhibit flow separation, so the absence of a point bar increases the tendency for flow separation in the North River estuary. Kranenburg et al. (2019) suggested that the reversed secondary circulation in this bend, with outward current near the bed, can limit sediment deposition at the inner bank and inhibit development of a point bar. Flow separation may be another reason for the relatively symmetric cross-channel bathymetric profile at the bend apex. A separation zone near the inner bank restricts the effective channel width at the apex and accelerates flow in the middle channel, and the accelerated velocity can maintain the deep scour at the center of the channel (e.g., Vermeulen et al., 2015). Despite lack of point bars, several shoals were found in the bends (e.g., Figure 2-1). These shallow bathymetry features create intermediate-scale roughness in bend flows (larger than bedforms but smaller than

bend-scale) and may influence the total drag by affecting the bottom stress, the secondary circulation patterns, or the form drag of flow separation in bends.

Open channel flow literature and engineering guide books typically suggest a drag increase of up to 30% in meanders (e.g., Chow, 1959; Arcement and Schneider, 1989), but observations from the North River estuary indicate that the overall drag increase compared to a straight channel can be much greater. The factors potentially contributing to the high drag in sinuous channels, including flow separation, secondary circulation, and bed forms, require more scientific investigation and engineering evaluation. Incorporation of these processes into numerical models requires either sufficient grid resolution to explicitly represent the complex flow structure or improved drag parameterizations to account for the processes resulting from flow curvature.

2.7 Conclusion

We observe in an estuary with channel curvature that the drag coefficients are $5 \times 10^{-3} - 20 \times 10^{-3}$, much greater than expected from bottom friction alone. C_D varies at both tidal and seasonal time scales. The C_D values are greater during flood tides than ebb tides, particularly during high spring tides. The tidal asymmetry corresponds with a C_D that increases with water depth. Ebb tide C_D decreases with river discharge but flood tide C_D shows no dependence on discharge. We observe flow reversal and adverse pressure gradients at the inside of a sharp bend, and the analysis shows that flow separation and the associated form drag is a leading factor in the high total drag. During the highest spring tides, decreased values of C_D were found for overbank flow cases, and that is explained by an inhibition of flow separation due to the locally increased friction. Similarly, baroclinic effects during ebbs may inhibit flow separation and explain the decreasing trend with discharge. Other factors may also contribute to the drag including secondary circulation, multiple-scales of bedforms, and shallow shoals, but the various lines of evidence suggest that flow separation plays a key role in the high total drag. [1]

[1] A realistic modeling study of the North River estuary is presented in chapter 4. The study further investigates the mechanisms of high drag in this sinuous estuary, and suggests that in addition to form drag due to flow separation, bottom stress enhancement due to secondary circulation also contributes to the high drag. Additionally, the interaction between stratification and secondary circulation discussed in this chapter is analyzed in detail in chapter 5.

Chapter 3

Flow Separation and Increased Drag Coefficient in Estuarine Channels with Curvature

Flow separation has been observed and studied in sinuous laboratory channels and natural meanders, but the effects of flow separation on along-channel drag are not well understood. Motivated by observations of large drag coefficients from a shallow, sinuous estuary, we built idealized numerical models representative of that system. We found that flow separation in tidal channels with curvature can create form drag that increases the total drag to more than twice that from bottom friction alone. In the momentum budget, the pressure gradient is balanced by the combined effects of bottom friction and form drag, which is calculated directly. The effective increase in total drag coefficient depends on two geometric parameters: dimensionless water depth and bend sharpness, quantified as the bend radius of curvature to channel width ratio. We introduce a theoretical boundary layer separation model to explain this parameter dependence and to predict flow separation and the increased drag. The drag coefficient can increase by a factor of $2-7$ in "sharp" and "deep" sinuous channels where flow separation is most likely. Flow separation also enhances energy dissipation due to increased velocities in bends, resulting in greater loss of tidal energy and weakened stratification. Flow separation and the associated drag increase are expected to be more common in meanders of tidal channels than rivers where point bars that inhibit flow separation are more commonly found. The increased drag due to flow separation reduces tidal amplitude and affects velocity phasing along the estuary, and could result in morphological feedbacks.

The material in this chapter has been published as Bo and Ralston (2020) in *Journal of Geophysical Research: Oceans* and is included with permission.

3.1 Introduction

3.1.1 Sinuous tidal channels

Rivers often have sinuous planforms (Langbein and Leopold, 1966). The natural processes that shape the sinuous form of river channels result from interactions between the fluid motion that carries sediment (e.g. along-channel flow and secondary circulation in a cross-sectional plane) and the erosion and deposition at river bed and bank (Langbein and Leopold, 1970; Seminara, 2006). In coastal systems where tides provide the dominant forcing, estuarine channels often exhibit similar sinuous geometry as river channels (Marani et al., 2002; Fagherazzi et al., 2004).

Channel curvature can cause secondary circulation in a lateral plane perpendicular to the flow direction, as a result of the local imbalance between the centrifugal acceleration and barotropic pressure gradient in the vertical (Thomson, 1877). Secondary circulation is predicted by the analytical solution presented by Rozovskii (1957) and Kalkwijk and Booij (1986), and observed in both rivers (e.g. Apmann, 1964) and tidal channel bends (e.g. Seim and Gregg, 1997; Chant, 2002; Buijsman and Ridderinkhof, 2008). This lateral circulation causes sediment transport across the channel and in turn provides feedbacks to meander morphology including erosion of outer bank, evolution of meander position, deposition at the inner bank, and growth of point bars. However, in curved estuarine channels, salinity stratification can suppress secondary circulation (e.g. Seim and Gregg, 1997) and the baroclinic pressure gradient can even reverse the sense of the lateral circulation compared to that expected for a river (e.g. Kranenburg et al., 2019). The reversed circulation due to baroclinic forcing may contribute to the absence of point bars in some tidal meanders, and the lack of bed-load transport in cohesive-bed tidal channels may also make it less likely for point bars to form (e.g. Jamieson et al., 2013).

Channel curvature can also cause flow separation of the along-channel velocity at the inside of bends, which is observed at sharp channel bends in both rivers (e.g. Ferguson et al., 2003) and tidal channels (e.g. Leeder and Bridges, 1975). The bend sharpness is customarily quantified as R/W, the ratio of bend radius of curvature to channel width. Typical values of R/W are in the range of $1.5 - 4.3$ for rivers (Leopold and Wolman, 1960) and $1.6 - 5$ for tidal channels (Marani et al., 2002), and the bends where flow separation occurs tend to be sharper than average, e.g. $R/W < 1.5$

(examined more below). Flow separation can significantly impact flow structure in curved channels and can increase along-channel drag (Leopold, 1960; James et al., 2001; Blanckaert, 2015), which will be discussed in the following section.

3.1.2 Increased drag coefficient in sinuous channels

In shallow coastal systems, bottom friction is a major source of drag, and it typically scales with physical roughness elements of the bed (bottom roughness z_0), whether grain size (Nikuradse, 1933) or bedforms (Grant and Madsen, 1982). Friction is customarily represented with quadratic velocity and a dimensionless drag coefficient C_D (see equation (3.1)). C_D can be related to z_0 and water depth by assuming a log-layer for near-bottom velocity. C_D is defined based on a reference velocity, usually taken at a fixed elevation (e.g., 1 m above the bed) or the depth-averaged velocity. A typical value for C_D of around $0.003 - 0.004$ for shallow coastal and estuarine flows corresponds with a $z_0 = 0.002$ m for a reference velocity at 1 m above the bed or for depth-averaged flow for a water depth of 5 m. Other approaches to characterizing the effect of friction on open channel flow include Manning's n, the Darcy Weisbach f and Chézy's C (James et al., 2001), but here we focus on the drag coefficient C_D.

In addition to bottom roughness, larger scale features can increase drag on the flow including coral reefs (e.g. Kunkel et al., 2006; Lentz et al., 2017; Rogers et al., 2018), vegetation (e.g. Kadlec, 1990; Nepf, 1999; Monismith et al., 2019) and form drag from topography (e.g. Warner and MacCready, 2014). This research will characterize a type of form drag, in particular on how channel meanders can increase the effective drag at larger scales. In this research, C_D is still defined based on quadratic velocity, but C_D quantifies the total drag instead of only bottom roughness. An example of form drag in a tidal flow was found for a headland in Puget Sound, where McCabe et al. (2006) and Warner and MacCready (2014) investigated the enhanced friction due to flow separation and internal wave generation.

Increased drag in sinuous channels compared with straight channels has been noted previously. In laboratory experiments with a sinuous channel, increased flow resistance and excess energy dissipation were observed around the bend (Leopold, 1960). In natural streams, meandering channels have been found to have Manning's n values as much as 30% greater than similar straight channels (Chow, 1959), and Arcement and Schneider (1989) suggested modifications to Manning's n to account for the increased drag in meandering rivers. Most of the examples of enhanced drag due to meanders are from rivers, but observations from a marsh also found increased surface slope in

a sharply sinuous channel (Leopold et al., 1993), suggesting that the sharp bends may have contributed to the enhanced drag and increased Manning's n.

Several processes have been suggested as potentially contributing to enhanced drag with channel curvature, including dissipation in hydraulic jumps at high Froude number F_r (Leopold, 1960), extra bottom stress from lateral circulation (Chang, 1984), and form drag from flow separation (James et al., 2001). In tidal channels, F_r is usually relatively low, so hydraulic jumps are unlikely to occur. Lateral circulation, that is generated by the centrifugal acceleration of flow around bends and potential interactions with the salinity field, can enhance near-bed velocities and increase bottom stress and turbulent dissipation. Flow separation, in which streamlines of the along-channel flow detach from the channel bank and lead to a separation zone, has been observed in natural meanders, headlands and islands (e.g. Leeder and Bridges, 1975; Wolanski et al., 1984; Signell and Geyer, 1991). Flow separation creates a low-pressure zone behind the separation point and generates vortices from the boundary layer that are injected into the interior flow (Signell and Geyer, 1991). Flow separation in sinuous channels has been studied through laboratory measurements and observations. Lee eddies were observed in sinuous open channel experiments with relatively high mean velocity and strong curvature, causing the deformation of the free surface and restricting the flow to a narrower part of the cross-section (Leopold, 1960). Inner bank separation and its influence on the flow structure were reported in sharp-bend flume experiments including Blanckaert (2011), Constantinescu et al. (2013) and Blanckaert (2015). In intertidal channels in the Solway Firth (Scotland), Leeder and Bridges (1975) noted that flow separation effectively decreased the width and increased the local velocity, and suggested that flow separation is to be expected in many natural systems. The formation of counter-rotating eddies near the apex of bends was reported by Seim et al. (2006) in the Satilla River estuary, and noted to have similarities with flow around headlands as in Signell and Geyer (1991). Flow separation in the lee of a bend and weak fluid recirculation in the separation zone were also observed in rivers, including the Embarras River (Frothingham and Rhoads, 2003) and the River Dean (Ferguson et al., 2003).

Although flow separation in sinuous channels has been widely observed, the influence of flow separation on resistance and drag remains mostly conceptual. James et al. (2001) investigated the drag increase associated with flow separation in laboratory sinuous channels and reported that vegetation can decrease drag compared to an unvegetated sinuous channel by reducing separation at sharp bend. James et al. (2001) showed the dependence of Manning's n on the curvature ratio R/W in unvegetated channels, but with limited physical explanation. Blanckaert (2015) calculated

the spatially distributed friction factor in a laboratory flume with bend-induced flow separation and noted the dependence of flow separation on H/W (depth to width ratio) and the curvature ratio R/W, but did not examine in detail the influence of these parameters on the drag. Leopold (1960) proposed that hydraulic jumps in the laboratory bend can explain the increased flow resistance and energy loss, but the flow in tidal channels rarely has sufficiently high F_r for this mechanism to apply.

3.1.3 Overview

In this project, we built idealized numerical models motivated by observations from the North River estuary (MA, USA) to explore the basic processes that lead to increased drag in sinuous channels. Previously, field studies were conducted in the North River estuary, a sinuous tidal channel through salt marsh that discharges into Massachusetts Bay (Kranenburg et al., 2019). The North River has relatively large tides ($2-3.5$ m range) and modest river discharge (typically < 5 m^3/s except for brief events of $10-30$ m^3/s), so stratification is weak and intermittent. The channel aspect ratio (channel width to depth, w/H) is about 10, and the bends are relatively sharp with the smallest R/W being 1.2. Measurements of velocity and pressure gradient in the North River resulted in a depth-averaged velocity drag coefficient C_D of $0.005-0.01$ during ebb tide and $0.01-0.02$ during flood tide (Bo et al., 2021). However, typical values for estuaries with similar bottom roughness and water depth are in the range of $0.002-0.005$ (e.g. Li et al., 2004). In the North River, local measurements of velocity and near-bed stress based on the turbulence spectra yielded a drag coefficient of 0.003 (Kranenburg et al., 2019), in this expected range and in sharp contrast to the C_D based on the pressure gradient that was greater by a factor of 2 to 7.

We examine the mechanisms by which flow separation in sharp sinuous channel bends can increase drag and energy dissipation using an idealized numerical model study scaled based on these observations. In section 3.2, we introduce the numerical model setup. Section 3.3 shows the effects of channel curvature on drag and tidal propagation, and investigates the increased drag and energy dissipation associated with flow separation. In section 3.4, we use numerical results to show the dependence of this increased drag coefficient on channel geometry. In section 3.5 we introduce a theoretical flow separation model to explain the parameter dependence and compare with our numerical results as well as previous research. In section 3.6, we discuss the influences of flow separation and the increased drag coefficient on sinuous channel dynamics and the broader application of the results, including comparison of rivers and tidal channels. Section 3.7 is a conclusion.

3.2 Model setup

We applied the Regional Ocean Modeling System (ROMS) (Shchepetkin and McWilliams, 2005; Haidvogel et al., 2008; Warner et al., 2010) for the idealized sinuous estuary channel modeling. ROMS is a 3D hydrostatic model based on the Reynolds-averaged Navier–Stokes (RANS) equations. The grid is structured, with high resolution in the sinuous region at the center of model domain and increasing grid spacing toward the open ocean boundaries and the upstream river boundary. A stretched, terrain-following coordinate is used with 16 layers uniformly distributed in the vertical direction. The sinuous estuary model (SIN1) has semi-diurnal tides imposed onto the open ocean boundaries with a 12-hour period, with a sinusoidal water level of 1-m amplitude (2-m tidal range) and velocity of 0.5 m/s. A constant river discharge of 5 m^3/s is input at the upstream boundary, corresponding to a mean velocity of 1 cm/s in the upper channel and 0.5 cm/s in the sinuous channel near the estuary mouth. Salinity is 32 psu on the open ocean boundaries and 0 psu on the river boundary, and it is initialized as a linear decrease from the shelf into the estuary. Temperature is uniform throughout the entire domain. The model was run for a 20-day period, i.e. 40 tidal cycles, to ensure that a quasi-steady state was reached. Model analysis was based on the last two tidal cycles. The generic length-scale (GLS) mixing scheme is used for the vertical turbulent mixing (Umlauf and Burchard, 2003; Warner et al., 2005) and the horizontal mixing coefficient K_H is set to 0.01 m^2/s. Bottom roughness z_0 is 0.002 m, a typical value for a bed with ripples (Grant and Madsen, 1982). A constant and uniform z_0 is used to avoid introducing other sources of variability that affect the drag, but we note that natural channels can have spatially and temporally variable physical roughness.

The shelf is 40-km long and 14-km wide, with depth linearly decreasing from 100 m to 7 m toward the coast. A narrow tidal inlet (700-m wide) is located at the estuary mouth, followed by a lagoon with a channel (400-m wide) in the middle and shallow flats on the side. The channel exponentially converges landwards (e.g. Langbein, 1963) until 6.5-km into the estuary, and after that the channel is uniform width $w = 200$ m, with 20 grid cells across the channel. A sensitivity test was also conducted with double the grid resolution and the results were the same. The sinuous region is located between 6.5 and 19-km, and the total along-channel length is approximately 40 km. Channel thalweg depth linearly decreases from 7 m at the mouth to 3 m at 22 km, with a slope of $\sim$ 0.18 m/km, and the thalweg depth is a uniform 3 m from 22 km to the landward boundary (Figure 3-1 **(b)**). The channel has a parabolic cross-sectional profile (e.g. Smith, 1982) with a minimum depth

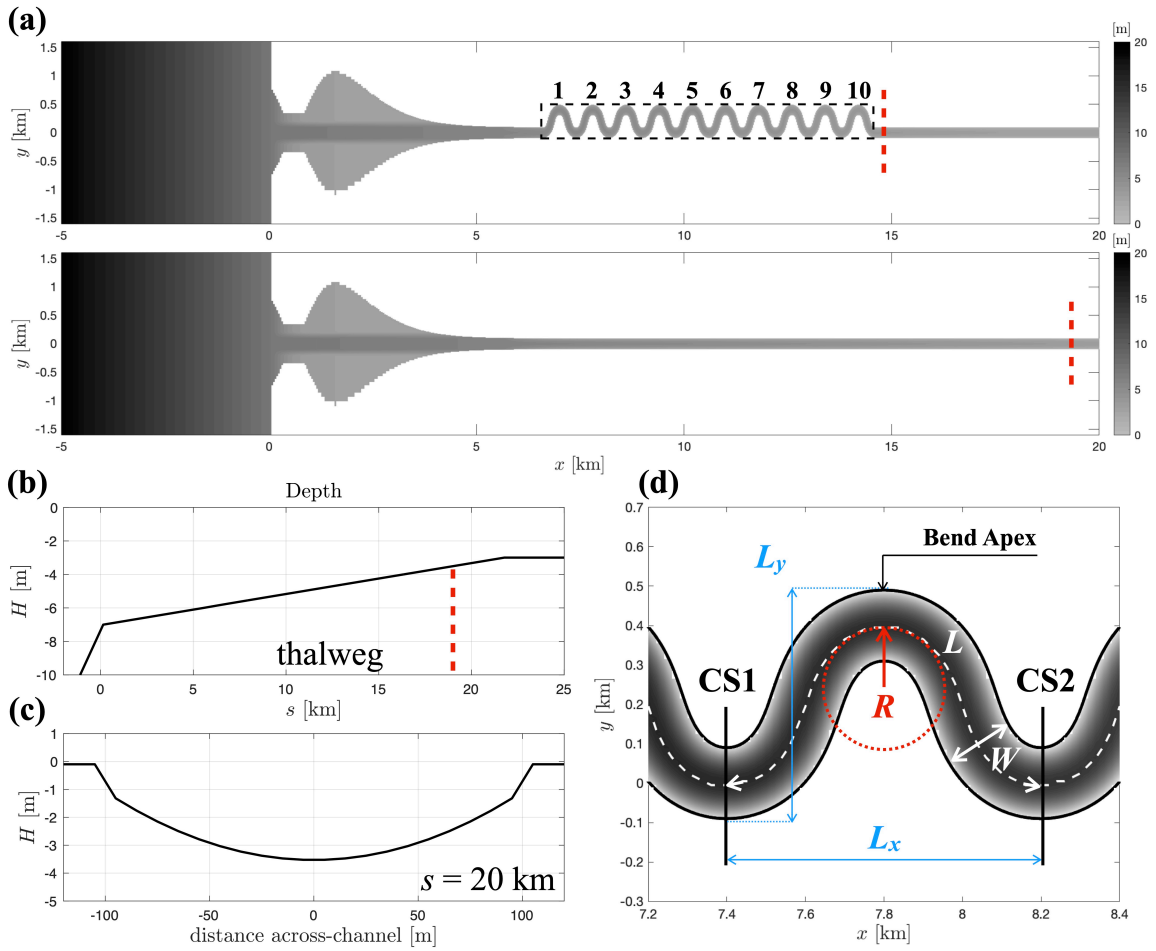

Figure 3-1: **(a)**: Model bathymetry of the idealized sinuous and straight channel estuaries (SIN1 and STR1). Only the center parts of the model grids are shown. The estuary starts from $x = 0$ and $x < 0$ is the shelf. The sinuous region is marked by dashed black lines. Channel bends are numbered as $1 - 10$. **(b)**: Depth of the channel thalweg as a function of along-channel distance s. **(c)**: Cross-sectional bathymetry at $s = 20$ km, corresponding to the cross-section denoted by the dashed red lines in subfigures **(a)** and **(b)**. **(d)**: Geometric parameters of channel bend 2. L_x is the Cartesian length; L_y is the Cartesian width; L is the along-channel length. R is the minimum radius of curvature of the channel centerline along the bend. w is the channel width. Black lines mark the position of cross-sections (CS1, CS2) used in the following model analysis.

of 1.5 m to ensure that the bed does not emerge at low tide (Figure 3-1 **(c)**). The sinuous channel shape is created following the form of sine-generated functions (Langbein and Leopold, 1970). The sinuous region is composed of ten continuous 144° bends, numbered in Figure 3-1 **(a)**, where we are focusing on just half the bends to limit redundancy. The minimum radius of curvature of the channel centerline is 164 m at the bend apex. The Cartesian length of each channel bend is 800 m and the Cartesian width is 600 m; the along-channel length of each bend is 1240 m (Figure 3-1 **(d)**).

A straight channel model (STR1) is used as a comparison of the sinuous channel model (SIN1).

Model	R [m]	h [m]	H [m]	w [m]	L [m]	R/W	H/W	H/L
STR1	–	$3-7$	$2-6$	200	–	–	$0.01-0.03$	–
STR2	–	$7-12$	$6-11$	200	–	–	$0.03-0.06$	–
SIN1	164	$3-7$	$2-6$	200	1240	0.82	$0.01-0.03$	$0.002-0.005$
SIN2	164	$7-12$	$6-11$	200	1240	0.82	$0.03-0.06$	$0.005-0.009$
SIN3	46	$3-7$	$3-5$	60	540	0.77	$0.05-0.08$	$0.005-0.009$
SIN4	270	$3-7$	$3-6$	200	1550	1.35	$0.01-0.03$	$0.002-0.004$
SIN5	185	$3-7$	$3-6$	200	1080	0.93	$0.01-0.03$	$0.003-0.006$
SIN6	185	$3-7$	$3-6$	160	1080	1.12	$0.02-0.04$	$0.003-0.006$
SIN7	185	$3-7$	$3-6$	120	1080	1.54	$0.03-0.05$	$0.003-0.006$
SIN8	185	$3-7$	$3-6$	140	1080	1.32	$0.02-0.04$	$0.003-0.006$

Table 3.1: Parameters of all the models. STR1 and STR2 are straight channel models and SIN1-SIN8 are sinuous channel models. R is the minimum radius of curvature. h is the thalweg depth. H is the cross-sctionally averaged water depth, which varies with distance along the channel and tidal water level. L is the along-channel length of each bend.

The boundary conditions, channel width, depth, bottom slope and lateral bathymetric profile are exactly the same in the two models and the only difference lies in the channel planform. The total along-channel length is also the same to make the total volume of the two estuaries identical. The grid is adjusted near the river boundary so that the straight model domain is longer than the sinuous model to ensure the same along-channel length, but the grid at the center of the domain (i.e. the high resolution region used for analysis) is the same.

Additional model grids with different sinuous channel shapes are used to explore parameter space (Table 3.1), but the overall structure and model settings are similar for the other cases. The tidal range is 2 m for all the models, consistent with the neap tide condition on the North River estuary. A 3.2-m tidal range representative of spring tides was also examined and produced similar results. SIN1 and STR1 are the pair of sinuous and straight channels introduced above. SIN2 and STR2 are another pair of sinuous and straight channels with the same channel shape as SIN1 and STR1 but greater depth. SIN3 – SIN8 are other sinuous channel cases that are also created using a series of sine-generated functions (Langbein and Leopold, 1970). The results and analysis in section 3.3 are based on models SIN1 and STR1. Sections 3.4 and 3.5 draw on results from all the models in Table 3.1. The channel aspect ratio among the model cases varies between 10 and 60, which covers a wide range of salt marshes, tidal flats and rivers, and the R/W (bend sharpness) ranges between $0.7-1.6$. The numerical experiments and the field study that inspired them focus on channel bends that are relatively sharp for rivers and tidal meanders (Leopold and Wolman, 1960; Marani et al., 2002) but they are within the range commonly found in nature (e.g. Nanson, 2010;

Schnauder and Sukhodolov, 2012; Marani et al., 2002).

3.3 Numerical model results

In this section, we analyze model results and explore the underlying physics that cause the increased drag in meanders. In section 3.3.1, we compare drag coefficients between the sinuous (SIN1) and straight (STR1) estuary models. In section 3.3.2, we examine the effects of the increased drag with channel curvature on tides and stratification. In section 3.3.3, we characterize flow separation and secondary circulation, and calculate the form drag. In section 3.3.4, we calculate the energy budget and show how flow separation increases energy dissipation.

3.3.1 Increased drag coefficient in meanders

It is customary to write drag force as

$$\tau = \rho C_D u_r |u_r|, \tag{3.1}$$

where τ is the total drag force, including bottom stress and other sources of drag. ρ is density, C_D is the drag coefficient and u_r is a reference velocity, often taken as the depth-averaged velocity or the velocity at a fixed elevation above the bottom. Here we take the reference velocity u_r as the cross-sectionally averaged streamwise velocity U.

The drag coefficient is used to represent resistance in the along-channel momentum equation

$$\frac{\partial U}{\partial t} + U\frac{\partial U}{\partial s} = -g\frac{\partial \eta}{\partial s} - \frac{1}{2}\beta g\frac{\partial S}{\partial s}H - C_D\frac{U|U|}{H}, \tag{3.2}$$

where η and H are the laterally averaged water level and water depth, and S is the cross-sectionally averaged salinity. β is the haline contraction coefficient. s is the along-channel coordinate. Local (depth-averaged) velocity, water level, salinity are often all that can be measured in field observations, but here we used the cross-sectional average of all the properties because of the large lateral variations in these quantities in the sinuous channel case. The advection term associated with cross-stream velocity is neglected in cross-sectionally averaged momentum budget because it is small. We can calculate an effective C_D that satisfies the momentum budget

$$C_D = \left(\frac{\partial U}{\partial t} + g\frac{\partial \eta}{\partial s} + \frac{1}{2}\beta g\frac{\partial S}{\partial s}H + U\frac{\partial U}{\partial s}\right) \Big/ \left(\frac{-U|U|}{H}\right). \tag{3.3}$$

We calculated the effective drag coefficient across the bend between sections CS1 and CS2 over a tidal cycle using (3.3). Only the bend-scale drag coefficient is calculated because form drag is usually defined as a spatial integral over the topography of interest (McCabe et al., 2006). The drag coefficient in the straight model is evaluated at locations with same along-channel distance. Data points near slack water are removed to avoid very small values in the denominator of (3.3). In both models, the water level gradient is the dominant term, and the unsteady, advective, and baroclinic terms are at least an order of magnitude smaller.

Model results show that the drag coefficient in the sinuous estuary is two to four times larger than the straight estuary, e.g. $0.006 - 0.015$ compared to $0.003 - 0.004$. The models are identical except for the channel meanders, suggesting that this increase in drag by a factor of $2 - 4$ is associated with the sinuous planform. C_D is averaged over flood and ebb tide separately in both models (Figure 3-2). In the straight model, C_D is slightly larger during ebb tide than flood tide, but differences are small. In the sinuous channel, the drag coefficient is larger during flood tides than ebb tides. The drag coefficient also shows temporal fluctuations during flood tides due to instability in the flow field, so the maximum C_D (e.g. ~ 0.015 in bend 1–3) is larger than the temporal average C_D (e.g. ~ 0.012 in bend 1–3) in Figure 3-2. Both the magnitude of the drag coefficient in the sinuous channel and the flood-ebb asymmetry are broadly consistent with field observations from the North River, on which the model grid was scaled (Bo et al., 2021).

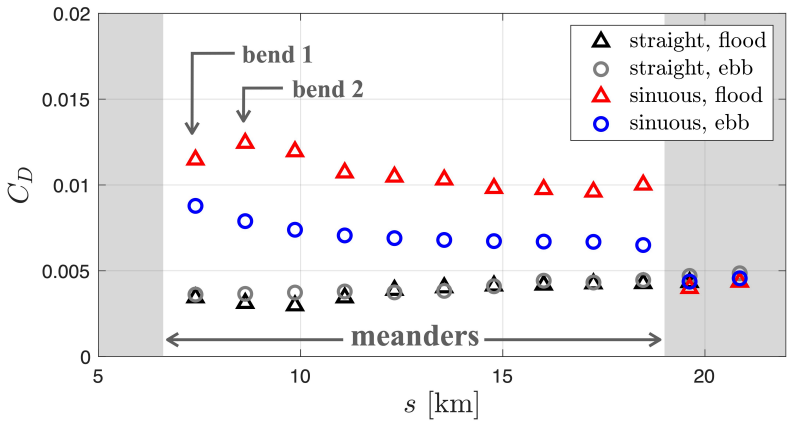

Figure 3-2: Drag coefficient as a function of along-channel distance. C_D is averaged over flood and ebb tide separately in both the straight and sinuous model. The black triangles and gray circles represent flood and ebb tide respectively in the straight model; the red triangles and blue circles represent flood and ebb tide in the sinuous model. The white background shows the range of meanders (the sinuous region) and the arrows mark the first two bends as a representative. The first ten points represent the ten bends in the sinuous region; the last two points show the drag coefficient at a similar spacing outside the sinuous region.

In the sinuous region, the drag coefficient is significantly larger than that of the straight model, while outside the sinuous region the drag coefficient decreases and is consistent with the straight model. The drag coefficient also has different along-channel trends in the two models. The drag coefficient in the straight model increases landwards, while in the sinuous model C_D has a decreasing trend. These opposite behaviors are related to the different depth dependence of C_D in the two models and will be explained in section 3.4. As a result, difference between the sinuous and straight models is greatest in the seaward bends, and we have focused the subsequent analyses on bend 2.

3.3.2 Along-channel change of tides and stratification

In shallow estuaries or inlet systems, the drag directly affects tidal propagation, including tidal amplitude decay and phase lag with distance along the estuary (e.g. Aubrey and Speer, 1985). The increased drag in tidal meanders can therefore have important influences on the water level change in estuaries, which impacts coastal flooding and marsh resilience. Harmonic analysis is employed to examine the influences of meanders on tidal elevation. The numerical system is forced by a 12-hour semi-diurnal tide, so in the harmonic analysis, M2 (12-hour) tide and M4 (6-hour) and M6 (4-hour) overtides are selected as three major tidal components for least-squares fitting.

The amplitude and phase of the dominant M2 tide is shown in Figure 3-3. In the straight model, the amplitude of M2 tide decays as it propagates into the estuary until being reflected near the upstream river boundary. The decay rate is ~ 0.024 m/km, which is mainly attributed to frictional dissipation. The sinuous model shows a faster tidal amplitude decay (~ 0.040 m/km) than the straight model, which indicates a greater energy loss (details discussed in section 3.3.4). Also, the M2 tidal phase lag is greater in the sinuous channel than the straight channel, as is expected from the increased effective drag (Aubrey and Speer, 1985).

Comparison of tidal elevation in the two models demonstrates that meanders can affect tidal water levels in the landward parts of the estuary. Meanders also can impact the growth of overtides and tidal asymmetries. The ratio of amplitudes M4/M2 is similar in the two models but M6/M2 is larger in the sinuous model than the straight model by almost a factor of 2, indicating greater non-linearity with the sinuous channel.

The cross-sectionally averaged velocity U is less in the sinuous channel than the straight, which is in agreement with the tidal amplitude decay in Figure 3-3. Decreased tidal amplitude indicates smaller estuary volume change associated with tidal fluctuations and, as a result, smaller volumetric flux and weaker cross-sectional average current. However, despite the weaker cross-sectionally

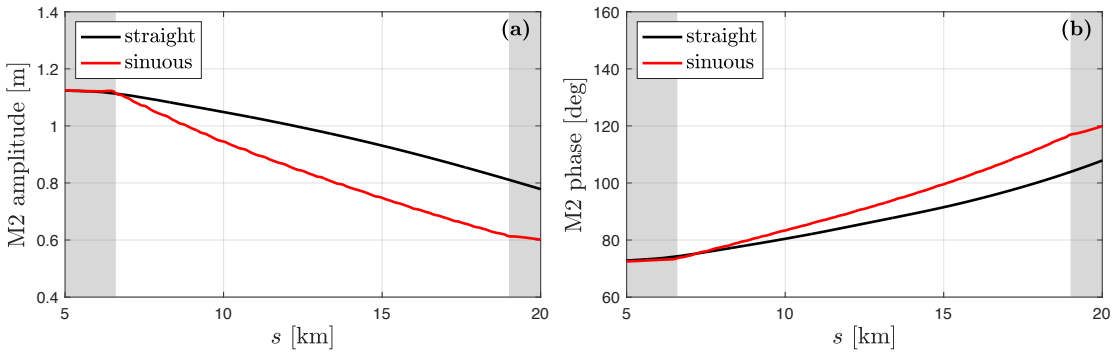

Figure 3-3: **(a)**: M2 tidal amplitude along the channel. **(b)**: M2 tidal phase along the channel. Red lines represent the sinuous model and black lines represent the straight model. The white background shows the range of the sinuous region.

averaged velocity, the maximum local velocities in the sinuous channel exceed those in the straight channel by up to 30%. This result suggests stronger lateral variations in the velocity field because of channel bends.

Differences in stratification are also apparent between the sinuous and straight channel cases. In both cases, the tidally averaged ΔS (difference between surface and bottom salinity) is less than 6 psu, relatively weak stratification that is consistent with the strong tidal currents and small river discharge. However, the sinuous model has a smaller tidally averaged ΔS than the straight channel, indicating weaker stratification due to the existence of channel bends. The mechanism of how sinuous channels decrease stratification is still unclear, and could be related to secondary circulation in the bend or flow separation near the bend apex.

3.3.3 Flow separation and form drag

Flow separation can generate recirculating eddies near the inner bank and produce a "dead zone" or "separation zone" in the lee of channel bends (e.g. Rozovskii, 1957; Ferguson et al., 2003; Blanckaert, 2011), which narrows the effective flow width and increases the local velocity (Leopold, 1960; Leeder and Bridges, 1975). Although outer bank separation is also observed in some channel bends (e.g. Blanckaert et al., 2013), the present research focuses on separation at the inner bank.

Flow separation is seen in model results at both maximum flood and maximum ebb, and here we take flood tide as an example (Figure 3-4 **(a)**). The lateral profile of velocity becomes deflected away from the inner bank and the separation zone grows from near the bend apex toward the lee of bend. The boundary of the separation zone is represented by the deflection points in the velocity profiles.

Streamlines at maximum flood are also displayed in Figure 3-4 **(a)**, with a recirculating eddy in the lee of the channel bend. Free surface deformation is observed in the lee of bend, which is related to the formation of recirculating lee eddies (Leopold, 1960). The water level field can be regarded as the depth averaged barotropic pressure field. A sudden pressure drop occurs near the boundary of the separation zone and a low pressure zone is located downstream of the bend. This pressure drop creates an extra "form drag" or "pressure drag", that increases the drag coefficient. Flow separation also increases instability in the velocity field, which is reflected in temporal fluctuations in C_D.

The separation zone decreases the main flow width and consequently increases the main flow velocity outside the separation zone. We define an effective width for the main flow due to the expansion of flow separation into the channel, as illustrated in Figure 3-4 **(b)**. The effective main flow region is defined by $\overline{u} > 0.5U$, with $\overline{u}$ being the local depth averaged streamwise velocity and U being the cross-sectionally averaged streamwise velocity. The effective width is decreased by $\sim 20\% - 30\%$ in the sinuous channel because of flow separation, while in the straight channel, the effective width is equal to the channel width. Along-channel momentum is more concentrated into a narrower main flow region in the sinuous channel and maximum velocity is intensified as a result of effective width decrease, which explains why the maximum velocity is greater in the sinuous model despite lower cross-sectional average velocities than the straight model (section 3.3.2).

The evolution of velocity field during early flood tide illustrates the occurrence of flow separation (Figure 3-4 **(c)**). During early flood prior to flow separation, flow is attached to the inner bank with the maximum streamwise velocity near the inside of the bend. This is common in flat bottom channel flow in the laboratory (e.g. Blanckaert, 2015) and natural meanders without a point bar (e.g. Jamieson et al., 2013; Kranenburg et al., 2019). Flow near the inner bank is decelerated after passing the bend apex because of the adverse pressure gradient set by channel curvature. As the tidal current grows, this adverse pressure gradient is strengthened and velocity near the inner bank keeps decreasing until the main flow detaches from the inner bank and flow separation occurs. The maximum velocity increases as the effective width of the main flow decreases, with the velocity maximum separated from the inner bank and shifted toward the center of the channel (also see Kranenburg et al. (2019) Fig. 7). Flow near the inner bank can slow to zero or reverse as the flow separation evolves, which leads to the formation of recirculating eddies.

Lateral water level variations are also increased as the tidal current grows (Figure 3-4 **(c)**). The lateral barotropic pressure gradient set by the water level combined with the centrifugal acceleration can generate the "normal" secondary circulation for homogeneous flow around a bend, with

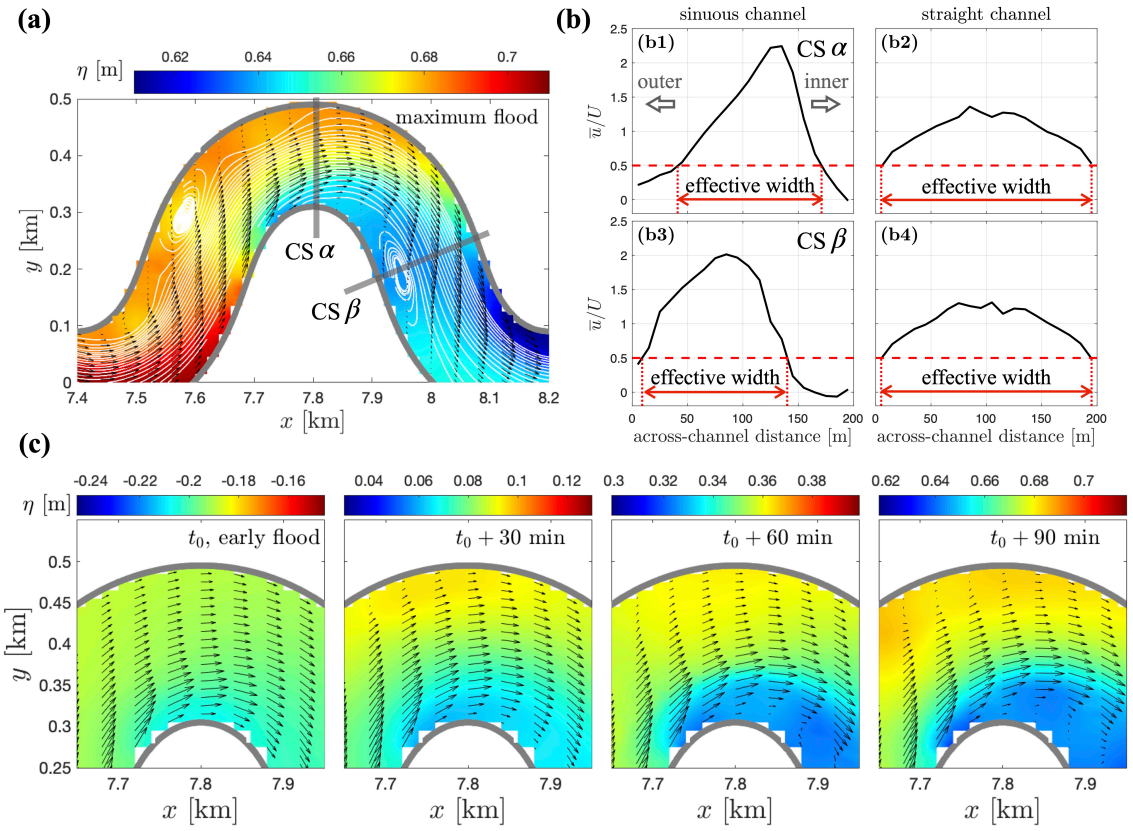

Figure 3-4: **(a)**: Water level, streamlines and velocity field of channel bend 2 at maximum flood tide. White lines show streamlines, including the main flow and the recirculating eddy in the lee of bend 2. Black arrows show the depth averaged velocity. Gray lines represent the river banks. **(b)**: Lateral profile of streamwise velocity scaled by local cross-sectional average velocity at two cross-sections in the sinuous channel and the same along-channel distance locations in the straight channel. The inner bank is on the right side of the graph. Effective channel width is defined as the lateral length of where $\overline{u} > 0.5U$, in which $\overline{u}$ is the local depth-averaged streamwise velocity and U is the cross-sectionally averaged streamwise velocity. **(b1)** and **(b3)** correspond to cross-sections CSα and CSβ in panel **(a)**, respectively. **(b2)** and **(b4)** show locations with the same along-channel distance in the straight channel. **(c)**: Evolution of flow field near the bend apex, with snapshots of four different times during early flood tide. The colormap shows the water level. The range of the colormap varies as water level grows during early flood but the span of the colormap is the same in all the small panels. t_0 is early flood tide and $t_0 + 90$ min is maximum flood tide.

cross-channel velocity toward the outside of the bend at the surface and toward the inner bank near the bottom. Normal secondary circulation is observed at ebb tide with a small counter-rotating circulation cell near the outer bank (Figure 3-5 **(c)**), similar as Blanckaert and Graf (2004) and Blanckaert (2011). At maximum ebb tide, the normal secondary circulation cell has shifted slightly away from the inner bank due to the flow separation with reversed along-channel flow occurring there (Figure 3-5 **(d)**).

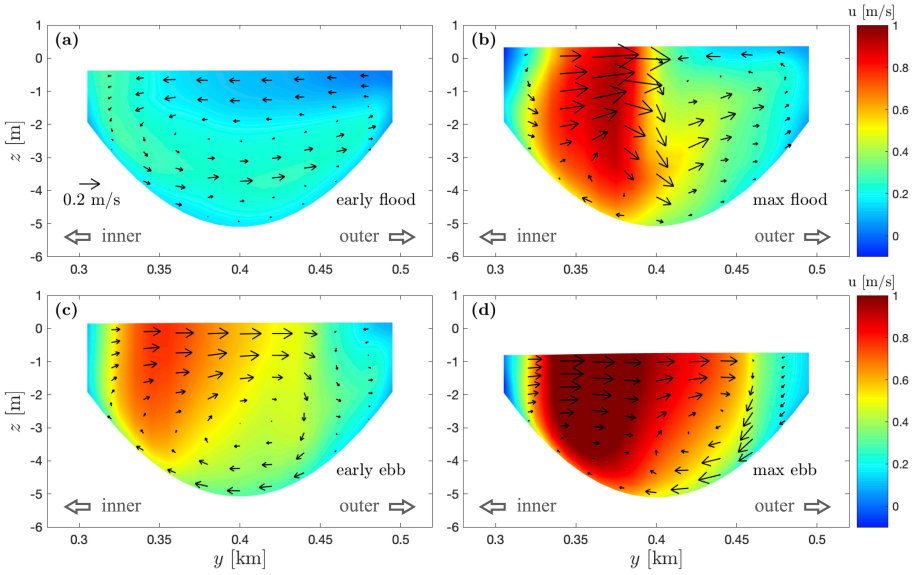

Figure 3-5: Along-channel velocity contours and secondary circulation structure in the cross section at the apex of bend 2. **(a)**: early flood tide; **(b)**: maximum flood tide; **(c)**: early ebb tide; **(d)**: maximum ebb tide. The colormaps shows the along-channel velocity. Note that the positive direction is landward for flood tide and seaward for ebb tide. Black arrows show the lateral and vertical velocity. The inner bank is on the left side and outer bank is on the right side in all panels.

Lateral salinity differences can also affect the lateral circulation, potentially reversing it from the normal homogeneous secondary circulation (e.g. Kranenburg et al., 2019). The reversed circulation is observed during early flood tide (Figure 3-5 **(a)**) when differential advection with relatively larger velocity near the inner bank (Figure 3-4 **(c)**) brings higher salinity to create a cross-channel density gradient, as is found in Kranenburg et al. (2019) Fig. 9. Lateral circulation cells become more complex at maximum flood tide when flow separation occurs near the inner bank (Figure 3-5 **(b)**). A normal secondary circulation cell grows driven by the strong along-channel vertical shear and the lateral water level gradient near the boundary of the flow separation zone (Figure 3-4 **(c)**), and the reversed lateral circulation cell that was predominant during the early flood is pushed toward the outer bank.

Secondary circulation increases momentum loss both through the cross-channel component of the bed shear stress and by redistributing the along-channel momentum (Blanckaert and de Vriend, 2003). The magnitude of cross-channel bottom velocity is about 0.1 m/s, and the along-channel bottom velocity is typically $0.3 - 0.5$ m/s. Thus, based on the quadratic drag formulation the total bottom stress including the cross-channel component is $\sim 10\%$ greater than for the along-channel component alone. The effects of secondary circulation redistributing along-channel momentum are

difficult to isolate because flow separation also redistributes the along-channel momentum by restricting the main flow to a narrower region. During early flood tide the reversed lateral circulation tends to bring higher momentum toward the inner bank (Figure 3-5 **(a)**), whereas the flow separation at max flood tide detaches the higher velocity zone from the inner bank and shifts it outward (Figure 3-5 **(b)**). The dominance of the flow separation on lateral redistribution around max flood suggests that flow separation plays a more important role than secondary circulation in the sinuous channel cases. These sinuous model cases have relatively sharp bends where flow separation is favored, and the relative influence of secondary circulation on the drag may be greater for channels with smoother bends.

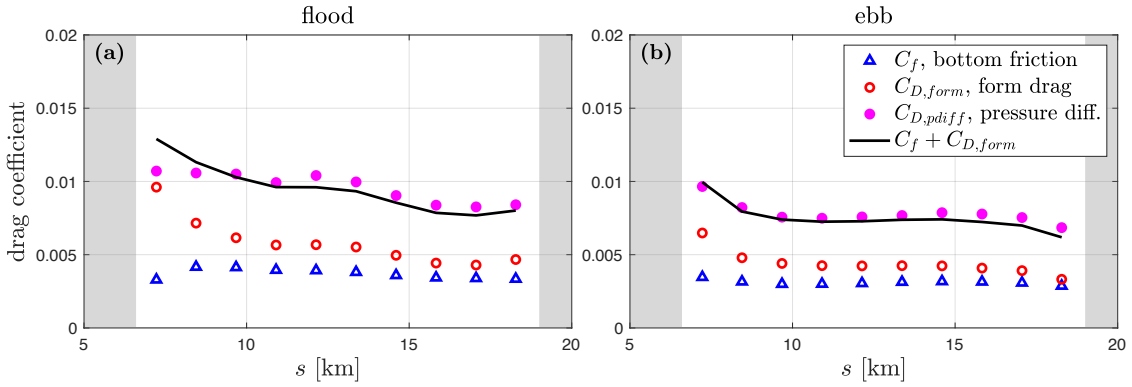

Figure 3-6: Drag coefficients corresponding to different terms of momentum loss. **(a)**: maximum flood tide. **(b)**:maximum ebb tide. Magenta dots represent the pressure difference around each bend; red circles represent the form drag; blue triangles represent bottom friction. Black lines are the sum of bottom friction and form drag, i.e. the total drag. All the terms are calculated or integrated over channel bend scale, and converted into corresponding drag coefficients. The white background shows the range of the sinuous region.

To quantify the form drag contribution directly, we write the integral form of the momentum equation (McCabe et al., 2006) over each bend as

$$\frac{\partial}{\partial t}\int_V \rho_0 u \mathrm{d}V + \int_{A_{CS1+CS2}} \rho_0 u\vec{u}\cdot\vec{n}\mathrm{d}A = \int_{A_{CS1}} p\mathrm{d}A - \int_{A_{CS2}} p\mathrm{d}A + \int_{A_w+A_b} p\xi_x \mathrm{d}A + \int_{A_b} \tau_{bx}\mathrm{d}A, \tag{3.4}$$

where ξ_x corresponds to the projection in x-direction. A_{CS1} and A_{CS2} represent the cross-sectional areas at each end of the control volume; and A_w and A_b represent the areas of the vertical sidewalls and channel bed. The density ρ_0 is homogeneous and stationary based on the Boussinesq approximation. The momentum budget is calculated at maximum flood and maximum ebb. The unsteady and advection terms on the left side of (3.4) are small, so the momentum budget in x-direction re-

sults primarily from the pressure difference between the two cross-section ends (first two terms on the right side of (3.4)), the form drag (third term) and the bottom friction (last term), as there is no friction on the surface or sidewalls of our model. Baroclinic effects are also small (section 3.3.1) so only the barotropic pressure is included in this calculation.

In the straight model, the pressure difference between the ends of the control volume is balanced by bottom friction, and there is no form drag due to the channel geometry (Appendix B). The decreasing thalweg depth along the channel also creates a large pressure force between the ends of the control volume that is balanced by the bottom slope, and we have removed this bottom-slope effect in calculating the momentum budget to focus on the pressure force and form drag associated with water level (Appendix B). In the sinuous model, the right-side terms in (3.4) are calculated over each bend and converted into corresponding drag coefficients based on the cross-sectional average velocity (Figure 3-6). $C_{D,pdiff}$, $C_{D,form}$ and C_f correspond to the pressure difference, form drag and bottom friction respectively. The drag in Figure 3-6 is calculated slightly differently from that in Figure 3-2 — Figure 3-2 shows the temporal average while Figure 3-6 uses snapshots at maximum flood and maximum ebb — but the results are consistent. The bottom friction in the sinuous channel is similar to the straight channel, e.g. $C_f \sim 0.003 - 0.004$. The pressure difference (total drag) is a factor of $\sim 2 - 3$ larger than bottom friction in the sinuous channel, indicating that there is another source of momentum loss, i.e. the form drag associated with flow separation. Integration of the sidewall and channel bed pressure (projected in the x-direction) directly represents the effect of the form drag on the momentum budget, and shows that it is up to a factor of 2 larger than bottom friction, and the momentum budget closes only when the pressure difference is balanced by the combination of bottom friction and form drag.

3.3.4 Energy dissipation

Flow separation not only causes an extra momentum loss by creating form drag, but also leads to a larger energy dissipation in the sinuous channel. The integral form of the energy equation (Gill, 1982; Zhong and Li, 2006) for horizontal velocities is

$$\int_{A_{CS}} \left(p + \rho_0 \frac{u^2+v^2}{2}\right) \vec{u} \cdot \vec{n} \mathrm{d}A = -\int_{A_b} \vec{u}_b \cdot \vec{\tau}_b \mathrm{d}A - \int_V \rho_0 K_V \left[\left(\frac{\partial u}{\partial z}\right)^2 + \left(\frac{\partial v}{\partial z}\right)^2\right] \mathrm{d}V$$
$$- \int_V \rho_0 K_H \left[\left(\frac{\partial u}{\partial x}\right)^2 + \left(\frac{\partial u}{\partial y}\right)^2 + \left(\frac{\partial v}{\partial x}\right)^2 + \left(\frac{\partial v}{\partial y}\right)^2\right] \mathrm{d}V. \tag{3.5}$$

The left side is the net energy flux and the unsteady term is neglected as we have focused on the tidally averaged energy balance. The right side is energy dissipation, which is composed of three parts: energy loss due to bottom shear stress ϵ_b (the surface and sidewall stress are zero in our models), vertical turbulent dissipation ϵ_v(the vertical viscosity K_V is set by the turbulence closure) and horizontal dissipation ϵ_h(the horizontal viscosity $K_H = 0.01$ m^2/s). Energy flux and the three dissipation terms in the energy budget are calculated along the channel and converted to depth-integrated and laterally-averaged results (Figure 3-7).

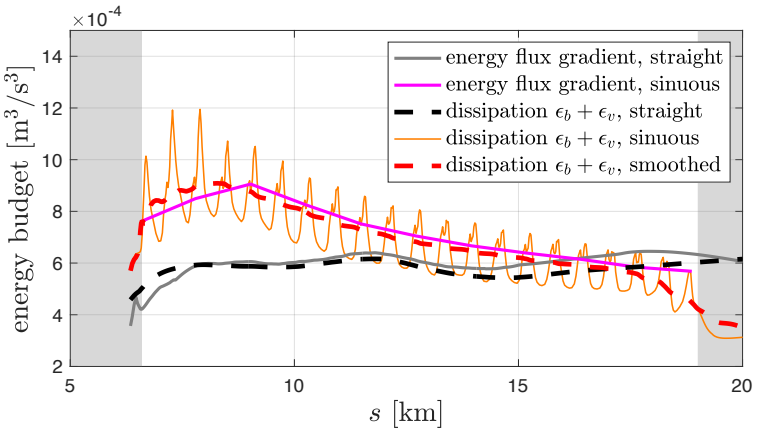

Figure 3-7: Terms in the energy budget in the sinuous and straight models as a function of along-channel distance. Solid gray and solid magenta lines represent the energy flux gradient in the straight channel and sinuous channel (evaluated at bend scale). Solid orange line: bottom dissipation ϵ_b and vertical dissipation ϵ_v in the sinuous channel. Dashed red line: $\epsilon_b + \epsilon_v$ in the sinuous channel smoothed (using a moving average) over the bend scale. Dashed black line: $\epsilon_b + \epsilon_v$ in the straight channel. The white background shows the range of the sinuous region.

In both the straight and sinuous models, the energy flux loss is generally balanced by the calculated total dissipation, which demonstrates that the energy budget closes in the models and numerical dissipation is negligible. Comparing the two models, we found that there is a larger energy loss in the sinuous model (Figure 3-7), which is consistent with the greater rate of decrease in tidal amplitude in section 3.3.2. The maximum dissipation values in the sinuous model, and therefore maximum energy loss rates, occur near the bend apexes.

The larger energy loss induced by meanders is caused by both increased dissipation associated with bed stress and enhanced vertical dissipation by turbulence. The bottom stress dissipation is larger in the sinuous model than the straight model, even though bottom stresses are similar in the two models (section 3.3.3). This can be explained by the decreased effective channel width due to flow separation near the bend apex, which accelerates the main flow because of continuity. Bottom

dissipation can be estimated as

$$\epsilon_b = \tau_b u_b \sim \rho C_f u_r^2 u_b, \tag{3.6}$$

where τ_b is the bottom stress, u_b is the bottom velocity and u_r is a reference velocity associated with the bottom friction coefficient C_f. The cubic dependence of dissipation on velocity, together with the greater velocity near the channel center due to flow separation, leads to a larger laterally averaged bottom stress dissipation in the sinuous channel.

The vertical turbulent dissipation depends on the vertical shear and vertical turbulent viscosity. Numerical results show that the vertical profile of streamwise velocity is more uniform in the sinuous model than the straight channel, so there is less streamwise vertical shear. However, the vertical turbulent viscosity is increased in the sinuous model as a result of weaker stratification compared with the straight channel. The source of this reduction in stratification and enhanced turbulence is still unclear, and it could be associated with the accelerated streamwise velocities or the stronger secondary circulation. For comparison, Nidzieko et al. (2009) found in a curved estuary channel that the destratification was caused by turbulent motions rather than an overturning produced by lateral circulation. As with bottom dissipation, the vertical turbulent dissipation scales with velocity cubed, so the increased turbulent dissipation in meanders also relates to the decreased effective channel width and velocity acceleration because of flow separation.

Secondary circulation increases both bottom shear stress and internal friction by introducing in stronger lateral velocity and lateral shear (Chang, 1984) and thus leads to additional energy loss. However, the extra dissipation contributed by secondary circulation (i.e. the bottom dissipation associated with lateral bottom shear stress and the turbulent dissipation created by the vertical shear of cross-channel velocity) is less than 30% compared to the total dissipation in the straight channel.

Horizontal dissipation also could contribute to the enhanced energy dissipation in the sinuous channel case. High vorticity fluid is generated near the inner bank due to the velocity shear set by the shallower bathymetry near the edges of the channel, and the high vorticity fluid can be injected into the center of the channel by flow separation, potentially increasing horizontal dissipation (e.g. Figure 3-9 **(a)**, **(c)**). Signell and Geyer (1991) discussed similar processes of eddy formation around headlands and injection of high vorticity fluid from the boundary layer into the interior flow. However, although we observed greater horizontal dissipation in the sinuous channel than the straight channel, that term is still two orders of magnitude smaller than the bottom stress and vertical turbulent dissipation terms.

Previous investigations of the energy loss induced by sinuous channels proposed that the major sources of energy loss included increased bed friction from secondary circulation, increased turbulence induced by secondary circulation and turbulence in eddies associated with flow separation (e.g. James et al., 2001). However, our research suggests that the momentum redistribution caused by flow separation, i.e. decreased effective width and increased local streamwise velocity, is an important source of energy loss. These results are particularly relevant to tidal channels, which are shallower than most of the laboratory channels based on aspect ratio. For shallow systems, dissipation is primarily related to the bottom stress and vertical shear even though there is strong horizontal variation in velocity induced by the complex geometry.

3.4 Parameter dependence of the drag coefficient

3.4.1 Parameter dependence on water depth

For turbulent open channel flow with small roughness compared to the water depth, Lentz et al. (2017) proposed an estimate for the drag coefficient based on the depth-averaged velocity

$$C_D \approx \kappa^2 \left[\log\left(\frac{H}{z_0}\right) + (\Pi - 1) \right]^{-2}, \tag{3.7}$$

in which $\kappa = 0.41$ is the von Kármán constant. z_0 is the bottom roughness and H is the water depth. Π is Cole's wake strength and $\Pi \approx 0.2$ for turbulent open channel flow (Nezu, 1993). In this formulation, C_D decreases as water depth increases, because velocity profile becomes less sheared in the upper water column with greater flow depth.

Results from the straight channel models (STR1 and STR2) show a decreasing trend with depth that is consistent with the theoretical C_D in (3.7), as Figure 3-8 shows. The simulation results do not exactly match the theoretical result because we have parabolic channels instead of flat bottom channels, and the velocity profile can be altered by stratification. In the straight channel, the estuary is more stratified during ebb tide and these stratified periods ($\Delta S > 3$) have a smaller drag coefficient than predicted by the formula, as are marked in Figure 3-8. The dependence of C_D in the straight channel is only on water depth H but not channel width w. Although H is non-dimensionalized by w to follow the convention of research on meanders, w is a constant in the models employed in Figure 3-8, so channel width does not affect the decreasing trend in the straight models.

In the sinuous channel models (SIN1 and SIN2), C_D increases with the water depth scaled by

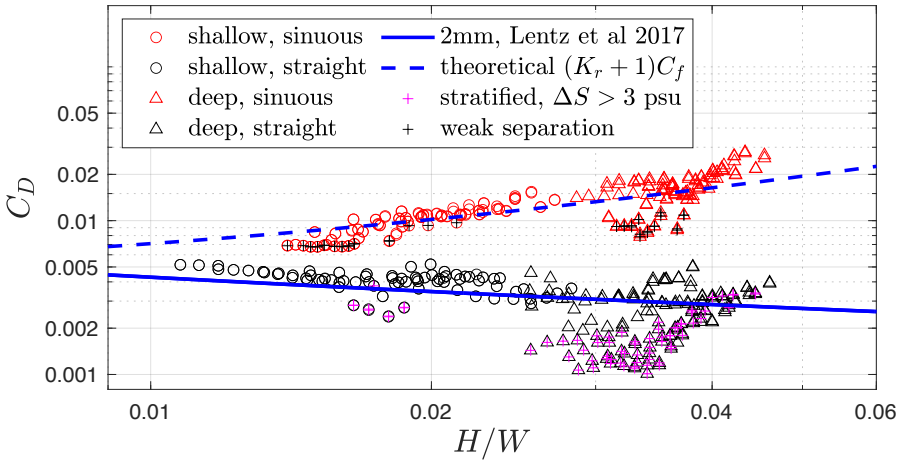

Figure 3-8: The drag coefficient as a function of H/W, with H being the laterally averaged water depth. Red circles: shallow sinuous model (SIN1); red triangles: deep sinuous model (SIN2); black circles: shallow straight model (STR1); black triangles: deep straight model (STR2). The solid blue line shows the C_D predicted by (3.7) with $z_0 = 2$ mm. The dashed blue line shows the C_D predicted by (3.13) in section 3.5. The two shallow channel models (SIN1 and STR1) were the original models employed in section 3.3 and the two deep channel models (SIN2 and STR2) have the same channel shape as the shallow models and a depth of $7 - 12$ m. In the straight model, stratified cases during ebb tide ($\Delta S > 3$) are filled with magenta plus signs. In the sinuous model, weak flow separation cases (effective width $> 0.9w$) are filled with black plus signs.

channel width, which indicates a different dominant mechanism in exerting drag from the straight channel. Calculations of C_D are based on 1-hour averages to filter out fluctuations caused by instability associated with flow separation. As is discussed in section 3.3.3, flow separation is the major source of drag instead of bed friction. Therefore, C_D in sinuous channels has the opposite depth relation because flow separation is stronger in deeper water where it is less inhibited by bottom friction, which thus leads to a larger momentum loss and a larger C_D. Some weak flow separation cases are marked out in Figure 3-8, identified as bends where the effective width $> 0.9w$ (w is channel width). These weak separation cases have relatively small drag coefficients, and occur only during ebb tide. The causes for this weak separation are still unclear, and may depend on inhibition by the shallow bathymetry near the inner bank, greater stratification, or the secondary circulation.

The dependence on water depth explains the flood-ebb asymmetry in C_D (section 3.3.1). Water is deeper during flood tide because of the phase lag between water level and velocity, and as a result, C_D is larger during flood tide (section 3.3.1). The increasing or decreasing trend of C_D along the channel (Figure 3-2) is also related to its dependence on water depth. The channel becomes shallower in the landward direction with a slope of ~ 0.18 m/km (section 3.2). In the straight

channel, C_D increases as water depth decreases (Figure 3-8), so C_D increases landwards in Figure 3-2. On the contrary, in the sinuous channel where flow separation creates form drag, C_D decreases as water depth decreases (Figure 3-8) and as a result C_D decreases landwards in Figure 3-2.

Unlike in straight channels in which C_D only depends on H, C_D in sinuous channels depends on both H and w. Blanckaert (2015) found that the width of flow separation zone primarily scales with the water depth. Consequently, changing the channel width alone can change the fraction of the channel affected by flow separation, and therefore affect C_D. The dependence on w is not shown above as the four models in Figure 3-8 have the same channel width, but cases with different channel widths will be examined in the following sections.

3.4.2 Parameter dependence on channel curvature

Previous research identified the dependence of flow separation and energy loss on bend sharpness, which is expressed as R/W with R being the bend radius of curvature and w being the channel width (e.g. Leopold, 1960; Leeder and Bridges, 1975). Although the mathematical model employed in Leopold (1960) was based on a hydraulic jump theory, which is different from our results (see section 3.5), their exploration of parameter space provides a useful framework. Other researchers have used the sinuosity (e.g. Arcement and Schneider, 1989), which is the ratio of the thalweg length to the straight line length in meanders, but James (1994) proposed that bend losses are not caused by sinuosity per se, but rather by the curvature of bend. In this research, we also chose bend sharpness as the geometric parameter to describe the effect of meanders on the flow.

Bagnold (1960) argued that the overall resistance in a sinuous channel should increase with decreasing curvature ratio R/W. An adjusted Manning's n that decreases with the curvature ratio was brought forward by James et al. (2001) from a flume experiment, consistent with the idea that the drag increases as bends become sharper. Blanckaert (2015) proposed several dominant geometry parameters controlling flow separation including R/W, where R is the minimum radius of curvature along the channel, and decreased R/W leads to stronger flow separation and thus a larger drag. Natural meanders usually show a variation in radius of curvature with a minimum at the bend apexes (e.g. Parsons, 2003), so in this research, we used the minimum centerline radius of curvature to define R/W and quantify bend sharpness.

The vorticity fields in two channel bends were compared to examine the effects of curvature on flow separation (Figure 3-9). The two bends have identical channel widths but different minimum radius of curvature and thus different R/W. In the sharp bend (model SIN1), flow separation is

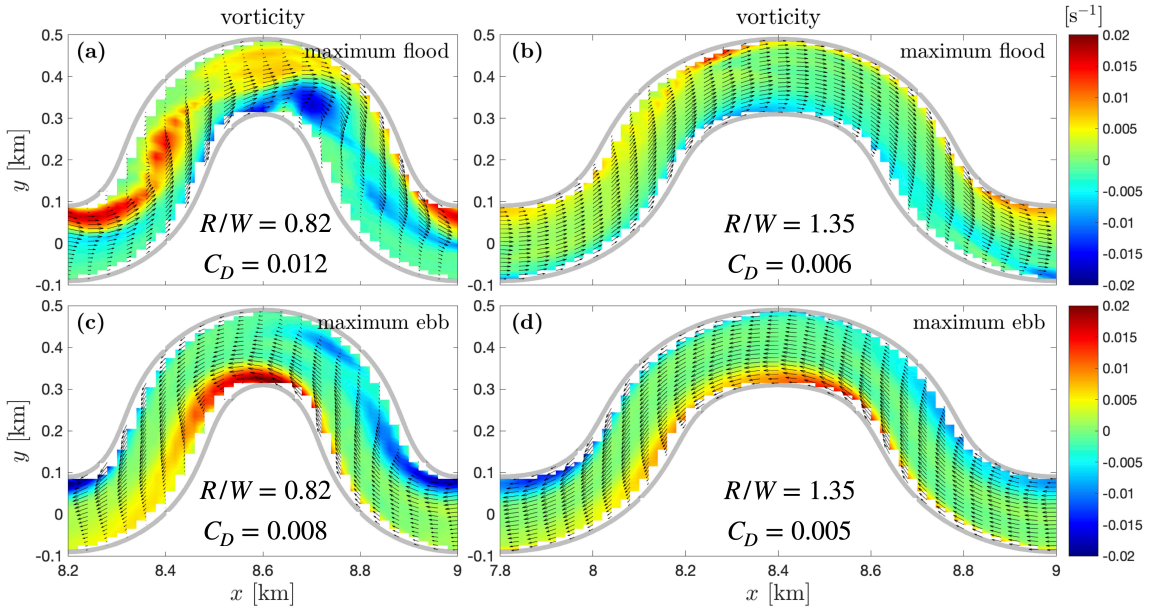

Figure 3-9: Vorticity field around the channel bend. Panels **(a)** and **(b)**: maximum flood tide; panels **(c)** and **(d)**: maximum ebb tide. Panels **(a)** and **(c)**: a sharp channel bend with $R/W = 0.82$ in model SIN1; panels **(b)** and **(d)**: a smooth channel bend with $R/W = 1.35$ in model SIN4. R is the minimum radius of curvature along the channel and w is the channel width. $w = 200$ m for both the sharp and smooth bends. The colormap represents the vorticity and arrows show the velocity field. Gray lines mark the river banks. The average drag coefficient in each case is also shown.

strong, and high vorticity is shed from the inner bank and injected into the main flow (Figure 3-9 **(a) (c)**). However, in the smooth bend (model SIN4), flow separation is weak with no change in the main flow width and no recirculating lee eddy is formed. Also, the deflection of the velocity field is minimal, and the high vorticity fluid generated near the wall remains attached (Figure 3-9 **(b) (d)**). Not surprisingly, the form drag in this smooth bend corresponds to a drag coefficient of $0.001 - 0.003$ and the total C_D is much less than that of the sharp bend, i.e. an average value of 0.006 compared to 0.01.

Vorticity in the sharp bend is stronger during flood tide than ebb tide, which is consistent with the stronger flow separation (and larger drag) during the deeper flood tide. The more complex vorticity field during flood tide is probably because deeper water makes flow separation less inhibited by bottom friction, and stronger lateral circulation may also contribute to flow complexity (e.g. Kranenburg et al., 2019). In the smooth bend where flow separation is relatively weak, vorticity is stronger during ebb tide. This is because the current is stronger during ebb tide due to a shallower water depth, creating greater shear and vorticity.

The dependence of flow separation and drag on bend sharpness is not only through the radius of

curvature R, but also the width w. Larger w leads to larger lateral variation in depth averaged velocity and stronger adverse pressure gradient near the inner bank that facilitates flow separation. James et al. (2001) showed that in the cases of wide channels in the laboratory, flow separation occurred and induced considerable energy dissipation, but no such separation occurred in narrow sinuous channels with same radius of curvature. They also observed a significant difference in resistance between the narrow and wide channels due to this additional energy loss associated with flow separation. Our numerical models showed similar results in which flow separation became weaker as channel width decreased while radius of curvature was kept constant. Detailed comparison of flow structure is not shown here, but the calculated C_D from the model results are summarized below in Figure 3-10.

3.4.3 Drag coefficient diagram

Drag coefficients of all the sinuous models in Table 3.1 are calculated to examine the influence of H/W and R/W and the results are summarized in Figure 3-10 **(a)**. Generally C_D shows an increasing trend with H/W. Within this dependence on H/W, smaller values of R/W are associated with increased C_D. The diagram illustrates how across a range of model configurations, larger H/W and smaller R/W lead to larger C_D, as shown in sections 3.4.1 and 3.4.2. The statistical R^2 from the 2D linear regression of C_D on H/W and R/W indicates that over 70% of the variance for C_D can be explained by these two geometric parameters.

Analysis of the theoretical flow separation model in section 3.5 suggests to non-dimensionalize H using the along-channel bend length L instead of w. The physical explanation of the dependence of C_D on H/L will be shown in section 3.5, but for the sake of comparison, the diagram as a function of H/L is also plotted in Figure 3-10 **(b)**. The conclusion is similar in that C_D increases with H/L and decreases with R/W, but using H/L gives a better collapse of the C_D data and higher R^2 than using H/W.

3.5 Theoretical flow separation model

In this section, we introduce a theoretical model based on boundary layer separation and compare it with numerical results to understand the parameter dependence of C_D. Outside the boundary layer, flow accelerates as it approaches an island, headland or channel bend, and decelerates after passing by the tip or apex, forming an adverse pressure gradient behind the tip or apex. The adverse

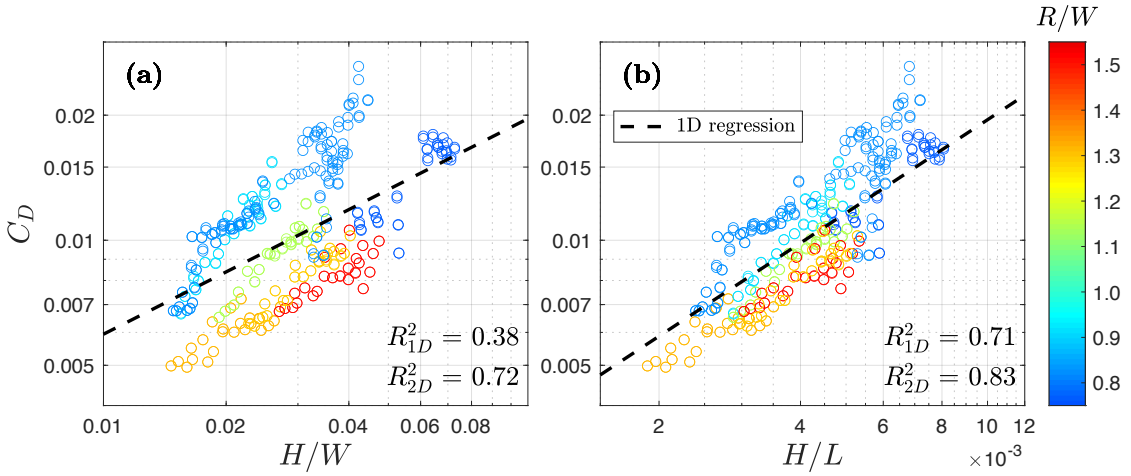

Figure 3-10: **(a)** The drag coefficient as a function of H/W with different R/W values. **(b)** The drag coefficient as a function of H/L with different R/W values. Different colors of the data points denote different R/W values, as is shown on the colorbar. R^2_{1D} represents the statistical R^2 from linear regression of C_D on H/W or H/L; R^2_{2D} represents the statistical R^2 from linear regression of C_D on both H/W or H/L and R/W. The dashed black lines represent the 1D linear regression on H/W or H/L; the 2D linear regression is not shown here.

pressure gradient is imposed by the outer potential flow onto the viscous boundary layer, which therefore decelerates and even reverses flow near the boundary and leads to boundary layer separation (Signell and Geyer, 1991). In a sinuous channel with limited width, the boundary layer is not always distinguishable from the main flow, but the basic physics are the same as the "outer potential flow and viscous boundary layer" model. Therefore, in this theoretical model, we will first assume potential channel flow to quantify the flow field and then include friction and viscosity to investigate the boundary layer separation.

3.5.1 Potential flow in an idealized sinuous channel

The planform of classical type meanders shows a variation in radius of curvature from a minimum at the bend apexes to infinity at the crossovers between bends (Parsons, 2003). Therefore, in the theoretical model, an idealized flat-bottom channel is built with the centerline radius of curvature described by

$$R = \frac{R_0}{\sin(\pi s/L)}, \tag{3.8}$$

in which s is the along-channel distance and L is the channel bend length. R_0 is the radius of curvature at the bend apex, which is also the smallest radius along the channel. The channel bend is symmetric around the bend apex. We also assume that the radius of curvature increases linearly

across the channel (e.g. Leopold, 1960), so that the radius at the inner bank is $R - w/2$ and the radius at the outer bank is $R + w/2$.

The potential flow solution in the idealized channel is derived in Appendix C. The cross-channel velocity profile shows an inversely proportional functional form of $u = K/r$, in which K is a constant and r is the cross-channel distance (Leopold, 1960). Therefore, the maximum velocity appears near the inner bank, which is consistent with the numerical result in Figure 3-4 **(b1)** and **(c)** as well as other research including Blanckaert (2015) and Kranenburg et al. (2019). The velocity along the inner bank of the channel can be expressed as

$$u_{inner} = \frac{U_0}{\left(\frac{R}{w} - \frac{1}{2}\right) \ln\left(\frac{R+w/2}{R-w/2}\right)}, \tag{3.9}$$

with U_0 being the uniform incident flow and $R = R(R_0, s)$. Flow near the inner bank accelerates as it enters the bend and then decelerates after passing by the bend apex. The maximum inner bank velocity is found at the bend apex.

3.5.2 Adverse pressure gradient around the channel bend

The dominant along-channel momentum balance in the horizontal boundary layer (Signell and Geyer, 1991) is

$$g\frac{\partial \eta}{\partial s} = -u\frac{\partial u}{\partial s} - C_f\frac{u^2}{H}. \tag{3.10}$$

where u represent the local along-channel velocity instead of the cross-sectional average U, and non-inertial effects of curvilinear coordinates are negligible. The unsteady term is negligible because the tidal period is much longer than the timescale of flow passing through one channel bend. The advection term containing v is also relatively small and therefore neglected, and baroclinic effects are ignored because we have assumed homogeneous flow in the theoretical model. Bottom friction is more important than the horizontal viscosity in shallow flows (e.g. Wolanski et al., 1984; Pattiaratchi et al., 1987; Signell and Geyer, 1991), so the horizontal viscous term is also neglected.

In the simplified momentum budget (3.10), the pressure gradient (the left side term) is balanced by advection (the first term on the right side) and friction (the second term on the right). C_f is the friction coefficient which describes the drag related to bed skin friction, which is the dominant source of drag in the absence of flow separation. C_f is set to be 0.004, a value similar to the C_D of the straight channel numerical model and that predicted by (3.7) with a bottom roughness of 2 mm

and water depth of $\sim 3-4$ m.

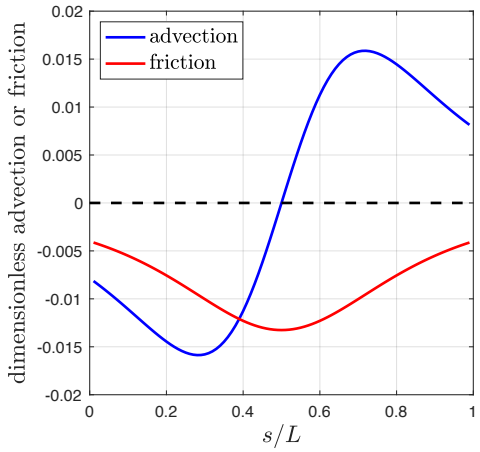

Figure 3-11: Advection and friction terms in (3.10) as a function of along-channel distance s in the theoretical flow separation model. L is the along-channel bend length. $s/L = 0.5$ represents the bend apex. Both terms are non-dimensionalized by U_0^2/H. As representative values, we set $H/L = 0.005$ and $R/W = 1$.

The pressure gradient associated with potential flow can be obtained by substituting the potential flow solution (3.9) into (3.10). We use the inner bank velocity because flow separation happens in the boundary layer near the inner bank. These two right-side terms that determine the pressure gradient are plotted in Figure 3-11. The friction term always results in a favoring pressure gradient. The advection term causes a favoring pressure gradient before the bend apex where flow is accelerated and sets up an adverse pressure gradient behind the bend apex where flow is decelerated. Therefore, flow separation can happen when the advection term exceeds friction and a strong adverse pressure gradient occurs behind the bend apex.

3.5.3 Parameter dependence of flow separation and drag coefficient

Flow separation can be predicted by taking the ratio of the advection term to the friction term. Using the potential flow solution, the advection-friction ratio K_r can be expressed as

$$K_r = -u\frac{\partial u}{\partial s}\Big/ C_f\frac{u^2}{H} = \alpha_1\alpha_2\frac{H}{C_f L}, \tag{3.11a}$$

$$\alpha_1 = \frac{1}{R - w/2}\left(1 - \frac{1}{(\frac{R}{w} + \frac{1}{2})\ln\left(\frac{R+w/2}{R-w/2}\right)}\right), \tag{3.11b}$$

$$\alpha_2 = -\pi R\cot\left(\frac{\pi s}{L}\right). \tag{3.11c}$$

α_1 is related to potential flow with curvature, i.e. $\partial u/\partial R$; α_2 is associated with the sinuous channel shape, i.e. $\partial R/\partial s$. For this analysis, s/L is chosen as 0.75 where advection (or adverse pressure gradient) reaches its maximum (Figure 3-11). Since both α_1 and α_2 are only functions of R_0/w, the advection-friction ratio can be re-written as

$$K_r = \frac{H}{C_f L}\mathcal{F}\left(\frac{R}{w}\right). \tag{3.12}$$

Henceforth we drop the subscript of R_0 for convenience and R will represent the smallest centerline radius of curvature along the channel bend. The ratio K_r depends on two dimensionless number, $H/(C_f L)$ and R/W. This dependence on dimensionless water depth and curvature ratio is in agreement with the parameter dependence of C_D in the numerical results in section 3.4. The water depth H can be either scaled by channel width w or along-channel length L, and both make sense physically. The dependence on H/W lies in the fact that the width of separation zone scales with water depth so the fraction of the main flow impacted by flow separation depends on H/W. H/L emerges by taking the ratio of advection to friction that predicts when flow separation happens. C_f is the bottom friction coefficient, which is a constant in the theoretical model and only varies within a small range in the numerical models, so the effect of C_f is not addressed in detail. $H/(C_f L)$ is analogous to a Reynold's number based on friction instead of viscosity (Pingree and Maddock, 1980; Signell and Geyer, 1991). $H/(C_f L)$ is also called a stability parameter in shallow flows where it is used to categorize island wakes, another example of flow separation (e.g. Jirka and Uijttewaal, 2004). Blanckaert (2010) and Blanckaert (2011) reported two similar control parameters of sinuous dynamics $C_f^{-1}H/W$ and w/R, although that analysis was based on a different conceptual model.

The theoretical ratio K_r is plotted as a function of H/L and R/W in Figure 3-12 **(a)**. K_r increases with H/L and decreases with R/W, suggesting that flow separation is stronger when H/L is larger and R/W is smaller. This is consistent with the similar dependence of C_D on H/L

and R/W in section 3.4, because C_D increases with greater form drag due to flow separation in the sharp bend models.

$K_r = 1$ is marked by a black line in Figure 3-12 **(a)**. For $K_r > 1$, advection dominates friction and flow separation is relatively strong, while for $K_r < 1$, friction dominates advection and flow separation is weak. This theoretical prediction is consistent with our numerical model results. For example, the simulation shown in Figure 3-9 **(b)** and **(d)**, with an $H/L \sim 0.002 - 0.003$ and $R/W = 1.35$, yields $K_r < 1$ in the theoretical model and exhibits weak flow separation in the simulation. Most of the other simulations fall in the regime of $K_r > 1$ and have relatively strong flow separation and larger C_D.

Leeder and Bridges (1975) proposed a dimensionless graph to predict flow separation as a function of bend sharpness R/W and Froude number F_r. Our research focuses on relatively low F_r flow between $0.1 - 0.2$, and we observed flow separation for an R/W of around $0.7 - 1.3$, which is consistent with that study. James et al. (2001) found that the curvature ratio was 2.3 for a narrow sinuous channel without flow separation and 0.89 and 0.54 for two wide sinuous channels with flow separation, with H/L of approximately 0.007, although this parameter is not directly reported. Their narrow sinuous channel falls above the $K_r = 1$ line on our diagram (Figure 3-12 **(a)**) and the wide sinuous channels are below the line, consistent with the theoretical model. A counter example comes from the laboratory channel in Kashyap et al. (2012) which had $H/L = 0.042$ and $R/W = 1.5$ and yet flow separation did not occur. The theoretical model is based on the shallow flow assumption, i.e. bottom friction dominates viscosity, and as a result the theoretical prediction may be less applicable in laboratory flumes where viscosity and friction from sidewalls may have greater influence on the total drag. We can also apply the theoretical model to field observations from the literature. Flow separations observed at two sharp bends on the River Dean, with $H/L \approx 0.04$, $R/W = 0.9$ and 1.4 respectively (Ferguson et al., 2003), and on the Tollense River at a bend with $H/L = 0.015$ and $R/W = 1.0$ (Schnauder and Sukhodolov, 2012) were consistent with the prediction given by Figure 3-12 **(a)**. These two rivers were both relatively deeper than our models. In many rivers, the existence of a point bar decreases water depth near the inner bend and may inhibit flow separation such that rivers must be deeper than tidal channels with similar bend sharpness for flow separation to happen.

While the influences of H/L and R/W are investigated in this research, the bottom friction coefficient C_f also appears in the theoretical result (3.12). The bottom roughness is uniform in all the numerical models, so there is not sufficient parameter range to investigate the influence of

C_f on flow separation. C_f depends on water depth, but the influence of water depth is greater on H/L than C_f. James et al. (2001) reported that vegetation can inhibit flow separation in channel bends and decrease the overall drag. Their research supports our theoretical result that increasing C_f will decrease the advection-friction ratio K_r and suppress flow separation, although in James et al. (2001) C_f is increased by vegetation stem friction rather than bottom roughness.

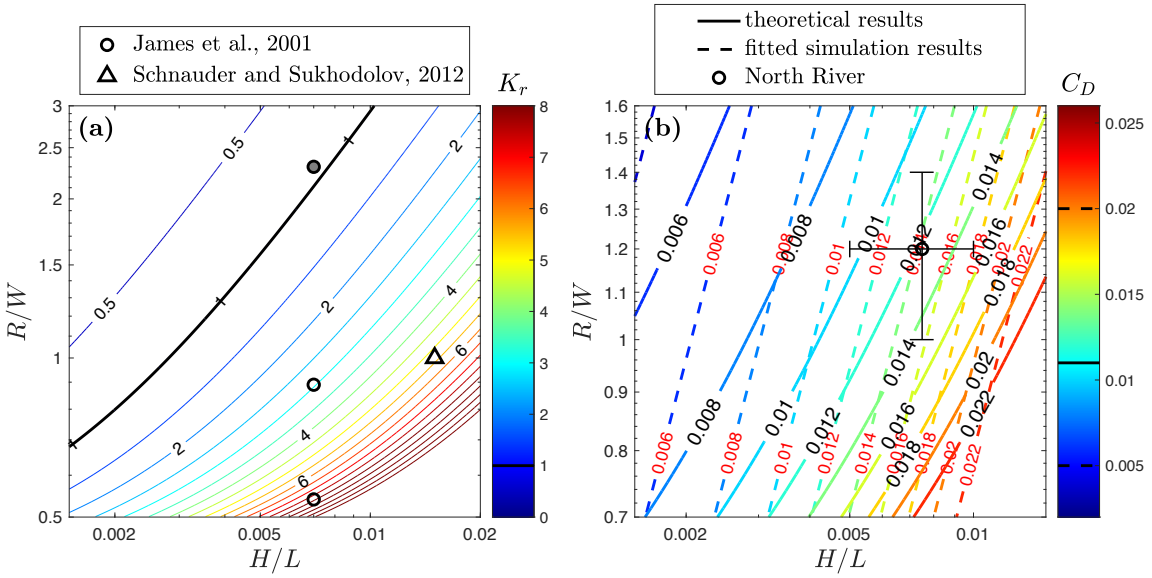

Figure 3-12: **(a)**: Contours of the ratio of advection to friction K_r as a function of H/L and R/W. $K_r = 1$ is marked by the black lines on the colorbar and contours. Circles represent laboratory experiments by James et al. (2001). The hollow circles show cases where flow separation happens; the circle filled with gray color shows the case where flow separation does not happen. The triangle represents observations by Schnauder and Sukhodolov (2012) at one bend on the Tollense River where flow separation happens. **(b)**: Contours of the drag coefficient C_D. Solid lines represent the C_D predicted by (3.13) using K_r of the theoretical model. Dashed lines represent the $2D$ linear fit of numerical results showed in Figure 3-10 **(b)**. The circle shows the estimation of geometric parameters for the North River, with error bars representing spatial and temporal variability. The solid black line on the colorbar represents the average C_D on the North River and two dashed black lines represent the range of observed C_D on the North River.

Comparing Figure 3-10 **(b)** to Figure 3-12 **(a)**, we can observe similar dependencies of K_r and C_D on H/L and R/W. K_r is the advection-friction ratio that predicts flow separation in the theoretical model, while C_D is dominated by form drag in sharp sinuous channels according to the numerical results. This correspondence between the theoretical model and numerical simulations provides further support that the increased drag coefficient is due to flow separation, and leads to the possibility of predicting C_D using the theoretical flow separation model. The ratio K_r can serve as a correction coefficient or amplification factor to the drag coefficient, i.e. $C_D = \mathcal{G}(K_r)C_f$. We

choose a simple linear expression,

$$C_D = (K_r + 1)C_f. \tag{3.13}$$

Although secondary circulation can be another contributing factor in increasing drag, this is not included in (3.13) as the effect of flow separation is dominant in the sharp channel bends of our models. This linear expression does not account for the effect of C_f on flow separation drag either, because it cancels with the C_f in the denominator of K_r. These results assume a fixed value for C_f, but this linear expression, as a speculation, can be used to represent the effects of the two geometric parameters H/L and R/W on C_D.

The predicted C_D given by (3.13) is plotted as the dashed line in Figure 3-8, which agrees reasonably well with our numerical results. The parameter H/L is converted to H/W for the convenience of comparison. In Figure 3-12 **(b)**, the $2D$ linear fit of the numerical results (Figure 3-10 **(b)**) is compared with the theoretical prediction by (3.13). The theoretical prediction shows consistency with the numerical results in the increasing trend with H/L and decreasing trend with R/W as well as the magnitude of C_D, even though we are only using a linear relationship (3.13) with constant C_f. For the North River estuary that initially motivated this study, the two geometric parameters are estimated from Kranenburg et al. (2019), with average $H/L \approx 0.008$ and $R/W \approx 1.2$. Using these values, the effective drag in the North River predicted by Figure 3-12 **(b)** is around 0.012 ± 0.003, where as observations found an average C_D of ~ 0.011, ranging between 0.005 and 0.02 (Bo et al., 2021). It is also worthwhile to note that the parameter dependence discussed above is only correct in the regime where flow separation happens. When there is no flow separation, e.g. when water is very shallow or the bend is very smooth, C_D will either decrease with H as is predicted by (3.7) for straight channels, or show a different parameter dependence if the increased drag is predominately due to secondary circulation.

3.6 Discussion

3.6.1 Flow separation and drag increase in sinuous channels

This research shows that the drag coefficient can be increased by channel meanders as a result of flow separation. Therefore, we suggest modifications to traditional drag coefficients for flow in sinuous tidal channels, e.g. an increase of up to a factor of $2 - 7$ depending on the strength of flow separation. Such a substantial increase to the drag can increase water level slope and result

in considerable water level changes along the channel, which influences wetland inundation and regulates the distribution of vegetation. The increased drag in sinuous channels can also affect tidal propagation (larger amplitude decay and increased phase lag) and potentially storm surge flooding. A sinuous planform may also enhance nonlinear tidal transformation and affect the growth of overtides, which then affects sediment transport.

Apart from the effects of increased drag, flow separation due to channel curvature has the potential to enhance erosion near the inner bank at bend apex, because it increases local velocity and injects fluid from the inner bank to the main flow. Erosion associated with flow separation could alter the sinuous channel morphology, e.g. by the erosion of a point bar. Reversal in the lateral circulation associated with the baroclinic pressure gradient has also been suggested as enhancing erosion near the inner bank and inhibiting formation of a point bar (Kranenburg et al., 2019). Flow separation together with the reversed lateral circulation can explain the absence of a point bar in many sharp bends in tidal meanders, while the absence of a point bar in turn allows for flow separation and the reversed lateral circulation. Flow separation increases deposition in the recirculating dead zone beyond the bend apex where currents are very weak, e.g. Schmidt (1990) found that sandbars form beneath recirculation zones in the Colorado River in the Grand Canyon. As a result, sandbars can grow in the lee of bends where flow separation occurs, and this growth may act differently in unidirectional flow of rivers than the bidirectional flow of tidal channels. The dead zone created by flow separation could also affect along-channel scalar transport by trapping tracers and increasing longitudinal mixing and dispersion (Thackston and Schnelle, 1970).

Key parameters that influence the increased drag coefficient were discussed in this paper — H/L (or H/W) and R/W — but other factors may also affect flow separation drag. Signell and Geyer (1991) mentioned that local acceleration can cause an adverse pressure gradient over headland scales comparable to the tidal excursion ($5 - 10$ km), which therefore impacts the strength of flow separation and magnitude of drag. In the sinuous channels of this study, the channel bends are around $100 - 1000$ m in length, which is much smaller than the tidal excursion so the effect of tidal flow unsteadiness can be neglected. However, channel bends with lengths of up to 10 km are also observed in nature (e.g. Marani et al., 2002) and the unsteadiness associated with tidal currents need to be considered in these cases. In addition, while the velocity field is conventionally considered to be reset at the cross-over point between channel bends (e.g. Abad and Garcia, 2009), interactions between meanders may occur for closely spaced bends (e.g. Leopold, 1960). The vortices shed from an upstream bend due to flow separation can interact with the vorticity field of the downstream

bends (Figure 3-9), and the enhanced instability through multiple bends may affect flow separation and the drag.

This research focused on the increased drag coefficient in sinuous channels associated with flow separation. Secondary circulation created by the sinuous planform can also increase drag by enhancing the lateral velocity and bottom stress (e.g. Chang, 1984; Pein et al., 2018). The drag coefficient increase due to secondary circulation is generally less than 30% in our model results, which is modest compared to the total drag increase associated with flow separation in these very sharp channel bends (a factor of $2-7$). However, in the channel bends that are less sharp, secondary circulation could be a bigger factor in increasing drag. Blanckaert and De Vriend (2010) and Blanckaert (2011) quantitatively expressed the magnitude of secondary circulation as a function of $C_f^{-1}H/W$ and w/R, and this provides a framework for exploring the parameter dependence of the C_D associated with secondary circulation. In addition to the direct effects of secondary circulation discussed above, interactions between the secondary circulation and flow separation (e.g. Figure 3-5) or stratification could also affect the total drag, and are topics which require further research.

In the numerical study, C_D is calculated based on U, the channel average velocity, as the velocity field shows large lateral variations in sinuous models. However, in field observations the channel average velocity is hard to directly measure, and C_D is usually applied to velocity measurements at one location. If field observations are made in the center of the channel where the main flow is accelerated as a result of flow separation, U in the denominator of (3.3) will be overestimated and the measured C_D will become smaller than that predicted by this study. On the contrary, if the current meter is located close to the dead zone, the measured C_D will become larger instead.

3.6.2 Similarity and differences between rivers and tidal channels

River meanders and tidal meanders show strong similarity in their planform geometry (Marani et al., 2002). The similarity lies in the bend sharpness, which is customarily quantified as R/W. Two thirds of the R/W values lie between 1.5 and 4.3 in a sample of 50 rivers (Leopold and Wolman, 1960), and R/W is found to be $1.6-5$ in tidal meanders (Marani et al., 2002). Very sharp bends in river meanders can have an R/W as small as 1.0 (Schnauder and Sukhodolov, 2012) and 0.6 (Nanson, 2010), and in tidal meanders the smallest R/W can reach 0.5 near sharp bend apexes (Marani et al., 2002). Previous studies have also found that fluvial and tidal meanders have similar channel sinuosity (the ratio between along-channel distance to meander wavelength) and similar

ratios of meander wavelength to channel width, for widths and wavelengths spanning three to four orders of magnitude (Leopold and Wolman, 1960; Leopold et al., 1995; Marani et al., 2002).

Key morphological differences between river meanders and tidal meanders lie in their aspect ratio (channel width to depth, w/H), and typically, the cross-channel depth distribution. In river channel bends, the aspect ratio usually falls between 10 and 50 (Millar, 2000). Tidal flat channels tend to have aspect ratios similar to rivers, in the range of $8 - 50$ (Marani et al., 2002), but in salt marsh channels the aspect ratio is typically around 6 (Marani et al., 2002), making them narrower or deeper than river meanders. Vegetation along salt marsh channels can help stabilize banks, reducing channel migration and further steepening banks (Redfield, 1972; Gabet, 1998). The cross-channel depth profile of tidal channels may also differ from rivers, where point bars are commonly found at the inside of bends (Leopold and Wolman, 1960) due to the cross-channel circulation and sediment transport that leads to shallower bathymetry at the inside of bends and deeper at the outside. While point bars also can occur in tidal channels (Barwis, 1977; Fagherazzi et al., 2004), in some sharp tidal channel bends the cross-channel bathymetry is relatively uniform, with an absence of a distinct point bar (e.g. Barwis, 1977; Nidzieko et al., 2009; Kranenburg et al., 2019).

The study site of the North River does not have distinct point bars, and the numerical models have symmetric lateral depth structure. A point bar can enhance the friction near the inner bank, i.e increase the C_f and decrease the effective depth H in (3.12), and thus inhibit flow separation and decrease the form drag. On the other hand, the presence of a point bar can decrease the effective width and increase the effective R/W, which reduces the bend sharpness and the strength of flow separation. Marriott (1998) found in the laboratory that when the flow went overbank and became very shallow near the inner bend, flow reversal and separation were no longer observed, which is similar to the influence of point bars. The prevalence of point bars may explain why flow separation and the associated drag increase are less common in the river literature. Therefore, the effect of cross-channel bathymetry profile needs to be carefully examined in the prediction of flow separation and drag coefficient. On the other hand, flow separation is reported in some rivers that are relatively deeper than our models (e.g. Ferguson et al., 2003; Schnauder and Sukhodolov, 2012), so this form drag may still be expected to occur in relatively deep rivers or tidal channels with a point bar.

Rivers and tidal channels also differ markedly in their hydrodynamic forcing. Rivers have unidirectional fluvial discharge, while tidal channels are influenced by bidirectional tidal flow. Estuarine tidal channels also have inputs of freshwater that create density differences and influence the dynamics. Baroclinic pressure gradients and stratification contribute to the flow structure in many

tidal channels, including by modifying turbulence (Geyer, 1993a) and lateral circulation (Chant and Wilson, 1997; Nidzieko et al., 2009). The differences in forcing correspond with differences in time scales of variability between rivers and tidal channels. Bidirectional tidal flow changes regularly at semi-diurnal to spring-neap periods, while in rivers, major discharge events may occur once a year or less frequently.

The theoretical model is based on the assumption that fluid is homogeneous. In our numerical models, the estuary was weakly stratified during early flood tide and early ebb tide and was vertically well-mixed during other tidal stages. Differences in lateral circulation were also observed between flood and ebb tides, associated with lateral baroclinic pressure gradients. Although the effects of stratification and lateral circulation on C_D require further investigation, the theoretical model without these factors can account for most of the variability in C_D, suggesting that stratification and baroclinic pressure gradients are secondary factors in weakly stratified channels. Conclusions of this study are not only restricted to estuarine tidal channels with mixed fresh and salt water but can also be applied to tidal freshwater or fluvial rivers with similar planform and cross-sectional geometry.

3.7 Conclusion

Increased drag coefficients are found in sinuous channel models, consistent with observations from the North River estuary. This drag increase leads to faster tidal amplitude decay and larger tidal phase lag in tidal channels with curvature. The increased drag coefficient is mainly due to flow separation, which creates a low pressure zone in the lee of bends and produces form drag. The curved estuarine channel also has larger energy dissipation as a result of decreased effective channel width, increased velocity in the center of the channel, and weakened stratification. The increased drag coefficient in sinuous channels depends on two geometric parameters, i.e. it increases with H/L, where H is the water depth and L is the along-channel bend length, and decreases with R/W, where R is the bend radius of curvature and w is channel width. A theoretical boundary layer separation model successfully represents this parameter dependence, which is based on the relative dominance of advection and friction. The theoretical model suggests that flow separation shows similar dependence on H/L and R/W and predicts conditions for flow separation to happen: $R/W < 1$ for "shallow" channels, e.g. $H/L \sim 0.003 - 0.005$ or an aspect ratio of $\sim 20 - 40$; $R/W < 1.5$ for "deep" channels, e.g. $H/L \sim 0.005 - 0.01$ or an aspect ratio of $\sim 10 - 20$. As

a result, the drag coefficient can increase by a factor of $2-7$ depending on channel geometry and strength of flow separation. A point bar can decrease water depth near the inner bank and potentially inhibit flow separation and prevent the drag increase. Although we focused on estuarine channels without a point bar, this research still suggests that the increased drag coefficient associated with flow separation is expected in river or tidal meanders with a point bar, when the bend is sharp and channel is deep enough. [1]

[1] Chapter 4 further analyzes how secondary circulation enhances bottom shear stress and contributes to drag increase in estuarine meanders, in addition to the flow separation and form drag investigated in this chapter.

Chapter 4

Sources of drag in estuarine meanders: momentum redistribution, bottom stress enhancement, and bend-scale form drag

Curvature can create secondary circulation and flow separation in tidal channels, and both have important consequences for the along-channel momentum budget. The North River is a sinuous estuary where drag is observed to be higher than expected, and a numerical model is used to investigate the influence of curvature-induced processes on the momentum distribution and drag. The hydrodynamic drag is greatly increased in channel bends compared to that for straight channel flows. Drag coefficients are calculated using several approaches to identify the different factors contributing to the drag increase. Flow separation creates low-pressure recirculation zones on the lee side of the bends and results in form drag. Form drag is the dominant source of the increase in total drag during flood tides, and is less of a factor during ebb tides. During both floods and ebbs, curvature-induced secondary circulation transports higher momentum fluid to the lower water column through vertical and lateral advection. Consequently, the streamwise velocity profile deviates from the classic log-profile and vertical shear becomes more concentrated near the bed. This redistribution by the lateral circulation causes an overall increase in bottom friction and contributes to the increased drag. Additionally, spatial variations in the depth-averaged velocity field due to the curvature-induced flow are non-linearly correlated with the bathymetric structure, leading to increased bottom friction. In addition to affecting the tidal flow, the redistributed momentum and altered bottom shear stress have clear implications for channel morphodynamics.

The material in this chapter has been accepted for publication as Bo et al. (2023) in *Journal of Physical Oceanography*.

4.1 Introduction

Meanders are ubiquitously found in rivers and tidal channels (e.g., Langbein and Leopold, 1970; Marani et al., 2002; Fagherazzi et al., 2004). Distinct flow processes can occur in channel bends as a result of the curvature effect, including secondary circulation (e.g., Thomson, 1877; Kalkwijk and Booij, 1986) and flow separation (e.g., Leopold, 1960; Leeder and Bridges, 1975). These curvature-induced hydrodynamic processes can significantly alter the streamwise momentum distribution in channel bends and therefore affect the along-channel momentum balance (e.g., Leopold, 1960; Chang, 1984; Seim et al., 2002; Blanckaert and Graf, 2004).

The drag force is a dominant sink term in the momentum budget that opposes the streamwise flow. The drag coefficient C_d is one of the typical ways to quantify the momentum loss, here defined as

$$C_d = \frac{\tau_t}{\rho \overline{u}|\overline{u}|}. \tag{4.1}$$

τ_t is the total drag, ρ is density, and $\overline{u}$ is the depth-averaged velocity. In shallow flows (e.g., in estuaries, rivers, and the coastal ocean), drag is mainly attributed to the bottom shear stress τ_b, i.e., $\tau_t = \tau_b$. Shallow flows typically have a logarithmic velocity in the bottom boundary layer, also known as the log law (e.g., Monin and Yaglom, 1971; Trowbridge and Lentz, 2018),

$$u = \frac{u_*}{\kappa} \ln\left(\frac{z}{z_0}\right). \tag{4.2}$$

where u is the streamwise velocity,

$$u_* = \sqrt{\frac{\tau_b}{\rho}} \tag{4.3}$$

is the shear velocity, $\kappa \approx 0.41$ is the Von Kármán constant, z is the distance above the channel bed, and z_0 is the bottom roughness length-scale. Therefore, a dependence of C_d on H and z_0 can be obtained by combining (4.1), (4.2), and (4.3) (e.g., Gross et al., 1999; Bricker et al., 2005; Lentz et al., 2017),

$$C_d = \left[\frac{\kappa}{\ln\left(\frac{H}{z_0}\right) - 1}\right]^2 \tag{4.4}$$

with H being the water depth. Common values for C_d used in estuaries and tidal channels are around 0.003-0.004 (e.g., Soulsby, 1990; Geyer et al., 2000), e.g., for $H = 5$ m and $z_0 = 0.002 - 0.005$ m.

The overall drag force directly affects the large-scale estuarine momentum balance, with consequences for tidal propagation, flooding potential, and marsh inundation. On the other hand, the local drag from bottom shear stress reflects the intensity of turbulence, which determines the strength of local mixing processes and rate of bed sediment erosion or deposition. Various factors can alter the flow structure, affect the momentum balance and drag, and lead to deviations of C_d from the typical value, including bedforms (Fong et al., 2009), vegetation (Nepf, 1999), stratification (Friedrichs and Wright, 1997), and large topographic features such as headlands (McCabe et al., 2006) and meanders (Seim et al., 2006).

Channel meanders can affect the momentum distribution and drag in an estuary through both secondary circulation and flow separation. The curvature-induced secondary circulation typically results from the local imbalance between the lateral pressure gradient and centrifugal acceleration. Open-channel flow with curvature generates a water level setup near the outer bank and a setdown near the inner bank, and the resulting inward pressure gradient forcing balances the outward centrifugal acceleration in the lateral direction (Thomson, 1877; Kalkwijk and Booij, 1986). The above two forcing terms have a depth-dependent imbalance because the along-channel flow is vertically sheared, and therefore, secondary circulation develops in the lateral plane, typically with inward flow near the bottom and outward flow near the surface, and with downwelling near the outer bank and upwelling near the inner bank for mass conservation. In estuaries, salinity variations can cause internal deformations in the density field and create lateral pressure gradients in addition to those due to water level disturbances, which thus affect the secondary circulation in bends (e.g., Lacy and Monismith, 2001; Nidzieko et al., 2009; Kranenburg et al., 2019).

Secondary circulation has been found to influence the streamwise momentum distribution and hydrodynamic drag in both laboratory and natural meanders (e.g., Chow, 1959; Chang, 1983; Seim et al., 2002; Blanckaert and Graf, 2004). Laboratory experiments have demonstrated that secondary circulation can increase the drag by creating an additional lateral bed shear stress component (e.g., Chang, 1983, 1984; Blanckaert and de Vriend, 2003). Furthermore, bottom stress can be enhanced as a result of the vertical advection of streamwise momentum (Einstein and Harder, 1954; Blanckaert and Graf, 2004; Blanckaert and De Vriend, 2010). A Manning's n is an engineering coefficient typically used to quantify the effect of friction for open channel flows, and meanders were found to have Manning's n values up to 30% greater than straight channels in the laboratory (Chow,

1959). In natural rivers meanders, Arcement and Schneider (1989) also suggested increased values of Manning's n to account for the increased drag. In a curved estuarine channel in San Francisco Bay, secondary circulation was found to laterally transport the high momentum from the center of the channel toward the sides (Lacy and Monismith, 2001), but the influence of the redistributed momentum on the bed shear stress was not investigated. Seim et al. (2002) observed high bottom shear stress in the sinuous Satilla River estuary and attributed it to the vertical advection of high velocity to the bed by secondary circulation, but the measurements did not fully resolve the flow field.

In addition to generating secondary circulation, curvature can induce horizontal flow separation in bends (Leeder and Bridges, 1975; Leopold, 1960). The water level setdown near the inner bank relaxes downstream of the bend apex as the curvature effect decreases, and this creates an adverse pressure gradient along the inner bank (Blanckaert, 2010; Vermeulen et al., 2015; Bo and Ralston, 2020). The adverse pressure gradient decreases the velocity near the inner bank and as a result, can cause the main flow to separate from the inner bank and generate recirculating eddies on the lee side of the bend.

Flow separation can increase the drag in meanders through two mechanisms, i.e., increasing the bed shear stress and creating form drag across the bend. Flow separation can redistribute the streamwise momentum and thereby affect the bottom stress in the bend. In the plan view, the maximum depth-averaged velocity occurs near the inner bank in a bend with laterally uniform bathymetry as a result of Bernoulli effect (e.g., Leopold, 1960; Blanckaert, 2015; Kranenburg et al., 2019). When flow separation occurs downstream of the bend apex, the maximum velocity detaches from the inner bank and shifts toward the center of the channel (Leopold, 1960; Vermeulen et al., 2015). The main flow is restricted to a narrower part of the cross-section by the recirculating separation zone and is thus accelerated. The bottom friction is locally enhanced in regions with the accelerated flow and reduced in the low-velocity separation zone. As a result, the overall bed shear stress increases in the bend with flow separation because of the quadratic dependence of stress on velocity (Bo and Ralston, 2020).

Moreover, flow separation can affect the large-scale momentum budget by creating form drag across the bend. The separation zone has a lower water level than the main flow, and the resulting pressure difference across the bend leads to form drag (Leopold, 1960; McCabe et al., 2006; Bo and Ralston, 2020). Form drag is the integrated pressure force normal to the channel boundaries, in contrast to bottom friction that results from shear near the bed. In an idealized modeling study, form drag was found to be the dominant contributor to drag increase in sinuous estuarine channels,

especially in sharp bends (Bo and Ralston, 2020). Observations from sinuous tidal channels have found effective C_d values in the range of 0.02-0.03 and more than twice greater than attributable to bed shear stress alone (Bo et al., 2021; Ortals et al., 2021), implying that form drag can cause a major increase in the total drag in natural channels.

In sinuous channels, all the above-mentioned mechanisms can potentially contribute to the drag increase, including vertical and lateral advection of momentum by secondary circulation, lateral squeezing of channel flow by the recirculating zone, and form drag created by flow separation. In this study, we use a realistic model of the North River estuary (MA, USA) to quantitatively diagnose the influences of curvature-induced processes on the momentum budget and drag force in channel bends. The North River estuary is a sinuous tidal channel (Kranenburg et al., 2019; Bo et al., 2021; Garcia et al., 2021) and the present research focuses on the mid-estuary region with several channel bends. High drag was observed in this region, and both the curvature-induced secondary circulation and flow separation were suggested as sources of the high drag (Bo et al., 2021). Idealized simulations inspired by the North River indicate that form drag due to flow separation can be the dominant source of drag increase in sharp idealized bends (Bo and Ralston, 2020), but the idealized model geometry did not include the bathymetric heterogeneity found in most natural systems. While the mechanisms of how secondary circulation affects drag have been brought up by several studies (Chang, 1984; Seim et al., 2002; Blanckaert and de Vriend, 2003; Blanckaert and Graf, 2004), a thorough assessment of the processes in natural meanders is lacking. Here we use the realistic North River model to evaluate directly the processes that contribute to drag increase in estuarine meanders, including secondary circulation and flow separation.

In section 4.2, we introduce the realistic North River estuary model. Section 4.3 presents the overall estuarine conditions, flow patterns in meanders, and the calculated drag coefficient. In section 4.4, we evaluate different sources of drag increase and investigate the underlying mechanisms. In section 4.5, we discuss the broader application of the results and their implications for meander morphodynamics. Section 4.6 is a conclusion.

4.2 Methods

4.2.1 Field site

The North River estuary (MA, USA) is a sinuous tidal channel through a salt marsh (Figure 4-1 **(a)**). The region of interest is the mid-estuary of the North River ($\sim 3-7$ km from the mouth), where

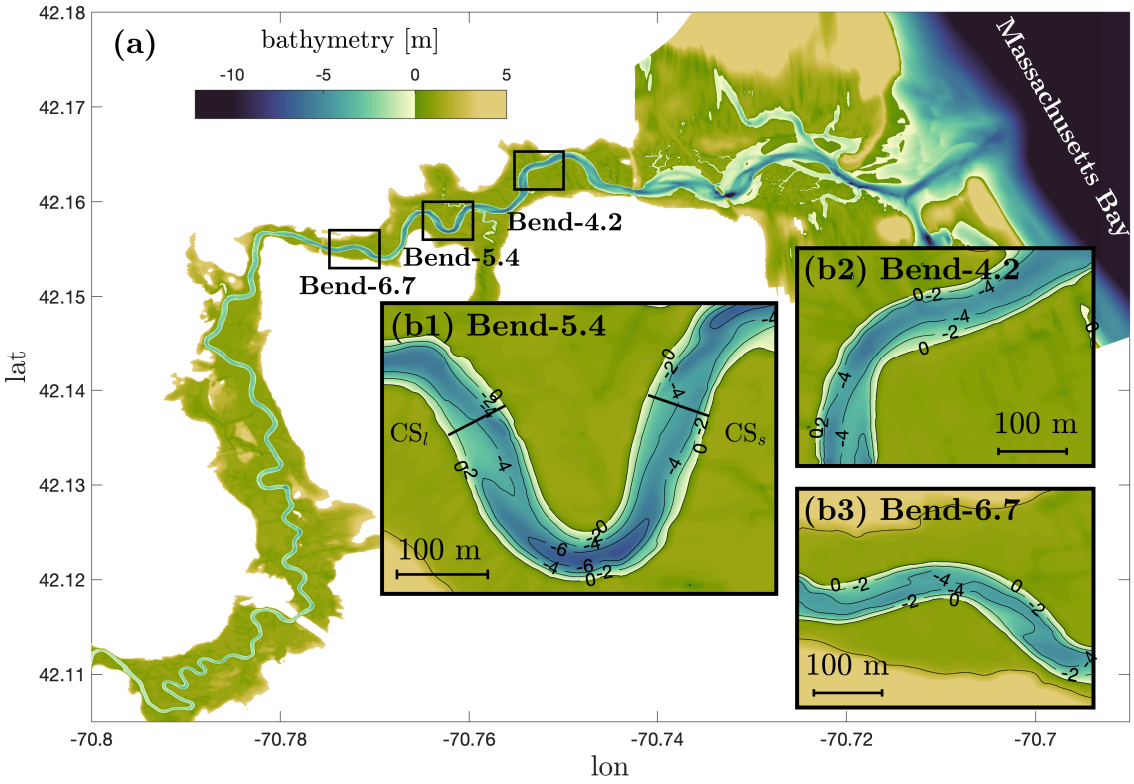

Figure 4-1: Model bathymetry. **(a)**: The North River estuary. **(b1)**: Bend-5.4 (the sharp bend) at 5.4 km into the estuary. The landward control surface CS$_l$ and seaward control surface CS$_s$ show the domain selected for drag calculation. **(b2)** and **(b3)**: Bend-4.2 (intermediate sharpness) at 4.2 km and Bend-6.7 (smooth) at 6.7 km into the estuary.

the channel width W is around 50 m and depth H is around 5 m, i.e., an aspect ratio W/H of 10, which is common for salt marsh meanders (Marani et al., 2002). The radius of curvature R ranges between $60 - 200$ m, yielding a curvature ratio R/W of around $1.2 - 4$. R/W is typically in the range of $1 - 5$ in river and tidal meanders (Leopold and Wolman, 1960; Marani et al., 2002), so the bend sharpness of the North River is representative of other sinuous channels in the nature. Most of the analysis presented here focuses on a relatively sharp bend at 5.4 km into the estuary (Bend-5.4 in Figure 4-1 **(b1)**). Bend-5.4 has an $R/W \approx 1.2$, which is at the lower end of the range of typical values but similar to R/W for bends in other systems (e.g., Marani et al., 2002; Nanson, 2010; Schnauder and Sukhodolov, 2012). The channel is deeper near the bend apex and shallower at the crossover regions between bends, with shoals growing from the inner bank on the seaward side of Bend-5.4 and also on the seaward side of the next bend landward. While shallow point bars are found at the inner bank in many fluvial bends, the cross-channel bathymetry near the apex of bends in the North River is typically symmetric with steep banks and no distinct point bar. The

analysis here also examines two bends that are less sharp at 4.2 km (Bend-4.2 in Figure 4-1 **(b2)**, intermediate sharpness, $R/W \approx 2$) and 6.7 km (Bend-6.7 in Figure 4-1 **(b3)**, relatively smooth, $R/W \approx 4$) to assess variability with the curvature ratio.

Observational data were collected in the North River mid-estuary region from mid-April to late-July in 2017 (Kranenburg et al., 2019; Bo et al., 2021). Five sets of conductivity-temperature-depth (CTD) sensors were deployed from 3 km to 8 km, namely Moor1-5 (see Appendix D for details). Moor3 is located at the apex of Bend-5.4 (the sharp bend). Velocity profile data were collected by upward-looking acoustic Doppler current profilers deployed near bottom CTD sensors at Moor1, 3, and 5. These data are used for evaluation of the realistic North River model that is introduced next.

4.2.2 Numerical model of the North River estuary

The Regional Ocean Modeling System (ROMS) is used to simulate the North River estuary. ROMS is a free-surface hydrostatic model based on the Reynolds-averaged Navier–Stokes (RANS) equations, with structured grids and terrain-following vertical coordinates (Shchepetkin and McWilliams, 2005; Haidvogel et al., 2008; Warner et al., 2008, 2010). The model domain extends from around 6 km off the coast to 18 km into the estuary (Figure 4-1 **(a)**). An orthogonal curvilinear grid follows the marsh platform with the highest resolution of 3-m in the channel (around $10 - 30$ grid cells across the channel) and increasing grid spacing in the ocean and over the marsh away from the channel.

The model has tidal and subtidal forcings on the open ocean boundary on the east side of the model domain. Tidal amplitudes were extracted from the ADCIRC database (Mukai et al., 2002), and subtidal fluctuations were obtained from the low-pass filtered water surface elevation record from the National Oceanic and Atmospheric Administration (NOAA) station at Boston (#8443970). River discharge input from the west side, with data from the U.S. Geological Survey (USGS) gage at Hanover (#01105730) multiplied by 2.3 to account for freshwater inputs below the gage.

Model bathymetry was constructed by combining existing datasets and new surveys. Digital elevation data from the U.S. Geological Survey (USGS) Coastal National Elevation Database (CoNED) and the U.S. Army Corps of Engineers (USACE) Topobathy Lidar Dataset were used for the marsh platform, the North River mouth region, the South River, and the offshore areas in Massachusetts Bay. Surveys in the North River were conducted using Unmanned Surface Vehicles with bathymetric sonar systems (Kimball et al., 2014; Francis and Traykovski, 2021).

The model has 16 uniformly distributed vertical layers, and the k-ϵ closure of the generic length-

scale (GLS) vertical mixing scheme is used for the vertical turbulent mixing (Umlauf and Burchard, 2003; Warner et al., 2005). The horizontal mixing coefficient is set to 0.01 m^2/s. The bottom roughness z_0 is 0.005 m and uniform in the domain, except that at around 7 km from the mouth, z_0 is locally increased to up to 0.2 m to represent a section with larger rocks on the bed. The Coriolis force is included in the model, and while Coriolis dominates the secondary circulation in some systems (e.g., Johnson and Ohlsen, 1994; Ott and Garrett, 1998; Lerczak and Geyer, 2004), it is negligible in narrow estuaries like the North River.

The simulations focus on a neap-to-spring transition from April 19 to 27 in 2017. During the simulated period, the freshwater discharge was moderate to high ($5 - 15$ m^3/s, corresponding to a mean seaward velocity of $2 - 6$ cm/s in the sharp bend), leading to intermittent stratification. Model results are compared with the observational data described above (Kranenburg et al., 2019; Bo et al., 2021). Model performance is assessed by calculating the Murphy skill score (Murphy, 1988; Ralston et al., 2017)

$$Skill = 1 - \frac{\sum(X_{model} - X_{obs})^2}{\sum(X_{obs} - \overline{\overline{X_{obs}}})^2}, \tag{4.5}$$

where X_{model} represents model predictions and X_{obs} represents observations with a time mean $\overline{\overline{X_{obs}}}$. $Skill = 1$ has perfect agreement between the model results and observations, and a $Skill$ of 0 has the root-mean-square error comparable to the standard deviation of the observations. Detailed results of model evaluation are presented in section 4-2 and Appendix D.

Based on comparison with time series of water level, velocity, and salinity at Moor1-5 along the estuary from observations in 2017 (Kranenburg et al., 2019; Bo et al., 2021), $z_0 = 0.005$ m is found to have the best overall model performance (see the sensitivity testing in Appendix D). This value of z_0 is also consistent with the observed ripples and mega-ripples (~ 0.1 m amplitude and 1 to 10 m wavelength) commonly found on the North River bed (Bo et al., 2021).

4.2.3 Drag coefficient C_d and bottom friction coefficient C_f

The drag coefficient and bottom friction coefficient are used to quantify the momentum loss in the bend. We investigate the influence of different flow processes on the momentum budget and separate out their contributions to the drag by comparing three different definitions of the drag and friction coefficients: $C_{d,xs}$ is the drag coefficient based on the cross-sectional-average flux of along-channel momentum, $C_{f,xs}$ is the friction coefficient based on the cross-sectional-average flux, and $C_{f,H}$ is the friction coefficient based on the depth-average flux.

$C_{d,xs}$ and $C_{f,xs}$ are both defined on cross-sectional-average flow properties. $C_{d,xs}$ quantifies the total drag including bottom friction and form drag, while $C_{f,xs}$ only quantifies the bottom friction. $C_{f,H}$ also quantifies the bottom friction but is defined based on the depth-average flow properties. Because of the spatial variations in channel bathymetry and flow field, the depth-average flow at different lateral locations may differ from the cross-sectional-average flow. Therefore, the friction coefficient could be sensitive to how it is defined, and $C_{f,H}$ and $C_{f,xs}$ can have different values and represent different physical meanings. Additional details are provided below and in section 4.4.

The depth-averaged along-channel momentum equation can be approximated as a balance between the tidal pressure gradient forcing and drag

$$-\frac{1}{\rho}\frac{\partial \overline{p}}{\partial s} = \frac{\tau_t}{\rho H}. \tag{4.6}$$

$\overline{p}$ is the depth-averaged pressure and s is the along-channel coordinate. τ_t is the total drag force, and H is water depth. While the advection term can be important locally, it is generally small at the bend-average scale (e.g., Seim et al., 2002; Rogers et al., 2018) and thus has been neglected in the bend-scale momentum budget examined here. The time-rate of change term is also small as we mainly focus on periods away from slack water. The pressure gradient $\partial\overline{p}/\partial s$ results from both the water level gradient and salinity gradient

$$-\frac{1}{\rho}\frac{\partial \overline{p}}{\partial s} = -g\frac{\partial \eta}{\partial s} - \frac{1}{2}\beta g\frac{\partial \overline{S}}{\partial s}H, \tag{4.7}$$

where η is the water level, $\overline{S}$ is the depth-averaged salinity, and β is the haline contraction coefficient. Substituting (4.1) and (4.7) into (4.6),

$$-g\frac{\partial \eta}{\partial s} - \frac{1}{2}\beta g\frac{\partial \overline{S}}{\partial s}H = \frac{C_d\overline{u}|\overline{u}|}{H}. \tag{4.8}$$

The momentum equation (4.8) is integrated through the bend to evaluate the overall drag, i.e.,

$$\int_0^L\int_0^W \left(-g\frac{\partial \eta}{\partial s} - \frac{1}{2}\beta g\frac{\partial \overline{S}}{\partial s}H\right)\mathrm{d}s\mathrm{d}r = \int_0^L\int_0^W C_d\frac{\overline{u}|\overline{u}|}{H}\mathrm{d}s\mathrm{d}r, \tag{4.9}$$

where r is the lateral coordinate, and L and W are the bend length and channel width, respectively.

Averaging (4.9) over the bend-scale, we can write a finite difference form of the momentum budget

$$-g\frac{\Delta\eta}{L} - \frac{1}{2}\beta g\frac{\Delta S}{L}\{\langle H\rangle\} = \{\langle C_d\frac{\overline{u}|\overline{u}|}{H}\rangle\}. \tag{4.10}$$

$\Delta\eta$ and ΔS are the water level and salinity difference between the bend exit and entrance (laterally or cross-sectionally averaged). $\{\cdot\}$ represents the along-channel average through the bend and $\langle\cdot\rangle$ represents the lateral average.

We define a cross-sectional-average drag coefficient $C_{d,xs}$ for the bend based on the cross-sectional average velocity $\langle\overline{u}\rangle$ and lateral average depth $\langle H\rangle$

$$\{\langle C_d\frac{\overline{u}|\overline{u}|}{H}\rangle\} = C_{d,xs}\{\frac{\langle\overline{u}\rangle|\langle\overline{u}\rangle|}{\langle H\rangle}\}. \tag{4.11}$$

Therefore, $C_{d,xs}$ is calculated as the pressure gradient across the bend divided by the bend-average of $\langle\overline{u}\rangle$ squared divided by $\langle H\rangle$, i.e.,

$$C_{d,xs} = \frac{-g(\Delta\eta/L) - \frac{1}{2}\beta g(\Delta S/L)\{\langle H\rangle\}}{\{\langle\overline{u}\rangle|\langle\overline{u}\rangle|/\langle H\rangle\}}. \tag{4.12}$$

$C_{d,xs}$ represents the total effective drag for a given amount of volumetric flux Q through the bend, with $Q = \langle\overline{u}\rangle\langle H\rangle W$ for each cross-section. Moreover, the volumetric flux Q is conserved through the bend, so by assuming no significant along-channel variability of the channel width and depth,

$$\{\frac{\langle\overline{u}\rangle|\langle\overline{u}\rangle|}{\langle H\rangle}\} = Q|Q|\{\frac{1}{\langle H\rangle^3 W^2}\} \approx \frac{Q|Q|}{\{\langle H\rangle\}^3\{W\}^2} \approx \frac{\{\langle\overline{u}\rangle\}|\{\langle\overline{u}\rangle\}|}{\{\langle H\rangle\}}, \tag{4.13}$$

$C_{d,xs}$ defined by (4.12) is thus similar to a bulk drag coefficient $C_{d,bulk}$:

$$C_{d,bulk} = \frac{-g(\Delta\eta/L) - \frac{1}{2}\beta g(\Delta S/L)\{\langle H\rangle\}}{\{\langle\overline{u}\rangle\}|\{\langle\overline{u}\rangle\}|/\{\langle H\rangle\}}. \tag{4.14}$$

$C_{d,xs}$ is based on the average of $\langle\overline{u}\rangle^2/\langle H\rangle$ through the bend, while $C_{d,bulk}$ is a more straightforward definition by averaging $\langle\overline{u}\rangle$ and $\langle H\rangle$ separately through the bend. $C_{d,bulk}$ is generally close to $C_{d,xs}$ in the North River, where the channel cross-sectional area does not notably change with distance along-channel. However, $C_{d,bulk}$ is not an applicable approximation of $C_{d,xs}$ in systems with large streamwise variations in depth and velocity, e.g., the flow over coral reefs in Lentz et al. (2017), so we use (4.12) to quantify the overall drag in this study.

Similar to the cross-sectional-average drag coefficient $C_{d,xs}$ that quantifies the total drag, we

define a cross-sectional-average bottom friction coefficient $C_{f,xs}$ that quantifies the effective bottom friction in the bend but not the form drag.

$$C_{f,xs} = \frac{\{\langle \tau_b/(\rho H)\rangle\}}{\{\langle \overline{u}\rangle|\langle \overline{u}\rangle|/\langle H\rangle\}}, \tag{4.15}$$

with τ_b being the bottom shear stress.

Since the drag varies with $\overline{u}^2$ and $1/H$, the lateral variations in each of them can non-linearly affect the total drag in ways that are not represented in the cross-sectional average velocity and depth. Therefore, a depth-average drag coefficient $C_{d,H}$ based on the local depth H and depth-averaged velocity $\overline{u}$ can be defined to account for this spatial variability.

$$\{\langle C_d \frac{\overline{u}|\overline{u}|}{H}\rangle\} = C_{d,H}\{\langle \frac{\overline{u}|\overline{u}|}{H}\rangle\}. \tag{4.16}$$

In this research, $C_{d,H}$ is not calculated, because there is form drag in the bend which has to be calculated as a spatial integral over the topographic feature of interest and cannot be estimated locally (McCabe et al., 2006; Bo and Ralston, 2020). Instead, we use the depth-average bottom friction coefficient $C_{f,H}$ that quantifies bottom shear stress alone.

$$C_{f,H} = \frac{\{\langle \tau_b/(\rho H)\rangle\}}{\{\langle \overline{u}|\overline{u}|/H\rangle\}}. \tag{4.17}$$

$C_{f,H}$ and $C_{f,xs}$ both have the bend-average bottom shear stress on the numerator, and the difference lies in the denominator term (velocity squared divided by depth) used to non-dimensionalize the drag. $C_{f,H}$ quantifies the bend-average bottom friction experienced by the locally varying flow, while $C_{f,xs}$ represents the overall effective bottom friction experienced by the cross-sectional average flux in the bend. As an example, in a straight channel with complex bathymetry, $C_{f,H}$ will be close to values estimated by (4.4) when a stable log-profile is established everywhere, but $C_{f,xs}$ can be increased due to correlations between spatially variable velocity and depth, e.g., when strong currents occur in shallow regions of the channel. It is also worthwhile to note that $C_{f,H}$ is usually difficult to estimate in the field given the requirement of high spatial resolution measurements of velocity and depth, but this definition is necessary to assess the influence of the horizontal variations in the flow field on the drag. The calculation of $C_{f,xs}$ is more achievable in the field with a knowledge of channel bathymetry and an estimation of the volumetric flux in a representative cross-section.

4.3 Results

4.3.1 Estuarine conditions and model evaluation

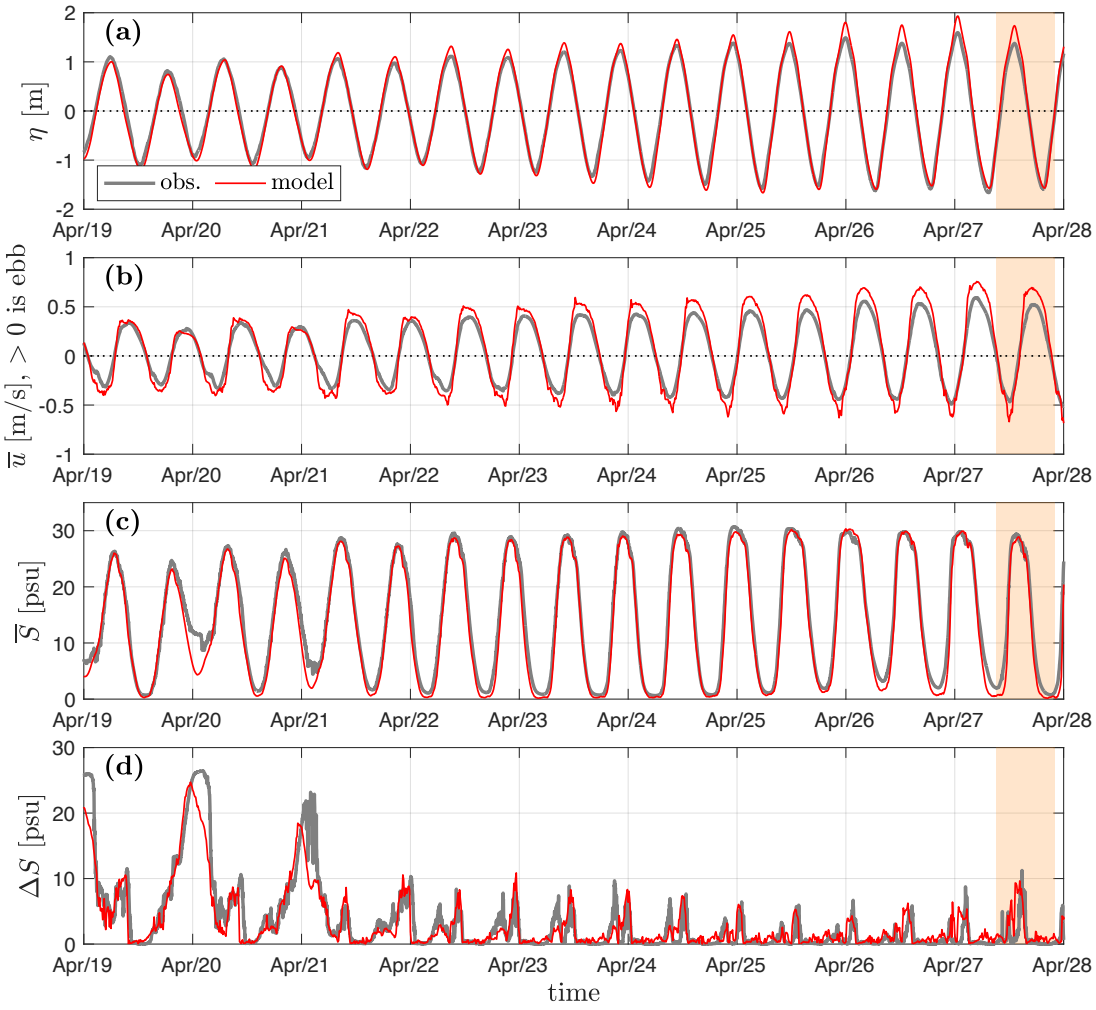

Figure 4-2: The modeled estuarine conditions compared with observations at Moor3 (at the apex of Bend-5.4) in April 2017. Thick gray lines represent observations, and thin red lines represent model results. **(a)**: Water level η. **(b)**: Depth-averaged velocity $\overline{u}$. **(c)**: Depth-averaged salinity $\overline{S}$. **(d)**: Stratification ΔS (bottom-surface salinity difference). Orange bands show the tidal cycle selected for detailed analysis.

The North River estuary is dominantly forced by semi-diurnal tides and during the observation period the tide range varied between around 2 m (April 19, neap tide) and 3 m (April 27, spring tide) (Figure 4-2). The maximum tidal current in Bend-5.4 that is the focus of this study is around $0.5 - 0.8$ m/s. Generally stratification is stronger during neap tides (instantaneous bottom-surface salinity difference ΔS up to $\sim$ 20 psu) and weaker during spring tides (ΔS up to $\sim$ 5 psu). Stratification

also has significant intra-tidal variations due to the along-estuary advection of salinity gradient by the tidal currents. In the mid-estuary, stratification mainly occurs from late flood tide to early ebb tide.

A tidal cycle on April 27 is selected for detailed analysis in the following sections as a representative of weakly stratified conditions (Figure 4-2 **(d)**). We mainly focus on periods around maximum tidal velocity when the drag is greatest. Stratification is weak around the times of maximum tidal currents for most of the spring-neap cycle, except during the weakest neap tides. In addition, discharge in the North River was relatively high during the observations in late April. Discharge is generally lower during other seasons, and thus stratification is weaker than during the study period. The following results and analysis mainly focus on periods with weak stratification, and the effects of stronger stratification will be discussed in section 4.5.

The model results are compared with observations, indicating an overall good model performance. At Moor3 (at the apex of Bend-5.4) skill scores are $Skill = 0.98$ for water level and $Skill = 0.97$ for salinity. Comparisons of velocity and stratification yield $Skill = 0.91$ and $Skill = 0.82$ respectively, which are slightly lower and more sensitive to the measurement location compared to the other two variables. Assessments of model performance at moorings located in other parts of the estuary are shown in Appendix D and generally have similar skill scores to Moor3.

4.3.2 Secondary circulation and flow separation

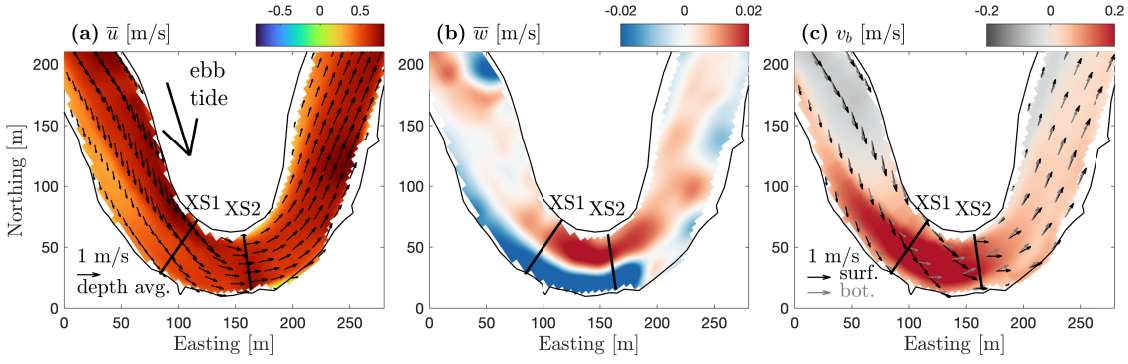

Figure 4-3: The ebb tide flow field in Bend-5.4 (at 3-hr after slack water). **(a)**: Depth-averaged streamwise velocity $\overline{u}$. Positive u means seaward velocity (ebb direction). Arrows show the depth-averaged horizontal velocity. **(b)**: Depth-averaged vertical velocity $\overline{w}$. **(c)**: Near-bed lateral velocity v_b. Positive means inward in the focused bend (approximately northward). Black arrows represent the surface velocity and gray arrows represent the bottom velocity.

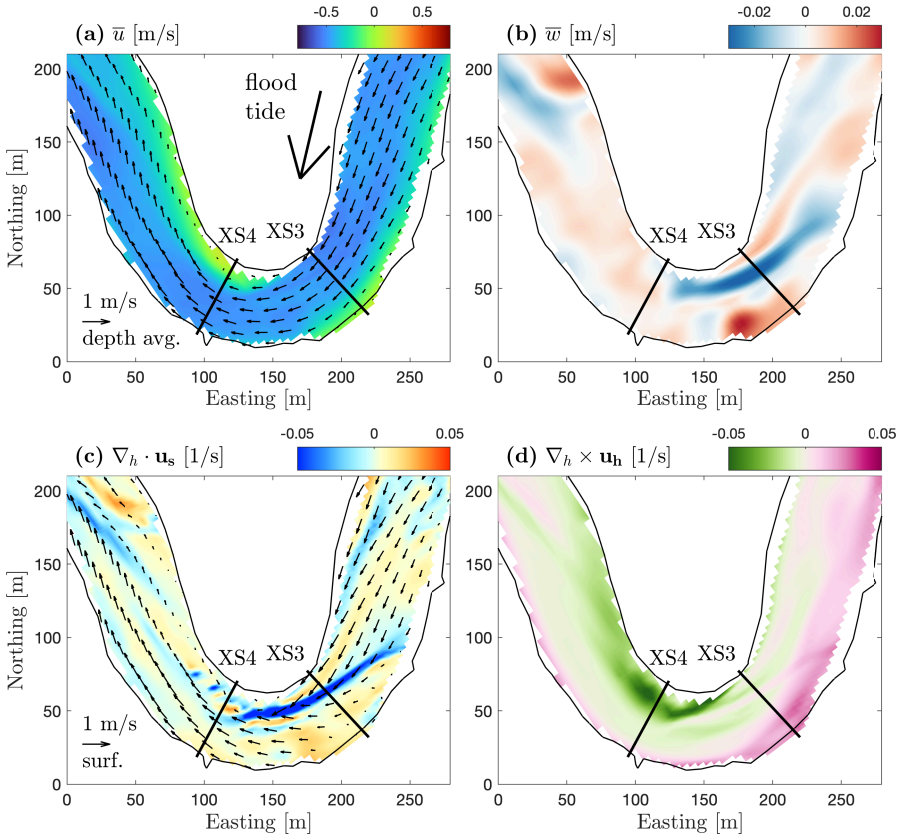

Figure 4-4: The flood tide flow field in Bend-5.4 (at 3-hr after slack water). **(a)**: Depth-averaged streamwise velocity $\overline{u}$. Negative u means landward velocity (flood direction). Arrows show the depth-averaged horizontal velocity. **(b)**: Depth-averaged vertical velocity $\overline{w}$. **(c)**: Surface divergence $\nabla_h \cdot \mathbf{u_s}$. Arrows show $\mathbf{u_s}$, the surface horizontal velocity vector. Blue color means surface convergence. **(d)**: Depth-averaged vertical vorticity $\nabla_h \times \mathbf{u_h}$, with $\mathbf{u_h}$ being the depth-averaged horizontal velocity vector.

Two key flow processes, i.e., secondary circulation and flow separation, influence the momentum budget and drag in meanders. Thus, in this section, we present the flow patterns in Bend-5.4 where observations have been previously been made (Kranenburg et al., 2019; Bo et al., 2021) and assess the influence of secondary circulation and flow separation on momentum distribution. The influences of curvature on drag also apply to other bends along the estuary, and those results are presented in a later section.

During the ebb tide, the classical helical flow develops in Bend-5.4 (Figure 4-3 and Figure 4-5 **(a)**, **(b)**), with inward secondary flow near the bed and outward flow near the surface. The maximum streamwise velocity occurs near the inner bank as flow approaches the bend apex (XS1 in Figure 4-5 **(a)**), as a result of the Bernoulli effect (e.g., Leopold, 1960; Blanckaert, 2015; Kranenburg et al., 2019). The outward lateral flow tends to advect the higher momentum toward the outer

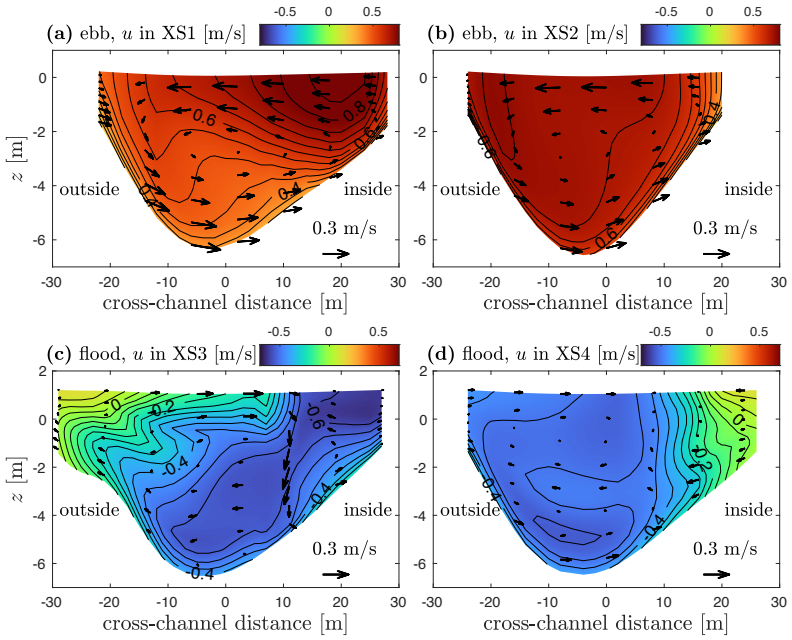

Figure 4-5: **(a)** and **(b)**: Along-channel velocity u in the cross-sections XS1 and XS2 during the ebb tide. Locations of XS1 and XS2 are marked in the map views in Figure 4-3. **(c)** and **(d)**: Along-channel velocity u in the cross-sections XS3 and XS4 during the flood tide. Locations of XS3 and XS4 are marked in the map views in Figure 4-4. Positive u means seaward velocity (ebb direction), and negative u means landward velocity (flood direction).

bank in the upper water column, and the vertical velocity near the outer bank transports higher momentum flow downward and increases the streamwise velocity near the bed. The higher momentum flow then is spread laterally inward by the secondary flow near the bed. As a result of the stirring (lateral and vertical advection) by secondary circulation, the streamwise velocity, which is concentrated near the surface at the inner bank upstream in the bend, becomes more uniformly distributed in the cross-section near the bend apex (XS2 in Figure 4-5 **(b)**). Maximum velocities in vertical profiles appear near the bed in the outer bend at the bend apex, similar to velocity profiles reported in laboratory studies of bends with uniform density and laterally uniform bathymetry (e.g., Blanckaert and Graf, 2004).

During the flood tide, the flow structures are different from the classical helical flow in meanders due to flow separation and more complex secondary circulation. The main flow detaches from the inner bank at the bend apex, with zero and even reversed streamwise velocity near the inner bank (Figure 4-4 **(a)**). Flow separation leads to the generation of horizontal vorticity (Figure 4-4 **(d)**), and a recirculating eddy occurs in the separation zone on the lee side of the bend. Similar flow separation has been reported in laboratory bends (e.g., Leopold, 1960; Blanckaert, 2015), idealized sinuous

channels (e.g., Bo and Ralston, 2020), natural rivers (e.g., Ferguson et al., 2003; Frothingham and Rhoads, 2003), and tidal channels (e.g., Leeder and Bridges, 1975) including the North River estuary (Bo et al., 2021).

While the maximum streamwise velocity is near the inner bank upstream of the bend apex (XS3 in Figure 4-5 **(c)**), the region with maximum along-channel momentum is shifted toward the center of the channel where flow separation occurs (XS4 in Figure 4-5 **(d)**). In addition, a low velocity zone is found near the outer bank upstream of the bend apex (XS3 in Figure 4-5 **(c)**), indicating flow separation near the outer bank. The outer bank separation occurs due to an adverse pressure gradient along the outer bank approaching the bend apex and is analogous to the inner bank flow separation downstream of the apex (Blanckaert, 2010; Blanckaert et al., 2013; Vermeulen et al., 2015). Outer bank separation can also squeeze and accelerate the main flow, although it is less commonly found in the North River model than inner bank separation.

In contrast to the classical curvature-induced secondary circulation during the ebb tide, multiple secondary circulation cells occur during the flood tide. This more complex secondary circulation appears due to the combined effect of channel curvature and salinity variations during floods, as was investigated by an observational study in this bend (Kranenburg et al., 2019). Upstream of the bend apex (XS3 in Figure 4-5 **(c)**), the laterally sheared along-channel velocity creates a lateral density difference through differential advection of the along-channel salinity gradient (Kranenburg et al., 2019), with saltier water and the maximum velocity near the inner bank. The resulting lateral baroclinic pressure gradient (BCPG) creates a primary secondary circulation cell in the outer part of the bend and a smaller cell near the inner bank, with surface convergence in between the cells at the streamwise velocity maximum (also see Figure 4-4 **(c)**). High momentum flow is transported to the lower water column by the downward velocity at the surface convergence and spreads laterally near the bed with the lateral velocity. Downstream of the bend apex flow separation occurs (XS4 in Figure 4-5 **(d)**) and the secondary circulation becomes more complex, but the higher momentum streamwise flow remains in the lower water column.

4.3.3 Drag and friction coefficients

The cross-sectional-average drag coefficient $C_{d,xs}$, cross-sectional-average bottom friction coefficient $C_{f,xs}$, and depth-average bottom friction coefficient $C_{f,H}$ are calculated through Bend-5.4 for the neap-to-spring transition from April 19 to 27. The control volume is selected as the channel between the bend crossovers (marked by two solid lines CS_l and CS_s in Figure 4-1 **(b1)**]), excluding

the marsh platform. The calculation is based on the model output of every 10 minutes, and we focus on $\sim$ 2-hr periods around maximum flood and ebb when the drag is greatest. During several of the strongest spring tides, the water level exceeds the bank height and the marsh is inundated from maximum flood tide to early ebb, and these periods are not included in the calculation.

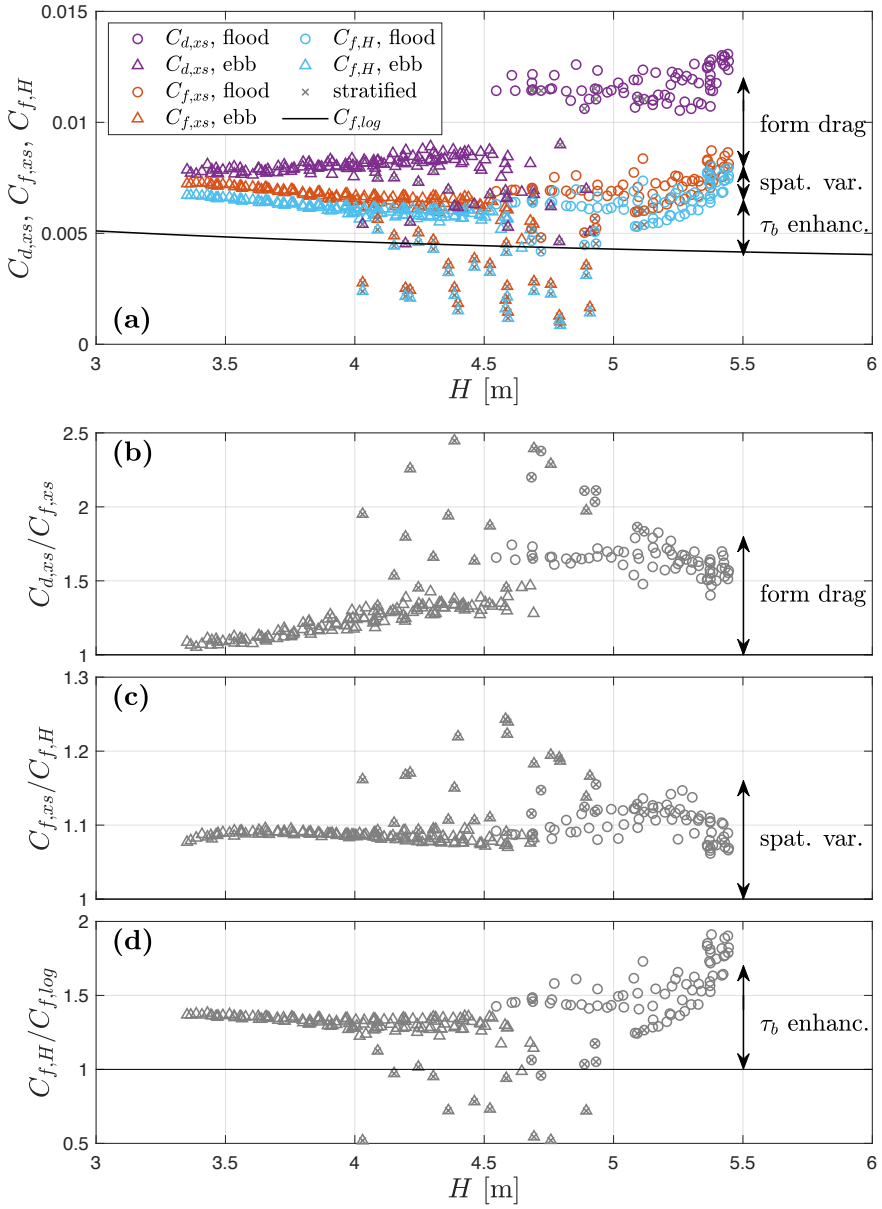

Figure 4-6: The calculated cross-sectional-average drag coefficient $C_{d,xs}$, cross-sectional-average friction coefficient $C_{f,xs}$, depth-average friction coefficient $C_{f,H}$, and their ratios as a function of water depth H in Bend-5.4. $C_{f,log}$ is calculated from the log-profile assumption (4.4). Triangles represent ebb tide and circles represent flood tide. Stratified cases are marked by crosses, defined based on $\Delta S > 2$.

The calculated $C_{d,xs}$, $C_{f,xs}$, and $C_{f,H}$ are plotted as a function of water depth H (Figure 4-6 **(a)**). Note that the water depth is greater during flood tides than ebb tides because the phase difference between tidal water level and velocity is less than 90°. The depth-dependence is examined because both previous research on flow separation (Bo and Ralston, 2020) and the classical solution to bottom boundary layer flow (4.4) suggest a dependence of drag on water depth. Assuming a log-profile for streamwise velocity, the corresponding friction coefficient (from (4.4), hereby named as $C_{f,log}$) is in the range of $0.004 - 0.005$ for $z_0 = 5$ mm and a depth of $3 - 6$ m. $C_{f,log}$ decreases as water depth increases for channel flow with log-profiles because the velocity profile becomes less sheared in the upper water column with increasing flow depth (e.g., Bricker et al., 2005; Lentz et al., 2017). The calculated $C_{d,xs}$, $C_{f,xs}$, and $C_{f,H}$ are all greater than the value of $C_{f,log}$ from the log-profile assumption, with the exception of some stratified cases that will be discussed later. The greater values are consistent with the observed high drag in the North River estuary (Bo et al., 2021) and reflect the increase in drag due to channel curvature. The total drag $C_{d,xs}$ can be up to a factor of 2 larger than the $C_{f,xs}$ due to bottom friction alone, suggesting that form drag due to flow separation sometimes dominates the additional momentum loss (Bo and Ralston, 2020). $C_{f,xs}$ and $C_{f,H}$ are also greater than the typical values of $0.004 - 0.005$, indicating that the bottom shear stress is enhanced in the bend. In addition, the calculated $C_{d,xs}$, $C_{f,xs}$, and $C_{f,H}$ in the bend display more complex depth-dependence compared to $C_{f,log}$, because of various contributing factors to the drag. In the following section, the contributions of the secondary circulation, form drag, and streamwise velocity distribution to enhancing the drag with flow curvature will be diagnosed through analysis of the different drag and friction coefficients.

4.4 Analysis

4.4.1 Identifying sources of drag increase

Form drag

The cross-sectional-average drag coefficient $C_{d,xs}$ is around $0.008 - 0.013$, and the cross-sectional-average bottom friction coefficient $C_{f,xs}$ is $0.006 - 0.008$. The ratio of $C_{d,xs}/C_{f,xs}$ compares the contribution of form drag versus bottom friction in the bend (Figure 4-6 **(b)**), and it indicates a total drag increase of up to 80% due to the form drag. Flow separation can create a low-pressure recirculation zone on the lee side of the bend, and the resulting pressure difference across the bend

leads to a net pressure force exerted by the channel boundaries on the flow, i.e., the form drag. Form drag has been suggested to be a dominant source of drag in the North River estuary based on previous observations Bo et al. (2021). Form drag was directly calculated in idealized models that scaled with the North River and it accounted for the difference between the total momentum loss and bottom friction (Bo and Ralston, 2020). The complex geometry and bathymetry of the realistic model here make the direct calculation of form drag prohibitively difficult. Nonetheless, the characteristics of the flow and the excess water level drop that is not balanced by the bottom friction clearly indicate the dominance of form drag in this situation.

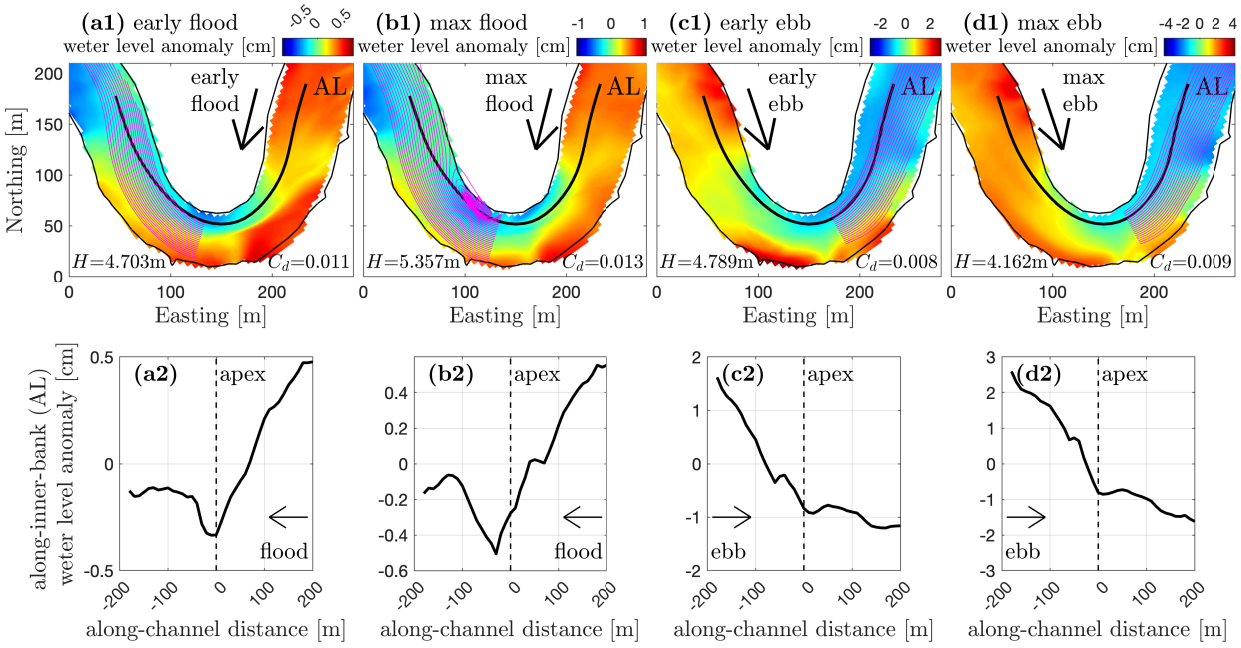

Figure 4-7: Water level anomaly in Bend-5.4. **(a1)**: early flood tide (1-hr after slack water); **(b1)**: max flood tide (3-hr after slack water); **(c1)**: early ebb tide (1-hr after slack water); **(d1)**: max ebb tide (3-hr after slack water). Magenta lines show streamlines starting from slightly downstream of the bend apex. Note that the streamlines are calculated based on the depth-averaged velocity field, and they only approximate the 3-d channel flow. The water level slightly exceeds the bank height at this max flood tide, so some streamlines are terminated at the marsh platform. **(a2)**-**(d2)**: water level anomaly on an along-inner-bank line (AL). The location of AL is marked in the map views.

Form drag is most notable during flood tides and can increase the drag by 50-80% compared to bottom friction alone. During ebb tides, form drag is smaller and even negligible. This flood-ebb asymmetry in form drag is consistent with the above-described flow field in the bend (section 4.3.2), where flow separation is mainly found during floods. Flow separation typically occurs as a result of the adverse pressure gradient along the inner bank downstream of the bend apex (Blanckaert, 2010;

Vermeulen et al., 2015; Bo and Ralston, 2020). While the curvature effect tends to set an adverse pressure gradient behind the bend that can lead to flow separation, bottom friction in the channel sets a favoring pressure gradient that can inhibit flow separation (Signell and Geyer, 1991; Bo and Ralston, 2020). An adverse pressure gradient occurs when the curvature effect exceeds the frictional effect, resulting in flow separation in the lee of a bend.

We investigate the along-inner-bank water level distribution to understand the flood-ebb asymmetry in flow separation and form drag (Figure 4-7). During early flood tide, the lowest water level is found near the bend apex on the inner bank, with an adverse pressure gradient along the inner bank downstream of the apex. As a result, flow separation develops later into flood tide and a low-pressure recirculation zone grows downstream. The low-pressure zone on the lee side wall results in a pressure difference across the bend, thus creating form drag. By contrast, a favoring pressure gradient along the inner bank persists during the ebb tide, and without an adverse pressure gradient flow separation and form drag do not occur.

The flood-ebb asymmetry in adverse pressure gradients, flow separation, and form drag can be partially explained by a depth-dependence. The water is deeper during flood tides, so the inertial effect of curved flows has greater influence on setting an adverse pressure gradient and reversing the flow direction (Bo and Ralston, 2020). However, during ebb tides the tidal stage is lower and with shallower water a stronger frictional effect tends to inhibit flow separation. The ratio of $C_{d,xs}/C_{f,xs}$ in the bend increases with water depth (Figure 4-6 **(b)**), which is consistent with the depth-dependence of form drag with flow separation (Bo and Ralston, 2020).

While the ratio of $C_{d,xs}/C_{f,xs}$ displays a more continuous depth-dependence (Figure 4-6 **(b)**), the value of $C_{d,xs}$ shows a larger gap between flood and ebb tides that cannot be explained by the difference in depth alone (Figure 4-6 **(a)**). We speculate that the distinct 3-d flow structure during flood tides favors the onset of flow separation compared to ebb tides and enhances the flood-ebb asymmetry of form drag. During flood tides downwelling occurs near the inner bank upstream of the bend apex as a result of the BCPG-driven secondary circulation (Figure 4-4 **(b)** and Figure 4-5 **(c)**). The secondary flow tends to maintain high streamwise momentum with a convergence zone near the inside of the bend. This increased streamwise momentum enhances the water level setdown at the bend apex due to the Bernoulli effect and favors the creation of an adverse pressure gradient downstream of the bend apex that can lead to flow separation (Figure 4-7). Additionally, the downwelling near the inside of the bend during floods alters the vertical structure of streamwise velocity, with low velocity and reversed vertical shear in the upper column. Consequently, the influence of

the bottom boundary layer is restricted to the lower water column (detailed analysis presented in section 4.4.2), and the tendency of bottom friction to inhibit flow separation is suppressed. Therefore, the frictional effect is weakened by the BCPG-driven secondary circulation during flood tides compared to that expected based on water depth alone, and this enhances the flood-ebb asymmetry of flow separation and form drag. By comparison, river meanders typically have helical flows similar to the ebb tide cases in our study, and flow separation is not commonly found in rivers except in distinctly deep and sharp river bends (e.g., Ferguson et al., 2003; Schnauder and Sukhodolov, 2012).

Increased overall bottom friction due to the spatial variability of flow field

The ratio of cross-sectional-average to depth-average bottom friction coefficient $C_{f,xs}/C_{f,H}$ represents the drag increase due to the spatial variability of the velocity and water depth and their non-linear correlation. $C_{f,xs}/C_{f,H}$ is essentially the ratio of $\{\langle\overline{u}|\overline{u}|/H\rangle\}/\{\langle\overline{u}\rangle|\langle\overline{u}\rangle|/\langle H\rangle\}$ (also see (4.15) and (4.17)), i.e., the spatial average of the local depth-average velocity squared divided by depth versus the cross-sectional average velocity squared divided by the lateral average depth. $C_{f,xs}/C_{f,H}$ is generally larger when higher velocities occur in shallower depths, i.e., more high local $\overline{u}|\overline{u}|/H$. For a given volume flux through the channel, the nonuniform bathymetry and resulting spatially variable velocity field can be nonlinearly correlated and lead to increased momentum loss compared to a uniform channel, even in the absence of additional factors like secondary circulation and flow separation. This part of drag increase is defined as the drag increase due to the spatial variability in streamwise velocity and water depth and is quantified by $C_{f,xs}/C_{f,H}$.

$C_{f,xs}/C_{f,H}$ in this bend indicates a 10% drag increase during ebb tides and up to 15% increase during flood tides. $C_{f,xs}/C_{f,H}$ can be slightly greater during flood tides because the curvature effect redistributes streamwise velocity such that faster flow occurs over shallow shoals. For example, maximum velocity usually occurs near the inner bank upstream of the bend apex (seaward for flood tide), which also is the location of a shallow shoal. The maximum velocity is shifted toward the outer bend by flow separation downstream of the bend apex and encounters a shallow shoal leading into the next bend landward (Figure 4-1 **(b1)**) and Figure 4-4 **(a)**). In comparison, during ebb tides higher velocity usually follows the deeper part of the channel and flow is weaker over the shoals (Figure 4-3 **(a)**). Tidal velocities in the North River are ebb-dominant (Kranenburg et al., 2019), so ebb currents are expected to dominate the morphological development and the channel would be deeper where ebb currents are stronger.

Enhanced local bottom friction due to deviation from the log-profile

The cross-sectional-average bottom friction coefficient $C_{f,H}$ is generally $0.005 - 0.007$, greater than the log-profile prediction $C_{f,log}$ of $0.004 - 0.005$. The ratio of $C_{f,H}/C_{f,log}$ represents the local bed shear stress enhancement due to deviation from the log-profile. $C_{f,H}/C_{f,log}$ indicates a $30 - 40\%$ drag increase during ebb tides and around 50% increase during flood tides compared to the log-profile assumption. This local bottom stress enhancement can be a dominant source of drag increase during ebb tides when flow separation and form drag do not occur. The enhancement of bottom shear stress relative to the log-profile assumption (4.4) suggests an alteration to the vertical profile of velocity. Secondary circulation in the bend can redistribute momentum in the cross-sections through vertical and lateral advection, and thus enhance the bottom shear stress. Note that in some stratified cases $C_{f,H}$ may be decreased compared to $C_{f,log}$, because stratification can inhibit turbulence and reduce the bottom shear stress (e.g., Turner and Turner, 1979; Friedrichs and Wright, 1997; Stacey and Ralston, 2005).

It is also worthwhile to note that flow curvature results in two types of momentum redistribution in the bend. One is the redistribution of depth-averaged velocity in the horizontal plane, which is mainly related to the lateral squeezing of the main flow by flow separation. This generally increases the spatial variability of the depth-average flow field and the magnitude of the stress relative to the cross-sectionally averaged velocity, thus increasing the ratio $C_{f,xs}/C_{f,H}$ by $\sim 10\%$. The other type of momentum redistribution is the alteration of the velocity profile in the vertical, which is mainly due to the vertical and lateral advection by the secondary circulation. This can cause a deviation from the log-profile and thus affect the local bottom shear stress, and it is reflected in $C_{f,H}/C_{f,log}$ that represents a greater increase of $\sim 40\%$. This redistribution of streamwise flow in the vertical by the secondary circulation and its influence on the drag is investigated in the following section.

4.4.2 Momentum redistribution and local bottom friction enhancement

Ebb tide

During ebb tide when the classical helical flow occurs in the bend, the bottom shear stress distribution primarily depends on the depth-averaged streamwise velocity (Figure 4-3 **(a)** and (Figure 4-8 **(a)**), e.g., maximum bottom stresses occur near the inner bank upstream of the bend apex where maximum velocity occurs, and this shifts toward the outer bank downstream of the bend apex as higher momentum flow is transported outward. We calculated the expected bottom stress from the

depth-averaged velocity and the log-profile assumption using $\tau_{b,log} = \rho C_{f,log,local}\overline{u}|\overline{u}|$ (Figure 4-8 **(b)**). However, the actual bottom stress shows deviations from the log-profile assumption. The actual bottom stress is enhanced compared to the log-assumption, especially near the bend apex where secondary circulation is developed (Figure 4-8 **(c)**). This suggests that the secondary circulation alters the vertical profile of streamwise velocity and affects the bottom stress.

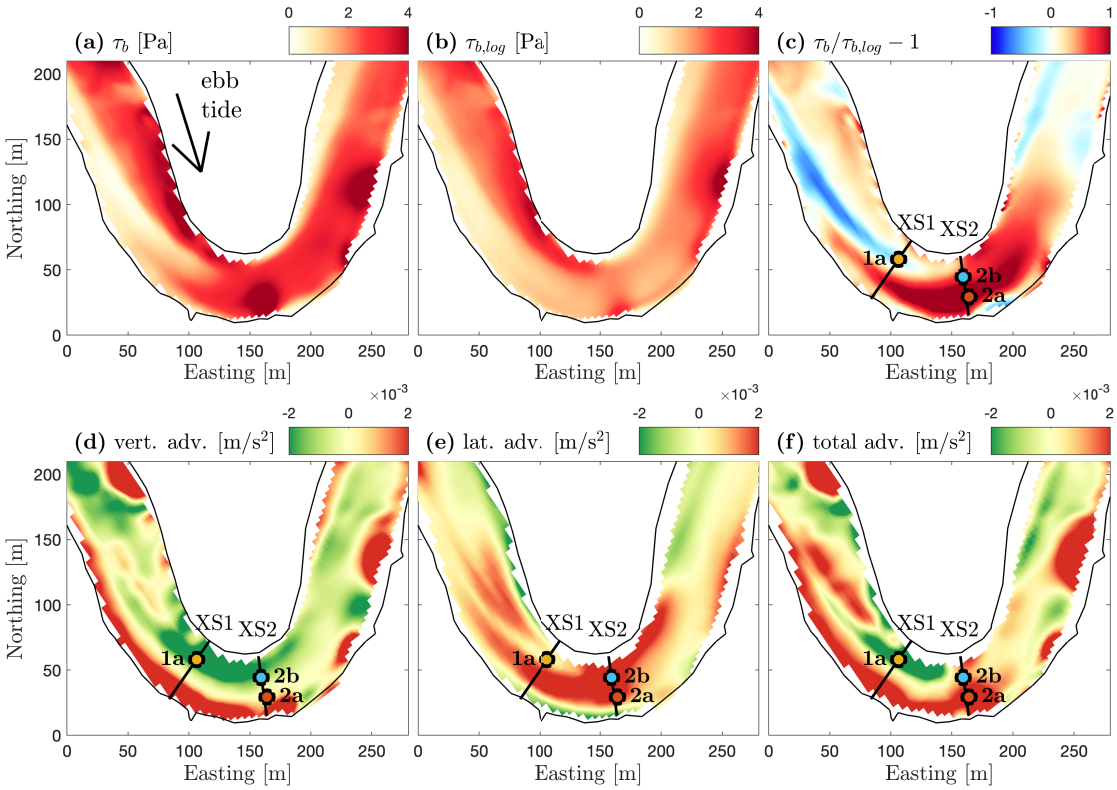

Figure 4-8: The ebb tide bottom stress and momentum redistribution terms in Bend-5.4. **(a)**: Bottom stress τ_b. **(b)**: Predicted bottom stress $\tau_{b,log}$ based on the log-profile assumption. **(c)**: Relative difference between τ_b and $\tau_{b,log}$. **(d)-(f)**: The vertical, lateral, and total advection terms of along-channel velocity in (4.18).

To investigate the momentum redistribution by secondary circulation, we examine the streamwise velocity transport equation in a cylindrical coordinate system (Batchelor and Batchelor, 2000; Blanckaert and Graf, 2004) .

$$\frac{\partial u}{\partial t} = \underbrace{-\frac{1}{1+r/R}u\frac{\partial u}{\partial s}}_{\text{along-channel advection}} \underbrace{-v\frac{\partial u}{\partial r} + \frac{1}{1+r/R}\frac{uv}{R}}_{\text{lateral advection}} \underbrace{-w\frac{\partial u}{\partial z}}_{\text{vertical advection}} -\frac{1}{1+r/R}\frac{1}{\rho}\frac{\partial p}{\partial s} + \frac{\partial}{\partial z}(\nu_t\frac{\partial u}{\partial z}). \tag{4.18}$$

s, r, and z represent the streamwise, lateral, and vertical coordinates, and u, v, and w are the cor-

responding velocity components. ν_t is the vertical eddy viscosity, and the horizontal viscosity is typically negligible in shallow flows. The first term on the right side represents streamwise advection; the second and third terms are the lateral advection; the fourth term is the vertical advection. The last two terms are the pressure gradient forcing (mainly due to water level gradient) and shear stress. The last two terms are dominant in the large-scale, depth-averaged momentum balance (4.6), but the other advection terms can be important at the local scales investigated here.

Near the outer bank where downwelling occurs (e.g., XS1 and XS2 in Figure 4-5 **(a)**,**(b)**), the vertical advection tends to increase the near-bed momentum (Figure 4-8 **(d)**). As a result, the vertical shear is more concentrated near the bed compared to a log-profile (e.g., loc 2a in Figure 4-9 **(b)**), and the bed shear stress is thus greater than that based on the log-profile assumption (Figure 4-8 **(c)**). By contrast, near the inner bank upstream of the bend apex, the upward velocity leads to decreased streamwise momentum and weaker vertical shear near the bed (e.g., loc 1a in Figure 4-8 **(c)**,**(d)**) and Figure 4-9 **(a)**), and thus, the bottom friction is less than the log-profile assumption.

Near the inner bank at the bend apex (e.g., loc 2b in Figure 4-8 **(c)**, **(d)**, **(e)** and Figure 4-9 **(c)**), the vertical velocity is upward and tends to decrease the momentum near the bed. At the same time, the lateral velocity advects the high momentum near the bed from the outer bank toward the inner bank (XS2 in Figure 4-5 **(b)**). The lateral advection that tends to increase the near-bed velocity dominates over the vertical advection that acts in the opposite way, and therefore the bottom stress is enhanced. The streamwise momentum becomes homogenized in the cross-sections at the bend apex and farther downstream (XS2 in Figure 4-5 **(b)**) as a result of the stirring (vertical and lateral advection) by secondary circulation and the bottom stress is thus enhanced across the channel (Figure 4-8 **(c)**).

Generally, the bottom stress deviation from the log-profile has a spatial pattern through the bend that is similar to the summed momentum advection terms (Figure 4-8 **(c)** and **(f)**). The along-channel advection of streamwise velocity (not shown) is smaller in magnitude than the lateral and vertical advection terms and corresponds less clearly with the bottom stress enhancement.

Regions with both increased and decreased bottom stress occur in the bend due to the momentum redistribution by secondary circulation, and the integrated effect influences the overall drag at the bend-scale. The bottom stress can be decreased by up to a factor of 2 compared to the classical log-profile where the streamwise momentum is decreased, and can be increased by more than a factor of 2 where the near-bed vertical shear is enhanced. The overall effect of momentum redistribution by secondary circulation is to enhance the bottom stress in the bend, because more locations

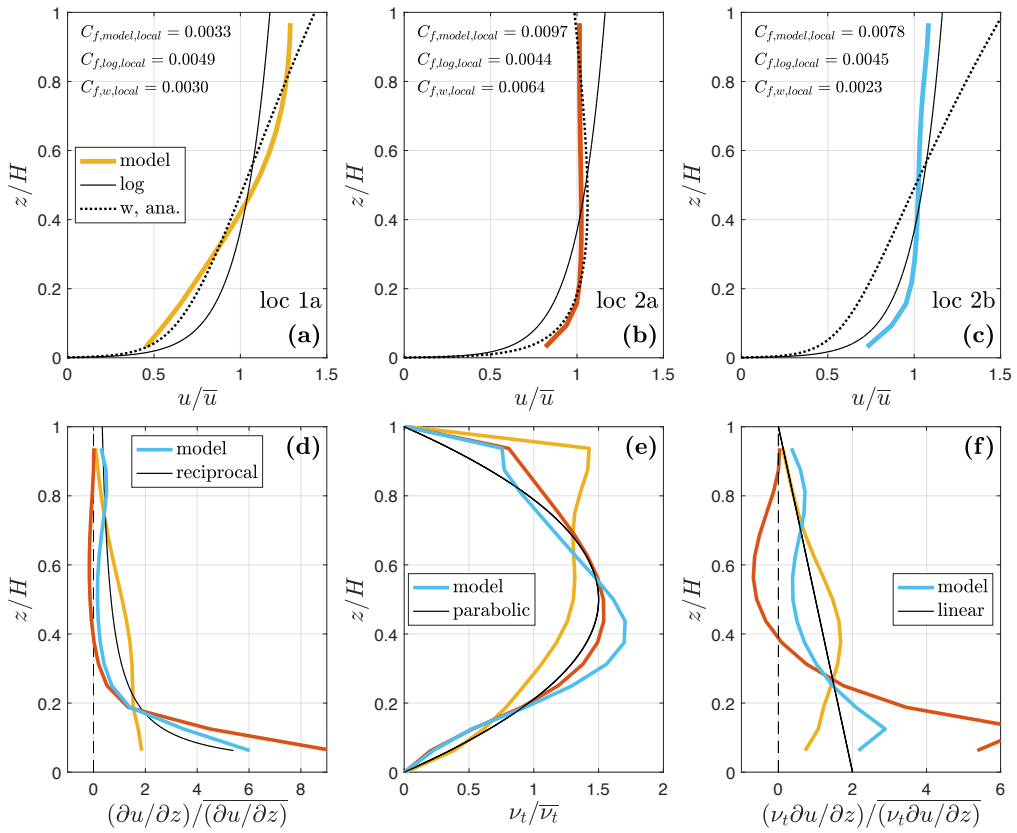

Figure 4-9: The vertical profiles of flow during ebb tide. **(a)-(c)**: Vertical profiles of streamwise velocity at three locations (marked in Figure 4-8). Velocity is non-dimensionalized by its depth-average. Colored lines are model results. The solid black lines show the log-profile, and the dotted black lines are the analytical solution with vertical advection using (4.23). $C_{f,model,local}$ is the local bottom friction coefficient from the model results; $C_{f,log,local}$ is from the log-assumption; $C_{f,w,local}$ is from the analytical solution with vertical advection. **(d)**: Vertical shear. The solid black line shows a reciprocal distribution as for the log profile. **(e)**: Eddy viscosity. The solid black line shows a parabolic distribution. **(f)**: Shear stress. The solid black line shows a linear distribution.

have increased near-bed velocity than decreased near-bed velocity and the stress has a quadratic dependence on velocity. This explains the greater calculated depth-average bottom friction coefficient $C_{f,H}$ compared to the typical log-profile prediction $C_{f,log}$ in section 4.4.1.

A 1-d analytical model

The vertical advection of momentum initiates the transport of high momentum to the lower water column, and lateral advection spreads higher momentum flow near the bed across the channel. In this subsection, we develop a simplified 1-d analytical model to deconstruct the complex patterns in the 3-d model and conceptually frame the linkage between vertical advection and bottom shear

stress enhancement.

When a steady and horizontally uniform boundary layer flow is established (without secondary flows), the streamwise momentum equation can be simplified as

$$\frac{1}{\rho}\frac{\partial p}{\partial s} = \frac{1}{\rho}\frac{\partial \tau}{\partial z} = \frac{\partial}{\partial z}(\nu_t \frac{\partial u}{\partial z}). \tag{4.19}$$

(4.19) is essentially a local depth-dependent form of (4.6) when the large-scale form drag is not considered. $\frac{1}{\rho}\frac{\partial p}{\partial s}$ is vertically uniform by neglecting baroclinicity, and thus τ typically has a linear distribution in the vertical $\tau = \tau_b(1 - z/H)$. Substituting in the definition of u_* in (4.3), we can write

$$u_*^2(1 - \frac{z}{H}) = \nu_t \frac{\partial u}{\partial z}. \tag{4.20}$$

The eddy viscosity ν_t typically has a parabolic distribution in the vertical direction $\nu_t = \kappa u_* z(1 - z/H)$, and (4.20) thus becomes

$$u_* = \kappa z \frac{\partial u}{\partial z}. \tag{4.21}$$

The solution to (4.21) is the canonical logarithmic velocity relationship (4.2).

We add the vertical advection term to (4.20) to investigate the momentum redistribution by vertical velocity w, so

$$u_*^2(1 - \frac{z}{H}) = \nu_t \frac{\partial u}{\partial z} - wu. \tag{4.22}$$

On the bottom boundary w vanishes and (4.22) reduces to (4.20). Assuming a parabolic distribution for the vertical velocity $w = w_0(z/H)(1 - z/H)$, we can write

$$u_*^2 = \kappa u_* z \frac{\partial u}{\partial z} - w_0 u \frac{z}{H}. \tag{4.23}$$

For given z_0 and w_0, this (4.23) can be solved numerically to get an analytical solution to the vertical profile of u and the modification to C_f by the vertical velocity. For example, the vertical velocity is typically ~ 1 cm/s in the bend for ~ 1-m/s streamwise tidal current, and in the analytical solution, C_f is increased by 31% for a downwelling case with $w_0/\overline{u} = -0.01$ and decreased by 33% for an upwelling case with $w_0/\overline{u} = -0.01$, given $H = 5$ m and $z_0 = 0.005$ m.

Solutions to (4.23) are compared with model results in Figure 4-9. w_0 is taken from the model results as the local normal-to-bed velocity, which squeezes or stretches the velocity profile perpendicularly relative to the boundary. Note that the normal-to-bed velocity is different from the vertical

velocity in the model output because the channel bed is not flat. The analytical solutions to (4.23) are consistent with the velocity profiles at loc 1a and 2a, where vertical advection is dominant in the momentum transport (Figure 4-8 **(d)**). For these locations, the bottom friction coefficient $C_{f,w,local}$ from the analytical solution with vertical advection is consistent with the bottom stress decrease or increase, although the values of $C_{f,w,local}$ and $C_{f,model,local}$ don't match exactly. At loc 2b where lateral advection dominates over vertical advection, the 1-d analytical solution fails because it does not account for the redistribution by the lateral velocity.

Generally, the analytical solution with vertical advection explains the altered bottom stress where vertical advection is dominant but it fails where lateral becomes more important. The analytical solution suggests that basic assumptions behind the log-profile are not violated, e.g., the eddy viscosity ν_t is generally consistent with a parabolic distribution (Figure 4-9 **(e)**), but deviations of local bottom stress occur because the log-profile theory ignores the locally strong influence of vertical advection. The vertical shear $\partial u/\partial z$ is more concentrated in the lower water column where secondary circulation brings higher momentum flow toward the bed. As a result, the shear stress $\nu_t \partial u/\partial z$ is enhanced near the bed (Figure 4-9 **(f)**), and this contributes to the overall increase in drag with curvature.

Flood tide

During the flood tide the secondary circulation is more complex than the typical single secondary circulation cell for ebbs, but the mechanisms of momentum redistribution and bottom stress enhancement are similar. During flood tide, a surface convergence zone with strong downwelling occurs near the inner bank (Figure 4-5 **(c)**, **(d)**). As a result, high momentum flow is vertically injected to the lower water column and spreads laterally near the bed to enhance the bottom shear stress in the downwelling region and nearby (Figure 4-10 **(c)**).

Vertical advection is the dominant term for redistributing momentum in the downwelling region (e.g., loc 3a in Figure 4-10 **(d)** and Figure 4-11 **(a)**), and the analytical solution with vertical advection (4.23) yields velocity profiles that are consistent with the 3-d model. Lateral advection is dominant adjacent to the downwelling region (e.g., loc 3b in Figure 4-10 **(e)** and Figure 4-11 **(b)**), and thus the 1-d analytical solution does not explain the velocity profile. The advection by the secondary circulation concentrates the shear near the bed (Figure 4-11 **(c)**) and leads to locally enhanced bottom friction. In addition, a region of negative shear stress is found near the surface (Figure 4-11 **(e)**), because the maximum streamwise velocity occurs in the lower water column with

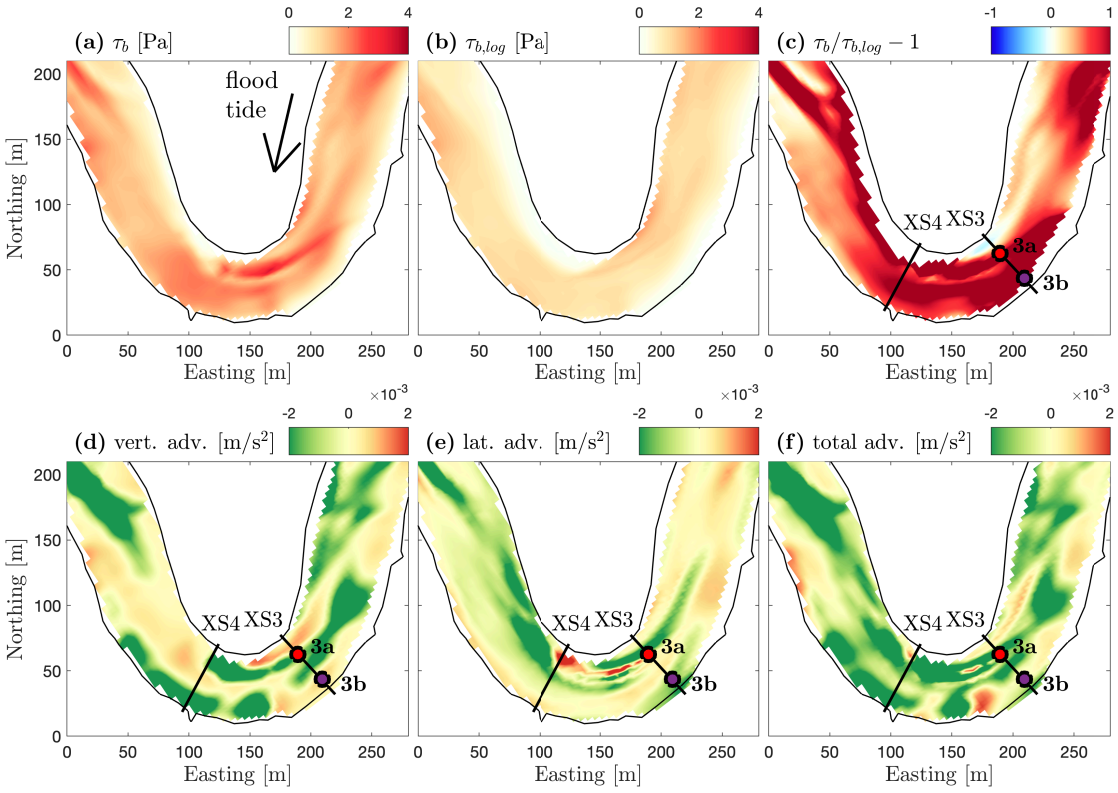

Figure 4-10: The flood tide bottom stress and momentum redistribution terms in Bend-5.4. Panels as in Figure 4-8. **(a)**: Bottom stress τ_b. **(b)**: Predicted bottom stress $\tau_{b,log}$ based on the log-profile assumption. **(c)**: Relative difference between τ_b and $\tau_{b,log}$. **(d)-(f)**: The vertical, lateral, and total advection terms of along-channel velocity in (4.18).

reversed vertical shear in the upper water column. This reversal in shear is consistent with the flood tide BCPG-driven secondary circulation noted in other studies (e.g., Lacy and Monismith, 2001; Lacy et al., 2003; Lerczak and Geyer, 2004).

4.4.3 Dependence on bend sharpness

While the analysis thus far has focused on a single sharp bend (Bend-5.4), secondary circulation, flow separation, and momentum redistribution also occur in other bends of the North River estuary with different sharpness. As an example, below we highlight two other bends: Bend-4.2 has intermediate curvature with a radius of curvature $R = 140$ m, width $W = 70$ m, and curvature ratio $R/W \approx 2$, and Bend-6.7 is one of the smoothest bends in the North River with $R = 200$ m, $W = 50$ m, and $R/W \approx 4$.

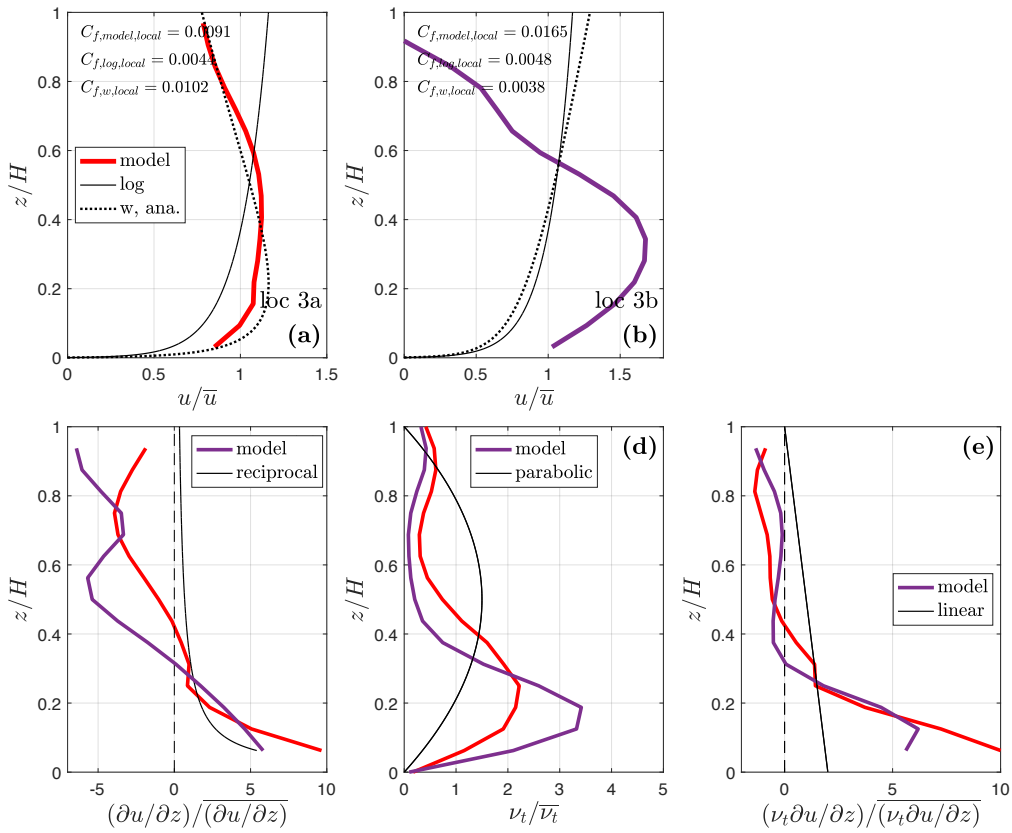

Figure 4-11: The vertical structures of flow during flood tide, at two locations marked in Figure 4-10. Panels and lines similar to Figure 4-9. **(a)**-**(b)**: Vertical profiles of streamwise velocity. **(c)**: Vertical shear. **(d)**: Eddy viscosity. **(e)**: Shear stress.

Ebb tide

During ebb tide, a single secondary circulation cell occurs in Bend-4.2 (Figure 4-12 **(a)**-**(d)**), similar to the sharper Bend-5.4. Upwelling near the inner bank tends to decrease velocity in the lower water column and decrease the bed shear stress, while downwelling near the outer bank transports higher momentum flow to the low water column and increases the bed stress. Downstream of the bend apex, the higher momentum flow is advected inward by the lateral flow near the bed, leading to enhanced bottom stress across the entire cross-section.

Similar helical flow is also found in the smoother Bend-6.7, leading to a region with decreased bottom stress from the inner bank of the upstream bend to the inner bank of Bend-6.7, and then shifted to the inner bank of the following bend, where upwelling decreases the near-bed velocity (Figure 4-12 **(f)**). Increased bottom stress is found in other regions where the near-bed momentum can be increased by secondary circulation. Although secondary circulation still affects the bottom

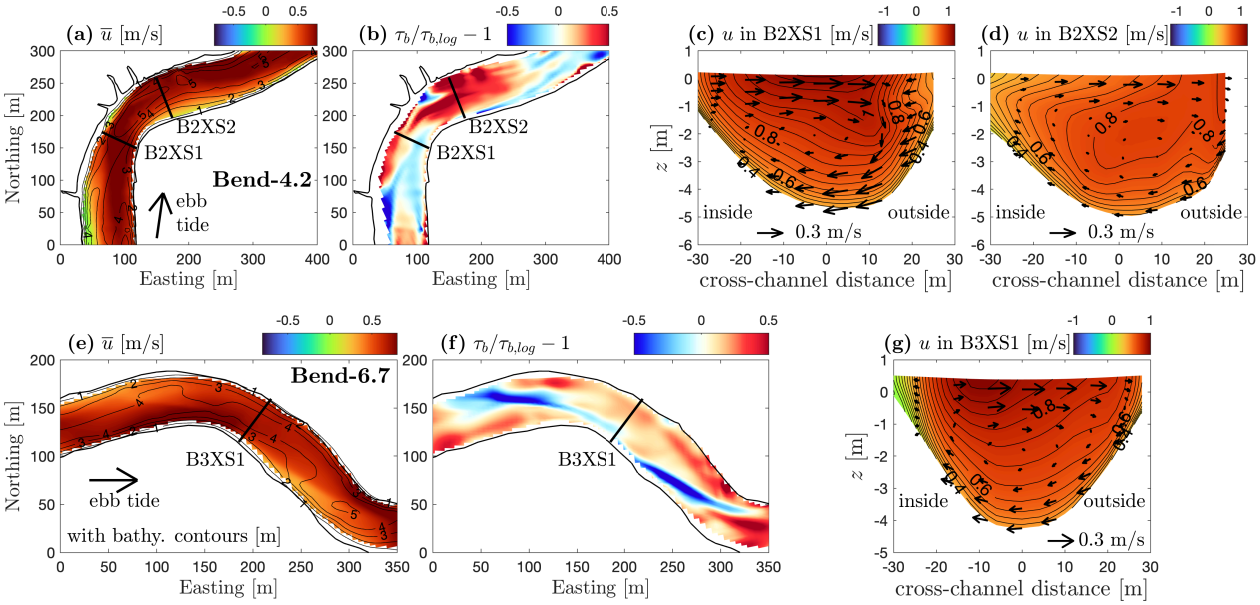

Figure 4-12: Ebb tide flow field in Bend-4.2 (panels **(a)**-**(d)**) and Bend-6.7 (panels **(e)**-**(g)**). **(a)** and **(e)**: Depth-averaged along-channel velocity $\overline{u}$, with contours of bathymetry. **(b)** and **(f)**: Relative bottom stress alteration compared to the log-profile assumption. **(c)**, **(d)**, and **(g)**: Along-channel velocity u in the cross-secitons marked in the map views.

stress in this smoothest Bend-6.7, the momentum distribution in a cross-section downstream of the bend apex is more vertically sheared and less homogenized by the secondary circulation than in the sharp Bend-5.4 (Figure 4-12 **(g)** compared to Figure 4-5 **(b)**). As a result, the overall bottom friction enhancement ($C_{f,H}/C_{f,log} - 1$) in Bend-6.7 is only around 20%. The above comparison suggests that secondary circulation is more effective at redistributing momentum and increasing bottom stress in sharp bends than in smooth bends, consistent with theories that the strength of secondary circulation increases with stronger curvature (Kalkwijk and Booij, 1986; Geyer, 1993b; Blanckaert and De Vriend, 2010; Ottevanger et al., 2012).

Flood tide

During flood tide, more complex secondary circulation patterns are found in both Bend-4.2 and Bend-6.7, as in the sharper Bend-5.4. Surface convergence zones with downwelling occur near the inner bank upstream of the bend apexes (Figure 4-13 **(c)**, **(g)**). Higher momentum flow is injected to near the bed by the downward velocity and reversed vertical shear occurs near the surface. The bottom shear stress near the convergence is increased compared to the log-profile and the overall bottom friction enhancement ($C_{f,H}/C_{f,log} - 1$) is up to 50% in both Bend-4.2 and Bend-6.7.

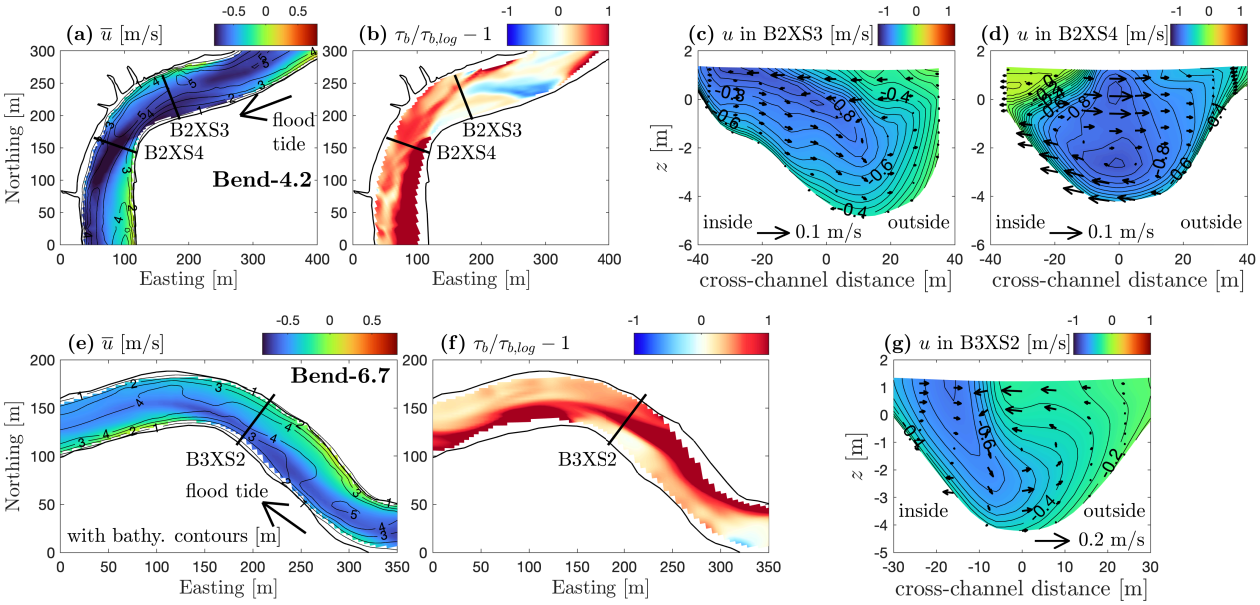

Figure 4-13: Flood tide flow field in Bend-4.2 (panels **(a)**-**(d)**) and Bend-6.7 (panels **(e)**-**(g)**). Panels as in Figure 4-12. **(a)** and **(e)**: Depth-averaged along-channel velocity $\overline{u}$, with contours of bathymetry. **(b)** and **(f)**: Relative bottom stress alteration compared to the log-profile assumption. **(c)**, **(d)**, and **(g)**: Along-channel velocity u in the cross-secitons marked in the map views.

Flow separation is found on the lee side of Bend-4.2, with a low velocity zone located near the inner bank and the main flow shifted toward the outer bank. Form drag due to the flow separation is up to 50% of the total bottom friction in Bend-4.2 (i.e., $C_{d,xs}/C_{f,xs}$ up to 1.5). Flow separation is less notable in the smoother Bend-6.7, which agrees with the theoretical prediction in Bo and Ralston (2020) that flow separation is less likely to occur in smooth bends. The ratio of $C_{d,xs}/C_{f,xs}$ is close to 1 in Bend-6.7, suggesting that the contribution from form drag is small (less than $\sim 10\%$) compared to bottom friction.

4.5 Discussion

4.5.1 The mechanisms of drag increase in meanders

We find that the momentum loss is increased in meanders compared with similar straight channels as a result of form drag due to flow separation, increased overall bottom stress due to the spatially variable flow field, and local enhancement of bottom stress due to momentum redistribution by the secondary circulation (Figure 4-14). Flow separation creates form drag by generating a low pressure circulation zone on the lee side of the bend and results in a drag coefficient increase of nearly a factor

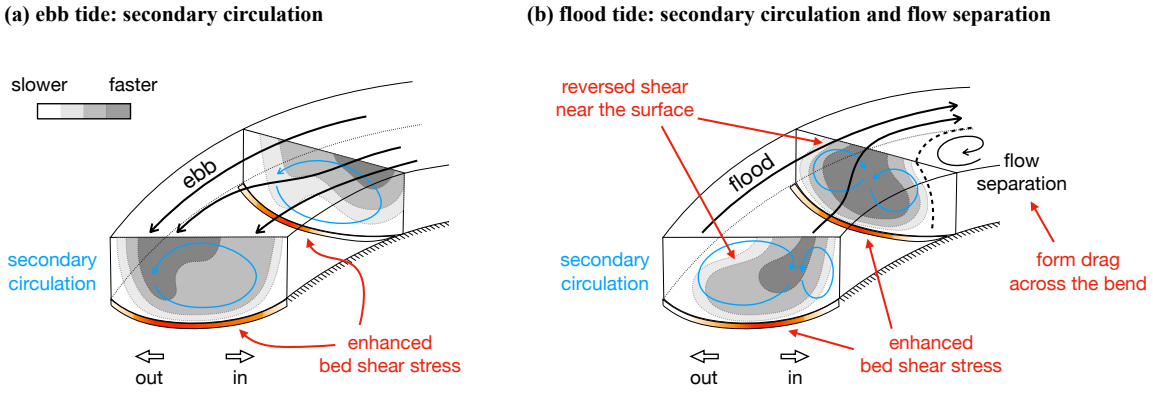

Figure 4-14: Schematic plots of flow field, momentum redistribution, and drag increase in bends. **(a)**: Ebb tide. Black arrows show the channel flow in the horizontal plane, and blue arrows show secondary circulation in cross-sections. The gray colors represent streamwise momentum. Red colors show regions with enhanced bottom shear stress compared to the log-profile assumption. High momentum is advected to near the bed, which increases the bottom friction. **(b)**: Flood tide. Lines and colors as in panel **(a)**. In addition to secondary circulation, flow separation creates a recirulating zone and leads to form drag across the bend.

of 2 in a sharp bend compared to the total bottom friction. Form drag is the dominant source of drag increase during flood tides when flow separation is most notable, and is less important during ebb tides. The spatial variability of bathymetry and velocity and their nonlinear correlation also cause an overall increase in frictional drag for a given volume flux through the channel, although that only accounts for an increase of around 10% in the friction coefficient. Secondary circulation due to curvature advects higher momentum flow from the surface toward the lower water column in downwelling regions near the inner bank (flood tide) or outer bank (ebb tide), and the near-bottom secondary circulation spreads the high momentum laterally. As a result, the bottom shear stress is enhanced, which leads to drag increases of $30 - 60\%$ compared to the bottom stress based on assuming a classical log-profile.

Note that the enhanced bottom stress investigated in this chapter does not contradict the conclusions of Chapter 3, where form drag was suggested to be the dominant source of drag in estuarine meanders. Flow separation is generally stronger in sharp bends and weaker in smoother bends (Blanckaert, 2010; Bo and Ralston, 2020), so form drag may be less important in the realistic meanders studied here that are typically smoother than the idealized bends investigated in Chapter 3. With form drag being less significant in these North River bends, the momentum redistribution and bottom stress enhancement can play a relatively more dominant role. In addition, the calculated bottom friction coefficient from the integrated momentum budget was close to the typical value 0.003

in those idealized bends (e.g., equation 3.4 and Figure 3-6), instead of exhibiting the bottom stress enhancement. This is because the integrated momentum budget was calculated in x-direction in the idealized models for the convenience of form drag calculation, and the bottom friction coefficient thus only corresponds to the x-component of bottom shear stress. An increased bottom friction coefficient would still be expected in those idealized bends if the calculation was based on the bottom stress in the along-channel direction.

The role of the curvature-induced secondary circulation in redistributing momentum and altering the bottom stress is not unique to this system. Similar mechanisms apply to other tidal meanders (Seim et al., 2002) and river meanders (Dietrich and Whiting, 1989; Frothingham and Rhoads, 2003). Moreover, secondary circulation can also affect the bottom boundary layer in systems without curvature, e.g., in straight estuarine channels with BCPG-driven secondary circulation (Nunes and Simpson, 1985; Lerczak and Geyer, 2004) and in large estuaries where Coriolis can dominate the secondary circulation (Valle-Levinson, 2011).

The lateral component of the near-bottom velocity due to the secondary circulation can also increase the drag on the streamwise flow by creating an additional bed shear stress component (Chang, 1984; Blanckaert and de Vriend, 2003). However, the nonlinear advection of streamwise momentum and enhancement of streamwise bottom stress have greater contributions to the drag enhancement in this system. The lateral component of bottom stress accounts for less than 10% of the total bottom stress in the model results, because shear stress scales with velocity squared and the streamwise velocities are much greater in magnitude than the lateral velocities.

We primarily analyzed flow conditions with weak stratification, and further investigation is needed to quantify how these processes affect drag in the presence of stronger vertical or horizontal salinity gradients. Strong stratification can suppress turbulence, inhibit the vertical transport of momentum, and decrease the bottom stress (e.g., Turner and Turner, 1979; Stacey and Ralston, 2005; Qian et al., 2022). Moreover, strong horizontal salinity gradients can affect the momentum budget through baroclinicity and alter the secondary circulation pattern. The multiple secondary circulation cells during flood tides result from baroclinic effects (Kranenburg et al., 2019). During ebb tides, the region of interest is mostly well mixed or fresh as the salt front is advected downestuary. As a result, baroclinicity is generally weak during ebbs and the classical helical flow occurs in the analyzed bends. In meanders where strong vertical or horizontal salinity gradients appear during ebb tides, reversed secondary circulation (Chant and Wilson, 1997; Bo and Ralston, 2022) or multiple layers of secondary circulation (Nidzieko et al., 2009) may occur as a result of the interac-

tion between stratification, baroclinicity, and secondary flows. Reversed secondary circulation can influence the momentum redistribution and alter the bottom stress enhancement compared to the classical helical flow. With multiple layers of secondary circulation, the vertical advection of momentum may be inhibited compared to the classical helical flow, potentially leading to less bottom stress enhancement.

While we have focused on the momentum budget in the above analysis, the increased momentum loss due to the channel curvature also corresponds with increased energy dissipation (Seim and Gregg, 1997; Seim et al., 2006; Warner et al., 2013; Bo and Ralston, 2020; Bo et al., 2021). The enhanced bottom stress associated with secondary circulation and altered velocity profiles in the vertical directly corresponds with an increased energy loss rate near the bed. Flow separation that creates form drag in the momentum budget can also contribute to the increased energy dissipation. The separation zone laterally squeezes and accelerates the main flow, which increases the spatial variability of depth-averaged velocity and increases both the overall bottom stress and the near-bed dissipation (Bo and Ralston, 2020). The horizontally variable flow field can be a more important contributor to energy dissipation compared to momentum loss because of the higher-order dependence on velocity of energy than momentum. In addition to the increased energy loss near the bed, interior dissipation can occur in the bend associated with the reversed vertical shear found in the upper water column during flood tides (Figure 4-5 **(c)**, **(d)** and Figure 4-11). This interior dissipation is not associated with the bottom boundary layer and bed friction, and could contribute to energy loss with the form drag.

4.5.2 Which C_d or C_f to choose to quantify the drag?

Our analysis shows that the drag coefficient C_d and bottom friction coefficient C_f vary depending on the choice of $\overline{u}|\overline{u}|/H$ (depth-averaged velocity squared over depth) used to scale the drag term in the depth-averaged momentum equation, especially in systems with complex bathymetry and flow distribution. For assessing the overall momentum loss in open-channel flows, the cross-sectional-average drag coefficient $C_{d,xs}$ in (4.12) should be used because that integrates any form drag from topographic features. $C_{d,xs}$ is defined based on the along-channel average of each cross-sectional average velocity and depth $\{(\langle\overline{u}\rangle|\langle\overline{u}\rangle|)/\langle H\rangle\}$, and can be rewritten as $Q|Q|\{1/\langle H\rangle^3 W^2\}$ assuming the flux $Q = \langle\overline{u}\rangle\langle H\rangle W$ is conserved along the channel. Therefore, in field observations, Q can be estimated based on the velocity and depth measurements in a single cross-section, and then $\{1/\langle H\rangle^3 W^2\}$ can be evaluated using an estimate of the along-channel variability of channel depth

and width. Similarly, the cross-sectional-average bottom friction coefficient $C_{f,xs}$ in (4.15) should be used to quantify the overall bottom shear stress experienced by a given amount of flux through the channel.

An alternative to quantify the bottom stress is to use the depth-average bottom friction coefficient $C_{f,H}$ in (4.17). In meanders, the curvature-induced flow processes can add to the spatial variability of depth-averaged velocity. In addition, complex bathymetric features are usually found in natural channels can also affect the depth-averaged velocity distribution through topographic steering (Dietrich and Smith, 1983; Blanckaert, 2010; Ottevanger et al., 2012). Consequently, the difference between $C_{f,H}$ and $C_{f,xs}$ may be significant. The calculation or measurement of $C_{f,H}$ can remove the drag increase due to the spatial variations in depth and depth-averaged velocity that are included in $C_{f,xs}$, and thus only quantify the bottom stress associated with the vertical structure of the local flow. $C_{f,H}$ is difficult to rigorously estimate in the field because it requires measuring velocity and depth with complete spatial coverage. Note that calculating $C_{f,H}$ based on the depth and depth-averaged velocity at a single location may introduce significant biases. $C_{f,H}$ has to be assessed using multi-location measurements of depth and velocity that are representative of the domain. In order to obtain an estimate of the spatial variability of bottom stress and calculate an appropriate $C_{f,H}$, either of the following approaches may be adopted: 1. deploying moorings not only in the deep channel but also in shallow regions where large values of $\overline{u}|\overline{u}|/H$ could appear; 2. combining mooring measurements with cross-sectional surveys of the distribution of $\overline{u}|\overline{u}|/H$ under a range of tidal/flow conditions.

4.5.3 Implications for morphodynamics

The increases in drag resulting from channel curvature, particularly the mechanisms associated with bottom friction, have implications for sediment erosion and deposition and for channel meander morphodynamics. The North River estuary is ebb-dominant (Kranenburg et al., 2019), so here we discuss the linkage between the ebb tide bottom stress and channel morphology in the sharp Bend-5.4. Secondary circulation tends to increase the near-bed velocity through the downward advection near the outer bank, and high momentum spreads laterally near the bed at the bend apex. The enhanced bottom stress would enhance erosion and inhibit sediment deposition in the cross-section at the bend apex (Figure 4-8), which can explain the observed deep scour hole and the absence of a point bar at the bend apex. By contrast, regions with decreased bottom stress due to secondary circulation upwelling extend from the inner bank of the next landward bend to the inner bank of

Bend-5.4, and then to the inner bank of the next seaward bend. These regions with decreased bottom stress favor sediment deposition, and could contribute to the growth of the shallow shoals extending along-channel from the inner banks of bends.

Flow separation mainly occurs during flood tide, so its influence on channel morphology may be more limited in this ebb-dominant river. Flow separation creates a low-velocity recirculation zone that could favor sediment deposition near the inner bank on the lee side of bends (Finotello et al., 2020). Additionally, the main flow is restricted to a narrower extent of the channel cross-section and thus accelerated, which may enhance sediment erosion in the center of the channel (Vermeulen et al., 2015).

4.6 Conclusion

We calculated the drag and friction coefficients in a sinuous estuary, and found that the momentum loss is much greater than expected for straight channels. The influence of curvature-induced processes on the momentum budget was investigated, and both flow separation and secondary circulation contribute to the drag increase in meanders. Flow separation can create form drag across a bend and is most notable during flood tides. Secondary circulation can increase the near-bed velocity through vertical and lateral advection during both ebb and flood tides, leading to increased bottom stress compared to the log-profile assumption. The altered momentum distribution and enhanced bottom stress may affect sediment transport in the bend and contribute to the observed morphology.

Chapter 5

Frontogenesis, mixing, and stratification in estuarine channels with curvature

Idealized numerical simulations were conducted to investigate the influence of channel curvature on estuarine stratification and mixing. Stratification is decreased and tidal energy dissipation is increased in sinuous estuaries compared to straight channel estuaries. We applied a vertical salinity variance budget to quantify the influence of straining and mixing on stratification. Secondary circulation due to the channel curvature is found to affect stratification in sinuous channels through both lateral straining and enhanced vertical mixing. Alternating negative and positive lateral straining occur in meanders upstream and downstream of the bend apex respectively, corresponding to the normal and reversed secondary circulation with curvature. The vertical mixing is locally enhanced in curved channels with the maximum mixing located upstream of the bend apex. Bend-scale bottom salinity fronts are generated near the inner bank upstream of the bend apex as a result of interaction between the secondary flow and stratification. Shear mixing at bottom fronts, instead of overturning mixing by the secondary circulation, provides the dominant mechanism for destruction of stratification. Channel curvature can also lead to increased drag, and using a Simpson number with this increased drag coefficient can relate the decrease in stratification with curvature to the broader estuarine parameter space.

The material in this chapter has been published as Bo and Ralston (2022) in *Journal of Physical Oceanography* ©American Meteorological Society, and is included with permission.

5.1 Introduction

Stratification is a key characteristic of estuaries. Stratification affects the along-estuary transport of salinity and other scalars, and it provides a control on the intensity of vertical mixing and thus influences the vertical distribution of momentum, sediment, chemicals, and biota (Simpson et al., 1990; Geyer and Ralston, 2011). Salinity stratification appears in estuaries due to the buoyancy input of freshwater as the influence of gravity tilts horizontal salinity gradients into the vertical direction (e.g., Geyer and Ralston, 2011). While estuarine stratification typically depends on the strength of freshwater input and tidal forcing, geomorphic features also affect vertical mixing and stratification, e.g., shallow shoals (Ralston and Stacey, 2005b; Geyer et al., 2020), sills (Farmer and Smith, 1980; Seim and Gregg, 1997), constrictions (Armi and Farmer, 1986; Geyer et al., 2017), and channel curvature (Seim and Gregg, 1997; Becherer et al., 2015).

Many estuaries have sinuous channels (e.g., Marani et al., 2002; Fagherazzi et al., 2004), and the channel curvature can lead to distinct hydrodynamic processes including the development of secondary circulation (e.g., Thomson, 1877; Rozovskii, 1957) and flow separation (e.g., Leopold, 1960; Leeder and Bridges, 1975). In curved open-channel flows, secondary circulation arises in a lateral plane perpendicular to the main flow as a result of the local imbalance between the centrifugal acceleration and barotropic pressure gradient (e.g., Thomson, 1877). Curvature-induced secondary circulation has been observed in rivers (e.g. Apmann, 1964) and estuaries (e.g. Seim and Gregg, 1997; Chant and Wilson, 1997), typically with flow toward the outer bank near the surface and toward the inner bank in the lower layer. However, in estuaries salinity stratification can alter the effect of curvature on the flow. Stratification can enhance the shear of the streamwise flow and thereby strengthen the secondary circulation (Geyer, 1993b). Alternatively, lateral baroclinic pressure gradients can reverse the sense of lateral circulation or lead to multiple circulation cells and more complex structure than in homogeneous density flow (Chant and Wilson, 1997; Lacy and Monismith, 2001; Nidzieko et al., 2009; Scully et al., 2009; Kranenburg et al., 2019). In addition to secondary circulation, flow separation can affect the velocity distribution in sinuous channels, with streamlines of the main flow detaching from the inner bank and recirculating eddies in the lee of bends (e.g., Leopold, 1960; Leeder and Bridges, 1975).

In sinuous estuarine channels, the curvature-induced secondary circulation can reduce stratification by enhancing vertical mixing. Secondary circulation was found to reduce stratification in a curved channel in Puget Sound by laterally overturning the water column and generating intense

mixing (Seim and Gregg, 1997). In that study, a bend Froude number was introduced to compare the overturning and mixing due to curvature with the stratification that suppresses overturning. In Elkhorn Slough, a shallow, sinuous salt marsh estuary, the bend Froude number was found to be below the criterion for overturning to occur, and instead, shear-generated turbulence was dominant in mixing (Nidzieko et al., 2009). Meanders were also found to enhance turbulent mixing in an idealized modeling study of the Ems estuary, although the detailed mechanism was not reported (Pein et al., 2018).

Frontogenesis is an important process that affects stratification and mixing in estuaries. Estuarine fronts can increase the streamwise baroclinic pressure gradient, locally enhancing shear of the streamwise flow and leading to intense mixing (Simpson and Linden, 1989; Geyer and Ralston, 2015; Warner et al., 2020). Typical examples of estuarine salinity fronts include, e.g., tidal intrusion fronts (Simpson and Nunes, 1981), river plume fronts (Garvine, 1974), and bottom fronts associated with constrictions (Geyer and Ralston, 2015). Salinity fronts result from interactions between the three dimensional flow and salinity gradients (Geyer and Ralston, 2015). Channel curvature can generate strong lateral velocities as well as lateral variations in salinity and streamwise momentum, and the interactions between the velocity and salinity distributions with flow curvature may provide rich additional means for frontogenesis.

In addition to frontogenesis, interactions between lateral velocities and lateral salinity gradients with flow curvature can affect stratification through the process of lateral straining. In straight channels, differential along-channel advection due to lateral bathymetric variations can create lateral salinity gradients, leading to lateral baroclinic circulation, positive lateral straining, and creation of stratification (e.g., Nunes and Simpson, 1985; Lacy et al., 2003; Ralston and Stacey, 2005a). However, in sinuous channels, the lateral circulation is not necessarily driven by the lateral salinity gradient since the lateral momentum balance depends on the centrifugal forcing due to channel curvature. As a result, lateral straining with curvature can be either positive or negative, either creating or destroying stratification. In a curved tidal channel in the Wadden Sea, the centrifugal forcing was found to be comparable to the baroclinic forcing in generating lateral circulation and lateral straining, but the tidal asymmetry in the sign of the curvature influence resulted in net positive lateral straining (Becherer et al., 2015). Flow separation at bends can also affect lateral straining by enhancing differential advection and generating secondary circulation that has positive lateral straining (Bo and Ralston, 2020).

In this study, we build idealized models to investigate the influence of channel curvature on

stratification. Straight and sinuous channel estuaries are compared, with geometric parameters and forcing conditions scaled off a shallow, sinuous estuarine channel with previous observations (Krakenburg et al., 2019; Bo et al., 2021). In section 5.2, we introduce the numerical models. In section 5.3, we show the hydrodynamic and stratification conditions in straight and sinuous channels, including the vertical salinity variance budget that is used to quantify the influences of straining and mixing on stratification. In section 5.4, we analyze the generation of curvature-induced bottom fronts and its role in enhancing mixing in meanders. We also introduce in an adjusted Simpson number scaling that accounts for the increased drag with channel curvature and parameterizes the decrease in stratification. Section 5.5 has discussion on the influence of curvature-induced bottom fronts and other mechanisms affecting stratification and mixing in sinuous channels. Section 5.6 presents conclusions.

5.2 Methods

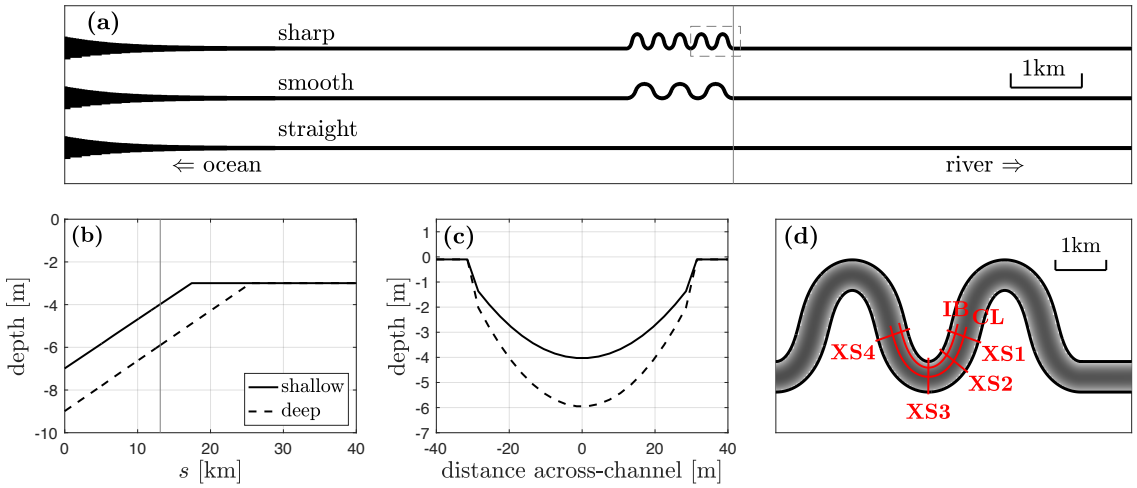

Figure 5-1: **(a)**: The sharp-bend, smooth-bend, and straight channel estuary models. The ocean is on the left side. **(b)** The channel thalweg depth as a function of the along-channel distance s. The solid line shows the shallow channel model and dashed line shows the deep channel model. **(c)** Cross-sectional bathymetry at $s = 13$ km, corresponding to the cross section denoted by the thin gray lines in panels **(a)** and **(b)**. **(d)** The up-estuary part of the meander region of the sharp-bend model, as is denoted by the dashed rectangle in panel **(a)**. Red lines show the cross-sections (XS1-4) and along-channel sections (CL and IB) analyzed in the following sections.

Model simulations were conducted using the Regional Ocean Modeling System (ROMS) (Shchepetkin and McWilliams, 2005; Haidvogel et al., 2008; Warner et al., 2008, 2010), a 3D hydrostatic model based on the Reynolds-averaged Navier–Stokes (RANS) equations. Twelve estuary models

were built that have different channel shapes, channel depths, tides, and river discharges (Table 5.1) to investigate the influence of channel curvature, channel depth, and forcing conditions on stratification. The sinuous channel shape is inspired by the North River estuary (MA, USA) (Kranenburg et al., 2019; Bo et al., 2021), a sinuous tidal channel with variable stratification in previous observations. Channel dimensions, tidal conditions, and river discharges are also scaled off conditions in the North River estuary. The channel has a 40-km total length, and it exponentially converges landwards (e.g. Langbein, 1963) from the mouth to around 6 km into the estuary, and farther landward the channel width is uniform ($W = 60$ m). The model analysis focuses on the mid-estuary region at around 12-14 km, which is in the middle of the salinity gradient and away from the river and ocean boundary conditions. Models with three different channel plan-forms were compared (Figure 5-1 **(a)**): a straight channel, a sinuous channel with 5 smooth bends, and a sinuous channel with 9 sharp bends, which have the same cross-channel geometry and tidal and discharge conditions. The sinuous channel shape is created following the form of sine-generated functions (Langbein and Leopold, 1970). The bend sharpness is quantified by the curvature ratio R/W (bend radius of curvature to width ratio), and R/W is 0.8 for the sharp-bend channel and 2.0 for the smooth-bend channel. The bend sharpness of the models is consistent with the North River estuary, i.e., $R/W \sim 1$ for sharp bends and $R/W \sim 2-4$ for smooth bends (Bo et al., 2021), and is similar to the typical range of $R/W \sim 1-5$ found in river meanders (Leopold and Wolman, 1960) and tidal meanders (Marani et al., 2002). The channel thalweg depth linearly decreases from the mouth to ~ 20 km, and is a uniform 3 m after that (Figure 5-1 **(b)**). A shallow and a deep channel were built for each channel planform to explore the parameter space, with thalweg depths H of 4 m and 6 m respectively in the focus region. The channel has a parabolic cross section (e.g. Smith, 1982) with a minimum depth of $1.5-2$ m near the banks (Figure 5-1 **(c)**).

The models are forced by semi-diurnal tides on the open ocean boundary. Tidal ranges of 1.6, 2.0, and 2.4 m (Table 5.1) correspond to maximum tidal currents of $0.5-0.8$ m/s in the focus region. Constant river discharges of 1.5 and 7.5 m^3/s input at the landward boundary (Table 5.1) correspond to mean velocities of 1 cm/s and 5 cm/s in the focus region. The models have constant salinity of 32 psu at the ocean boundary and 0 psu at the river boundary. Temperature is constant and uniform throughout the domain. The model was run to a periodic (semi-diurnal) steady state. The analysis primarily focuses on the sharp-bend, smooth-bend, and straight channel models with the shallow thalweg depth, 2-m range tides, and 1.5-m^3/s discharge, which corresponds with common conditions of intermediate tides and low discharge in the North River estuary.

Model	R [m]	H [m]	W [m]	R/W	tidal range [m]	river discharge [m^3/s]
sharp1 $\star$	50	4	60	0.8	2.0	1.5
sharp2	50	4	60	0.8	1.6	1.5
sharp3	50	6	60	0.8	2.0	7.5
sharp4	50	6	60	0.8	2.4	7.5
smooth1 $\star$	120	4	60	2	2.0	1.5
smooth2	120	4	60	2	1.6	1.5
smooth3	120	6	60	2	2.0	7.5
smooth4	120	6	60	2	2.4	7.5
straight1 $\star$	–	4	60	–	2.0	1.5
straight2	–	4	60	–	1.6	1.5
straight3	–	6	60	–	2.0	7.5
straight4	–	6	60	–	2.4	7.5

Table 5.1: Geometric parameters and tidal and discharge conditions of all the sharp-bend, smooth-bend, and straight channel models. Note: The models selected for detailed analysis are marked with stars. R is the bend radius of curvature. H is the thalweg depth of the focus region. W is the channel width.

The model grids are structured, with 3-m resolution in the focused region, i.e., around 20 grid cells across the 60-m wide channel, and grid spacing increases toward the boundaries. A terrain-following coordinate with 16 uniformly distributed layers is used in the vertical direction. The generic length-scale (GLS) mixing scheme is used for the vertical turbulent mixing (Umlauf and Burchard, 2003; Warner et al., 2005) and the horizontal mixing coefficient K_H is set to 0.01 m^2/s. In addition, numerical mixing is assessed following the approach of (Burchard and Rennau, 2008). Numerical mixing arises from discretization errors of the tracer advection scheme, and can be calculated as the difference between the advected square of the tracer and the square of advected tracer (e.g., Burchard and Rennau, 2008; Ralston et al., 2017; Kalra et al., 2019). Bottom roughness z_0 is 0.002 m, a typical value for a bed with ripples (Grant and Madsen, 1982). The Coriolis force is included in the models. While the Coriolis effect could be crucial for estuarine salinity dynamics (e.g., Valle-Levinson, 2008; Scully et al., 2009; Valle-Levinson, 2011), it is negligible in the narrow estuaries investigated in the present study.

5.3 Results

In this section, we compare sinuous and straight channel models to investigate the influence of channel curvature on the flow field and salinity stratification. In section 5.3.1, the general features of tides and salinity field are compared. In section 5.3.2, we examine the curvature-induced secondary

circulation and its impact on salinity distribution in the channel bend. In section 5.3.3, we apply the vertical salinity variance budget analysis to investigate straining, mixing, and their influences on stratification in the sinuous and straight channel models.

5.3.1 Tides and stratification

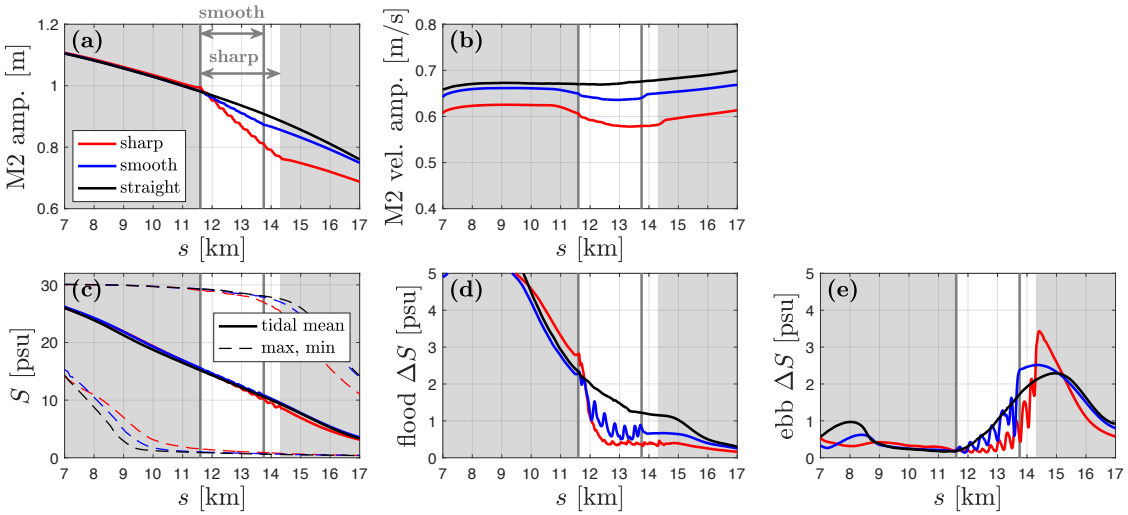

Figure 5-2: Along-channel change of tides and salinity in the sharp-bend, smooth-bend, and straight models with shallow depth, 2-m tidal range, and 1.5-m^3/s discharge. The white background shows the range of sharp bends, and the vertical gray lines show the range of smooth bends. **(a)**: M2 tidal amplitude. See legends for details. M2 amplitude is 1 m on the ocean boundaries. **(b)**: M2 velocity amplitude. **(c)**: Tidal mean salinity (solid lines) and maximum/minimum salinity (dashed lines). **(d)** and **(e)**: Mean stratification during flood and ebb tides, respectively. Stratification is quantified as the bottom-surface salinity difference ΔS.

Comparison of the sharp-bend, smooth-bend, and straight channel models illustrates the influence of channel curvature on tidal amplitude and stratification (Figure 5-2). The models have the same tidal and river boundary conditions, channel depth, and channel shape except for the sinuous region at around $12 - 14$ km. The three models have 1-m amplitude (2-m range) M2 tides imposed on the ocean boundaries, and the M2 tidal amplitude increases inside the estuary mouth because of channel convergence. Landward of around 6 km channel width becomes uniform and M2 amplitude decays due to drag (Figure 5-2 **(a)**). Tidal amplitude decays more rapidly in the meander regions of the sinuous models because channel curvature increases the drag through enhanced bottom friction and additional form drag around bends (e.g., Leopold, 1960; Chang, 1984; Bo and Ralston, 2020). Tidal amplitude decays faster in the sharp-bend model than the smooth-bend model because greater drag is expected for stronger channel curvature (e.g., James, 1994; Bo and Ralston, 2020). M2 ve-

locity amplitude is decreased in sinuous models compared to the straight model (Figure 5-2 **(b)**), because of the reduction in tidal amplitude with channel curvature.

The mean along-channel salinity distribution is similar among the three models (Figure 5-2 **(c)**). The tidal excursion is around 10 km in the straight channel model, and is $0.5 - 1$ km shorter in the sinuous models, which can be explained by the decreased tidal currents due to the meanders. The tidal excursion is comparable to the salinity intrusion length, and is much longer than the topographic features of interest, i.e., channel bends, which is common for short estuaries like the North River (Garcia et al., 2021). The salinity intrusion propagates landward of the meander region ($12 - 14$ km) during flood tide, and retreats seaward of the meanders during ebb.

All of the channel configurations illustrated here are periodically stratified. Stratification is created near the estuary mouth and advected landward to ~ 15 km during flood tide and disappears after maximum flood. Likewise, during early ebb tide stratification appears landward of the meander region and moves seaward until being completely mixed by maximum ebb tide. The sinuous models are generally less stratified than the straight channel during both flood and ebb tides, and stratification is weaker in the sharp-bend model than the smooth-bend model (Figure 5-2 **(d)**,**(e)**). While the weaker tidal current in sinuous channels (Figure 5-2 **(b)**) is expected to lead to weaker tidal mixing and stronger stratification, stratification instead decreases through the meander region, indicating that channel curvature can decrease stratification. Moreover, the sinuous models are less stratified than the straight model landward of the meanders during flood tide, which implies the non-local influence of meanders in decreasing stratification. During ebb tide, stratification landward of the meanders is slightly stronger than the straight model due to the relatively weaker tides in the sinuous cases (Figure 5-2 **(a)**,**(b)**). Comparison of the three models suggests that channel curvature generally reduces stratification, and the underlying mechanisms will be investigated in the following section. In addition to the example cases, model results across the range of forcing conditions and channel depths consistently demonstrate the influence of channel curvature in decreasing stratification. For example, the case with a deeper channel and stronger river discharge is permanently stratified as a straight channel but has tidally periodic stratification in both cases with curvature.

5.3.2 Secondary circulation and salinity distribution

During ebb tides, secondary circulation is observed in the meander region of all the sinuous models, and here we take one example from the sharp bend model with shallow thalweg depth, 2-m range tides, and 1.5-m^3/s discharge. The "normal" secondary circulation due to flow curvature develops

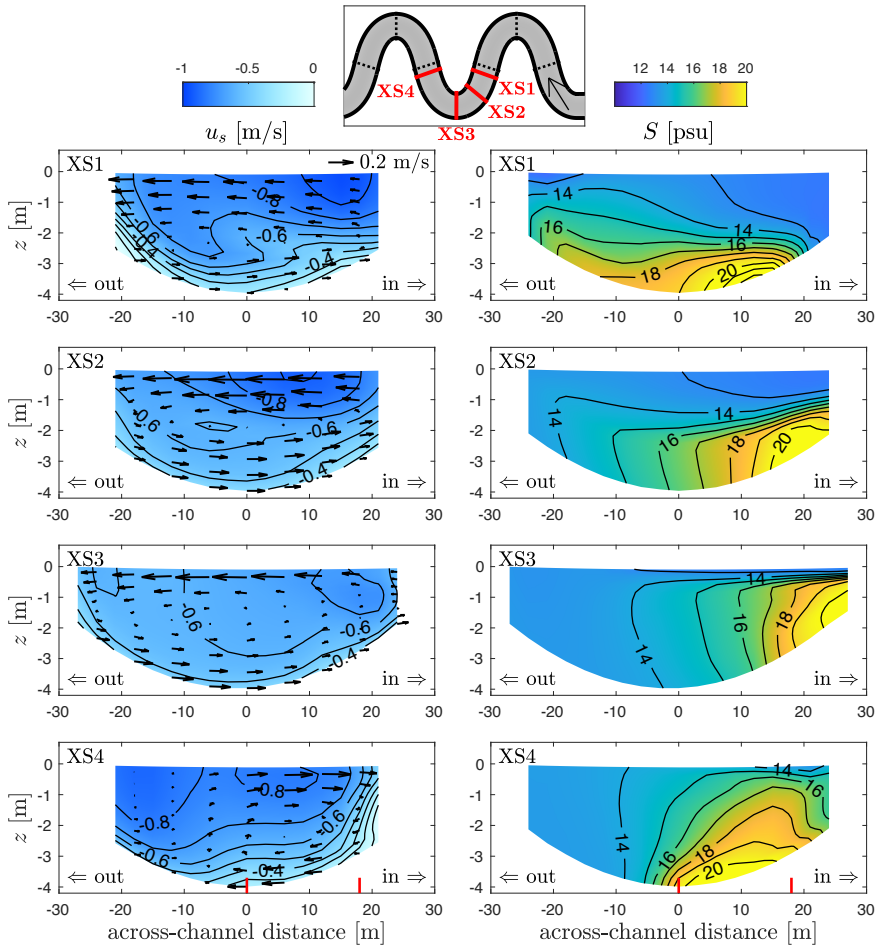

Figure 5-3: Streamwise velocity u_s (left) and salinity S (right) in four cross-sections in a bend at 2-hr into ebb tide. Negative streamwise velocity means seaward flow. Black arrows show the secondary circulation. The inner bank is on the right side, and outer bank is on the left side in all panels. In the small panel, red lines show locations of the four cross-sections, and dotted black lines represent the bend apexes and crossovers. Red vertical lines in the lowest panels show locations of the along-channel sections (CL, IB) in Figure 5-4.

in the cross-sections from the bend entrance to the apex, with the lateral flow toward the outer bank near the surface and toward the inner bank near the channel bed (Figure 5-3 XS1,2,3). As a result, as the stratified flow enters the bend, the downward vertical velocity near the outer bank advects fresher water with relatively high streamwise momentum from the surface toward the lower layer and squeezes isohalines closer to the bed (Figure 5-3 XS1). Correspondingly near the inner bank, as flow approaches the bend apex the halocline is lifted by the upwelling that is fed by inward flow of high salinity water near the bed. High salinity water builds up near the inner bank at the apex (Figure 5-3 XS3), and stratification almost disappears because secondary circulation has transformed the vertical salinity gradient coming into the bend into a lateral gradient at the apex.

Downstream of the bend apex, the sense of lateral circulation is reversed because the lateral baroclinic forcing from the lateral salinity gradient becomes greater than the centrifugal forcing, resulting in inward flow near the surface and outward flow near the bottom (Figure 5-3 XS4). Consequently, the lateral salinity gradient is converted back to a vertical gradient by the reversed secondary circulation, and stratification is restored before the flow enters the next bend. Similar interactions between stratification and secondary flows including the reversal of secondary circulation by the lateral baroclinic pressure gradient have been observed around a headland in the Hudson River estuary (Chant and Wilson, 1997).

The lateral momentum balance (e.g., Chant and Wilson, 1997; Nidzieko et al., 2009; Kranenburg et al., 2019) is examined to investigate the driving force for the secondary circulation patterns, with the depth-average lateral momentum balance

$$\frac{\partial u_r}{\partial t} = -\frac{u_s^2 - \overline{u_s^2}}{R} - \beta g \left(\int_z^0 \frac{\partial S}{\partial r} \mathrm{d}z - \overline{\int_z^0 \frac{\partial S}{\partial r} \mathrm{d}z} \right) - \left(u_s \frac{\partial u_r}{\partial s} - \overline{u_s \frac{\partial u_r}{\partial s}} \right) - \left(\frac{\partial \langle u_r' w' \rangle}{\partial z} - \frac{\tau_{b,r}}{\rho H} \right), \tag{5.1}$$

where Coriolis has been neglected. u_s, u_r, and w are the streamwise, lateral, and vertical velocities. β is the haline contraction coefficient, S is salinity, and $\tau_{b,r}$ is the lateral component of the bed shear stress. An overbar stands for depth average and brackets represent time-average in the Reynolds stress. The time rate of change term is usually negligible due to the quasi-steady ebb flow. The first term on the right side is the centrifugal acceleration (CFA), and the second term is the baroclinic pressure gradient force (BCPG). The above forcing terms are typically balanced by the streamwise advective acceleration term (third term on the right side), i.e., the nonlocal adjustment of the secondary flow (e.g., Nidzieko et al., 2009), and the friction term (fourth term). Note that the depth-averaged momentum balance has been subtracted to investigate the vertical deviations of the driving forces, so that the barotropic pressure gradient does not appear in equation (5.1) (Nidzieko et al., 2009).

The CFA is inward in the lower layer and outward in the upper layer due to the vertical shear in the streamwise flow (Figure 5-4 **(d)**), This drives the "normal" secondary circulation before the bend apex, which is identical to the sense of secondary circulation for homogeneous flow. The BCPG increases along the bend as a result of the lateral salinity gradient created by secondary circulation, and that opposes the CFA (Figure 5-4 **(e)**). Therefore, CFA+BCPG becomes outward in the lower layer and inward in the upper layer downstream of the bend apex (Figure 5-4 **(f)**), which thus reverses the sense of secondary circulation (Figure 5-4 **(c)**). As a result, the lateral circulation

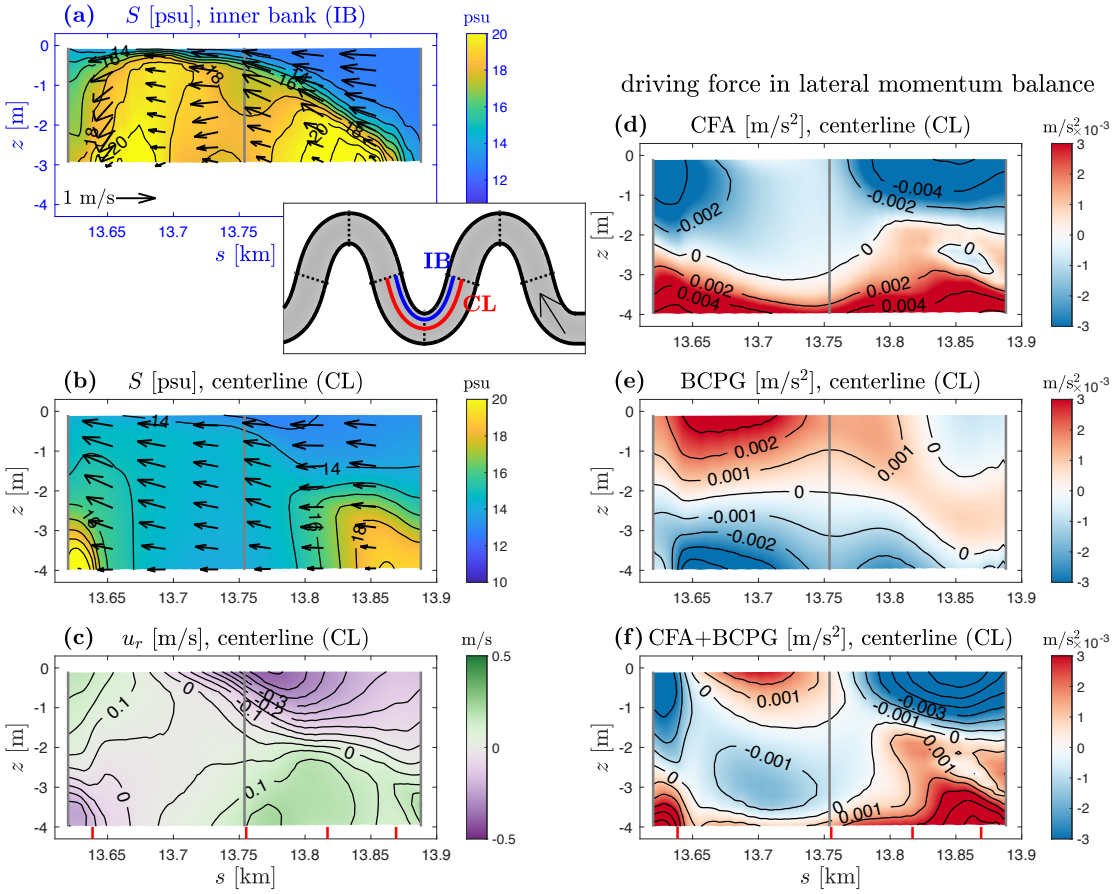

Figure 5-4: Along-channel sections in a bend at 2-hr into ebb tide. **(a)**: Salinity in an along-channel section near the inner bank (18 m from the centerline). Black arrows show the streamwise and vertical velocities. The bend apex is marked by the gray line at around $s = 13.75$ km. **(b)**: Salinity along the centerline. **(c)**: Lateral velocity u_r along the centerline. The positive direction is inward and negative direction is outward. **(d)**, **(e)**, and **(f)**: Driving force in the lateral momentum balance (centrifugal acceleration CFA, baroclinic pressure gradient force BCPG, and CFA+BCPG). Positive values represent inward forcing. In the small panel, the blue line shows the section along the inner bank (IB, for **(a)**), and the red line shows centerline (CL, for all other panels). Dotted black lines represent the bend apexes and crossovers. Red vertical lines in the lowest panels show locations of the cross-sections (XS1-4) in Figure 5-3.

reverses sense and the associate lateral straining tends to be destratifying before the bend apex and restratifying after the bend apex (Figure 5-4 **(b)**). Moreover, a bottom salinity front can be observed along the inner bank upstream of the bend apex corresponding with the build up of high salinity water there (Figure 5-4 **(a)**).

During flood tide (not shown), a more complex secondary circulation is observed in meanders. Streamwise velocity has lateral variations due to the channel curvature effect, and the lateral baroclinic pressure gradient forcing (BCPG) resulting from differential advection plays a more important

role (e.g., Lacy and Monismith, 2001; Nidzieko et al., 2009; Pein et al., 2018; Kranenburg et al., 2019). Multiple circulation cells appear in the bend during flood tide, leading to multiple regions of downwelling or upwelling (surface convergence or divergence) and resulting in both along-channel and lateral fluctuations in the salinity field. Note that the lateral BCPG during flood tide results from the differential advection of the along-estuary salinity gradient by the laterally sheared streamwise velocity, while the lateral BCPG during ebb tide is due to the interaction between stratification and the curvature-driven secondary circulation. Moreover, during flood tide, flow separation and recirculating eddies are observed in the lee of the bend apex, enhancing the lateral shear of the streamwise velocity and influencing the differential advection, lateral momentum balance, and secondary circulation.

Similar to ebb tide, during flood tide the meander regions have less stratification than in the straight channel case, but the following salinity variance budget analysis finds that more mixing occurs during ebb tides than flood tides (section 5.3.3). During ebb tides, a single secondary circulation cell occurs and the longitudinal straining of the salinity gradient is stratifying. The stratification dynamics during flood have added complexity compared with the ebb, as advection of the along-channel salinity gradient leads to multiple secondary circulation cells and longitudinal straining tends to destratify the water column. Therefore, the subsequent analysis will examine in detail how channel curvature influences the stratification and mixing during ebb tides, and flood tide conditions will be addressed in section 5.5.

5.3.3 Vertical salinity variance budget

As illustrated in the channel cross-sections in Figure 5-3, the curvature-induced lateral circulation greatly affects the salinity distribution in the meanders. To quantify the variability in stratification and processes affecting it with channel curvature, we calculate the vertical salinity variance budget. The depth-averaged vertical salinity variance budget is (Burchard and Rennau, 2008; Li et al., 2018):

$$\frac{\partial}{\partial t}\frac{1}{h}\int (S_v')^2 \mathrm{d}z = -\frac{1}{h}\nabla\cdot\int \mathbf{u}(S_v')^2\mathrm{d}z - \frac{1}{h}\int 2\mathbf{u}_v' S_v'\cdot\nabla\overline{S}\mathrm{d}z - \frac{1}{h}\int 2K_z\left(\frac{\partial S}{\partial z}\right)^2\mathrm{d}z - \frac{1}{h}\int \mathcal{M}_{num}\mathrm{d}z. \tag{5.2}$$

$\overline{S}$ is the depth-averaged salinity, and S_v' is the deviation from the depth average. $(S_v')^2$ is the vertical salinity variance that corresponds with stratification in the water column. ∇ is the horizontal gradient operator. $\mathbf{u}$ is the horizontal velocity vector (u_s and u_r), and $\mathbf{u}_v'$ stands for vertical deviations. K_z is the vertical salinity mixing coefficient (eddy diffusivity). The vertical salinity variance budget

is vertically integrated and averaged over the water depth h. The left side is the unsteady term (time rate of change). The first term on the right side is the advection term. The second term on the right side represents straining that can either increase or decrease the vertical variance, including both along-channel straining and lateral straining. The third term is physical mixing (dissipation of variance) that irreversibly decreases the vertical salinity variance. The fourth term is the additional numerical mixing due to discretization of tracer advection in the model (Burchard and Rennau, 2008; Ralston et al., 2017, also see section 5.2).

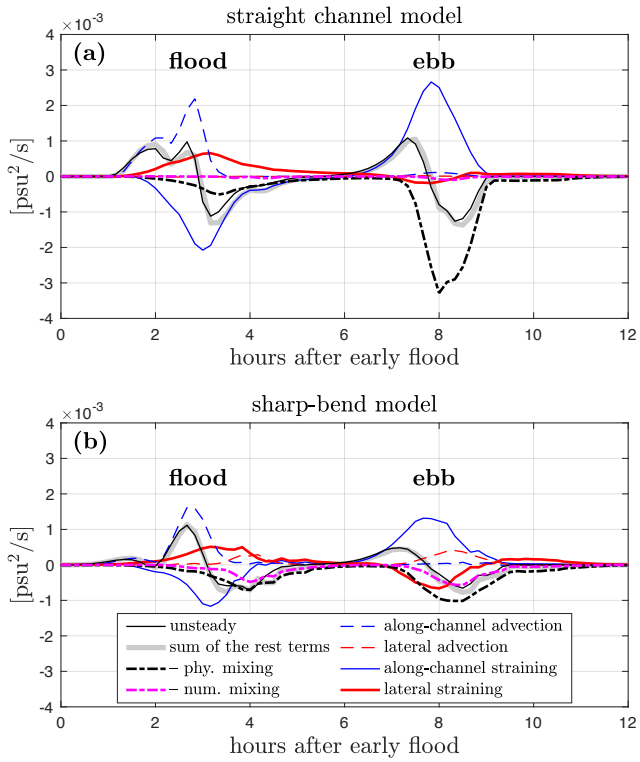

Figure 5-5: Vertical salinity variance budget in the straight channel model **(a)** and sharp-bend sinuous model **(b)**, as a function of tidal hours. The budget is calculated as the spatial average over $6 - 20$ km into the estuary. The solid black line is the unsteady term (time rate of change), and the solid gray line is the summation of the other terms that is supposed to balance with the unsteady term. See legend for details.

The estuary-scale vertical salinity variance budget is evaluated over a control volume from 6 km (end of channel convergence) to 20 km (landward of salt intrusion). In the straight channel, stratification is created near the mouth during the ebb-to-flood transition by along-channel straining, because the tidal flow in the lower water column turns landward before the upper column due to baroclinicity. The stratification created near the mouth is advected into the control volume by flood currents as a positive term in the salinity variance budget (Figure 5-5 **(a)**). During flood tide in

the straight channel, differential advection and baroclinic lateral circulation also tend to increase stratification with positive lateral straining (Lacy et al., 2003; Ralston and Stacey, 2005a; Geyer et al., 2020). Stratification is decreased by the negative along-channel straining of boundary layer shear advecting saltier water over fresher water and by irreversible mixing. During ebb tide, stratification increases due to straining of the along-channel salinity gradient (Simpson et al., 1990), and diminishes after max ebb tide due to mixing. In contrast to flood tide, the lateral straining is almost negligible during the ebb. The unsteady term agrees well with summation of the other terms, indicating that the variance budget closes in the calculation. Numerical mixing is negligible in the straight channel through the entire tidal cycle.

In the sinuous model, the vertical salinity variance budget is overall similar to the straight channel model at the estuary scale (Figure 5-5 **(b)**), e.g., positive along-channel advection and negative along-channel straining during flood tide, and positive along-channel straining during ebb. However, numerical mixing accounts for around 30% of the total mixing in the sinuous model and the variance budget closes only when numerical mixing is included. In addition, the net lateral straining is negative in the sinuous model during ebb, whereas in the straight channel the lateral straining during ebb was negligible. This suggests that curvature-induced lateral circulation plays a key role in the reduction in stratification, as will be examined below. The total lateral advection is expected to be zero because the control volume begins and ends in straight channel regions. However, positive values of total lateral advection appear in the sinuous model, due to the adjustment of the flow at transitions between meanders and straight channel regions, but the lateral advection term is always close to zero away from the transitions.

The laterally averaged vertical salinity variance budget is calculated to investigate the local effects of meanders during ebb (Figure 5-6). The analysis primarily focuses on the second bend to avoid the initial flow adjustment from the straight channel in the first bend. Negative lateral straining before bend apexes decreases vertical salinity variance and increases lateral variance, and lateral variance is converted back to vertical variance by the positive lateral straining after each bend apex (Figure 5-6 **(a)**, **(b)**). This alternating pattern of lateral straining is the same as the reduction in stratification by the normal secondary circulation upstream of the apex and the regeneration of stratification by the reversed secondary circulation downstream of the apex (section 5.3.2). In straight channels, the lateral straining typically increases stratification, e.g., due to the baroclinic two-cell lateral circulation during flood tides (Lerczak and Geyer, 2004). However, negative lateral straining that decreases stratification occurs in the sinuous channel because of the additional forcing

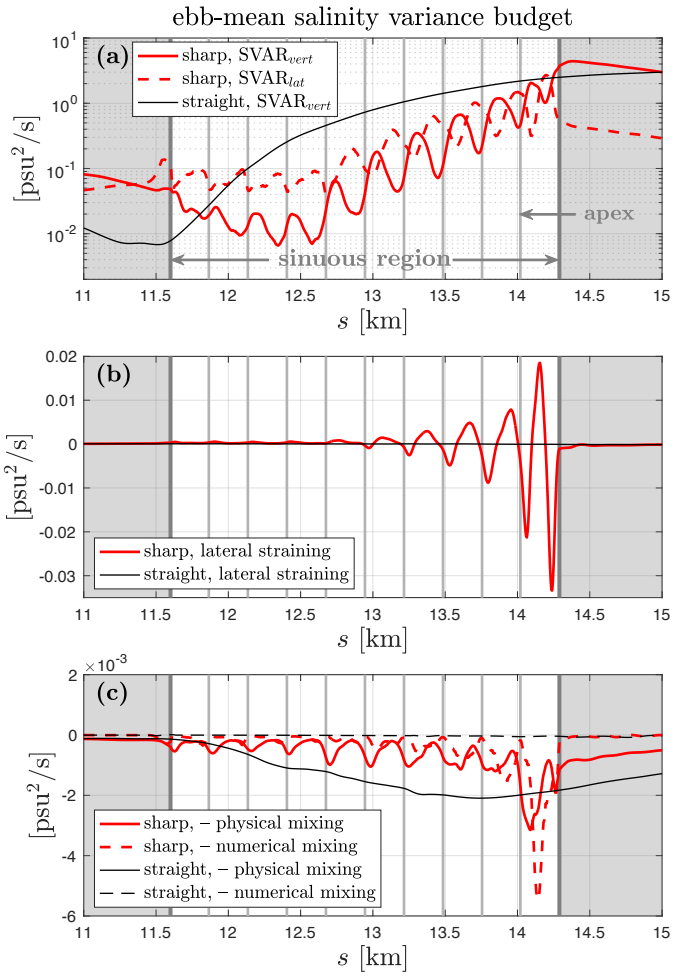

Figure 5-6: Vertical salinity variance budget as a function of along-channel distance. The budget is laterally averaged, and calculated as the time average over ebb tide. **(a)**: Vertical salinity variance (SVAR$_{vert}$) in the straight model and the sharp-bend sinuous model, and lateral salinity variance (SVAR$_{lat}$) in the sinuous channel. Note that the vertical axis is on a log scale in panel **(a)**. See legend for details. **(b)**: Lateral straining. **(c)**: Physical mixing and numerical mixing. Note the different vertical axis ranges in panels **(b)** and **(c)**. The vertical gray lines show the range of the sinuous region and locations of bend apexes.

by the channel curvature.

While both positive and negative lateral straining occur in the sinuous channels, the integrated effect of the lateral straining during ebb is to decrease stratification. The lateral circulation and straining transfers salinity variance between vertical and lateral components through a bend. During the ebb tide, the magnitude of lateral straining decreases seaward through the meanders (Figure 5-6 **(b)**), because stratification overall decreases seaward and leads to less salinity variance for the lateral straining to convert back and forth in each consecutive bend (Figure 5-6 **(a)**). As a result, the reduction in stratification upstream of each bend apex by the negative straining is greater than

the creation of stratification downstream of each apex by positive straining. The net lateral straining is therefore negative (Figure 5-5 **(b)**), indicating an integrated effect to decrease stratification in meanders.

While straining can reduce stratification by converting it to horizontal salinity variance, mixing reduces stratification through the irreversible destruction of vertical salinity variance. Channel curvature can decrease stratification by locally enhancing vertical mixing (Figure 5-6 **(c)**). As the stratified flow enters the meanders, both physical mixing and numerical mixing are greater in the sinuous model than the straight model. Multiple hot spots of mixing are observed in meanders, mostly upstream of the bend apexes and close to the inner bank (Figure 5-7 **(e)**,**(f)**). Moreover, locations of enhanced mixing coincide with strong bottom along-channel salinity gradient, indicating that mixing in meanders is associated with bottom fronts (see details in the analysis section).

The strength of mixing decreases seaward as stratification is progressively destroyed by the mixing through the bends. Although strong mixing occurs in regions with channel curvature, the spatially integrated total mixing in the sinuous model is less than the straight model (Figure 5-5). In the straight channel along-channel straining continuously creates stratification that can then be mixed, whereas in the sinuous channel the enhanced mixing rapidly exceeds the along-channel straining, inhibiting the growth of stratification. Stratification progressively decreases through the bends due to this imbalance, reducing the stratification that could be mixed in bends downstream. Consequently, both the total mixing and the stratification in the sinuous channel are less than the straight channel.

Numerical mixing usually occurs at similar locations as physical mixing (Figure 5-7 **(e)**,**(f)**). While numerical mixing is greatest upstream of the bottom fronts in bends, physical mixing mostly occurs downstream of the fronts. Numerical mixing acts to diffuse horizontal gradients that otherwise would be smoothed by the turbulent or horizontal mixing processes, and the evolution of the stratification in the model is determined by the combination of physical mixing and numerical mixing (Ralston et al., 2017; Li et al., 2018). Numerical mixing is around 30% of the total mixing in the sharp-bend model, less than 20% in the smooth-bend model, and negligible in the straight channel model. While the different models have the same grid resolution and mixing schemes, the contribution of numerical mixing increases as channel curvature increases. Moreover, numerical mixing can be locally stronger than physical mixing, e.g., in the most landward bend (Figure 5-6 **(c)**). The results clearly demonstrate the importance of accurately representing numerical mixing in sinuous channels, and anywhere strong horizontal salinity gradients combined with streamwise

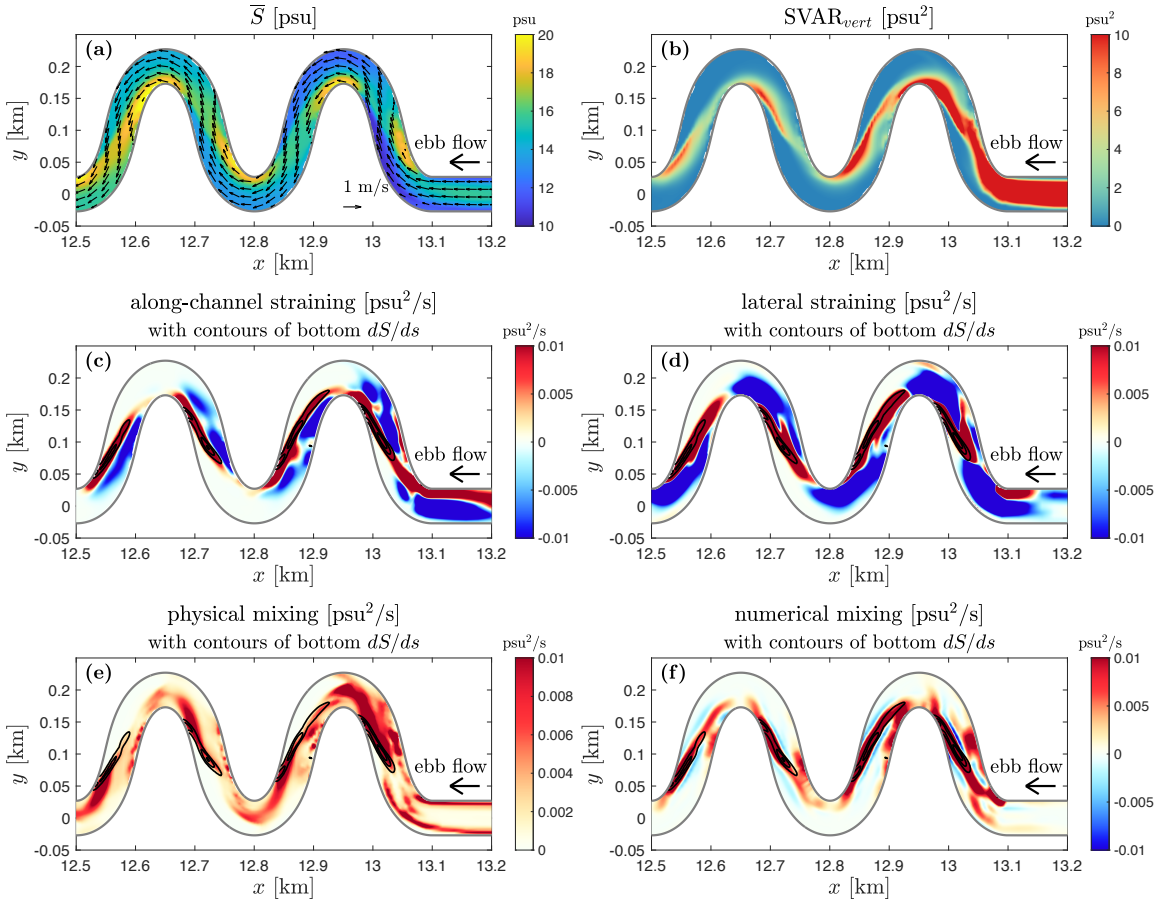

Figure 5-7: Map views of the landward bends of the sharp-bend sinuous model at 2-hr into ebb. **(a)**: Depth-averaged salinity $\overline{S}$. **(b)**: Vertical salinity variance SVAR$_{vert}$. **(c)**: Along-channel straining, with contours of bottom along-channel salinity gradient. **(d)**: Lateral straining. **(e)**: Physical mixing. Positive values (red color) show magnitudes of physical mixing, but its influence is always to decrease the variance in the budget. **(f)**: Numerical mixing. Note that negative numerical mixing can appear because of the anti-diffusive corrections in the model (e.g., Burchard and Rennau, 2008; Kalra et al., 2019), but the total numerical mixing is positive (dissipating the variance).

currents (details examined in the analysis).

5.4 Analysis

5.4.1 Shear mixing at bend-scale salinity fronts

The salinity variance budget calculation suggested that channel curvature can decrease stratification through locally enhancing vertical mixing in meanders, with the strongest mixing occurring upstream of bend apexes (section 5.3.3). In this section, we further investigate the three-dimensional distribution of mixing in a bend and the underlying mechanisms. Intense mixing happens near the

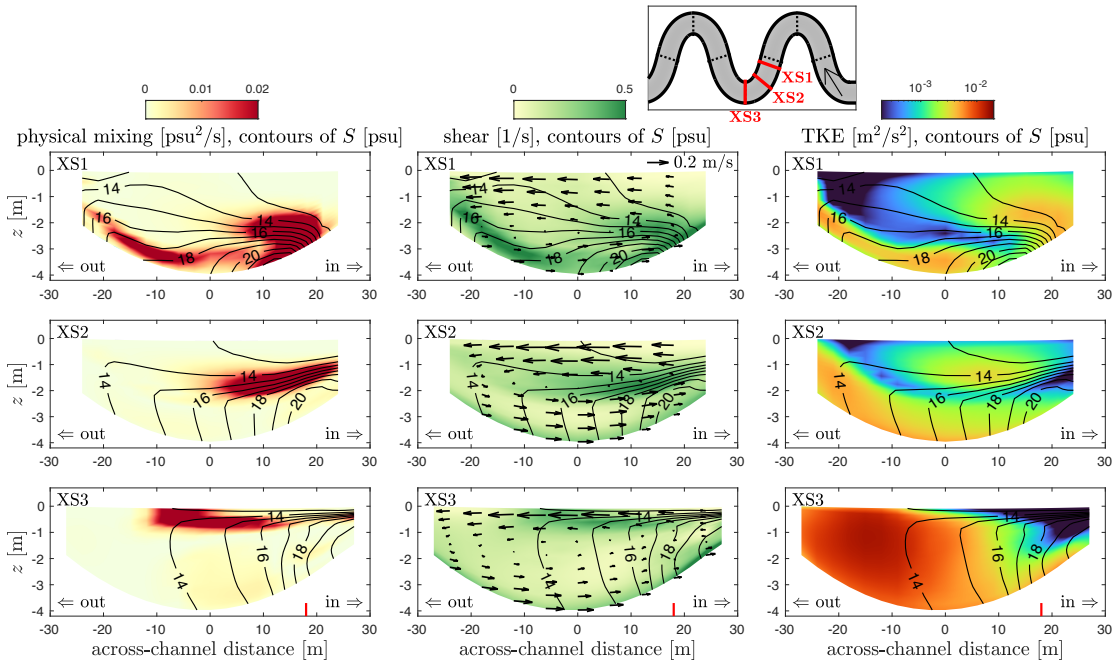

Figure 5-8: Physical mixing (left), vertical shear (middle), and turbulent kinetic energy (right) in three cross-sections in a bend at 2-hr into ebb tide. Salinity contours are shown in black. Arrows show the secondary circulation. The inner bank is on the right side, and outer bank is on the left side in all panels. In the small panel, red lines show locations of the three cross-sections, and dotted black lines represent the bend apexes and crossovers. The red vertical line in the lowest panels shows the location of the along-channel section (IB) in Figure 5-9.

inner bank as flow approaches the bend apex (Figure 5-8 XS1-3) and the secondary circulation lifts the halocline upward (section 5.3.2). The upstream edge of the intensified mixing corresponds with the bend-scale bottom salinity front near the inner bank (Figure 5-9). Enhanced shear at the salinity front decreases the gradient Richardson number Ri_g to below the critical value, which allows for intensified turbulence and mixing (Figure 5-9 **(a)** and **(b)**).

Overturning mixing is found near the bend apex where secondary circulation tends to laterally advect saltier water over fresher water and create negative buoyancy (Figure 5-8 XS3). Maximum overturning mixing occurs near the bend apex (Figure 5-10), in contrast to the shear-driven mixing that is strongest upstream of the apex. However, overturning mixing is minimal compared to the shear-driven mixing, with total overturning mixing that is $\sim 5\%$ of the shear mixing in the sharp-bend channel. For comparison, overturning was found to be the dominant source of mixing in a energetic tidal flow with channel curvature in Puget Sound by Seim and Gregg (1997) (e.g., their Figure 15), whereas in the shallower tidal channel of Elkhorn Slough, Nidzieko et al. (2009) found that turbulent motions associated with the along-channel flow dominated the mixing rather than

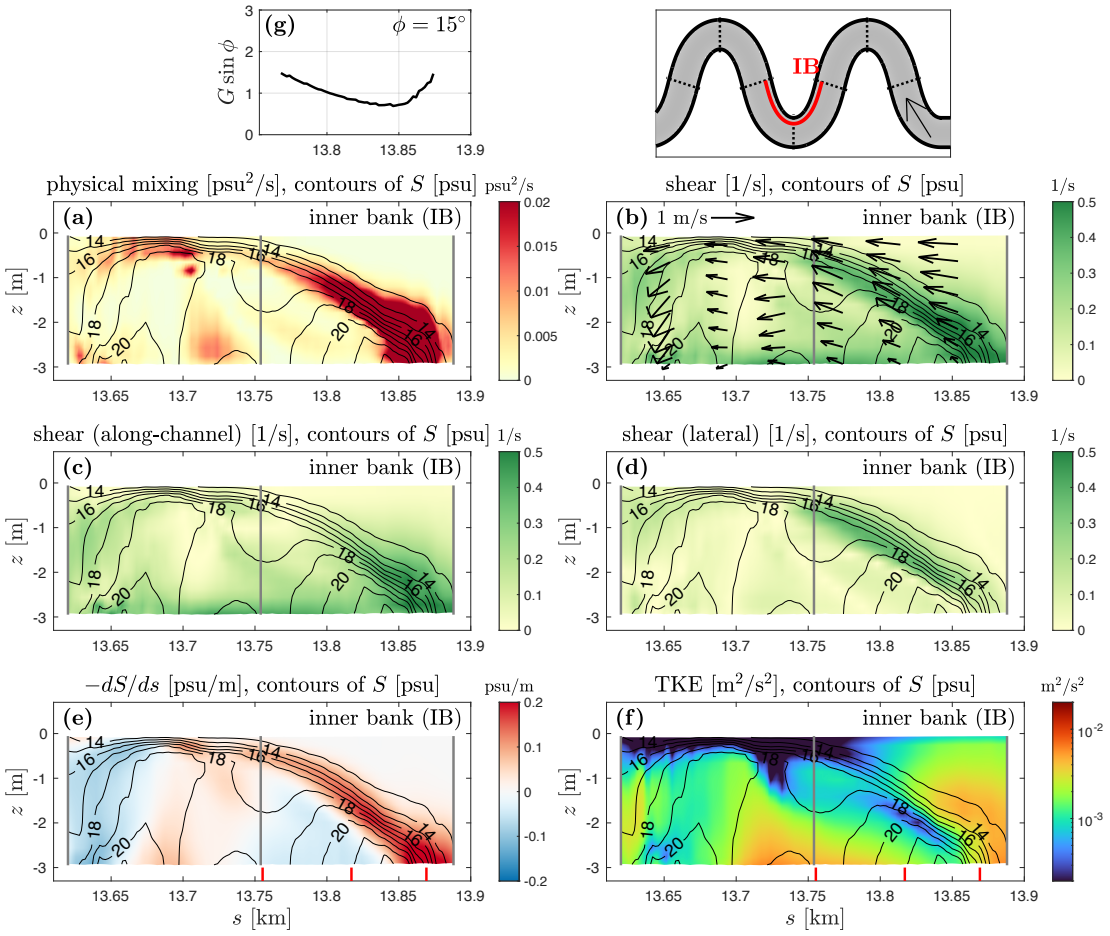

Figure 5-9: An along-channel section near the inner bank of a bend (18 m from the centerline) at 2-hr into ebb tide. **(a)**: Physical mixing. Salinity contours are shown in black. The bend apex is marked by the gray line at around $s = 13.75$ km. **(b)**, **(c)**, and **(d)**: Total vertical shear, and the shear of along-channel flow and lateral flow. Black arrows show the streamwise and vertical velocities. **(e)**: Along-channel salinity gradient. Red color means salinity increasing seaward. **(f)**: Turbulent kinetic energy. **(g)**: Composite Froude number G. The angle ϕ of the salinity front to the bottom velocity is around $15°$ (Froude angle). In the small map, the red line shows the along-channel section near the inner bank (IB). Dotted black lines represent the bend apexes and crossovers. Red vertical lines in the lowest panels show locations of the cross-sections (XS1-3) in Figure 5-8.

overturning. As found in the observations of overturning in Puget Sound (Seim and Gregg, 1997), the strongest turbulent kinetic energy (TKE) in the sinuous model appears at the bend apex, and this turbulence could potentially drive mixing (Figure 5-8 XS3). However, mixing requires both turbulence and stratification (Li et al., 2018; Warner et al., 2020). Stratification has been reduced by the negative lateral straining with channel curvature and thus mixing is relatively weak near bend apexes, even as the overturning circulation generates strong turbulence there. Note that ROMS is a hydrostatic model and non-hydrostatic processes associated with overturning may not be resolved,

so the calculated contribution of overturning mixing should be considered approximate. Nevertheless, the estuarine dynamics are not favorable for overturning mixing in the sinuous channel because the sense of secondary circulation reverses downstream of the bend apex due to the lateral baroclinic pressure gradient (section 5.3.2), effectively limiting the overturning to near the bend apex. This is in contrast to previous studies where overturning circulation could develop more continuously (Seim and Gregg, 1997).

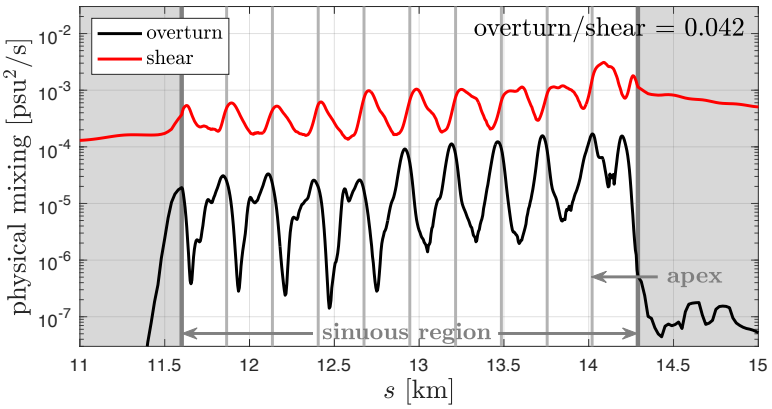

Figure 5-10: Laterally averaged shear mixing and overturning mixing as a function of along-channel distance, averaged over ebb tide. Note the vertical axis has a log-scale. The vertical gray lines show the range of the sinuous region and locations of bend apexes.

The most intense mixing is found upstream of bend apexes, where bend-scale bottom salinity fronts provide a combination of stratification and active turbulence due to the strong vertical shear. Shear of the along-channel flow is amplified at bottom salinity fronts due to the combined influences of the bottom boundary layer (e.g., within $0.5 - 1$ m above the bed) and baroclinicity. The along-channel baroclinic pressure gradient across the frontal zone can locally enhance the vertical shear of along-channel flow and thus lead to increased turbulence and mixing. Along-channel salinity gradients are tilted to the vertical direction by the enhanced shear, which corresponds with the positive along-channel straining observed near the toe of the bottom fronts (Figure 5-7 **(c)**) and adds to the stratification available for mixing. As flow approaches the bend apex and the halocline rises to the upper column, the normal secondary circulation develops due to the channel curvature effect and, as a result, the shear of the lateral flow becomes greater than the along-channel component, contributing to the enhanced mixing (Figure 5-7 **(d)**).

Mixing is also locally enhanced near the outer bank at the entrance to the bend (e.g., Figure 5-8 XS1), where the downward velocity of the secondary circulation pushes stratification into the

bottom boundary layer. This is a second mechanism by which the curvature-induced lateral circulation brings together stratification and turbulence to increase mixing. The total mixing resulting from this vertical advection of stratification into the boundary layer is less than is associated with the bottom salinity front near the inner bank.

While we have focused on physical mixing in this analysis, the numerical mixing has similar spatial and temporal distribution patterns as the physical mixing, so it does not alter the underlying mechanisms. Numerical mixing arises from the advection of salinity gradients, and the regions of physical mixing typically have sharp salinity gradients and strong velocities that can thus lead to numerical mixing. In an along-channel section near the inner bank, strong numerical mixing occurs at the bend-scale salinity front (not shown) in a similar form as physical mixing (Figure 5-9 **(a)**), except that numerical mixing happens slightly upstream of the frontal zone (also reflected in Figure 5-7 **(e)**,**(f)**).

5.4.2 Frontogenesis in meanders

To characterize the bottom fronts that cause mixing in the sinuous model, frontogenesis in meanders is analyzed by using the tendency equation of along-channel salinity gradient (Geyer and Ralston, 2015)

$$\frac{\partial}{\partial t}\frac{\partial S}{\partial s} + \mathbf{u}\cdot\nabla\frac{\partial S}{\partial s} = -\frac{\partial u_s}{\partial s}\frac{\partial S}{\partial s} - \frac{\partial u_r}{\partial s}\frac{\partial S}{\partial r} - \frac{\partial w}{\partial s}\frac{\partial S}{\partial z} - \frac{\partial}{\partial s}\frac{\partial}{\partial z}\langle S'w'\rangle. \tag{5.3}$$

The left-side terms represent the local tendency and advection of the along-channel salinity gradient. Terms on the right side represent physical processes that affect the along-channel salinity gradient, including the along-channel convergence/divergence (first term), twisting of lateral and vertical salinity gradients due to the along-channel gradients in lateral and vertical velocity (second and third term, respectively). The fourth term on the right side is the along-channel gradient of vertical mixing, which is negligible here because the idealized channels have uniform cross-sectional shape and do not have steeply sloping bathymetry that might create spatial gradients in mixing in the along-channel direction.

In straight channels, generation of along-estuary bottom salinity fronts is typically dominated by the along-channel convergence (first term on the right side) (e.g., Geyer and Ralston, 2015). However, in sinuous estuarine channels, the secondary circulation can make lateral and vertical processes more important for frontogenesis. Near the toe of the bottom front, formation of the along-channel salinity gradient is dominated by the lateral process (second term) (Figure 5-11 **(b)**).

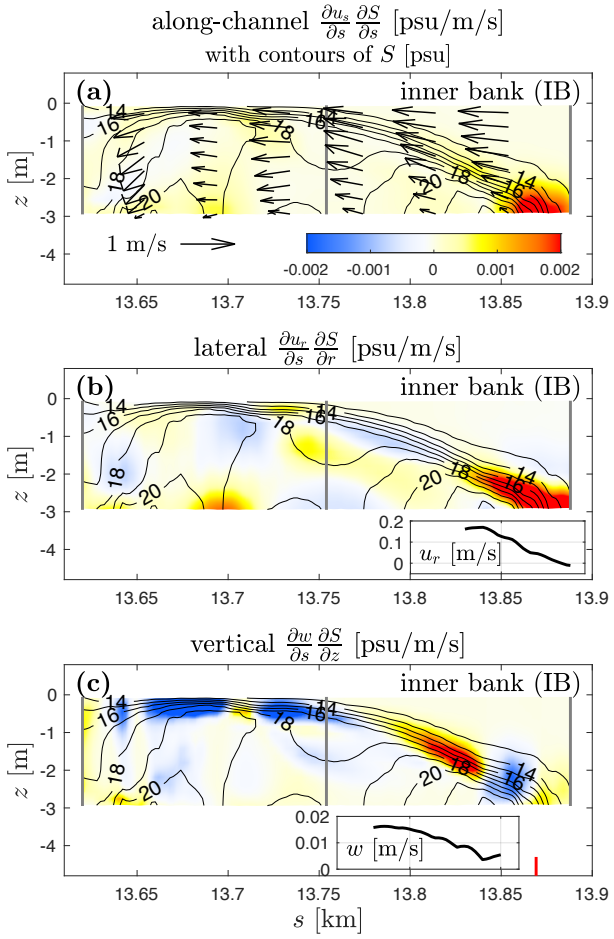

Figure 5-11: Terms affecting the along-channel salinity gradient in equation (5.3). **(a)**: Along-channel convergence. Salinity contours are shown in black. Black arrows show the streamwise and vertical velocities. **(b)**: Twisting of lateral salinity gradients due to the along-channel gradient in lateral velocity. The small panel shows the along-channel distribution of near-bed lateral velocity (positive means toward the inner bend). **(c)**: Twisting of vertical salinity gradients due to the along-channel gradient in vertical velocity. The small panel shows the along-channel change of vertical velocity in the mid-water column. Red color means contributing to the generation of the along-channel front. This is the same along-channel section near the inner bank (IB) as in Figure 5-9, at 2-hr into ebb tide. The red vertical line in the lowest panels marks the location of the cross-section (XS1) near the toe of the front.

The inward secondary flow near the bed develops after flow enters the bend, twisting lateral salinity gradients into the along-channel direction. In the mid-water column, the upward vertical velocity near the inner bank increases as stratified flow goes toward the bend apex, and vertical salinity gradients are thus distorted into the along-channel direction (third term), contributing to formation of the along-channel salinity front (Figure 5-11 **(c)**).

The twisting of lateral salinity gradients by lateral currents is the biggest contributor to frontoge-

nesis, and the source of the lateral salinity gradient has been investigated by the tendency equation of lateral salinity gradient (not shown, similar to equation (5.3)). Generation of the lateral salinity gradient is mainly driven by the lateral gradient of vertical mixing in the parabolic cross section, where the shallow bathymetry at the channel edges creates stronger vertical mixing, similar to the horizontal salinity gradient formed over the shelf slope (e.g., Gawarkiewicz and Chapman, 1992; Lerczak and Geyer, 2004; McWilliams, 2021). As a result, strong lateral salinity gradients occur in the inner bend near the toe of the bottom front with lower salinity near the bank (e.g., Figure 5-3 XS1), which then is twisted by the secondary flow and leads to generation of the along-channel front (Figure 5-11 **(b)**).

Overall, the frontogenesis analysis suggests that both the curvature-induced secondary circulation, i.e., the lateral and vertical flows, and the lateral variability of bathymetry and associated boundary layer mixing are crucial for the formation of along-channel salinity fronts in meanders. The bottom salinity fronts that result from the curvature-induced secondary circulation provide the dominant mechanism for mixing and explain the decreased stratification in the sinuous channel.

To understand the hydraulic state of the curvature-induced bottom front, we calculate the composite Froude number G for two-layer flow (e.g., Armi and Farmer, 1986; Geyer and Ralston, 2015).

$$G^2 = F_1^2 + F_2^2 = \frac{u_1^2}{g' H_1} + \frac{u_2^2}{g' H_2}, \tag{5.4}$$

where F_1 and F_2 are the Froude numbers for the upper and lower layers. u_1 and u_2 are the average velocities of each layer, and H_1 and H_2 are the layer thickness. $g' = g(\Delta\rho/\bar{\rho})$ is the reduced gravity based on the density difference between the upper and lower layers. The bottom front is obliquely oriented to the channel flow, and the angle ϕ of the front to the bottom velocity is around $15°$ (Figure 5-7). The effective composite Froude number $G\sin\phi$ is calculated to account for the Froude angle theory in MacDonald and Geyer (2005), i.e., evaluate the component of G normal to the front. The bottom front in the bend exists during around 1-3 hr into ebb and is relatively stationary. $G\sin\phi$ is close to 1 (critical condition) at the toe of the bottom front (Figure 5-9 **(g)**), and thus, the stationary and oblique bottom front is consistent with a critical front (MacDonald and Geyer, 2005).

5.4.3 Simpson number in sinuous estuarine channels

Stratification is decreased in the sinuous channel cases due to enhanced vertical mixing, and we would like to relate that to implications for stratification in the broader estuarine parameter space. One approach is to consider the Simpson number Si, which is defined as the ratio of potential energy input due to tidal straining to tidal mixing (Stacey et al., 2001; Burchard et al., 2011; Geyer and Ralston, 2011)

$$Si = \frac{\beta g(\partial S/\partial s)H^2}{C_D u_T^2}. \tag{5.5}$$

$\partial S/\partial s$ is the along-estuary salinity gradient (typically taken over the estuary-scale). C_D is the drag coefficient and u_T is the tidal velocity. The Si relates to stratification conditions in estuaries because it represents the balance between the creation of stratification by along-estuary straining and destruction of stratification due to vertical mixing (Stacey et al., 2001).

The drag coefficient C_D in the denominator of Si relates to the strength of tidal mixing. C_D is a typical way to quantify the drag force experienced by the tidal flow, and C_D also relates to the turbulent energy dissipation rate and the strength of turbulent mixing. Drag in estuarine channels is usually attributed to bottom friction, and a common value for C_D is around 0.003 (e.g., Dronkers, 1964; Sternberg, 1968; Soulsby, 1990). However, channel curvature can lead to an increased C_D of up to ~ 5 times larger than the typical value by enhancing bottom shear stress and creating form drag (e.g., Chang, 1984; Warner and MacCready, 2014; Bo and Ralston, 2020).

The present study indicates that channel curvature can lead to decreased stratification through enhanced vertical mixing (sections 5.3.1 and 5.4.1), and this is consistent with the increased drag and turbulent dissipation found in sinuous channels from previous studies. To link the tidal energy dissipation to the strengthened mixing and decreased stratification, we can use the increased value of C_D for the sinuous channel in the Si calculation. C_D is evaluated in the model results based on the momentum equation over a length-scale similar to the meander length (Bo and Ralston, 2020), and this calculated C_D represents the total drag on the flow including, e.g., enhanced bottom shear stress caused by secondary circulation and form drag due to flow separation across the bend. While C_D ranges between 0.002 and 0.004 in the straight channel models depending on stratification conditions, C_D is increased to $0.005 - 0.007$ in the smooth bend models and $0.009 - 0.010$ in the sharp bend models due to the channel curvature effect.

The strength of the stratification is quantified using the buoyancy frequency N (e.g., Stacey

et al., 2011), which is defined by

$$N^2 = -\frac{g}{\rho}\frac{\partial \rho}{\partial z} \approx -\frac{\beta g \Delta S}{H}, \tag{5.6}$$

where ΔS is the bottom-surface salinity difference. The Si and N^2 are calculated for the straight and sinuous models (Table 5.1) (Figure 5-12). Only ebb tide results are analyzed because we have focused on the flow patterns and mixing mechanisms of ebb tides, and the stratifying along-estuary straining represented in Si only occurs during ebb tides. $\partial S/\partial s$ is estimated using the maximum along-channel gradient during ebb near the meander region, which typically appears when the salinity intrusion retreats to the meander region. H is the channel thalweg depth. u_T is the tidal maximum and C_D is calculated around the maximum tidal velocity. In this way, the estimated Si characterizes the ratio of maximum straining and maximum mixing during the ebb tide.

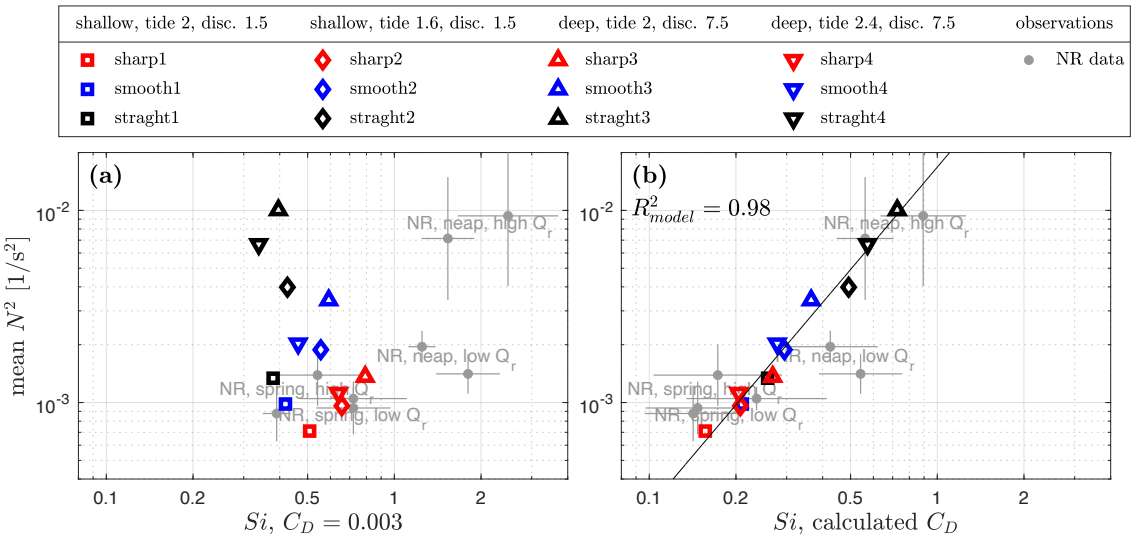

Figure 5-12: N^2 versus Si. Si is defined based on: **(a)** a constant $C_D = 0.003$ and **(b)** the calculated C_D from the momentum budget. See legends for the channel shape and tidal and discharge conditions of the twelve idealized models (Table 5.1), and the black line in **(b)** shows the linear regression for the model results. Gray dots are the observational data from the North River (NR) estuary with spring/neap tides and high/low discharge (Q_r) conditions. N^2 in 1/s^2 generally scales with ΔS in psu divided by 100.

The calculated C_D is generally $0.005 - 0.01$ in the sinuous channel models, up to three times greater than the typical value 0.003 but comparable to the observed C_D of $0.005 - 0.02$ in the North River estuary (Bo et al., 2021). In the deeper straight channel models with strong stratification, C_D is $0.0015 - 0.002$ and smaller than the typical value 0.003 because turbulence has been inhibited

by stratification. Defining Si based on a constant $C_D = 0.003$ leads to a scattered $N^2 - Si$ plot and no dependence of stratification on Si in the model results (Figure 5-12 **(a)**). Typically a Si close to 1 corresponds with stratified conditions during the ebb tide (e.g., Geyer and MacCready, 2014; Geyer et al., 2020). However, using $C_D = 0.003$ for the sharp-bend models results in Si of around 1 for periods with weak ebb stratification of N^2 of 0.001 (corresponding to $\Delta S \sim 1$) (Figure 5-12 **(a)**). This suggests that defining Si based on $C_D = 0.003$ underestimates the turbulent energy dissipation rate and strength of mixing in sinuous channels. Alternatively, for the deeper straight channel models that are strongly stratified during ebbs, using a constant $C_D = 0.003$ leads to an overestimate of mixing and an underestimate of Si (Figure 5-12 **(a)**). By contrast, N^2 has a positive dependence on Si that incorporates the calculated C_D, and the simulation results collapse onto a single line (Figure 5-12 **(b)**). The strong correlation between N^2 and Si emphasizes the importance of using an appropriate C_D in calculating Si.

For comparison, we have plotted observational data from the North River estuary collected in 2017 from April to July (Kranenburg et al., 2019; Bo et al., 2021). The tidal range varied with the spring-neap cycle between 2 m and 3 m, and the river discharge was $1 - 10$ m^3/s during the observational period. Stratification in the North River estuary varied tidally and with tidal and discharge conditions, with ΔS between 0 and 20 psu. The observations covered a representative range of spring/neap tides and high/low discharge periods. Average values of N^2 and Si and the standard deviations of two three-day windows (six tidal cycles) are shown for spring/neap tides and for high/low discharge conditions (Figure 5-12). The North River N^2 and Si are calculated for the mid-estuary region that includes several bends with the curvature ratio R/W ranging between 1 and 2 and has a typical channel depth of 5 m. The channel geometry and estuarine conditions of the idealized models are broadly similar to the observed range of the North River estuary.

Defining Si based on $C_D = 0.003$ for the North River observations leads to Si of around 1 during high/low discharge spring tide conditions and low discharge neap tide conditions that were weakly stratified (Figure 5-12 **(a)**), whereas strong stratification would typically be expected for Si values of around 1 (Geyer and MacCready, 2014; Geyer et al., 2020). Incorporating the increased C_D into Si for the North River observations leads to values of Si that make the observed stratification more consistent with results from other systems (Figure 5-12 **(b)**). Note that the correlation between N_2 and Si is similar for the observations with $C_D = 0.003$ or the calculated C_D, because the calculated C_D in the North River estuary has less variability than the idealized models with different channel morphology, and the key difference in the observational results is the general shift in

Si values. Overall, our analysis suggests that incorporating a representative C_D into the Si scaling can be an effective way to predict stratification conditions in estuarine channels with curvature.

5.5 Discussion

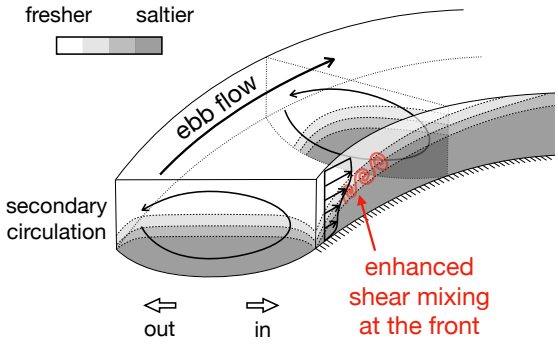

Figure 5-13: A schematic plot of flow, salinity, and frontogenesis in an estuarine bend. The stratified ebb flow goes into the bend, with secondary circulation in the cross-sections. The gray colors and dashed lines represent salinity and isohalines. An along-channel front is created in the inner bend due to the interaction between secondary circulation and the stratified flow. Enhanced shear mixing occurs at the front.

The present research finds that bend-scale bottom fronts can be generated in meanders during ebb tides (Figure 5-13). The bottom fronts result from the combined effects of curvature-induced secondary circulation, stratification, and boundary layer mixing (twisting of lateral and vertical gradients into the along-channel direction, section 5.4.2). The vertical shear of along-channel velocity is enhanced at these salinity fronts due to the along-channel baroclinic pressure gradient across the front (e.g., Geyer and Ralston, 2015; Warner et al., 2020). As a result, enhanced shear mixing occurs at bend-scale salinity fronts, providing the dominant source of mixing that leads to weaker stratification in meanders.

The analysis has focused on the shallower sharp-bend model with 2-m range tides and 1.5-m^3/s discharge, but similar curvature-induced bottom fronts and shear mixing also appear in all the other sinuous channel cases with sharp or smooth bends, shallower (4 m) or deeper (6 m) thalweg depth, and different tidal and discharge conditions. While the bend-scale bottom fronts are commonly found in these idealized sinuous estuaries, corroborating observational evidence is needed. Lateral bathymetric variability that leads to lateral variations in boundary layer mixing is important for frontogenesis, and therefore, local bathymetric features in bends that are not present in the idealized channels, e.g., points bars, scour holes, sills, and shallow shoals, may introduce additional

complexity to the frontogensis.

The present research has focused on relatively shallow tidal channels, e.g., less than 10 m, but similar mixing fronts are also expected to occur in other estuarine and coastal environments with flow curvature, e.g., deeper estuaries and around headlands. The spin-up time of secondary circulation relates to the lateral advection time scale

$$T_{adv,lat} = \frac{W}{u_r}, \tag{5.7}$$

which is around 10 minutes for the model tidal channels with width W around 50 m and lateral velocity u_r around 0.1 m/s. The time scale for bottom boundary layer mixing and generation of bottom fronts can be described by the frictional time scale (Geyer, 1993a; Chant and Wilson, 1997)

$$T_f = \frac{H}{C_f u_s}, \tag{5.8}$$

where C_f is the bottom friction coefficient, similar to C_D except that it only accounts for the bottom shear stress but not the total drag. We estimate that T_f is around 40 minutes using $H = 4$ m, $C_f = 0.003$, and $u_s = 0.5$ m/s. Both $T_{adv,lat}$ and T_f are much less than the 12-hr tidal time scale, which allows for frontogensis and the associated mixing to occur in shallow tidal channels. However, in deeper channels, taking the Tacoma Narrows of Puget Sound in Seim and Gregg (1997) as an example, $T_{adv,lat} \approx 2$ hr with $W = 1500$ m and $u_r = 0.2$ m/s, and $T_f \approx 18$ hr with $H = 100$ m, $C_f = 0.003$, and $u_s = 0.5$ m/s. T_f can be larger than the tidal time scale for deep systems, potentially limiting the growth of bottom fronts and strength of shear mixing. Therefore, overturning mixing may play a more important role as in Seim and Gregg (1997). As a comparison, the ratio of overturning mixing to shear mixing increases by a factor of 1.5 in our deeper sharp-bend model compared to the shallower sharp-bend model, though it remains small overall. Internal wave generation and breaking from flow around topographic features may also contribute to mixing in deep estuarine channels, as was observed in curved tidal flows around headlands by Edwards et al. (2004).

The mixing and frontogenesis have been investigated for ebb tides, when the alternating normal and reversed lateral circulations occur in meanders. Bend-scale bottom fronts are also expected to be found during flood tides that have similar lateral circulation patters (e.g., Seim and Gregg, 1997; Chant and Wilson, 1997). However, more complex secondary circulation can develop during flood tides as a result of differential advection due to the channel curvature effect (Lacy and Monismith,

2001; Nidzieko et al., 2009; Pein et al., 2018; Kranenburg et al., 2019). Multiple circulation layers in the vertical and multiple cells in the lateral can occur, leading to salinity fronts with more complex structures. The locations and mechanisms of enhanced mixing during flood tides, as well as frontogenesis associated with twisting by lateral and vertical flows, thus require more detailed investigation.

Moreover, flow separation can occur during flood tide behind the bend apex with eddies generated in the inner bend and main flow separated toward the outer bend (Bo and Ralston, 2020). The strong lateral shear across the boundary of the separation zone can further enhance the differential advection, and thus potentially affects secondary circulation, frontogenesis, and mixing. The increased C_D in the Si scaling (section 5.4.3) can include both bottom friction enhancement associated with secondary circulation and form drag due to flow separation (e.g., Chang, 1984; Bo et al., 2021), but the respective influences of enhanced bottom stress and form drag on mixing are not clear. The linkage between drag increase and mixing enhancement, especially for form drag, still merits further investigation.

5.6 Conclusion

Stratification is decreased in the idealized sinuous estuaries compared to straight channel estuaries. Analysis of the vertical salinity variance budget reveals that channel curvature can affect stratification through generation of alternating signs of lateral straining and through local intensification of mixing. The mixing in meanders is dominated by shear mixing at bend-scale bottom fronts rather than overturning mixing. These bottom fronts are generated as a product of interaction between the secondary circulation and stratification, and also depend on lateral bathymetric variations. Finally, an adjusted Simpson number that incorporates the increased drag coefficient with channel curvature can be used to parameterize the decreased stratification and enhanced vertical mixing associated with meanders.

Chapter 6

Tidal intrusion fronts, surface convergence, and mixing in an estuary with complex topography

Observations from a tidal estuary show that tidal intrusion fronts occur regularly during flood tides near constrictions and bends. A realistic model is used to study the generation of these fronts and their influence on stratification and mixing in the estuary. At the constriction, flow separation occurs on both sides of the jet flow downstream of the narrow opening, leading to sharp lateral salinity gradients and baroclinic secondary circulation. A tidal intrusion front, with a V-shaped convergence zone on the surface, is generated by the interaction between secondary circulation and the laterally sheared streamwise flow. Stratification is created at the front due to the straining of lateral salinity gradients by secondary circulation. Though stratification is expected to suppress turbulence, strong turbulent mixing is found near the surface front. The occurrence of mixing is attributed to the enhanced vertical shear due to both baroclinicity and the twisting of lateral shear into vertical shear by secondary circulation. In bends, the mechanism of frontogenesis and enhanced mixing is similar to that at the constriction. Flow separation occurs along the inner bank, resulting in lateral salinity gradients and secondary circulation. In contrast to the V-shaped front near the constriction, an oblique linear surface convergence front occurs in the bend, which can be thought of as a one-sided tidal intrusion front. Moreover, curvature in bends adds to the secondary circulation, enhancing vertical shear and increasing mixing. Overall in the estuary, the near-surface mixing associated with tidal intrusion fronts during flood tides is similar in magnitude to bottom boundary layer mixing

that occurs primarily during ebbs.

6.1 Introduction

Surface fronts are ubiquitous in estuaries (e.g., Simpson and Turrell, 1986; Largier, 1992; O'Donnell, 1993). As regions where two distinct water masses interact and generate sharp density gradients (Largier, 1993), estuarine surface fronts usually have strong horizontal convergence due to baroclinicity resulting from the frontal density gradient (Valle-Levinson et al., 2000; Giddings et al., 2012; Collignon and Stacey, 2012). The convergence means these surface features are typically identifiable by accumulated foam and debris, in addition to sharp color discontinuities that are often visible (Brown et al., 1991; Largier, 1992). Correspondingly, fronts have important implications for transport and aggregation of pollutants, phytoplankton, and larvae (Tyler et al., 1982; Brown et al., 1991; Wang et al., 2022).

Examples of surface fronts in estuaries include tidal intrusion fronts (Simpson and Nunes, 1981), axial convergence fronts (Nunes and Simpson, 1985), and plume fronts (Garvine, 1974). These categories are not mutually independent, e.g., tidal intrusion fronts, which appear as denser water intrudes into a basin of buoyant water, are dynamically similar to plume fronts that form when buoyant water discharges into a region with denser water (O'Donnell, 1993). Both tidal intrusion fronts and axial convergence fronts result from the advection of longitudinal density gradients by tidal currents (Simpson and Turrell, 1986), and axial convergence fronts have been observed to originate at the apex of tidal intrusion fronts (Largier, 1992). Moreover, axial convergence fronts can produce buoyancy-driven flow structures that propagate away from the generation region as plume fronts (O'Donnell, 1993).

This research focuses on tidal intrusion fronts that form as seawater is advected into estuaries by flood tide currents. Tidal intrusion fronts typically exhibit a V-shaped configuration, with horizontal re-circulation zones on both sides of the front and intense surface convergence along the centerline (Simpson and Nunes, 1981; Largier, 1992). Nevertheless, the mechanisms of frontogenesis and mixing investigated here also apply to other surface fronts with different morphologies but similar dynamics, as will be discussed later.

Topographic complexity, e.g., channel constrictions, shallow shoals, confluences, headlands, and meanders, are often important sites for estuarine frontogenesis (e.g., Largier, 1992; Giddings et al., 2012; Geyer and Ralston, 2015). Complex topographic features can generate 3-d flow struc-

tures that interact with the salinity field, and fronts are created as secondary circulation sharpens salinity gradients through normal or shear straining (McWilliams, 2021). Constrictions and channel-shoal bathymetry can lead to strong lateral shear in tidal flows and create lateral salinity gradients through differential advection (Nunes and Simpson, 1985; Lacy et al., 2003; Collignon and Stacey, 2012; Li et al., 2014). The associated lateral baroclinic forcing drives secondary circulation in the channel cross-section, resulting in lateral convergence near the surface, increasing lateral salinity gradients, and contributing to frontogenesis. In addition to differential advection, lateral salinity fronts may result from lateral trapping by side channels or mudflats (Valle-Levinson et al., 2000; Giddings et al., 2012; Garcia et al., 2021), with baroclinic dynamics and secondary circulation similar to differential advection. In channel bends, curvature can drive secondary circulation through the centrifugal acceleration in the lateral momentum balance (Thomson, 1877; Kalkwijk and Booij, 1986; Geyer, 1993b). The development of secondary circulation, as well as its interaction with the salinity field and influence on frontogenesis, thus depends on both centrifugal acceleration and baroclinic forcing in sinuous estuaries (Lacy and Monismith, 2001; Nidzieko et al., 2009; Becherer et al., 2015; Kranenburg et al., 2019).

In addition to its influence on frontogenesis, secondary circulation associated with topographic complexity plays crucial roles in affecting stratification, vertical mixing, and horizontal dispersion. For example, secondary circulation and lateral straining of salinity gradients can increase or decrease stratification (Lacy et al., 2003; Giddings et al., 2012; Scully and Geyer, 2012; Becherer et al., 2015; Bo and Ralston, 2022). In a shallow estuary in the Salish Sea, Giddings et al. (2012) observed that a surface front and the associated secondary circulation led to enhanced stratification in late flood tide, thus suppressing vertical turbulent mixing. In contrast, Collignon and Stacey (2013) reported that secondary circulation was responsible for turbulence generation in late ebb tides at the channel-shoal interface in South San Francisco Bay. Similarly, in the James River, Huguenard et al. (2015) found that near-surface turbulence and mixing was related to secondary circulation during ebb tides. Secondary circulation associated with topographic complexity, e.g., channel-shoal systems and meanders, can also affect the subtidal structure of salinity and longitudinal velocity fields, thereby impacting the landward salt flux (e.g., Lerczak and Geyer, 2004; Ralston and Stacey, 2005a; Becherer et al., 2015; Geyer et al., 2020)

In this research, we conduct a numerical modeling study of the North River estuary (MA, USA), an intermittently stratified, shallow tidal channel with complex topography (Kranenburg et al., 2019; Bo et al., 2021; Garcia et al., 2021). Surface fronts have been regularly observed during flood tides at

multiple locations along the estuary, and fronts are particularly associated with topographic features like channel constrictions and bends. We investigate the frontal structures and associated secondary circulation at two representative locations, i.e., constrictions and bends. The influences of fronts and secondary circulation on stratification and turbulent mixing in the estuary are also examined. In section 6.2, we introduce the study site, model setup, and the theoretical framework for secondary circulation, stratification, and mixing. Section 6.3 presents the results and analysis, and we discuss their implications in section 6.4. Section 6.5 is a conclusion.

6.2 Methods

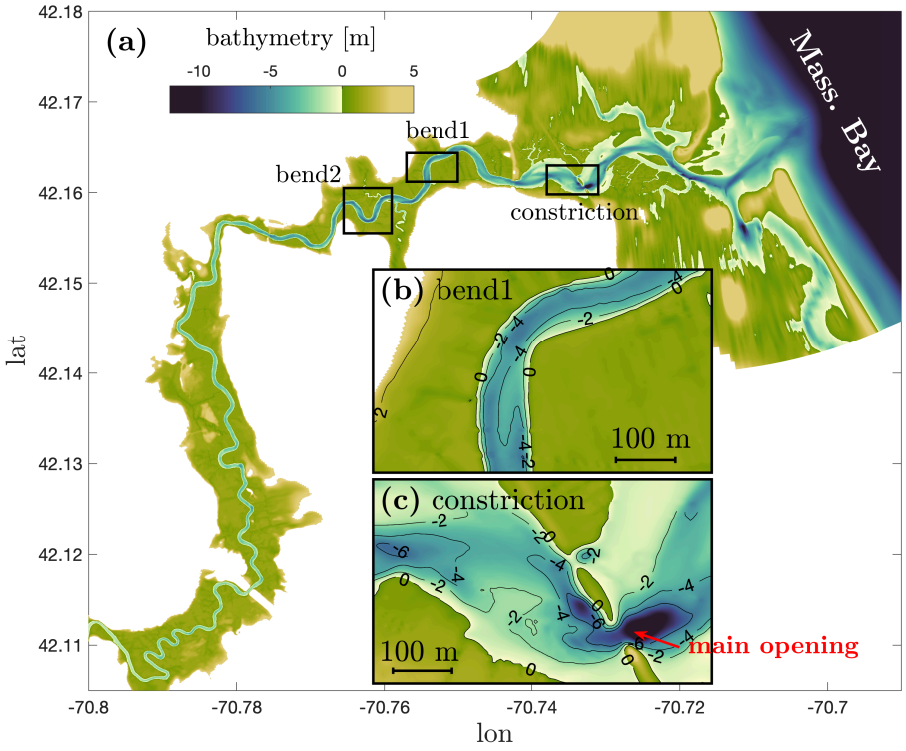

Figure 6-1: **(a)**: North River estuary model bathymetry. The constriction is located at around 2 km into the estuary. Bend1 is at around 4 km into the estuary, and this bend is selected for detailed model analysis. Bend2 is at around 5.5 km into the estuary, where drone imagery was obtained. **(b)**: Bathymetry of the bend region (bend1). **(c)**: Bathymetry of the constriction region.

6.2.1 Study site

The North River estuary (MA, USA) is a sinuous tidal channel that connects to Massachusetts Bay (Figure 6-1 **(a)**). The typical channel depth is around 5 m and width is $50 - 100$ m. The tides in the

estuary are dominantly semi-diurnal, with a tidal range between 2 m and 4 m (Kranenburg et al., 2019; Bo et al., 2021). The maximum tidal velocity in the estuary varies between 0.5 m/s and 1 m/s with the neap-spring cycle. The freshwater discharge is usually less than 10 m^3/s, corresponding to a mean velocity of < 0.05 m/s, but can be up to 30 m^3/s due to rainfall events. The salinity intrusion distance typically varies from around 8 km to 14 km (Garcia et al., 2021).

Two examples of characteristic topographic features are a channel constriction at 2 km into the estuary (Figure 6-1 **(c)**) and a channel bend at 4 km (Figure 6-1 **(b)**). In the constriction region, constructed embankments from an abandoned railroad impose lateral topographic constraints on the channel. The main opening is on the south side with a width of 40 m and depth of 10 m (Figure 6-1 **(c)**). A smaller, secondary opening is on the north side with a width of less than 10 m and depth less than 1 m. Landward of the constriction, the channel expands to $100 - 200$ m wide, and a shallow shoal in the southern part of the channel has a depth of ~ 2 m. The channel curvature is mild near the constriction, with a radius of curvature of around 300 m. In this study, we focus on the main opening that conveys most of the tidal exchange.

In the bend at around 4 km, the channel undergoes a nearly 90-degree turn (Figure 6-1 **(b)**) with a radius of curvature of around 100 m. The channel width is $60 - 80$ m and relatively uniform through the bend, and the depth is around 5 m. Other bends in the mid- and lower estuary similarly have widths of $50 - 100$ m and radii of curvature of $50 - 300$ m. This corresponds to curvature ratios (bend sharpness) of around $1 - 5$, which is in the typical range for natural river and tidal meanders (Leopold and Wolman, 1960; Marani et al., 2002). The bend at 4 km is selected as a representative example, but similar surface fronts and frontal dynamics occur in many other bends in the North River estuary.

6.2.2 Numerical simulations

The Regional Ocean Modeling System (ROMS) (Shchepetkin and McWilliams, 2005; Haidvogel et al., 2008; Warner et al., 2008, 2010) is used to simulate the North River estuary (Figure 6-1 **(a)**). An orthogonal curvilinear grid is built that extends from Massachusetts Bay to around 18 km into the estuary. The finest horizontal resolution is 3 m in the channel (around $10 - 30$ grid cells across the channel) and grid spacing increases offshore and in the marsh away from the channel. A terrain-following coordinate with 16 uniformly distributed layers is used in the vertical direction. The k-ϵ closure of the generic length-scale (GLS) turbulence closure scheme is used for the vertical mixing (Umlauf and Burchard, 2003; Warner et al., 2005). The bottom roughness z_0 is a uniform of 0.005 m

in the domain, except that z_0 is locally increased to 0.2 m in a section with large rocks on the bed located around 7 km from the mouth to better represent the decrease in tidal amplitude in that region. A third-order upwind advection scheme is used for horizontal advection, and the horizontal mixing coefficient is 0.01 m^2/s.

The simulations cover a one-month period from early October to early November in 2021. Tidal fluctuations on the ocean boundaries were extracted from the ADCIRC database (Mukai et al., 2002), and subtidal fluctuations were obtained from the low-pass filtered water surface elevation record from the National Oceanic and Atmospheric Administration (NOAA) station at Boston (#8443970). River discharge was input as a freshwater source on the western boundary based on data from the U.S. Geological Survey (USGS) gage at Hanover (#01105730) multiplied by 2.3 to account for freshwater inputs below the gage. Wind forcing was not included in the model.

The model setup is essentially the same as that described in Bo et al. (2023) to study the hydrodynamic drag in the North River. The model was evaluated in Bo et al. (2023) by comparing it with the measured tidal water levels, velocities, and salinity from long-term moorings and shipboard surveys in 2017. In this research, we focus on simulations of a one-month period in 2021, and the model results are compared with observations in 2021 (described in the following section) for a skill assessment (Murphy, 1988). The skill scores are higher than 0.95 for water level, in the range of 0.9 to 0.95 for velocity, and around 0.8 for salinity (Figure 6-2).

6.2.3 Field observations

Field measurements were made in the North River estuary from September to November 2021. Four long-term moorings were deployed at around 0 km, 2 km (near the constriction), 5 km, and 8 km into the estuary. At each mooring, pressure and salinity time series were measured by conductivity-temperature-depth (CTD) sensors mounted near the surface and the bed. Velocity profile data were collected at each of the three seaward mooring sites by an upward-looking Aquadopp profiler mounted on the bed. The long-term measurements of water level, salinity, and velocity were used for model assessment. In addition, aerial drone imagery of surface fronts was obtained at multiple topographic features, including the constriction and several bends, by a DJI Phantom 4 drone. The drone imagery was used to characterize the structures of surface fronts.

6.2.4 Theoretical framework

To develop the theoretical framework for analyzing tidal intrusion fronts, stratification, and mixing, we introduce the momentum and vorticity equations for secondary circulation with curvature. We also present the salinity variance budget to quantify the stratification, straining, and mixing associated with tidal intrusion fronts.

Momentum equations

The streamwise and lateral momentum equations for flow with curvature are

$$\frac{\mathrm{D}u}{\mathrm{D}t} = -g\frac{\partial \eta}{\partial x} - \beta g \int_z^\eta \frac{\partial s}{\partial x}\mathrm{d}z + \mathrm{sgn}\,(R)\,\frac{uv}{R} + \frac{\partial}{\partial z}K_v\frac{\partial u}{\partial z}, \tag{6.1a}$$

$$\frac{\mathrm{D}v}{\mathrm{D}t} = -g\frac{\partial \eta}{\partial y} - \beta g \int_z^\eta \frac{\partial s}{\partial y}\mathrm{d}z - \mathrm{sgn}\,(R)\,\frac{u^2}{R} + \frac{\partial}{\partial z}K_v\frac{\partial v}{\partial z}, \tag{6.1b}$$

where

$$\frac{\mathrm{D}}{\mathrm{D}t} = \frac{\partial}{\partial t} + u\frac{\partial}{\partial x} + v\frac{\partial}{\partial y} + w\frac{\partial}{\partial z}. \tag{6.2}$$

The local coordinates generally follow the channel orientation, with x, y, z being the streamwise, lateral, and vertical directions, and u, v, w being the corresponding velocity components. $+x$ is generally eastward (ebb direction) in the study area of the North River, and $+y$ is generally Northward (90-degree counterclockwise rotation of the ebb direction). η is water level and s is salinity. β is the haline contraction coefficient and K_v is the vertical eddy viscosity. R is the radius of curvature; $\mathrm{sgn}\,(R) > 0$ when the $+y$ direction is toward the center of the bend, and vice versa. Note that here $\frac{\mathrm{D}}{\mathrm{D}t}$ is not the material derivative in curvilinear coordinates, but we use this expression for simplicity and put the non-inertial terms (curvature forcing terms) on the right side for the convenience of the following analysis. Coriolis has been neglected as it is usually not important in small estuaries like the North River.

To study the terms responsible for secondary circulation, we subtract the depth-averaged (6.1b) from (6.1b) (e.g., Geyer, 1993b; Chant and Wilson, 1997; Nidzieko et al., 2009) and write

$$\underbrace{\frac{\partial v}{\partial t}}_{\text{unsteady}} + \underbrace{\left(u\frac{\partial v}{\partial x} - \overline{u\frac{\partial v}{\partial x}}\right)}_{\text{advection}} = \underbrace{-\beta g\left(\int_z^\eta \frac{\partial s}{\partial y}\mathrm{d}z - \overline{\int_z^\eta \frac{\partial s}{\partial y}\mathrm{d}z}\right)}_{\text{BCPG}} \underbrace{-\mathrm{sgn}\,(R)\,\frac{u^2 - \overline{u^2}}{R}}_{\text{CFA}} + \underbrace{\left(\frac{\partial}{\partial z}K_v\frac{\partial v}{\partial z} + \frac{\tau_{b,y}}{\rho H}\right)}_{\text{friction}}, \tag{6.3}$$

with an overbar representing the depth average, and $\overline{v} = 0$ by definition. The lateral and vertical

advection terms have been neglected. $\tau_{b,y} = K_v(\partial v/\partial z)\big|_{bed}$ is the lateral component of the bed shear stress, and surface stress is zero in the model. H is water depth and ρ is density. The first term on the left side is the unsteady term (time rate of change). The second term represents streamwise advection, i.e., the downstream adjustment of secondary circulation (e.g., Nidzieko et al., 2009). The first term on the right side is the baroclinic pressure gradient force (BCPG), and the second term is the centrifugal acceleration (CFA), and the third term is friction.

Vorticity equations

In addition to the momentum balance, we use the streamwise component of vorticity ω_x to quantify secondary circulation following Becherer et al. (2015). The vertical shear of lateral velocity usually dominates over the lateral shear of vertical velocity in determining ω_x, since $v \gg w$ and $\Delta y \gg \Delta z$. In a similar way, we can identify the lateral component of vorticity ω_y as the vertical shear of streamwise velocity. Therefore, we write

$$\omega_x = \frac{\partial w}{\partial y} - \frac{\partial v}{\partial z} \approx -\frac{\partial v}{\partial z}; \tag{6.4a}$$

$$\omega_y = \frac{\partial u}{\partial z} - \frac{\partial w}{\partial x} \approx \frac{\partial u}{\partial z}. \tag{6.4b}$$

Taking the vertical derivative of (6.1), substituting in (6.4), and rearranging

$$\frac{\mathrm{D}\omega_x}{\mathrm{D}t} = -\beta g \frac{\partial s}{\partial y} + \mathrm{sgn}\,(R)\,\frac{2}{R} u\omega_y + \mathcal{R}_{\omega x}; \tag{6.5a}$$

$$\frac{\mathrm{D}\omega_y}{\mathrm{D}t} = \frac{\partial u}{\partial y}\omega_x + \beta g \frac{\partial s}{\partial x} - \mathrm{sgn}\,(R)\,\frac{1}{R} u\omega_x + \mathcal{R}_{\omega y}. \tag{6.5b}$$

The transport equation for ω_x (6.5a) is essentially a representation of the lateral momentum balance (6.3). While the momentum balance straightforwardly shows the terms responsible for lateral flows, the vorticity approach can provide a more consistent framework for understanding the generation and interaction of vorticity components (Becherer et al., 2015), and vorticity directly links to the vertical shear that affects mixing processes. Note that in (6.5), we have only kept the vorticity twisting, baroclinicity, and curvature terms that relate to secondary circulation (e.g., Nidzieko et al., 2009; Becherer et al., 2015; Kranenburg et al., 2019), and we collect the other terms in $\mathcal{R}_{\omega x}$ and $\mathcal{R}_{\omega y}$, e.g., turbulent viscosity (friction) and velocity convergence or divergence.

Vertical salinity variance budget

To assess the overall influence of secondary circulation and tidal intrusion fronts on stratification we use the vertical salinity variance budget. The depth-integrated vertical salinity variance budget (Burchard and Rennau, 2008; Li et al., 2018) is

$$\underbrace{\frac{\partial}{\partial t}\int (s_v')^2 \mathrm{d}z}_{\text{unsteady}} = \underbrace{-\nabla_h \cdot \int \mathbf{u}(s_v')^2 \mathrm{d}z}_{\text{advection}} \underbrace{- \int 2\mathbf{u}_v' s_v' \cdot \nabla_h \overline{S} \mathrm{d}z}_{\text{straining}} \underbrace{- \int 2K_s \left(\frac{\partial s}{\partial z}\right)^2 \mathrm{d}z}_{\text{turb. mixing}} \underbrace{- \int \mathcal{M}_{num} \mathrm{d}z}_{\text{num. mixing}} . \tag{6.6}$$

$\overline{s}$ is the depth-averaged salinity, and s_v' is the deviation from the depth average. $(s_v')^2$ is the vertical salinity variance that corresponds with stratification in the water column. ∇_h is the horizontal gradient operator. $\mathbf{u} = (u, v)$ is the horizontal velocity vector, and $\mathbf{u}_v'$ represents the vertical deviations of horizontal velocity. K_s is the eddy diffusivity for vertical salinity mixing. The left-side term represents the temporal change of the vertical salinity variance. The first term on the right side represents advection, and the second term represents straining. The third term is turbulent mixing that irreversibly dissipates the vertical variance. The fourth term is the additional numerical mixing $\mathcal{M}_{num}$ that arises from discretization errors of the tracer advection scheme in the model. $\mathcal{M}_{num}$ is calculated as the difference between the advected square of the tracer and the square of advected tracer (e.g., Burchard and Rennau, 2008; Ralston et al., 2017; Kalra et al., 2019).

6.3 Results and analysis

6.3.1 Estuarine conditions

During the observation period of October and November 2021, the tidal range in the North River estuary was between 2 m and 4 m, with a tidal velocity amplitude of $0.4 - 0.8$ m/s (Figure 6-2). The tides in this system are dominated by the semi-diurnal M2 tidal constituent, with stronger and weaker spring-neap tides each lunar month due to the semi-diurnal S2 and N2 tidal constituents. During the study period, stronger spring tides occurred in early October and early November. A storm event in late October caused the subtidal water level to increase by 0.7 m due during the weak neap tide and increased the freshwater discharge from background levels of $0 - 5$ m^3/s to a peak of 30 m^3/s .

The salinity and stratification varied at tidal time scales at the mooring locations. The tidal maximum stratification (bottom-surface salinity difference) was typically $5 - 10$ psu, and was up to

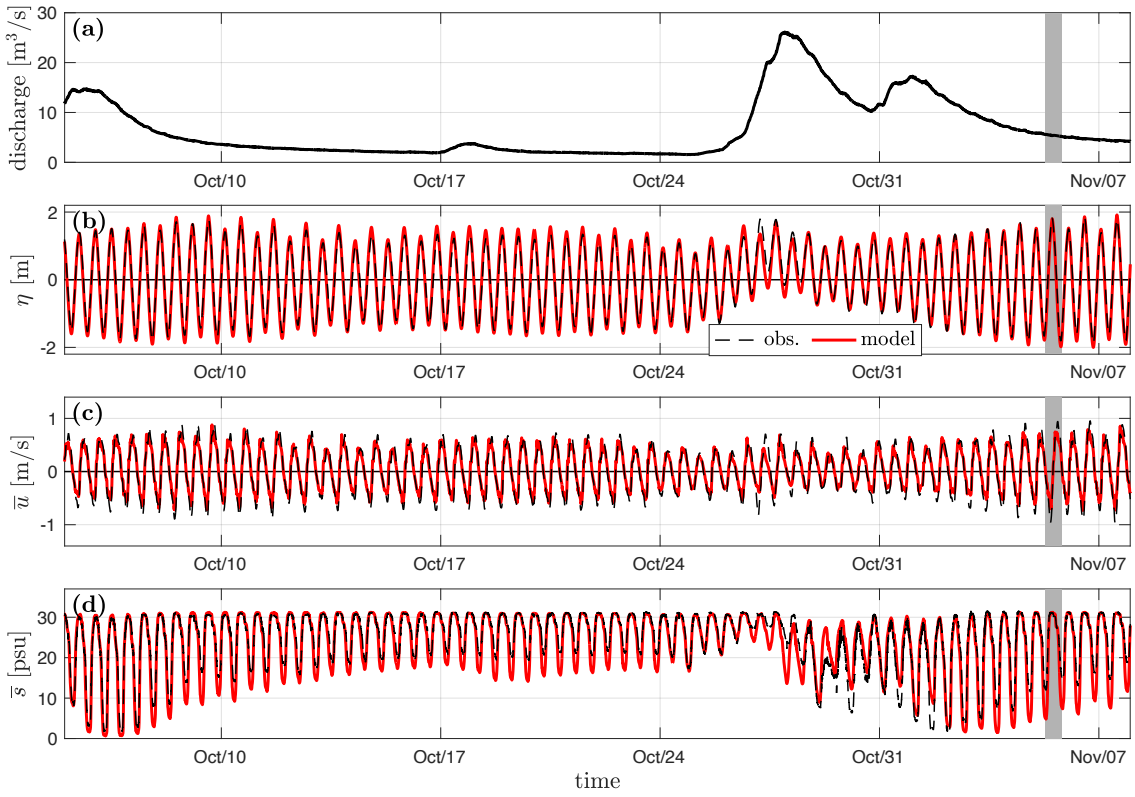

Figure 6-2: **(a)**: North River discharge in October and November 2021. **(b)** - **(d)**: the modeled estuarine conditions compared with observations at the mooring site near the constriction (around 2 km into the estuary). Red lines represent model results and dashed black lines represent observations. **(b)**: Water level η. **(c)**: Depth-averaged velocity $\overline{u}$. Negative u means landward velocity (flood direction). **(d)**: Depth-averaged salinity $\overline{s}$. Gray bands show the tidal cycle selected for detailed analysis.

20 psu during the high discharge event.

6.3.2 Drone imagery of surface fronts

In this section, we present drone imagery of surface fronts at two locations during spring flood tides in October and November, 2021. These observational results are primarily explained at a descriptive level to demonstrate the motivation for this study, and a more thorough analysis is conducted in the numerical model study in the following sections.

A V-shaped tidal intrusion front occurred downstream (landward) of the constriction at around 2 km into the estuary, as is shown in the drone imagery in Figure 6-3 **(a)**. The tidal flow through the constriction intruded into the ambient, lower salinity water downstream of the constriction, leading to a V-shaped surface convergence zone with white foam accumulated on the surface. Higher veloc-

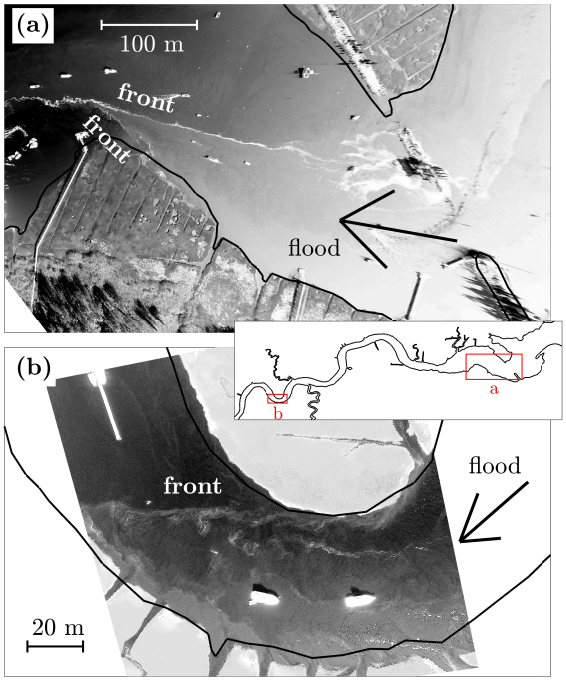

Figure 6-3: Drone imagery during spring flood tides. **(a)**: The constriction region at around 2 km into the estuary (at 11 am on Oct 7, 2021). **(b)**: A bend at around 5.5 km into the estuary (at 12 pm on Oct 8, 2021). Locations of the surveyed constriction and bend are shown by red rectangles on the map.

ities inside the V-shape brought higher salinity water landward through differential advection and created sharp salinity gradients across the V-shaped front.

Another example of surface fronts is shown in the drone imagery from a bend at around 5.5 km into the estuary (Figure 6-3 **(b)**). Flow separation occurred in the bend as a result of the curvature effect (Bo et al., 2021), with a low-velocity separation zone along the inner bank and higher stream-wise velocities shifted toward the outer bend. Correspondingly, salinity was greater in the outer part of the bend as a result of differential advection. This lateral salinity gradient consequently formed an oblique surface front that can accumulate foam and debris, as seen in the drone image (Figure 6-3 **(b)**).

Detailed analysis of frontal dynamics will be presented in the following model investigation. Note that here the bend with observations is located around 5.5 km into the estuary, whereas the bend selected for model analysis is at around 4 km (Figure 6-1 **(b)**). We have selected the bend at 4 km for model analysis because it exhibits stronger surface convergence and mixing than found in other bends, but the frontal processes are broadly similar in the different bends.

6.3.3 Surface fronts and secondary circulation

In this section, we analyze the tidal intrusion fronts and associated secondary circulation at a constriction and a bend in the numerical model. At both locations, flow separation occurs and creates lateral salinity gradients through differential advection. The lateral salinity gradients thus lead to secondary circulation in the cross-section, which interacts with the salinity field and contributes to frontogenesis. The following analysis focuses on a stronger spring tide on November 5 as a representative of spring tide conditions when the surface fronts are most noticeable in the observations and in the model results.

The constriction

During flood tides, the tidal current is accelerated to over 1 m/s in the main opening as a result of the lateral constriction. Flow separation occurs on the landward side of the constriction, with strong lateral shear across the separation zones (Figure 6-4). The high-velocity jet advects higher salinity water to landward of the main opening, while lower salinity water remains in the adjacent low-velocity zone. This differential advection creates sharp horizontal salinity gradients along with the strong lateral shear. Moreover, surface convergence occurs due to baroclinicity resulting from the horizontal salinity gradient, with two V-shaped surface fronts formed downstream of the constriction (F1 and F2 in Figure 6-4). The smaller V-shaped surface convergence front (F1) is attached to the narrow opening and the larger V-shaped front (F2) is over the shallow shoal downstream of the opening. The frontal dynamics relates to the generation of secondary circulation in cross-sections, as will be explained in detail below.

In the cross-section at the constriction (XSC1 in Figure 6-5), the jet flow brings higher salinity to the central channel, with a pair of lateral fronts on both sides of the jet flow. The salinity gradients across these lateral fronts lead to a pair of counter-rotating secondary circulation cells. The circulation cell on the north side has southward velocity near the surface and northward velocity near the bed and the cell on the south side has an opposite sense of circulation. As a result, a surface convergence zone occurs near the center of the cross-section, which corresponds to the V-shaped front F1 near the constriction in the map view (Figure 6-4).

We examine the lateral momentum balance (6.3) in XSC1 to investigate the dynamics of the secondary circulation pattern (Figure 6-7). The baroclinic pressure gradient (BCPG) associated with the lateral density variability is the dominant term in driving the pair of counter-rotating circu-

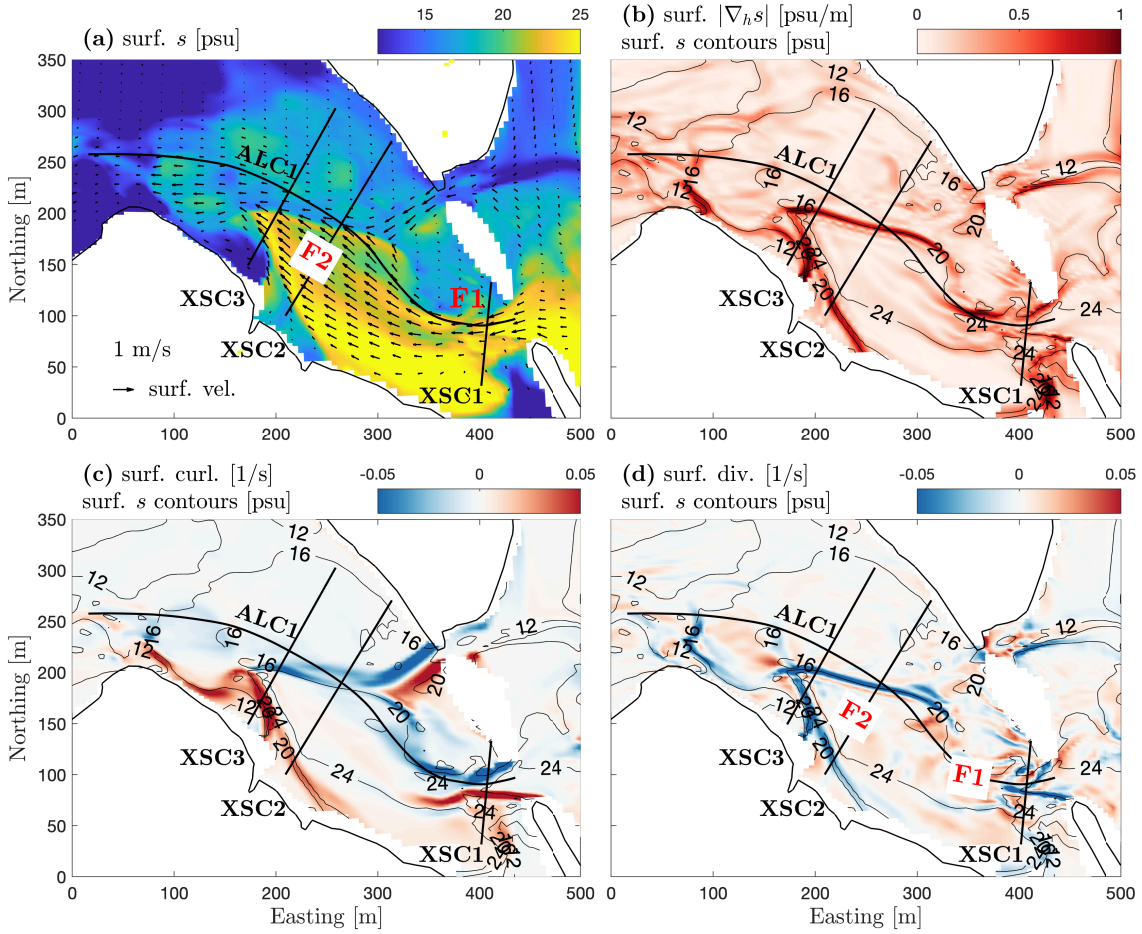

Figure 6-4: Flood tide flow field in the constriction region. **(a)**: Surface salinity. Arrows show surface velocity. **(b)**: Horizontal gradients of surface salinity, with contours of surface salinity. **(c)**: Curl of surface velocity (vorticity). **(d)**: Divergence of surface velocity, and blue colors represent surface convergence. Black lines show locations of the cross-sections XSC1-3 and the along-channel section ALC1 taken for detailed analysis. The red "F1" and "F2" in **(a)** and **(d)** mark the two V-shaped surface convergence fronts near the constriction.

lation cells. The centrifugal acceleration (CFA) is less important since the curvature effect is relatively weak here. The frictional effect is weak in the channel center and increases on the shallower south side of the channel. Instead of friction, the BCPG is mainly balanced by the advection term (downstream adjustment of secondary circulation) in this strongly advective system, consistent with Nidzieko et al. (2009) and Kranenburg et al. (2019). Given the dominance of BCPG in the lateral momentum balance, the secondary circulation is thus called BCPG-driven secondary circulation.

Farther landward, the jet flow expands as it encounters the shallower region downstream from the constriction (Figure 6-1 and Figure 6-4), and the two BCPG-driven secondary circulation cells and the corresponding surface convergence zones are separated farther apart (XSC2 in Figure 6-9).

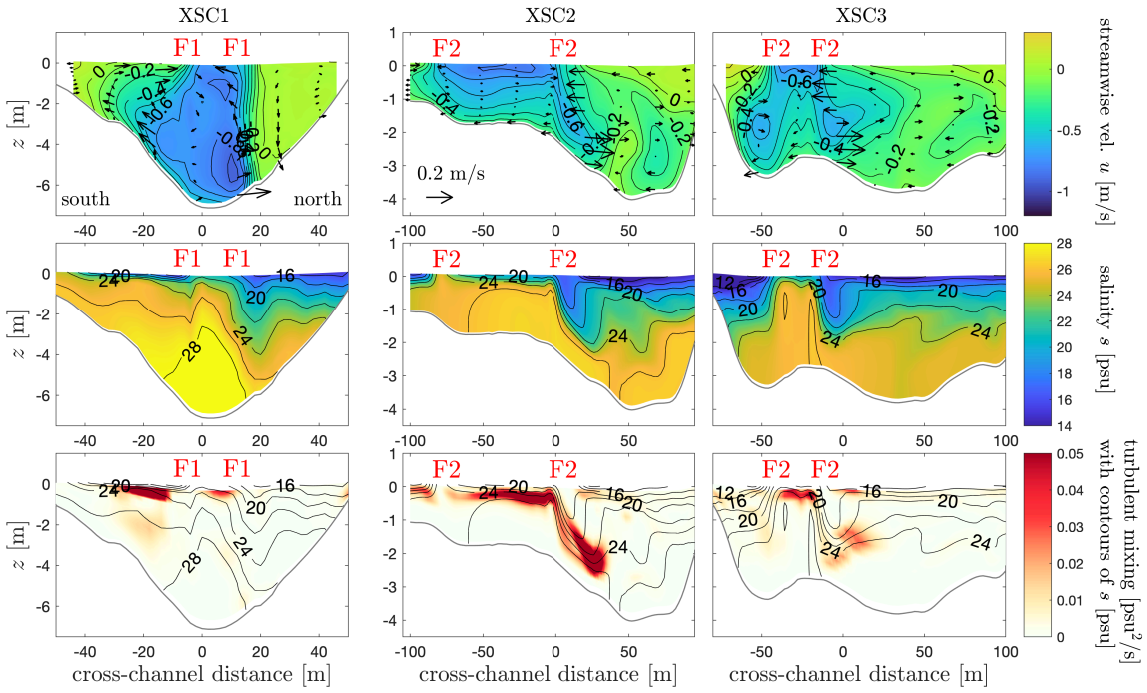

Figure 6-5: Streamwise velocity u, salinity s, and mixing in cross-sections XSC1, XSC2, and XSC3. Locations of cross-sections are shown in the map views in Figure 6-4. Negative u means landward velocity (flood direction). Arrows show secondary circulation. Locations of the V-shaped surface convergence zones are marked by the red "F1" and "F2". The southern bank is on the left side.

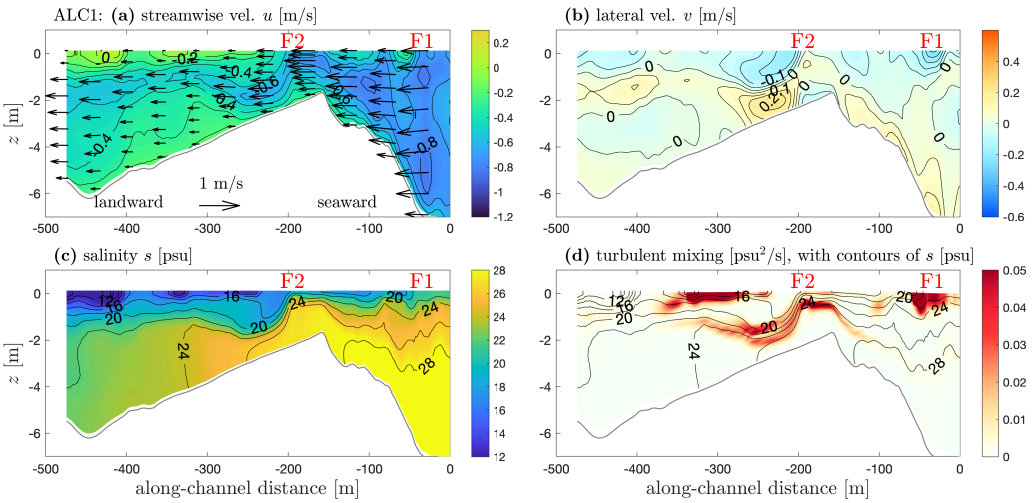

Figure 6-6: The along-channel section ALC1 (location shown in Figure 6-4). **(a)**: Streamwise velocity u. **(b)**: Lateral velocity v. Positive v is northward. **(c)**: Salinity s. **(d)**: Mixing, with contours of s. The red "F1" and "F2" show the locations of the V-shaped surface convergence zones. Negative distance means landward direction, and the constriction opening is at 0 m.

Secondary circulation redistributes streamwise velocity in the cross-section. Taking the lateral front in the northern part of XSC2 as an example, the laterally sheared streamwise flow, with weaker

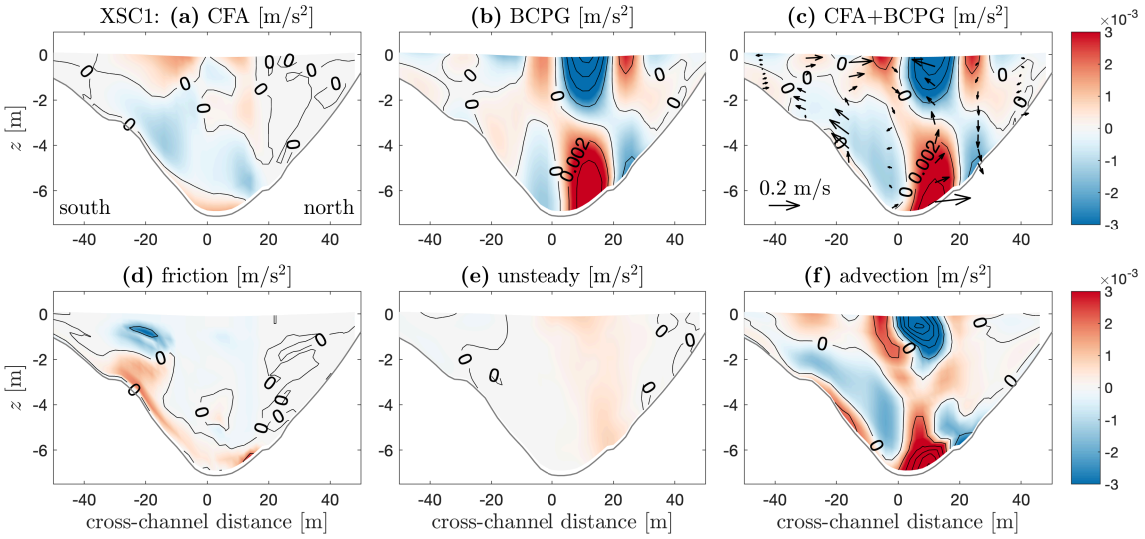

Figure 6-7: Terms in the lateral momentum balance (6.3) in the cross-section XSC1.

velocity on the north side, is twisted by the clockwise secondary circulation. This downward and northward intrusion of high streamwise momentum leads to a reversal in vertical shear, with lower velocity in the upper water column. The BCPG-driven secondary circulation also laterally transports salinity near the front, with the near-bottom lateral flow advecting saltier water northward and the near-surface flow advecting fresher water southward. As a result, lateral salinity gradients initially created by differential advection are converted to vertical gradients by the secondary circulation, creating stratification through this lateral straining.

In addition to the creation of stratification, mixing that acts to destroy stratification also occurs at the north-side front in XSC2 (Figure 6-5). Regions with enhanced turbulent mixing span from the surface to the middle water column, suggesting that the front may also provide a source of turbulence generation. The south part of XSC2 is only $1-2$ m deep, and the greater influence of the bottom boundary leads to different mechanisms of mixing, which will be discussed separately. The front on the north side is in deeper water and is more representative of other tidal intrusion fronts in the system.

The pair of lateral surface fronts converge near the center of the jet flow (e.g., comparing XSC2 and XSC3). As a result, the surface convergence zones are oblique to the streamwise current and display a second, larger V-shape of a tidal intrusion front (Simpson and Nunes, 1981; Largier, 1992), as is shown in the map view (front F2 in Figure 6-4). The composite Froude number G for two-layer flow (e.g., Armi and Farmer, 1986; Geyer and Ralston, 2015) is examined to understand the oblique

angle of the front.

$$G^2 = \frac{u_1^2}{g' H_1} + \frac{u_2^2}{g' H_2}, \tag{6.7}$$

where u_1 and u_2 are the average velocities of the upper and lower layers, and H_1 and H_2 are the layer thickness. $g' = g(\Delta\rho/\bar{\rho})$ is the reduced gravity based on the density difference between the two layers. The composite Froude number $G \approx 3$ at the front F2, indicating a supercritical condition. Nevertheless, the front is relatively stationary during several hours in the flood tide, rather than moving landward with flood tidal currents. A stationary front can occur under a supercritical condition when it is oblique to the main flow direction, with a critical condition satisfied in the direction normal to the front (Largier, 1993; MacDonald and Geyer, 2005; Geyer and Ralston, 2015). In this case, the front F2 has an oblique angle $\phi \approx 20°$, so that $G \sin\phi$ is close to 1, the critical condition.

In an along-channel section, the surface front is located where the streamwise flow of higher salinity water subducts (front F2 in Figure 6-6). The surface convergence at the front mainly results from the lateral circulation, but the streamwise flow that encounters the oblique front enhances the convergence at the surface as well. While the V-shaped convergence zone on the surface is prominent both in the model and in the field, the flow and salinity fields associated with the tidal intrusion front are strongly 3-d (see the cross-sections in Figure 6-9 and the along-channel section Figure 6-6). The V-shaped surface convergence zone and 3-d frontal structure are also generally consistent with observations from drone imagery (Figure 6-3 **(a)**) and shipboard measurements (Appendix E).

Note that the volumetric flux through the smaller opening on the north side is much less than through the main opening, so here we focus on the jet flow from the main opening that is the primary source of the tidal intrusion front (Figure 6-4). To confirm the minor influence of the smaller opening, we ran a test case where the smaller opening was removed from the model bathymetry and found that the velocity and salinity fields in the front were similar.

The two V-shaped fronts F1 and F2 near the constriction are dynamically similar, as they both inherit from the jet flow, lateral shear, differential advection, baroclinic forcing in the lateral momentum balance, and a pair of secondary circulation cells. The subsequent analysis focuses on front F2 because of its larger size and greater total mixing. Note that while tidal currents are usually slower over shallow regions due to topographic steering (e.g., Dietrich and Smith, 1983), in this case, faster currents occur over the shoal inside of the V-shaped front F2. This demonstrates that the lateral shear across front F2 is associated with the jet flow from the narrow opening instead of due

to the bottom frictional torque. In addition to this sharp constriction at the railroad embankment, similar tidal intrusion fronts also occur during the flood tide at other locations along the estuary where flow separation occurs, e.g., at a sand spit near the mouth and in meanders.

The bend

In the bend, a surface front occurs that has similar underlying dynamics to the front at the constriction, including flow separation, differential advection, secondary circulation, and surface convergence. The channel flow detaches from the inner bank at the bend apex, with a low-velocity separation zone formed near the inner bank in the lee of the bend (Figure 6-8). The main flow is accelerated in the outer bend as it is restricted to a narrower part of the channel due to flow separation. Salinity is higher near the outer bank and lower near the inner bank as a result of the differential advection, leading to a lateral front at the boundary of the separation zone.

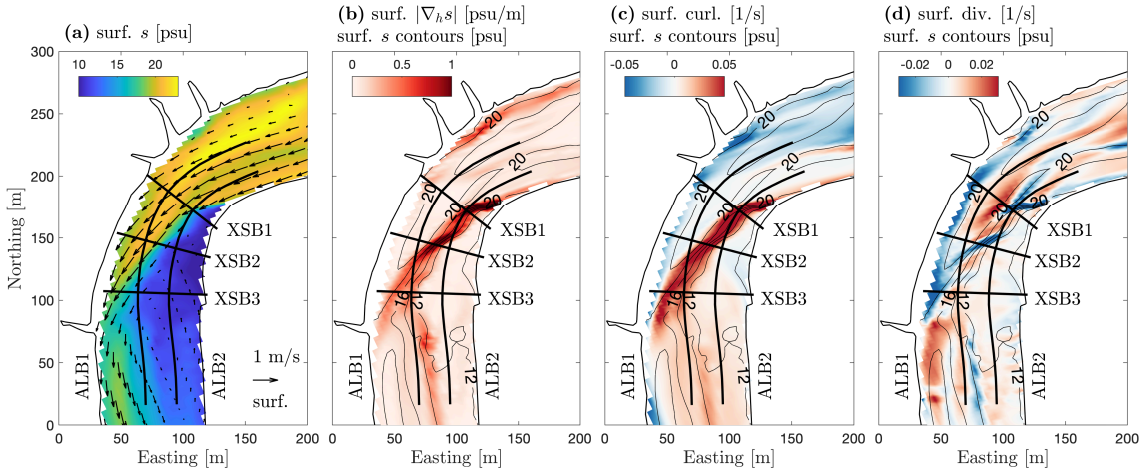

Figure 6-8: Flood tide flow field in the bend region. **(a)**: Surface salinity. Arrows show surface velocity. **(b)**: Horizontal gradients of surface salinity, with contours of surface salinity. **(c)**: Curl of surface velocity (vorticity). **(d)**: Divergence of surface velocity, and blue colors represent surface convergence. Black lines show locations of the cross-sections and along-channel section taken for detailed analysis.

A single secondary circulation cell occurs in the cross-section (Figure 6-9) with outward velocity in the upper water column and inward velocity in the lower column. Secondary circulation laterally transports lower salinity toward the outer bank near the surface, and thus increases stratification through lateral straining. Likewise, the lower-velocity separation zone expands outward near the surface, leading to lower velocity on top of higher velocity in the water column. Intense turbulent mixing occurs in the upper water column at the frontal boundary with reversed vertical

shear. While stratification is expected to inhibit turbulence, the occurrence of mixing indicates that the surface front may also favor turbulence generation, similar to the front at the constriction.

Overall, the frontal dynamics, secondary circulation, and mixing in the bend region are similar to the constriction region: (1) A tidal intrusion front (surface convergence, Figure 6-8) occurs due to flow separation, spanning from the inner bank of the bend apex to the downstream outer bank, and the front has an oblique angle to the main channel flow direction; (2) secondary circulation strains the lateral salinity gradient and creates stratification (Figure 6-9); (3) secondary circulation twists the laterally sheared streamwise flow and leads to reversed vertical shear in the upper water column; (4) intense near-surface mixing occurs at the salinity front at the boundary of the flow separation zone (Figures 6-9 and 6-10).

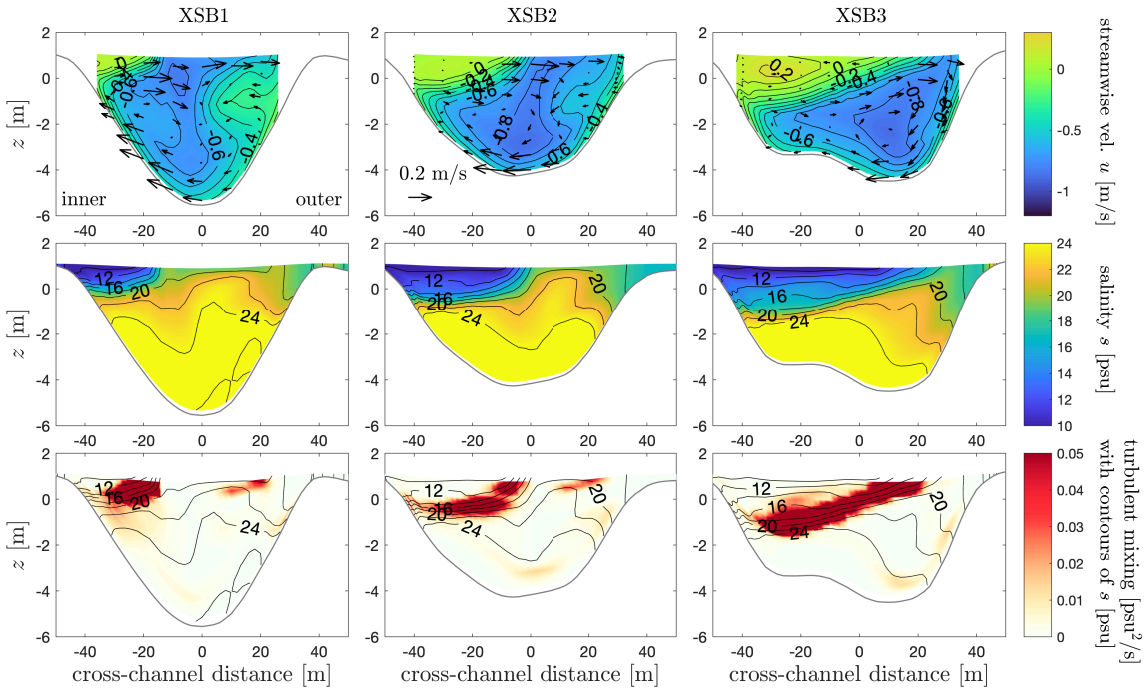

Figure 6-9: Streamwise velocity u, salinity s, and mixing in cross-sections XSB1, XSB2, and XSB3. Locations of cross-sections are shown in Figure 6-8. Arrows show secondary circulation. The inner bank is on the left side.

One major difference between the bend and the constriction is the mechanism of flow separation. In the constriction region, flow separation occurs on both sides of the jet flow from the narrow opening. In the bend, flow separation only occurs near the inner bank downstream of the bend apex due to the channel curvature effect (Leeder and Bridges, 1975; Blanckaert, 2015; Bo and Ralston, 2020). As a result, a single surface front is created in the bend and instead of two fronts converging in a V-shape as with the constriction. The fronts in both cases are oriented at an angle to the channel

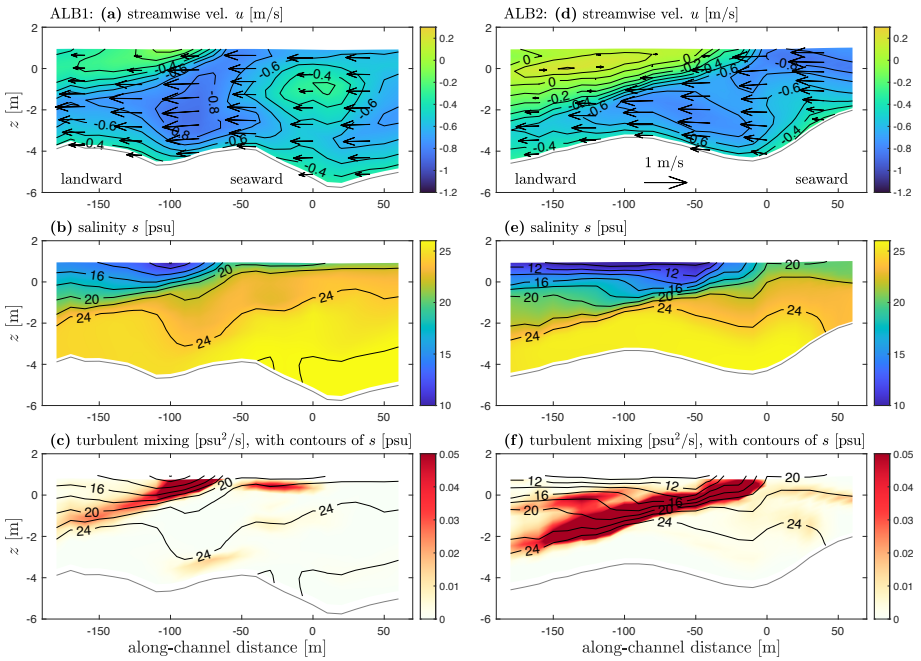

Figure 6-10: Streamwise velocity u, salinity s, and mixing in along-channel sections ALB1 and ALB2. Locations of ALB1 and ALB2 are shown in Figure 6-8. Negative distance means landward direction, and the bend apex is at 0 m.

due to the Froude number, so essentially the bend front resembles half of the V-shape of the tidal intrusion at the constriction (Figure 6-8).

Another difference between the bend and the constriction lies in the driving force for secondary circulation in the lateral momentum balance (6.3) (XSB1 in Figure 6-11). The lower salinity near the inner bank and higher salinity near the outer bank generally create BCPG forcing that is outward near the surface and inward near the bottom, and this BCPG contributes to the clockwise secondary circulation. In addition, the CFA has comparable magnitude to the BCPF and a similar tendency to drive clockwise secondary circulation. While the BCPG dominates over CFA in the constriction region, both terms are important for the lateral momentum balance in the bend, consistent with previous observations (Kranenburg et al., 2019).

6.3.4 Quantifying mixing and straining

The vertical salinity variance budget (6.6) is calculated to quantitatively understand the influences of straining and mixing associated with surface fronts on stratification. In the constriction region, strong positive straining is found at the V-shaped tidal intrusion front that tends to increase stratification (Figure 6-12 **(b)**). Locally, the straining term is dominantly due to the lateral component in

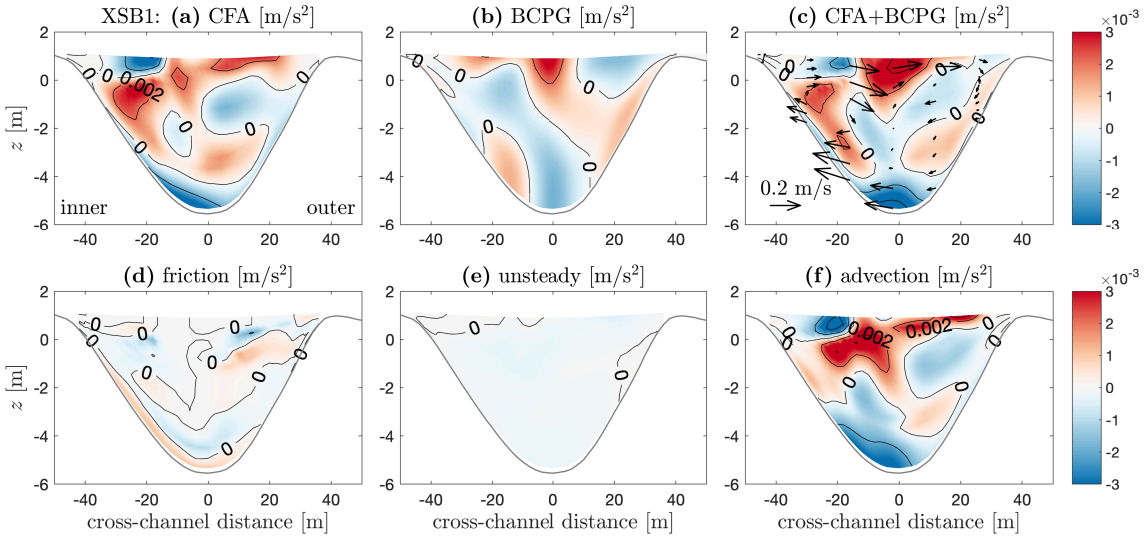

Figure 6-11: Terms in the lateral momentum balance (6.3) in the cross-section XSB1.

(6.6), i.e., the interaction between vertical variations of lateral velocity and lateral salinity gradients. This positive straining in the variance budget converts lateral gradients to stratification through the BCPG-driven secondary circulation at the front (see the cross-sectional plots in Figure 6-5). Note that some negative straining occurs north of the V-shaped front. This is because the downward velocity of secondary circulation locally suppresses the pycnocline and creates weak lateral salinity gradients north of the downwelling region, with higher salinity north of lower salinity (e.g., in the north part of XSC2 and XSC3 in Figure 6-5)). Negative straining occurs as the BCPG-driven lateral flows twist these weak lateral salinity gradients north of the front. Overall, positive straining at the front is much larger than negative straining north of the front, and the net effect of straining is to increase stratification.

While the positive straining at the tidal intrusion front is a source of stratification, the strong turbulent mixing near it tends to destroy salinity variance (Figure 6-12 **(c)**). Turbulent mixing is increased near the front due to the vertical shear and increased eddy diffusivity from the turbulence closure. While the strongest positive straining is collocated with the surface convergence front in the map view, the strongest turbulent mixing is adjacent to the convergence zone, outside of the V-shape. This reflects the 3-d structure of the front, as most of the turbulent mixing occurs away from the surface convergence where the frontal boundary extends into the water column (Figures 6-5 and 6-6).

Additional dissipation of salinity variance occurs due to numerical mixing at the surface convergence zone where salinity gradients are sharpest (Figure 6-12 **(d)**). Numerical mixing results

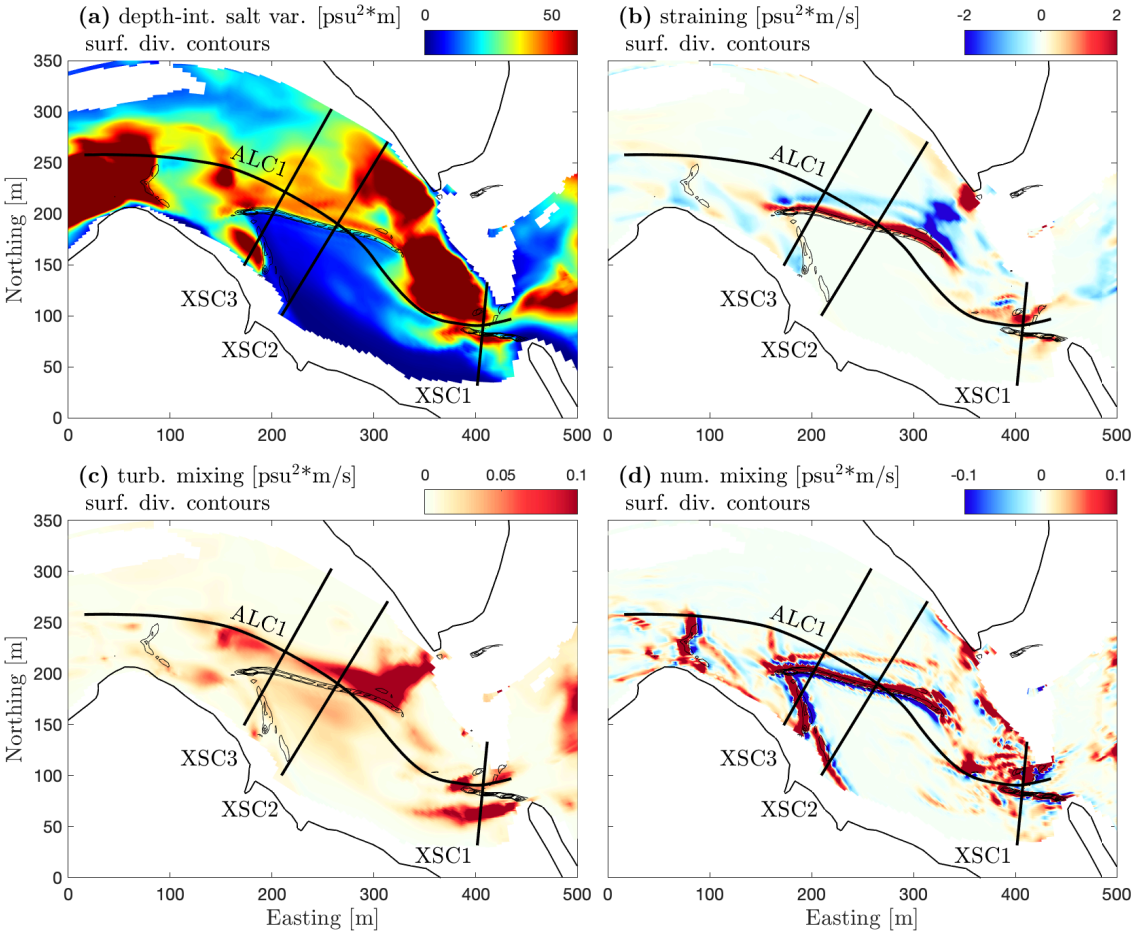

Figure 6-12: Terms in the vertical salinity variance budget (6.6) in the constriction region. **(a)**: Depth-integrated salinity variance, with contours of surface divergence. **(b)**: Depth-integrated straining. **(c)**: Depth-integrated turbulent mixing. **(d)**: Depth-integrated numerical mixing. For mixing and numerical mixing, positive values (red colors) stand for destruction of stratification; for straining, positive values (red colors) stand for creation of stratification. Note the different color ranges of mixing and straining. The local magnitude of turbulent mixing can be much smaller than numerical mixing and straining, but their spatially-integrated effects are comparable in the variance budget.

from the discretized tracer advection scheme in the model (Burchard and Rennau, 2008). Generally, numerical mixing acts to diffuse salinity gradients that otherwise would be smoothed by the turbulent or horizontal mixing processes (Ralston et al., 2017). Numerical mixing can locally be either positive or negative, but the integration of numerical mixing is usually positive, i.e., an overall effect to decrease stratification.

Spatially integrating the variance budget over the constriction region, straining (mostly lateral straining) is the dominant source of stratification during the flood tide. The created stratification is destroyed by the combination of turbulent mixing (60%) and numerical mixing (40%).

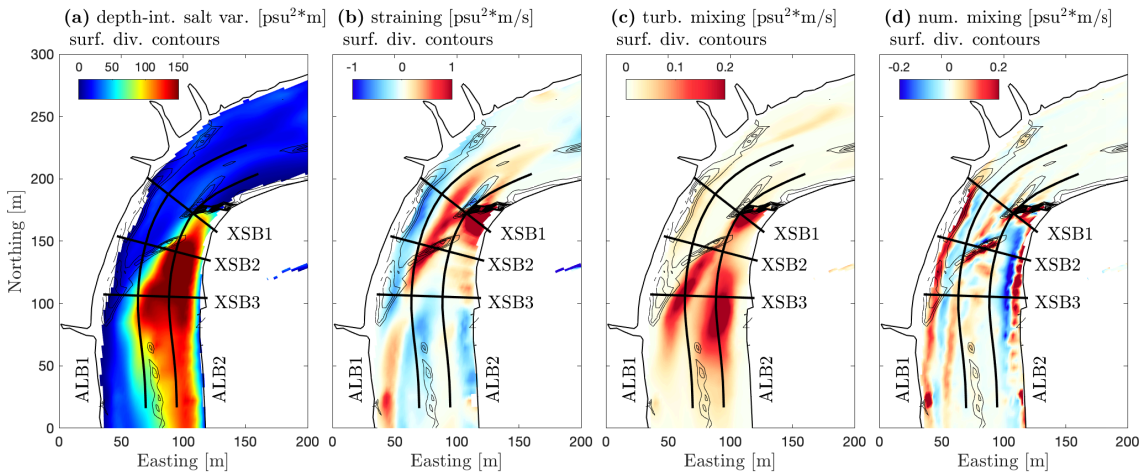

Figure 6-13: Terms in the vertical salinity variance budget (6.6) in the bend region. **(a)**: Depth-integrated salinity variance, with contours of surface divergence. **(b)**: Depth-integrated straining. **(c)**: Depth-integrated turbulent mixing. **(d)**: Depth-integrated numerical mixing.

In the bend region, straining and mixing have similar patterns as in the constriction. Intense positive straining occurs at the surface convergence front (Figure 6-13 **(b)**), which represents the creation of stratification by secondary circulation (see cross-sectional plots in Figure 6-9). Regions with strong turbulent mixing are offset from the surface convergence zone in the map view (Figure 6-13 **(c)**), which corresponds to the enhanced mixing at the inclined, subsurface frontal zone (Figures 6-9 and 6-10). Numerical mixing is weaker in the bend region, and turbulent mixing accounts for 80% of the total mixing.

While the straining of salinity and creation of stratification associated with surface fronts has been reported in estuaries (e.g., Largier, 1992; O'Donnell, 1993; Giddings et al., 2012), the co-occurring mixing has received less attention. Our analysis suggests that strong turbulent mixing can happen near the surface convergence zone and tends to destroy the stratification created by straining. The horizontal salinity gradient across the front drives secondary circulation, which interacts with the streamwise velocity to create shear and turbulence in addition to creating stratification. Mixing can thus occur as a result of the enhanced vertical shear near the front, and the detailed mechanism will be examined in the following section.

6.3.5 Shear and mixing at the front

In this section, we investigate the dynamical processes that lead to turbulent mixing near the tidal intrusion front. The north-side front in XSC2 (at cross-channel distance of 0 to 50 m, the northern

part of the V-shaped front F2) in the constriction region is selected as an example. Enhanced vertical shear is created at the front (Figure 6-14 **(a)**), which provides a source of turbulence generation (Figure 6-14 **(d)**) and mixing (Figure 6-5 XSC2).

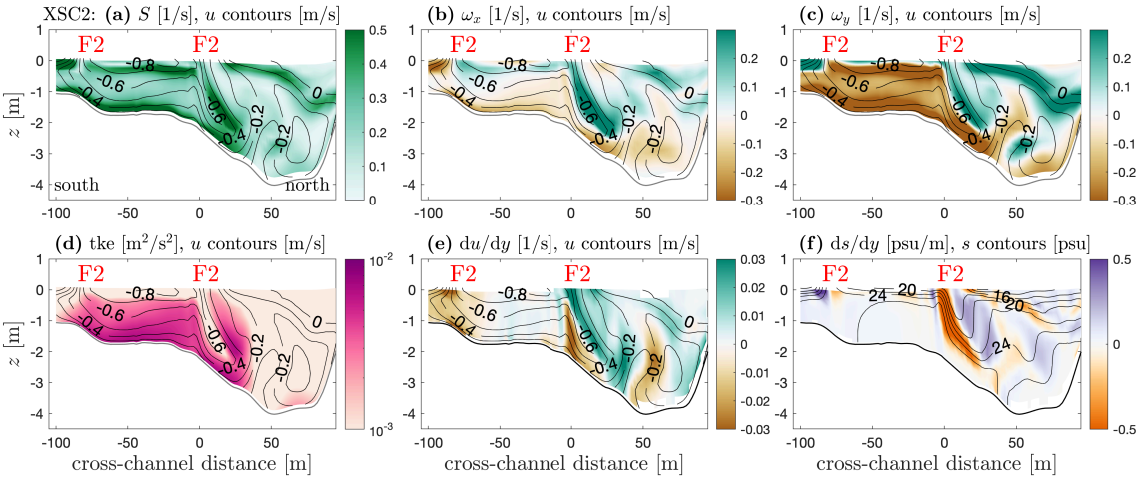

Figure 6-14: **(a)**: Total vertical shear S in the cross-section XSC2, with contours of streamwise velocity. **(b)**: ω_x (vertical shear of lateral velocity). **(c)**: ω_y (vertical shear of streamwise velocity). **(d)**: Turbulent kinetic energy tke. **(e)**: Lateral shear of streamwise velocity. **(f)**: Lateral salinity gradient, with contours of salinity s.

The gradient Richardson number Ri_g is defined as

$$\mathrm{Ri}_g = \frac{N^2}{S^2} = \frac{-\beta g \frac{\partial s}{\partial z}}{\left(\frac{\partial u}{\partial z}\right)^2 + \left(\frac{\partial v}{\partial z}\right)^2}, \tag{6.8}$$

where S is the total vertical shear, and N is the buoyancy frequency.

$$N = \left(-\frac{g}{\rho_0}\frac{\partial \rho}{\partial z}\right)^{\frac{1}{2}} = \left(-\beta g \frac{\partial s}{\partial z}\right)^{\frac{1}{2}}, \tag{6.9}$$

as temperature is uniform in the model and the density only depends on salinity. Ri_g compares the stabilizing effect of stratification to the destabilizing effect of vertical shear (Miles, 1961; Collignon and Stacey, 2013). A critical value $\mathrm{Ri}_{g,cr} \approx 0.25$ is used for determining the growth of instability in the water column (Miles, 1961; Howard, 1961). The gradient Richardson number Ri_g remains close to the critical value $\mathrm{Ri}_{g,cr} \approx 0.25$ near the north-side front in XSC2 as a result of the enhanced vertical shear, thus allowing for turbulence and mixing (Figure 6-5 XSC2).

The vorticity equations (6.5) are examined to understand the factors contributing to the vertical shear. The vertical shear is contributed by both the shear of lateral flow (longitudinal vorticity ω_x)

and the shear of streamwise flow (lateral vorticity ω_y) (Figure 6-14 **(b)**, **(c)**). The positive longitudinal vorticity ω_x at the front corresponds to the clockwise BCPG-driven secondary circulation downstream of the constriction. ω_x is primarily forced by the lateral salinity gradient (see Figure 6-14 **(f)** and equation (6.5a)), consistent with the momentum balance analysis where the BCPG is dominant in driving secondary circulation (equation (6.3) and Figure 6-7). In the transport equation (6.5b) for the lateral vorticity ω_y, the vorticity twisting (third term on the right side) is most important for the creation of ω_y. Secondary circulation (ω_x) can twist the laterally sheared streamwise flow ($\partial u/\partial y$, i.e., part of the vertical vorticity, as Figure 6-14 **(e)** shows), and thus generate ω_y at the front. The along-channel salinity gradient in (6.5b) also has a tendency to increase ω_y, as the saltier water from the constriction encounters the fresher ambient water and thus subducts. However, this baroclinic term is less important than the vorticity twisting at this front, because the orientation of the front is closer to the along-channel direction, so that along-channel baroclinicity is weak and the lateral shear and lateral baroclinicity are strong. The curvature effect is generally negligible in the constriction region where curvature is mild.

Note that the lateral vorticity ω_y is positive at the front (Figure 6-14 **(c)**), and it corresponds to the reversed vertical shear of the streamwise current, i.e., slower flood current above faster flood current (also see Figure 6-5). In contrast to the bottom boundary layer where the no-slip condition causes velocity to increase with distance above the bed and creates negative ω_y, this reversed shear provides corroborating evidence that the pattern of shear and mixing is mainly associated with surface dynamics. Negative ω_y (normal shear) is found over the shoal in the south part of XSC2 (Figure 6-14 **(c)**), because of the greater influence of the bottom boundary in this shallow region. Over the shallow shoal, the influence of secondary circulation on salinity straining and shear twisting is weaker compared to near the front. Instead, the bottom boundary layer shear has a strong influence on mixing in this shallow region. As stratified water coming from the constriction encounters the shallow shoal, the strong bottom boundary shear and turbulence can decrease Ri_g and thus lead to mixing (i.e., mixing occurring inside the V-shape in the map view Figure 6-12 **(c)**).

In the bend region, the processes that affect vertical shear are generally similar to the north-side front in the constriction region, i.e., the lateral baroclinic exchange and vorticity twisting. Moreover, the curvature effect plays a greater role in the bend in enhancing the shear and destabilizing the water column, which is consistent with the more prominent contribution of CFA in the lateral momentum balance (see equation (6.3) and Figure 6-11).

Overall, the surface fronts in the constriction and bend regions are intrinsically similar, where

flow separation differentially advects salinity, interacts with secondary circulation, and leads to the generation of 3-d frontal structures. Intense mixing occurs at both the constriction and bend fronts, because the combined effects of baroclinicity and twisting of the streamwise shear by secondary circulation enhance vertical shear and turbulence.

6.3.6 The importance of near-surface mixing

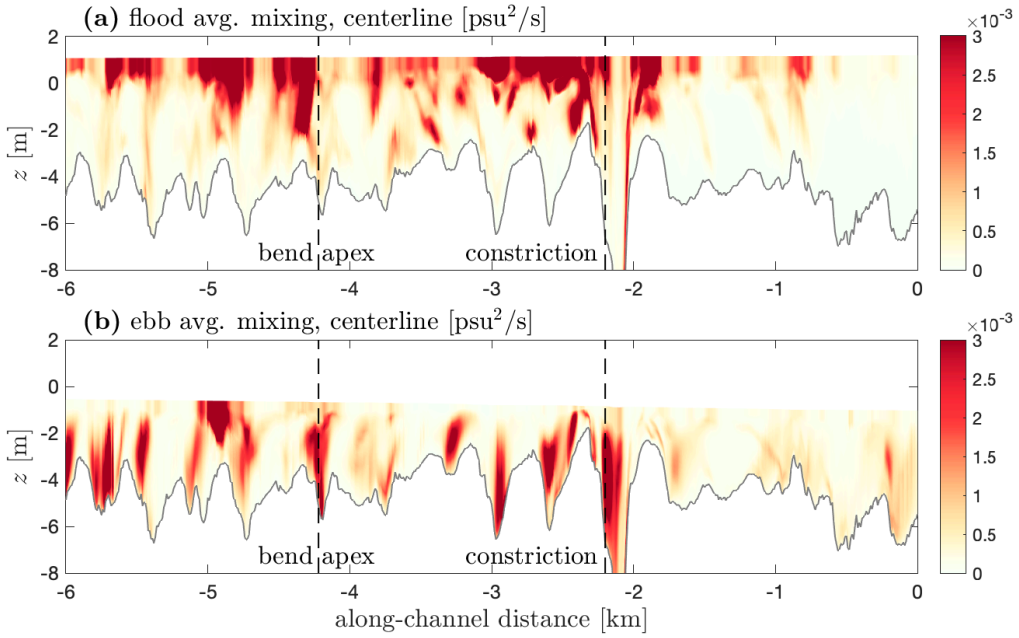

Figure 6-15: Vertical distribution of mixing along the North River centerline, from the mouth to 6 km into the estuary. **(a)**: Flood tide average. **(b)**: Ebb tide average.

The mixing associated with flood tide intrusion fronts occurs primarily in the upper water column (Figure 6-15), in contrast to bottom-generated turbulence and mixing that is usually dominant in shallow tidal estuaries in absence of winds (e.g., Stacey et al., 1999; Geyer et al., 2000; Scully et al., 2011). To illustrate the tidal asymmetry in mixing, the time-averaged mixing along the North River centerline during the flood and ebb tide is compared in Figure 6-15. During the ebb tide, the strongest mixing generally occurs in the lower water column in the bends, and that corresponds to bottom boundary layer mixing at bend-scale bottom salinity fronts created by the channel curvature effect as proposed by Bo and Ralston (2022). Note that an exception is found at around 5 km into the estuary where mixing is mostly near the surface during the ebb tide. A tributary creek merges into the main stem of the North River at around 5 km (Garcia et al., 2021), and the plume of buoyant water from the creek leads to near-surface mixing locally during the ebb tide.

In contrast to the ebb tide when most of the mixing is associated with the bottom boundary layer, mixing predominantly occurs near the surface during the flood tide. We calculate the proportion of mixing that happens in and outside of the bottom boundary layer to assess the contribution of near-surface mixing. The bottom boundary layer height H_{bbl} is defined based on the vertical shear stress (Reynolds stress) distribution in a similar way to Stacey and Ralston (2005), with H_{bbl} being the distance above the bed where shear stress becomes smaller than 10% of the bottom shear stress. Integrating along the estuary from the mouth to the $\sim$ 7 km region with large bottom roughness (excluding the marsh platform and tributary channels), around 80% of mixing during the flood tide happens above the bottom boundary layer. This contrasts with the mixing during the ebb tide, where around half of the mixing occurs within the bottom boundary layer and most of the rest is near the top of the bottom boundary layer.

In addition to the flood-ebb asymmetry in the vertical distribution of mixing in the water column, we also calculate the temporal distribution of mixing between flood and ebb tides. During the spring tide with moderate discharge examined here, around 60% of the mixing occurs during the flood and 40% of the mixing occurs during the ebb tide. With mixing mostly occurring in the upper water column during the flood tide, the near-surface mixing associated with tidal intrusion fronts is thus of comparable importance to bottom boundary layer mixing in this system.

6.4 Discussion

6.4.1 Key mechanisms

We investigated the tidal intrusion fronts that occur during flood tides near two types of topographic features, i.e., a constriction and a bend, as well as their influences on stratification and mixing. Downstream of the channel constriction, flow separation occurs on both sides of the jet flow from the narrow opening. The strong lateral shear zones between the jet and ambient flow create sharp lateral salinity gradients through differential advection. The resulting lateral baroclinic forcing leads to a pair of counter-rotating secondary circulation cells with convergence near the surface. Driven by secondary circulation, the fresher ambient water on both sides of the saltier jet propagates toward the center near the surface (surface-converging lateral gravity currents). The competition between lateral surface currents and the along-channel jet flow leads to the oblique angle of surface fronts to the streamwise direction, and subduction also occurs as the saltier jet flow encounters the frontal zone. Therefore, a tidal intrusion front is generated downstream of the constriction, with a classical

V-shaped convergence zone near the surface.

Stratification is created at the tidal intrusion front as a result of lateral straining by the BCPG-driven secondary circulation. While stratification is expected to inhibit turbulence and mixing, intense turbulent mixing is found near the front. Mixing occurs because both the vertical shear of secondary circulation and the reversed vertical shear of streamwise velocity contribute to destabilizing the water column. The reversed vertical shear of streamwise velocity, with the flood-tide current decreasing toward the water surface, results from the twisting of laterally sheared jet flow by the secondary circulation.

Analysis in the constriction region reveals that tidal intrusion fronts are hotspots of mixing. Channel bends can lead to similar surface convergence fronts with intensified mixing, and the mechanisms are analogous to the constriction region. In the bend, flow separation occurs near the inner bank behind the bend apex as a result of the channel curvature effect. Similar to the constriction region, lateral salinity gradients are enhanced at the boundary of the separation zone as a result of differential advection and result in BCPG-driven secondary circulation. A tidal intrusion front occurs with the surface convergence zone being oblique to the main flow, spanning from the bend apex on the inner bank to the downstream outer bank. Enhanced mixing occurs at the tidal intrusion front in the upper water column, akin to the constriction region. In contrast to the V-shaped front downstream of the constriction, the tidal intrusion front in the bend resembles half of a V-shape since flow separation only occurs on the inner bank. Moreover, in the bend the curvature effect enhances the secondary circulation and mixing, in addition to the lateral BCPG that dominates in the constriction region.

Based on a salinity variance budget analysis, the mixing associated with tidal intrusion fronts is capable of destroying the stratification created by lateral straining. Moreover, the associated mixing predominantly occurs near the surface during the flood tide, in contrast to the ebb tide when mixing mostly occurs in the lower water column. The flood tide near-surface mixing is found to be comparable to the bottom boundary layer mixing during the ebb tide in the North River estuary.

6.4.2 Instability and mixing

White and Helfrich (2013) conducted an idealized numerical study of a horizontal shear layer with a horizontal density gradient, and mentioned two end-member regimes where instabilities can grow, i.e., a pure well-mixed horizontal shear layer and a pure gravity current without horizontal shear. Our analysis provides a realistic intermediate case between the two end-member regimes, where

the interaction between lateral shear and lateral gravity current can generate a third component of vorticity, i.e., the reversed vertical shear of streamwise velocity near the surface, and this reversed shear is also important for destabilizing the water column and leading to turbulent mixing. The vorticity twisting and near-surface turbulence and mixing is also consistent with observations in Collignon and Stacey (2013) and Huguenard et al. (2015).

By contrast, Giddings et al. (2012) reported inhibition of turbulence near a lateral front in late flood tide. That could be a case where the additional reversed shear resulting from vorticity twisting was less influential because the streamwise tidal current was weak during the late flood stage. As a result, in those observations, the vertical shear of lateral gravity current alone was insufficient to overcome the stabilizing effect of its creation of stratification.

In addition, the longitudinal baroclinicity may also enhance the reversed vertical shear near the surface, since the surface front is usually oblique to the upstream flow. While the longitudinal baroclinicity is not dominant at the tidal intrusion fronts here, it could be important for leading to turbulence and mixing when the front is more perpendicular to the tidal current. This research also suggests that channel curvature contributes to the secondary circulation, enhanced vertical shear, and turbulence in bends, and thus provides an additional source of mixing in sinuous estuaries. In addition to the 3-d processes emphasized in the present study, other mechanisms based on 2-d dynamics can still be important for leading to fronts, instability, and mixing, e.g., nonuniformity in horizontal density gradients (Simpson and Linden, 1989) and gradual channel width change (Geyer et al., 2017).

6.4.3 Broader implications

The analysis presented here focused on a spring tide with moderate discharge conditions and found that around 60% of the mixing occurs during the flood tide, primarily associated with surface fronts. In model results, the intensified mixing at surface fronts during flood tides consistently occurs across spring-neap cycles and under varying river forcing conditions. The fraction of the total mixing during flood tides varies between 30% and 60% during the simulation period, with the minimum flood-to-ebb ratio during neap tides with high river discharge in late October 2021. During that period, flood tide mixing still mostly happens near the surface and is associated with tidal intrusion fronts. Tidal currents (and thus the lateral shear) are weaker during neap tides, which leads to weaker differential advection and smaller lateral salinity gradients to drive secondary circulation and surface convergence. As corroborating evidence, the surface convergence features are generally

less noticeable in both the model and observations during neap tides than spring tides. In addition, stronger stratification appears during that period due to the weaker tidal currents and higher river flow, and stratification can suppress secondary circulation (Chant and Wilson, 1997) and thus hinder the development of fronts and mixing. By contrast, intense mixing still occurs during the ebb stage when the pycnocline meets regions with strong bottom boundary turbulence, even with the stronger stratification. While the flood tide accounts for a smaller portion of the mixing during neap tides and high discharge, surface fronts remain an important factor in the total mixing and stratification in the estuary.

Similar near-surface mixing is also expected to occur in other estuaries where tidal intrusion fronts have been observed (e.g., Simpson and Nunes, 1981; Largier, 1992; Marmorino and Trump, 1996). In particular, strong tidal currents and topographic features that can enhance the lateral shear are important for differential advection, frontogenesis, and mixing. Additionally, moderate stratification could favor the formation of fronts, as strong stratification may inhibit secondary circulation and thus the occurrence of convergence. With weak stratification, secondary circulation is still likely to occur, but it might lead to axial convergence fronts instead of classical tidal intrusion fronts (Nunes and Simpson, 1985; Simpson and Turrell, 1986).

Nunes and Simpson (1985) studied axial convergence fronts, and used an analytical solution to predict the strength of the associated secondary flow with the magnitude of lateral salinity gradient. We examined their analytical prediction with the tidal intrusion fronts and secondary circulation in our model. At the constriction, the analytical solution is generally effective in predicting the strength of secondary circulation based on the lateral salinity gradient due to differential advection. While the Nunes and Simpson (1985) solution assumed that the lateral pressure gradient forcing is balanced by friction, the frictional effect is relatively weak our results (Figures 6-7), and the advection term replaces the role of friction in adapting to the pressure gradient forcing (Nidzieko et al., 2009; Kranenburg et al., 2019). In the bend region, the secondary circulation from the analytical prediction by Nunes and Simpson (1985) is correlated with the model results but has a much smaller magnitude. This discrepancy is likely due to the influence of the centrifugal forcing of flow curvature on the secondary circulation in addition to baroclinic forcing from differential advection.

Nevertheless, the correlation between the Nunes and Simpson (1985) solution and our model results indicates the intrinsic similarities between axial convergence fronts and tidal intrusion fronts, in terms of the lateral shear, differential advection, BCPG-driven secondary circulation, and surface convergence. We further speculate that the axial convergence front corresponds to an instance of

the tidal intrusion front with weak stratification, even though they are named differently. The lateral gravity current propagation speed is small compared to the streamwise velocity when horizontal and vertical salinity gradients are weak, and the surface front thus resembles a single convergence line following the channel orientation, instead of exhibiting a conspicuous oblique angle to the upstream flow.

In addition, plume fronts were suggested to be dynamically related to tidal intrusion fronts as both have buoyancy-driven flow structures (O'Donnell, 1993). Tidal intrusion fronts typically occur as saltier water is forced into estuaries by the strong flood tide current. The flood current may therefore oppose the motion of buoyant ambient water inside estuaries (moving at internal disturbance propagation speed), leading to a strong surface convergence zone with an oblique angle to the flood current. By comparison, in a river plume where fresher water discharges into saltier water, the internal disturbance propagation direction usually conforms to the direction of the inertial momentum of plume water. Therefore, the shape of a plume may be more dispersed on the surface compared to the V-shape found in tidal intrusion fronts (Armi and Farmer, 1986; Largier, 1992). Nevertheless, the existence of ambient coastal current can introduce in additional momentum that is against the plume, which may thus sharpen the shape of plume and lead to intense surface convergence and mixing (O'Donnell, 1997; MacDonald and Geyer, 2005).

6.5 Conclusion

We studied tidal intrusion fronts during flood tides in an estuary with complex topography, with a particular focus on two topographic features, i.e., channel constrictions and bends. Flow separation and differential advection are important for creating lateral salinity gradients at both locations, which leads to secondary circulation and generates surface convergence fronts, or tidal intrusion fronts. Secondary circulation creates stratification at fronts through lateral straining, and also enhances vertical shear through baroclinic exchange and twisting of the streamwise shear to lead to intense mixing near fronts. The constriction and bend regions have similar frontal dynamics and mixing mechanisms, except that differences in the flow separation due to channel geometry result in different frontal shapes. Additionally, curvature in bends favors the development of secondary circulation, enhanced shear, and mixing. Overall, the near-surface mixing that is primarily associated with tidal intrusion fronts is similar in magnitude to bottom boundary layer mixing in this estuary.

Chapter 7

Conclusions and future work

This thesis investigated the influences of channel curvature on hydrodynamic drag, vertical mixing, and stratification in estuaries. Channel meanders, a common topographic feature, were identified as important locations for both drag increase and mixing enhancement. An integrated approach was used combining field observations, realistic numerical simulations, and idealized numerical simulations of estuaries that are scaled off the North River estuary.

In Chapter 2, an observational study found that drag coefficients in the sinuous North River estuary are much greater than typical values for similar estuaries with straight channels. The drag coefficients also displayed large variability at tidal and seasonal time scales. Flow separation was observed in a sharp bend in the estuary, and the analysis revealed a linkage between flow separation and the high values and temporal variability of the drag. Curvature-induced secondary circulation was also suggested to potentially interact with flow separation and affect drag, but this was challenging to quantify with the observational data alone.

In Chapter 3, an idealized modeling study was conducted to investigate the mechanisms for drag increase in estuaries with curvature. Flow separation generates low-pressure recirculating eddies on the lee side of bends, and thus creates bend-scale form drag for the along-channel flow. This additional form drag, i.e., the integrated pressure force normal to the channel boundaries, is an important contributor to the increased total drag, particularly in sharp and deep bends. While secondary circulation also occurred in the idealized model, its influence on drag was less than flow separation.

In Chapter 4, a numerical model of the North River estuary was constructed to quantify the sources of drag in realistic estuarine meanders. The large values for the drag coefficient found in

the numerical model were consistent with observations in Chapter 2. The influence of curvature-induced processes on the momentum budget was investigated, and both flow separation and secondary circulation contribute to the drag increase with the realistic bathymetry. Flow separation creates form drag across bends, consistent with the mechanism identified in the idealized models in Chapter 3. Moreover, secondary circulation increases the near-bed velocity through vertical and lateral advection. As a result, the bottom boundary layer velocity structure deviates from a logarithmic profile and the bed shear stress is enhanced. With the realistic bathymetry, both form drag due to flow separation and the enhanced bed stress due to secondary circulation contribute substantially to the increased drag.

In Chapter 5, we investigated how channel curvature impacts salinity mixing and stratification through an idealized model study. Stratification is decreased in sinuous estuaries compared to straight-channel estuaries. Analysis of the vertical salinity variance budget reveals that channel curvature affects stratification through the generation of alternating signs of lateral straining and through local intensification of mixing. The mixing in meanders is primarily due to enhanced shear mixing at bend-scale bottom salinity fronts. These bottom fronts are generated as a result of interaction between curvature-induced secondary circulation and stratification. Furthermore, an adjusted Simpson number that incorporates the increased drag with channel curvature is introduced to parameterize the decreased stratification associated with meanders. We note that the curvature-induced bottom fronts and mixing occur primarily during ebb tides when a single secondary circulation cell develops in the cross-section and flow separation is weak.

In Chapter 6, a numerical model analysis of the North River estuary was combined with field observations to understand how channel curvature and other topographic features affect mixing during flood tides. Flow separation occurs in both meanders and at constrictions, leading to differential advection of the longitudinal salinity gradient and creating sharp lateral salinity gradients. The associated lateral baroclinic forcing acts with the curvature-induced centrifugal forcing to create secondary circulation. Secondary circulation further interacts with the laterally sheared flow and generates surface convergence fronts. These surface fronts affect stratification by intensifying lateral straining and mixing during flood tides. Mixing occurs because secondary circulation twists lateral shear into the reversed vertical shear of streamwise velocity, contributing to the generation of turbulence. Moreover, mixing associated with convergence fronts during flood tides is primarily near the surface, instead of resulting from bottom-generated turbulence.

This research revealed the importance of channel curvature for the dynamics of tidally-dominated,

well-mixed estuaries like the North River. Similar curvature-induced processes, as well as the associated influences on hydrodynamic drag and salinity dynamics, are also expected to occur in estuaries in other parts of parameter space. As an example, flow separation has been observed to create form drag in curved channels in the Salish Sea estuary (McCabe et al., 2006; Warner et al., 2013), a much deeper and more stratified fjord estuary. Similarly, the interaction between curvature-induced secondary circulation and the salinity field has been found in bends in both the Salish Sea estuary (Seim and Gregg, 1997) as well as the Hudson River estuary (Chant and Wilson, 1997), a partially mixed estuary. The dependence of curvature-induced processes on dimensionless geometric parameters, like the curvature ratio (dimensionless radius of curvature) and aspect ratio (dimensionless depth), provide references for exploration of parameter space (e.g., as was discussed in Chapters 2 and 5). The mechanisms investigated in this thesis may thus apply to other meanders with similar dimensionless geometric parameters, even for those in large estuaries. However, in addition to the curvature effect associated with the channel shape, other factors like Coriolis, river flow, tidal amplitude, and stratification conditions could also affect how curvature alters estuarine dynamics (Valle-Levinson, 2011; Geyer and MacCready, 2014). Therefore, the dependence on other dimensionless parameters, e.g., those comparing the channel curvature with Earth's rotation, or characterizing variability in tidal and river forcing, also need to be investigated to more broadly assess the influence of meanders on estuarine dynamics.

This thesis focused on the channel curvature effect on increased drag and enhanced mixing. The two topics are physically linked, because the increased drag in meanders reflects an increased energy decay rate and enhanced turbulence generation, which is also expected to intensify mixing of salinity. The drag force, as a sink of energy, is therefore intrinsically linked to mixing of stratification, i.e., the sink of salinity variance. The adjusted Simpson number scaling in Chapter 5 proposes a quantitative link between the increased drag and enhanced mixing in estuarine meanders. However, the strength of mixing is not necessarily directly correlated with drag because the mixing efficiency, i.e., the portion of shear production of turbulent kinetic energy that contributes to destroying buoyancy, is not necessarily constant and uniform. Therefore, further investigation is required to reveal the linkage between drag increase and mixing enhancement in estuaries, and in particular, efforts should be devoted to understanding the complex spatial and temporal patterns of energy loss, mixing, and mixing efficiency.

In addition to channel curvature, other topographic features in estuaries can also affect drag, mixing, and stratification in similar manners. Topographic features add boundary constraints to

estuarine flows, introduce rotational coordinates, and create complex local 3-d processes, as with meanders. Chapter 6 identifies similar mechanisms of flow separation, secondary circulation, frontogenesis, and mixing associated with both meanders and constrictions. Other topographic features like headlands and barrier islands have also been reported to generate flow separation and secondary circulation, and these local 3-d processes can potentially influence tidal and salinity dynamics. Future work may extend the focus here on channel bends to understand similarities or differences in the dynamics of other types of topographic features. This broader framework could even parameterize the effects of topographic-induced flow processes based on geometric descriptions of channel or coastline irregularities. Topographic features could thus be treated as intermediate-scale roughness elements in estuaries through parameterization, as is done for small-scale roughness elements like bed forms and vegetation.

Appendix A

Mean along-estuary momentum balance

The depth-integrated along-channel momentum equation is (Nihoul and Ronday, 1975)

$$\frac{\partial q}{\partial t} + \frac{\partial}{\partial s}(\frac{q^2}{h}) = -gh\frac{\partial \eta}{\partial s} - \frac{C_f}{h^2}q|q| - \frac{\partial}{\partial s}\int_{-h_0}^{\eta}\int_{z}^{\eta}\beta g S \mathrm{d}z\mathrm{d}z, \tag{A.1}$$

where we have neglected wind stress and assumed no bottom slope. q is the depth-integrated flux. h is the total water depth, η is water level, and h_0 is the bathymetry depth. $h = h_0 + \eta$. S is salinity. C_f is the bottom friction coefficient. q is given as

$$q = \int_{\eta-h}^{\eta} u \mathrm{d}z = Uh, \tag{A.2}$$

with u being the streamwise velocity and U being the depth average. η is

$$\eta = \overline{\eta} + \eta', \tag{A.3}$$

where η' is the measured water level fluctuations and $\overline{\eta}$ is the mean water level that was not directly resolved in the North River observations. We use an overbar to denote time averages of other properties and a prime to denote temporal fluctuations, so

$$q = \overline{q} + q', \tag{A.4a}$$

$$U = \overline{U} + U', \tag{A.4b}$$

$$h = \overline{h} + \eta', \tag{A.4c}$$

$$\overline{h} = h_0 + \overline{\eta} \sim h_0. \tag{A.4d}$$

The mean along-estuary momentum balance can be derived by taking the time average of (A.1), where the unsteady term is zero after averaging and the other three nonlinear terms in (A.1) can lead to time-mean forcing. Averaging the water level gradient term in (A.1) gives rise to two terms,

$$\overline{gh\frac{\partial \eta}{\partial s}} = g\overline{h}\frac{\partial \overline{\eta}}{\partial s} + g\overline{\eta'\frac{\partial \eta'}{\partial s}}. \tag{A.5}$$

The first term on the right side is the mean barotropic pressure gradient (BTPG, or water level gradient forcing) and the second term relates to the tidal stress τ_t.

$$\tau_t = -\rho g\overline{\eta'\frac{\partial \eta'}{\partial s}}. \tag{A.6}$$

The tidal stress, as a manifestation of the radiation stress from a tidal wave (Zimmerman, 1978), has been reported in observational studies including on the North Sea (Prandle, 1978) and in San Francisco Bay (Walters and Gartner, 1985). Rearranging (A.6) and assuming sinusoidal tides,

$$\tau_t = -\frac{1}{2}\rho g\frac{\overline{\partial(\eta'^2)}}{\partial s} = -\frac{1}{4}\rho g\frac{\partial}{\partial s}\left(\|\eta\|^2\right), \tag{A.7}$$

where $\|\eta\|$ is the norm of tidal water level fluctuation, i.e., tidal amplitude.

Averaging the advection term in (A.1), we get

$$\frac{\partial}{\partial s}\overline{\left(\frac{q^2}{h}\right)} \sim \frac{1}{h}\frac{\partial}{\partial s}\overline{(q'^2)}. \tag{A.8}$$

The mean forcing associated with the advection term is generally small. Moreover, velocity is nonuniform laterally due to bathymetry variation and channel curvature, so the along-channel flux gradient based on measurements at a single location in the North River estuary is not representative for use in this estimate. Therefore, we have neglected this advection term in the mean momentum balance.

The average of the frictional term in (A.1) represents the friction of the mean flow, which consists of the freshwater discharge and the Eulerian return flow of the landward Stokes drift of the tidal wave (Zimmerman, 1979; Uncles and Jordan, 1980). For estuaries with small or moderate discharge (e.g., the North River estuary), $\overline{U} \ll \|U\|$, where $\|U\|$ is the norm of tidal velocity U'. The mean

flow friction $\tau_{b,\overline{u}}$ can thus be estimated as (e.g., Parker, 2007)

$$\tau_{b,\overline{u}} = -\overline{\frac{C_f}{h^2}\rho q|q|} = -\overline{C_f \rho U|U|} = -\frac{4}{\pi} C_f \rho \|U\| \overline{U}. \tag{A.9}$$

Averaging the salinity gradient term in (A.1) yields the mean baroclinic pressure gradient (BCPG) forcing

$$-\overline{\frac{\partial}{\partial s}\int_{-h_0}^{\eta}\int_{z}^{\eta} \beta g S \mathrm{d}z\mathrm{d}z} \approx -\overline{\frac{1}{2}\beta g h^2 \frac{\partial \langle S \rangle}{\partial s}} \approx -\overline{\frac{1}{2}\beta g h \frac{\partial \langle S \rangle}{\partial s}}\overline{h}, \tag{A.10}$$

where $\langle S \rangle$ is the depth-averaged salinity.

Therefore, in the mean momentum budget, the mean BTPG is balanced with three terms, the tidal stress τ_t, the mean flow friction $\tau_{b,\overline{u}}$, and the mean BCPG. The mean BTPG can be estimated as

$$g\frac{\partial \overline{\eta}}{\partial s} = \frac{1}{\rho h}\left(\tau_t + \tau_{b,\overline{u}}\right) - \overline{\frac{1}{2}\beta g h \frac{\partial \langle S \rangle}{\partial s}}, \tag{A.11}$$

where τ_t and $\tau_{b,\overline{u}}$ are given by (A.7) and (A.9). We have compared the estimation from (A.11) with the mean BTPG in model results from Bo and Ralston (2020), and found that the estimation agrees well ($R^2 = 0.85$).

We calculated τ_t, $\tau_{b,\overline{u}}$, and the mean BCPG from the observations in the North River estuary (section 2.3.2) and examined their dependence on tides and discharge (Figure A-1). τ_t is primarily dependent on tides, and as the tidal amplitude increases, the tidal decay rate increases and the tidal stress becomes stronger. Freshwater discharge creates the mean river flow and tides can lead to a return flow, and therefore, $\tau_{b,\overline{u}}$ is correlated with both discharge and tidal amplitude. The mean BCPG has a negative correlation with tidal amplitude and a weak positive dependence on discharge.

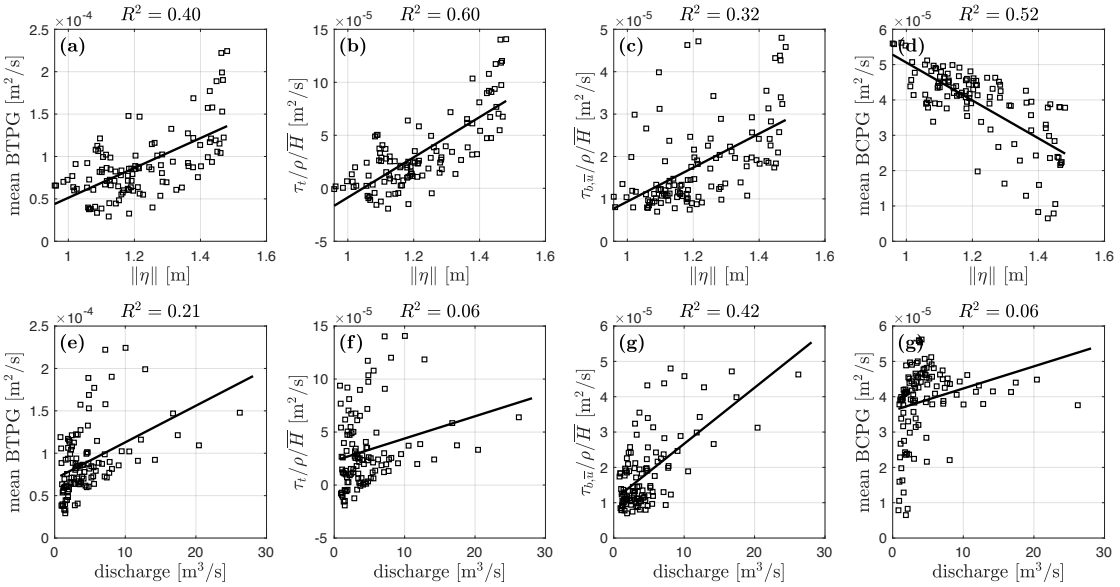

Figure A-1: Correlation between the mean BTPG, τ_t, $\tau_{b,\overline{u}}$, the mean BCPG, and tidal amplitude, river discharge.

Appendix B

Integral form of the momentum budget

Simplify (3.4) and the integral form of the momentum equation for the straight channel can be written as

$$\int_{A_{CS1}} p\mathrm{d}A - \int_{A_{CS2}} p\mathrm{d}A + \int_{A_b} p\xi_x \mathrm{d}A + \int_{A_b} \tau_{bx}\mathrm{d}A = 0. \tag{B.1}$$

where A_{CS1} and A_{CS2} represent the cross-sectional areas at each end of the control volume and A_b represents the area of the channel bed. ξ_x corresponds to the projection in x-direction. There is no integrated pressure on the sidewalls because the projected area in the x-direction is zero in the straight model so the integral over A_w has been removed from (3.4). The unsteady and advection terms are neglected, and only barotropic pressure is included because baroclinic effects are small.

Momentum balance is achieved among the total pressure difference force

$$P_{diff,total} = \int_{A_{CS1}} p\mathrm{d}A - \int_{A_{CS2}} p\mathrm{d}A, \tag{B.2}$$

the pressure force exerted by the decreasing thalweg depth along the channel (the bottom-slope effect)

$$P_{slope} = \int_{A_b} p\xi_x \mathrm{d}A = \int_{A_b} \rho g(h+\eta)\xi_x \mathrm{d}A, \tag{B.3}$$

and the bottom friction F_{bot} (the last term in (B.1)). A considerable part of $P_{diff,total}$ is contributed by the channel depth difference between $CS1$ and $CS2$ and this part is exactly canceled by the bottom-slope pressure force P_{slope} in the momentum budget. To quantify the pressure difference created only by the water level and get rid of the bottom-slope effect, we write a pressure correction term by applying linear approximation to the water level field in (B.3) (i.e. the water level linearly

changes along the channel)

$$P_{corr} = \int_0^w \frac{1}{2}(h_1 + \eta_1 + h_2 + \eta_2)(h_1 - h_2)\mathrm{d}y. \tag{B.4}$$

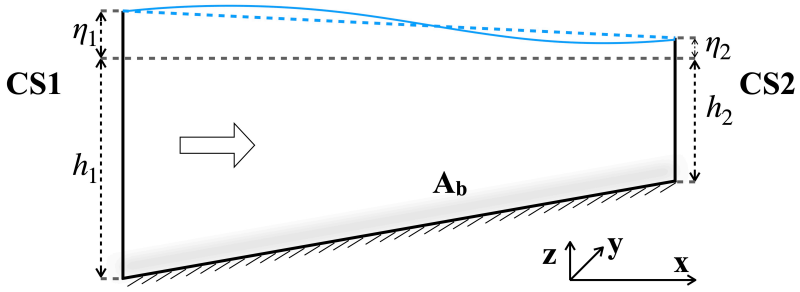

Figure B-1: Schematic of the sideview of the straight channel with decreasing thalweg depth. $CS1$ and $CS2$ represent the cross-sections at each end of the control volume and A_b represent the channel bed. h_1 and h_2 represent the depth of channel bed below mean water level; η_1 and η_2 represent the water level. h_1, h_2, η_1 and η_2 are functions of y. The solid blue line is the water level and the dashed blue line is the linear approximation of the water level.

The bottom-slope pressure force P_{slope} in (B.3) is calculated directly by integrating over the bottom A_w. The pressure correction term P_{corr} in (B.4) is calculated based on the linear approximation by using only water level and channel depth at the ends of the control volume. P_{corr} can balance P_{slope} (Figure B-2) and the remaining "form drag" in the straight channel is zero, by subtraction (B.4) from (B.3). Therefore, we can write the corrected pressure difference force by subtracting P_{corr} from (B.2)

$$P_{diff} = \int_{A_{CS1}} p\mathrm{d}A - \int_{A_{CS2}} p\mathrm{d}A - P_{corr}, \tag{B.5}$$

which only accounts for the pressure difference associated with water level and does not incorporate the bottom-slope effect. In the straight channel, the corrected pressure difference P_{diff} is generally equal to the bottom friction F_{bot} for both flood and ebb tide (Figure B-2), indicating that the momentum budget closes with these two terms, and corresponds to a drag coefficient of $0.003 - 0.004$, consistent with the calculation in section 3.3.1. Therefore, the pressure correction based on the linear approximation is effective for removing the bottom-slope effect in the straight channel, and this same approach can be applied to the sinuous channel. The pressure force associated with bottom slope is much larger than the pressure difference created by water level and the bottom friction (Figure B-2), as the bottom slope is greater than the water level slope, which again illustrates the need to remove the bottom-slope effect in calculating the momentum budget.

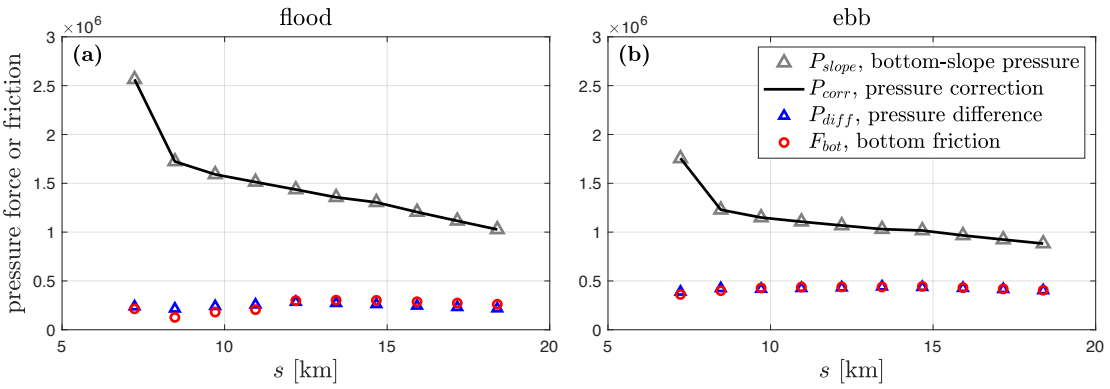

Figure B-2: Pressure force and bottom friction in the momentum budget (B.1) of the straight channel. **(a)** Maximum flood tide. **(b)** Maximum ebb tide. Blue triangles represent the corrected pressure difference in (B.5) and red circles represent the bottom friction. Gray triangles are the pressure force associated with along-channel depth decrease calculated directly by integrating over the bottom using (B.3). Black lines are the pressure correction term used to cancel the bottom-slope effect calculated by using (B.4).

The pressure difference in the sinuous channel is calculated in a similar way as (B.5) to remove the pressure force associated with along-channel depth decrease. The form drag of the sinuous channel is also calculated by subtracting the pressure correction term P_{corr} from the third right-side term in (3.4),

$$P_{form} = \int_{A_w+A_b} p\xi_x \mathrm{d}A - P_{corr}, \tag{B.6}$$

to remove the bottom-slope effect and only keep the form drag associated with water level variations around the bend. A_w is included in (B.6) for the sinuous channel, which did not appear in the straight channel where there is no wall normal to the x-direction.

Appendix C

Potential flow model

Assume potential flow in a flat-bottom channel and the radius of curvature of the centerline is

$$R = \frac{R_0}{\sin(\pi s/L)}, \tag{C.1}$$

in which s is the along-channel distance and L is the channel bend length. R_0 is the radius of curvature at the bend apex, which is also the smallest radius along the channel. The channel bend is symmetric around the bend apex. We also assumed that the radius of curvature increases linearly across the channel (e.g. Leopold, 1960), so that the radius at the inner bank is $R - w/2$ and the radius at the outer bank is $R + w/2$, where w is the channel width.

Assume the flow entering the bend is uniform with velocity U_0 and water depth H. The along-channel Bernoulli equation is

$$gH(s,r) + \frac{1}{2}u(s,r)^2 = gH_0 + \frac{1}{2}U_0^2, \tag{C.2}$$

where both water depth H and velocity u are a function of along-channel distance s and cross-channel distance r. We assume no lateral or vertical velocity so u only represents streamwise velocity. Differentiating (C.2) in the cross-channel direction gives

$$g\frac{\partial H}{\partial r} = g\frac{\partial(H_0+\eta)}{\partial r} = g\frac{\partial \eta}{\partial r} = -u\frac{\partial u}{\partial r}, \tag{C.3}$$

with η being surface elevation. The cross-channel Euler equation is

$$g\frac{\partial \eta}{\partial r} = \frac{u^2}{r}. \tag{C.4}$$

Substituting (C.3) into (C.4) and we obtain

$$u = \frac{K}{r}. \tag{C.5}$$

The cross-channel velocity profile is inversely proportional to cross-channel distance with K being a constant at each cross-section (Leopold, 1960).

Combining the along river conservation of mass

$$\int_{R-w/2}^{R+w/2} u(s,r)H(s,r)\mathrm{d}r = U_0 H_0 w \tag{C.6}$$

and the along-channel Bernoulli equation (C.2), we get an expression to solve for K (Shapiro and Sonin, 2018),

$$U_0 H_0 w = K H_0 \left(1 + \frac{U_0^2}{2gH_0}\right) \ln \frac{R + w/2}{R - w/2} - \frac{K^3}{4g(R - w/2)^2} \left(1 - \left(\frac{R - w/2}{R + w/2}\right)^2\right). \tag{C.7}$$

The water level differences are negligible compared to the total water depth in the mass flux (but the water level change related to Bernoulli should never be neglected), so K can be approximated as

$$K \approx \frac{U_0 w}{\ln\left(\frac{R+w/2}{R-w/2}\right)}. \tag{C.8}$$

Therefore, we get the inner bank velocity at $r = R - w/2$,

$$u_{inner} = \frac{U_0}{\left(\frac{R}{w} - \frac{1}{2}\right) \ln\left(\frac{R+w/2}{R-w/2}\right)}, \tag{C.9}$$

with $R = R(R_0, s)$.

Appendix D

North River model-data comparison

D.1 Model evaluation

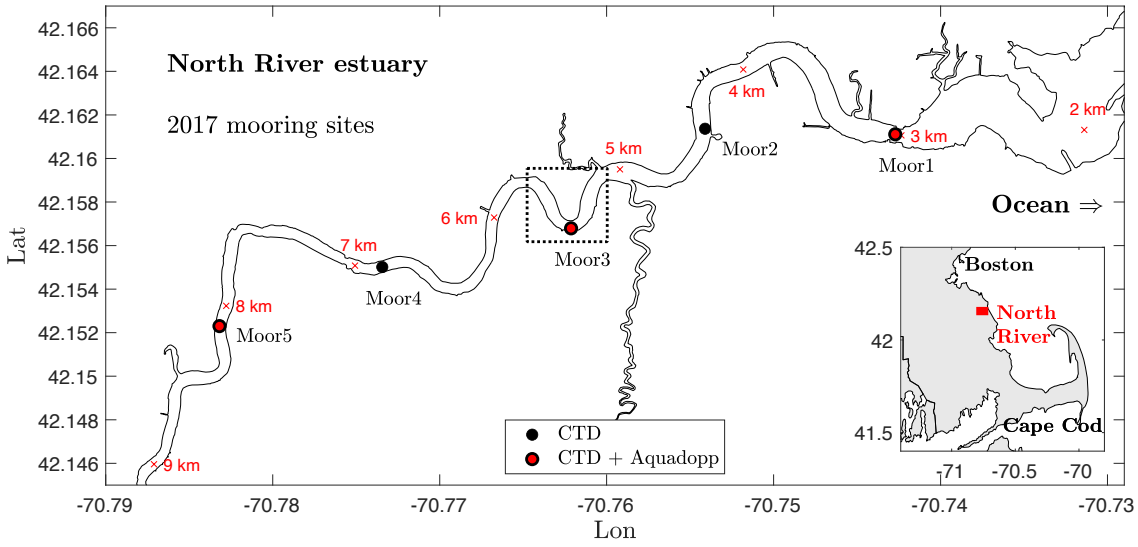

Figure D-1: The North River estuary, with locations of mooring sites (CTD sensors and acoustic Doppler current profilers). Shipboard surveys were conducted in the sharp bend marked by the rectangle. Red crosses show the along-channel distance from the mouth. The location of the North River estuary is shown in the small map on the bottom right.

The observational data used for model evaluation were collected from mid-April to late-July in 2017 (Kranenburg et al., 2019; Bo et al., 2021). Salinity and pressure were measured by five sets of conductivity-temperature-depth (CTD, 2-min sample interval) sensors deployed from 3 km to 8 km, namely Moor1-5 (Figure D-1). Five sensors were deployed at Moor3 and were evenly distributed in the water column; two sensors were deployed near the surface and bed at each of the other four

mooring sites. Velocity profile data were collected by upward-looking acoustic Doppler current profilers (0.2-m vertical resolution and 10-min sample interval) deployed near bottom CTD sensors at Moor1, 3, and 5. Moor3 is at the apex of the sharp bend (Bend-5.4) studied in the main text. In addition, shipboard surveys were conducted in this bend on April 18, 19, and 27, May 17, and July 24, 25, 28, and 31, with acoustic Doppler current profiler measurements (ADCP, cell size 0.50 m, profile interval 0.25 s) and temperature-salinity profile measurements (continuous CTD casts, sample frequency 12Hz) over several cross-sections.

Comparison of the modeled water level, velocity, salinity, and stratification with observations at the five mooring sites are shown in Figures D-2–D-5 (results for Moor3 shown in the main text). The skill parameter is calculated following equation **(5)** in the main text to evaluate the model performance. Moor2 and Moor4 did not have velocity measurements. The surface CTD sensor at Moor1 failed, so Moor1 did not have stratification data. Overall the modeling results agree well with observations at all the mooring sites. $Skill > 0.9$ for both water level and salinity. Velocity has a skill score of 0.88 at Moor3 (sharp bend apex), and $Skill > 0.95$ at Moor1 and Moor5. $Skill = 0.82$ for stratification at Moor3, and the skill score is around -2 to -1 at other mooring locations. Note that the skill score can be negative according to its definition (Murphy, 1988). The modeling results predict well the occurrence time periods and temporal trends of stratification, and negative skill scores are due to differences in the magnitude of stratification between the observations and modeling results. The strength of stratification is more sensitive to the spatial location of measurement and more temporally variable than the other variables, so matching the observed time series precisely is more challenging. However, the plots show that the model is representing the spatial differences between the mooring locations as well as the temporal variability at tidal time scales.

In addition to the comparison with long-term mooring data, the modeling results are compared with observed velocity and salinity from cross-sectional shipboard surveys. As an example, we present the depth-averaged velocity in the sharp bend at around 3-hr into flood tide and 3-hr into ebb tide on April 27, which is during spring tides (Figure D-6). Detailed analysis is done in the main text for the modeling results on April 27. The modeled magnitudes and lateral distributions of velocity are consistent with observations at the cross-sections. The cross-sectional distributions of along-channel velocity, lateral velocity, and salinity are also compared with modeling results for the ebb tide (Figures D-7, D-8) and flood tide (Figures D-9, D-10) on April 27. The modeling results are broadly consistent with the cross-sectional observations, including the secondary circula-

tion patterns, the redistribution of streamwise momentum by secondary flows, flow separation (low streamwise velocity zone near the inner bank during flood tide in cross-section XSD), and salinity distribution in the bend.

D.2 Sensitivity to bottom roughness z_0

The observed lengths and heights of channel bedforms (ripples and mega-ripples) suggest an estimated z_0 of around 0.002 m to 0.01 m in most part of the North River (Bo et al., 2021). A sensitivity test has been done for $z_0 = 0.002$ m, 0.005 m, and 0.01 m (Table D.1). The model performance is not sensitive to z_0 in this range, and skill scores are similar for the three values of z_0. A larger z_0 leads to a slightly better prediction of the tidal water level and velocity, while a smaller z_0 has a slightly better prediction of the salinity intrusion and stratification. Therefore, $z_0 = 0.005$ m is selected for the best overall performance of the tidal and salinity dynamics.

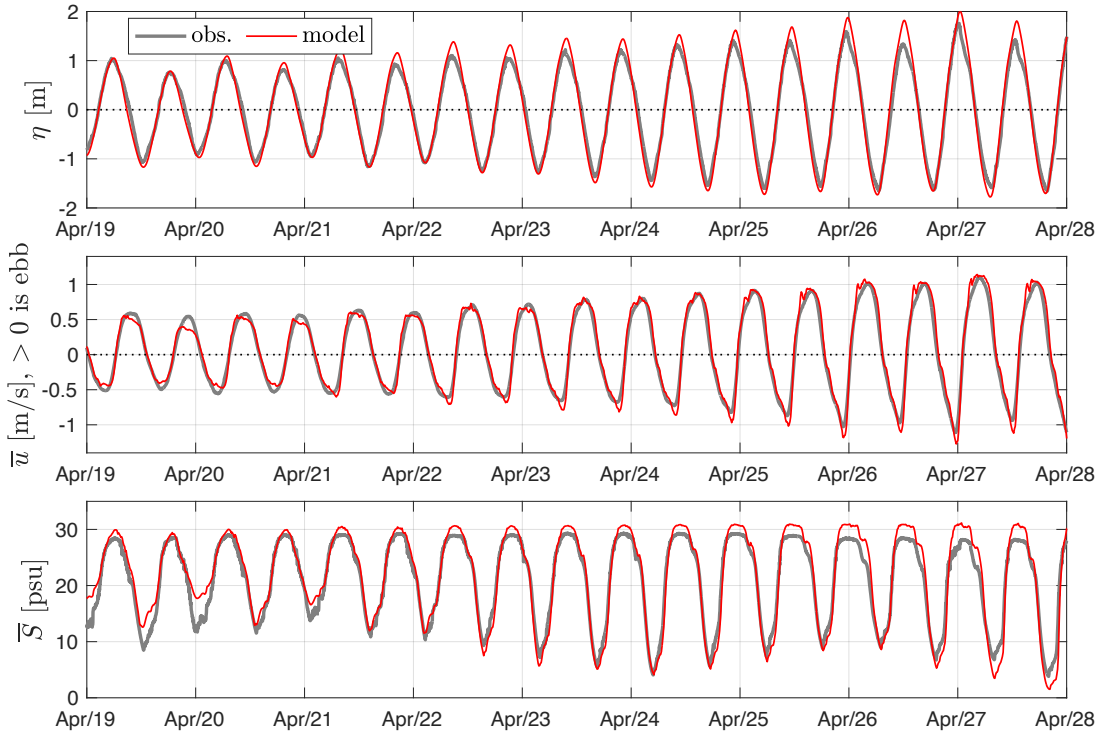

Figure D-2: The modeled estuarine conditions (thin red lines) compared with observations (thick gray lines) at Moor1, including water level η, depth-averaged velocity $\overline{u}$, and depth-averaged salinity $\overline{S}$.

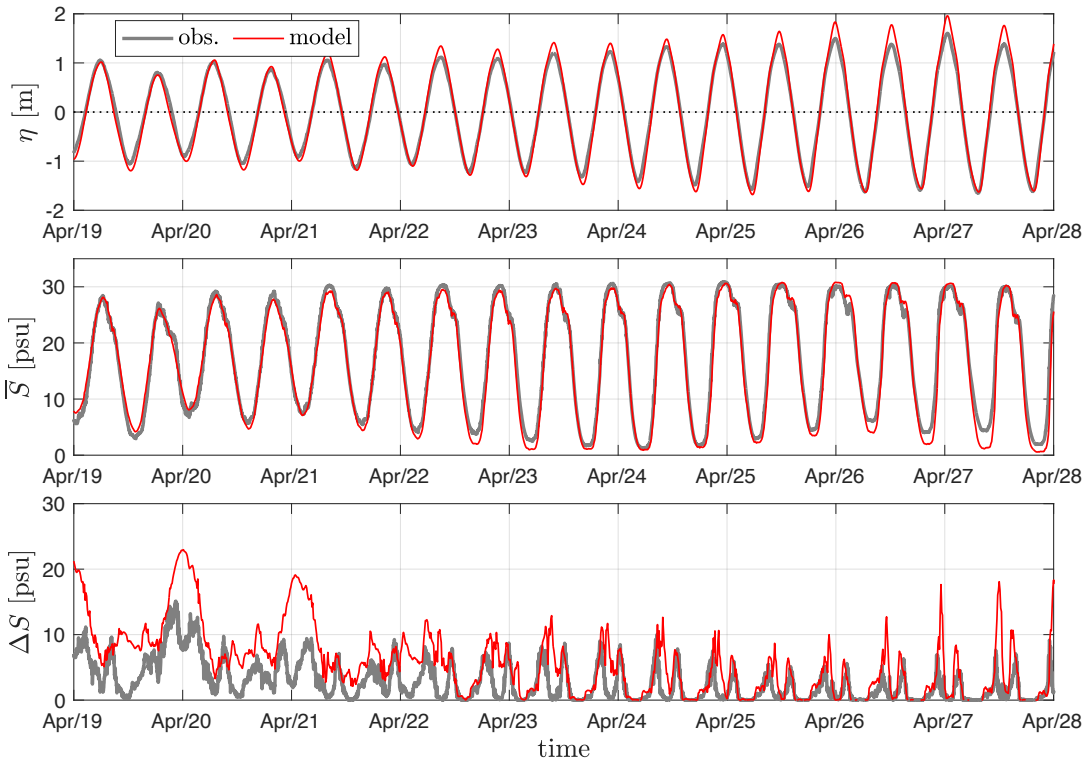

Figure D-3: The modeled estuarine conditions (thin red lines) compared with observations (thick gray lines) at Moor2, including water level η, depth-averaged salinity $\overline{S}$, and stratification ΔS (bottom-surface salinity difference).

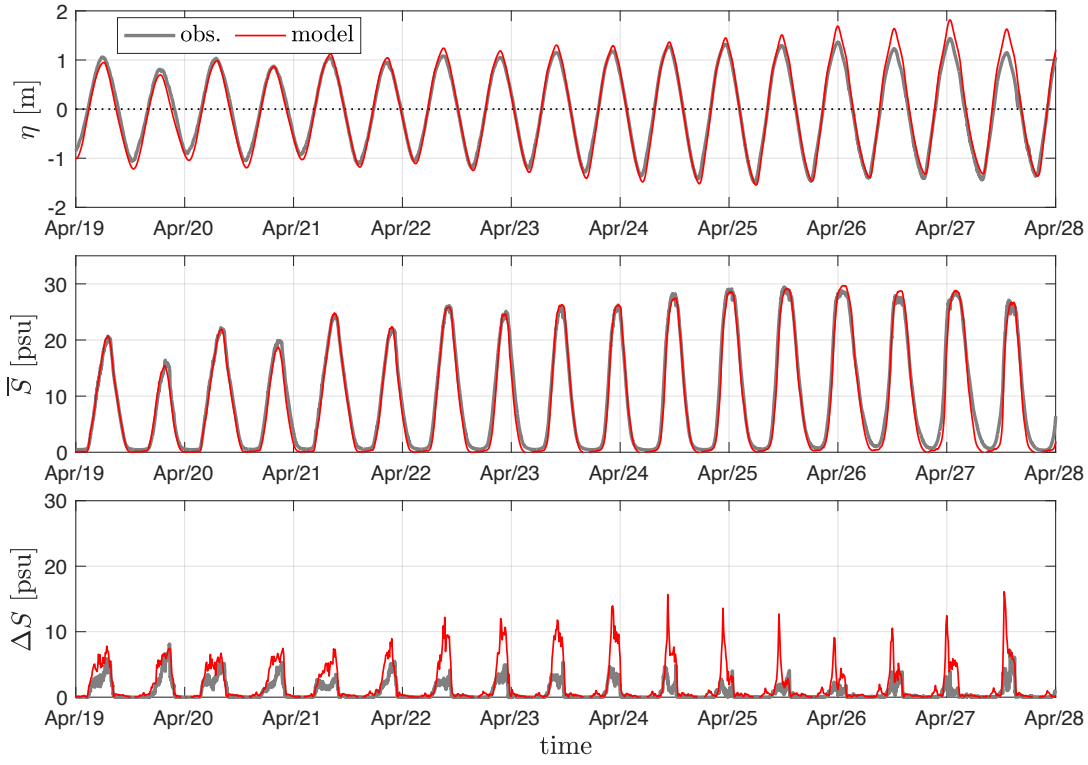

Figure D-4: The modeled estuarine conditions (thin red lines) compared with observations (thick gray lines) at Moor4, including water level η, depth-averaged salinity $\overline{S}$, and stratification ΔS.

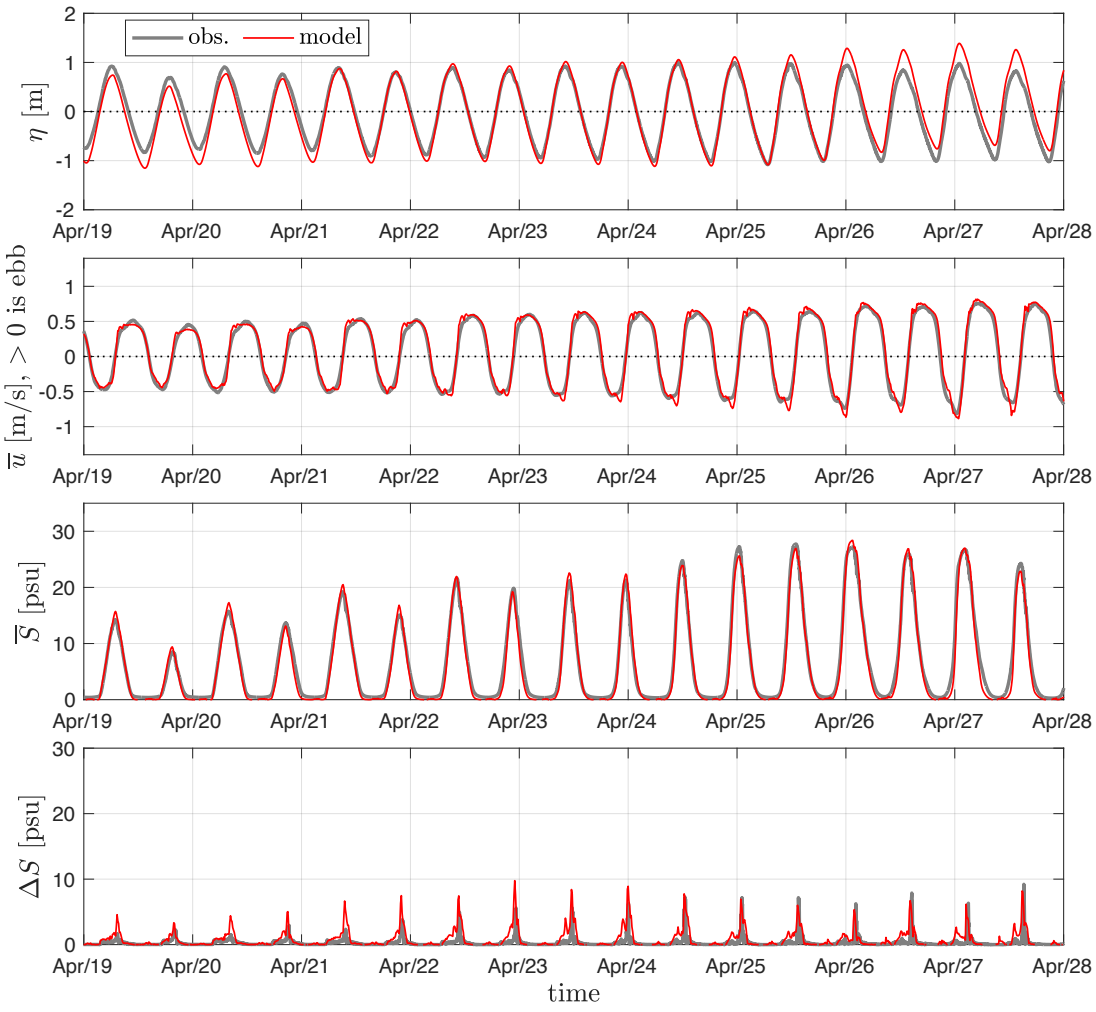

Figure D-5: The modeled estuarine conditions (thin red lines) compared with observations (thick gray lines) at Moor5, including water level η, depth-averaged velocity $\overline{u}$, depth-averaged salinity $\overline{S}$, and stratification ΔS.

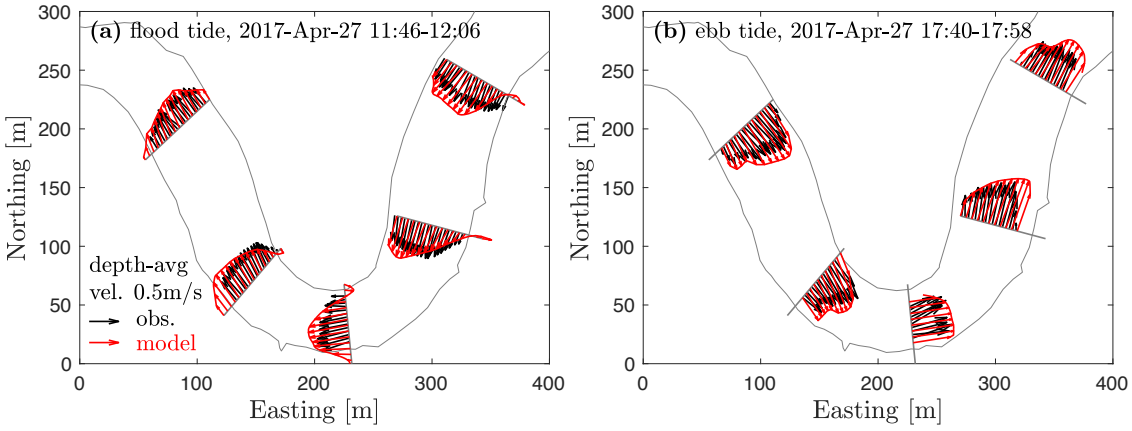

Figure D-6: Depth-averaged velocity of the modeling (red) and observational (black) results in the sharp bend on April 27. (a): Flood tide. (b): Ebb tide.

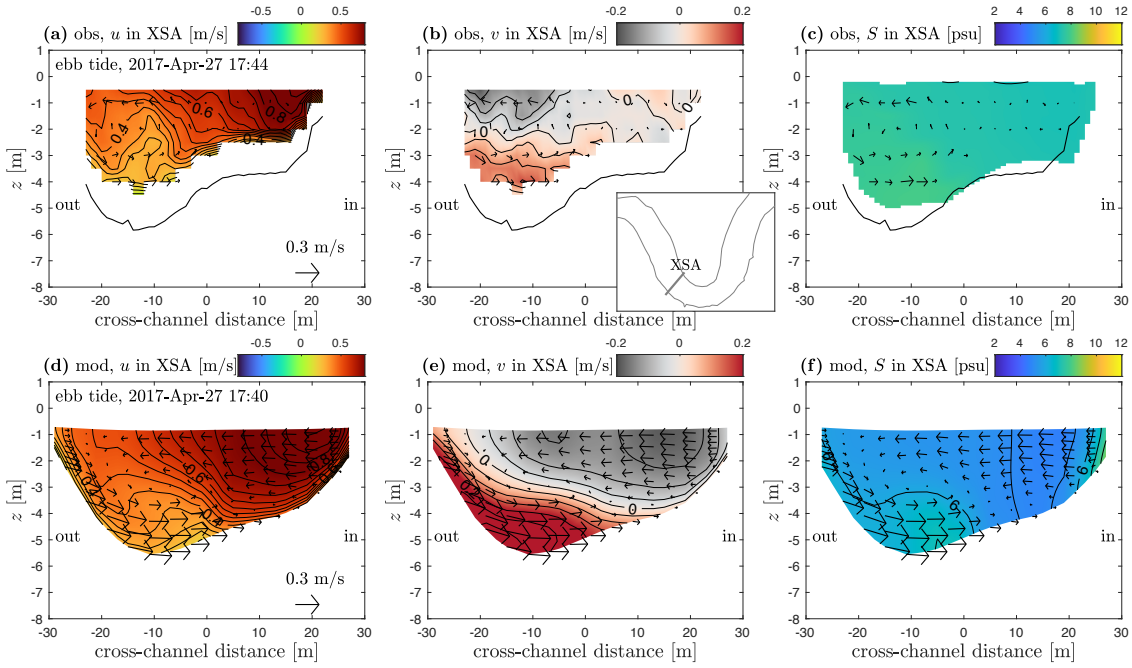

Figure D-7: Ebb tide results in cross-section XSA (location shown in the small map) in the sharp bend on April 27. u is the along-channel velocity (positive means seaward), v is the lateral velocity (positive means inward), and S is salinity. **(a)-(c)**: observational results; **(d)-(e)**: modeling results.

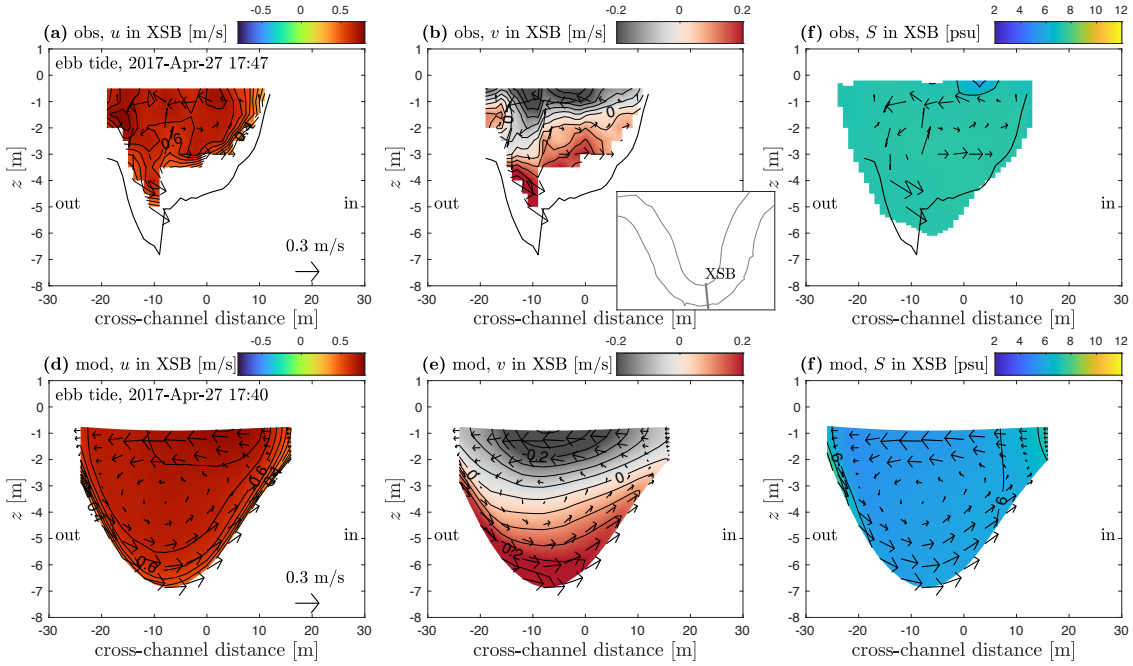

Figure D-8: Ebb tide results in cross-section XSB (location shown in the small map) in the sharp bend on April 27. u is the along-channel velocity (positive means seaward), v is the lateral velocity (positive means inward), and S is salinity. **(a)**-**(c)**: observational results; **(d)**-**(e)**: modeling results.

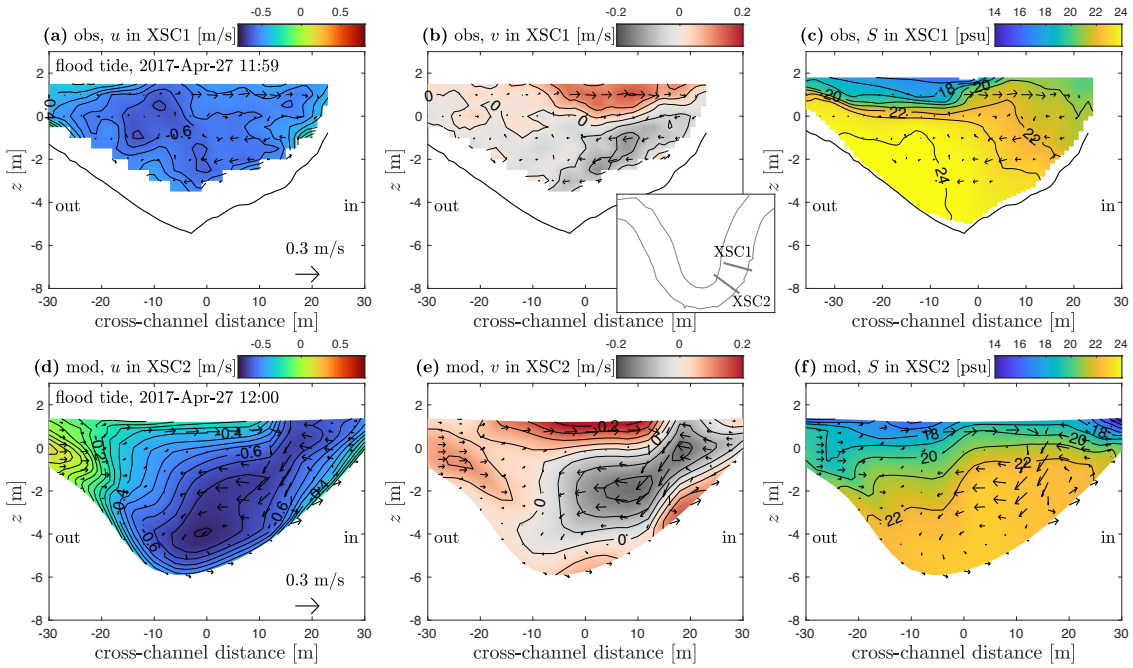

Figure D-9: Flood tide results in cross-sections XSC1 and XSC2 (locations shown in the small map) in the sharp bend on April 27. u is the along-channel velocity (negative means landward), v is the lateral velocity (positive means inward), and S is salinity. **(a)-(c)**: observational results in XSC1; **(d)-(e)**: modeling results in XSC2. The modeling results (mainly lateral velocity) in XSC2 are more consistent with observations in XSC1, compared to modeling results in XSC1. This discrepancy suggests that the along-channel development of secondary circulation in the model is slower than indicated by observations, but the secondary circulation patterns are still broadly consistent. Therefore, here we present the modeling results in XSC2.

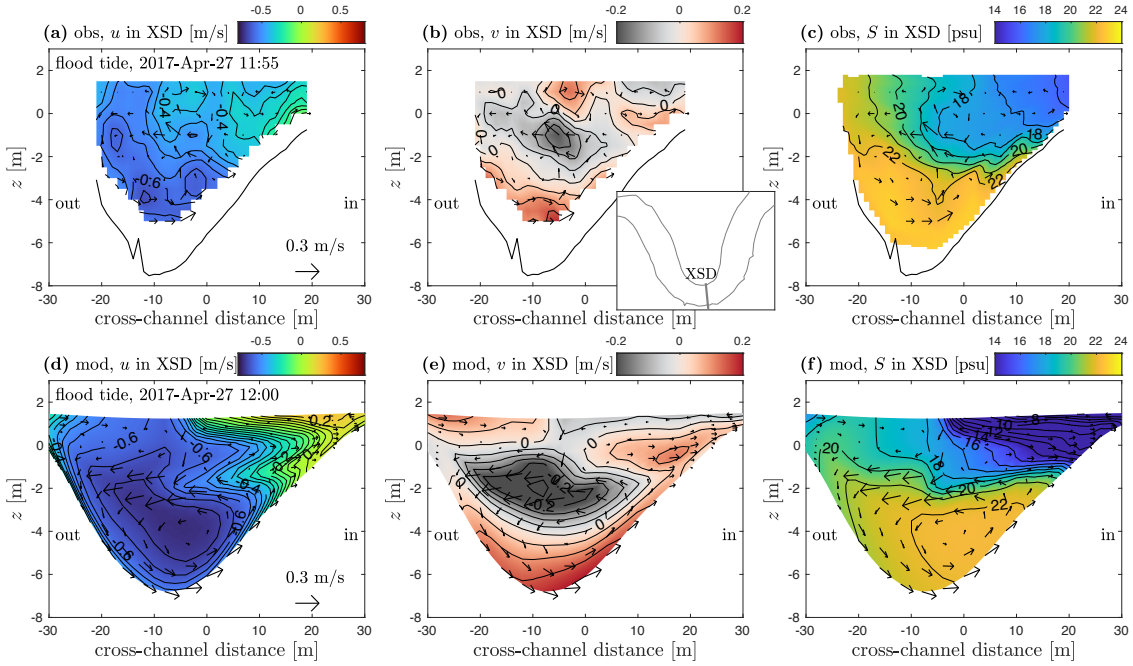

Figure D-10: Flood tide results cross-section XSD (location shown in the small map) in the sharp bend on April 27. u is the along-channel velocity (negative means landward), v is the lateral velocity (positive means inward), and S is salinity. **(a)-(c)**: observational results; **(d)-(e)**: modeling results.

	water level	velocity	salinity	stratification
$z_0 = 5$ mm $\star$				
Moor1	0.96	0.97	0.93	–
Moor2	0.98	–	0.97	-1.80
Moor3	0.98	0.88	0.96	0.82
Moor4	0.97	–	0.98	-2.17
Moor5	0.90	0.98	0.98	-1.17
$z_0 = 2$ mm				
Moor1	0.96	0.96	0.93	–
Moor2	0.97	–	0.98	-1.06
Moor3	0.98	0.84	0.97	0.71
Moor4	0.97	–	0.98	-1.16
Moor5	0.90	0.97	0.97	-0.65
$z_0 = 1$ cm				
Moor1	0.96	0.97	0.92	–
Moor2	0.98	–	0.96	-2.66
Moor3	0.98	0.91	0.94	0.84
Moor4	0.97	–	0.98	-1.16
Moor5	0.90	0.97	0.94	-1.91

Table D.1: Skill scores for three choices of z_0: 0.002 m, 0.005 m, and 0.01 m. The modeled water level, velocity, salinity, and stratification are compared with observations at five mooring sites Moor1-5. $z_0 = 0.005$ m is used for the numerical study.

Appendix E

Shipboard surveys at the constriction and bend

During the observational period, shipboard surveys were conducted at multiple cross-sections and along-channel sections near the constriction and in several bends in the North River estuary. Continuous salinity and temperature data were collected with a towed CTD array that had three or four CTD sensors in the vertical, and velocity profile data were collected with a shipboard acoustic Doppler current profiler. The sensor depths of the towed array were actively adjusted depending on the local bathymetry to maximize the vertical coverage, with a typical vertical spacing of $0.5 - 2$ m between sensors. The towed array sampling was needed to resolve sharp density gradients at fronts better than possible with discrete CTD profiles.

Measurements in several representative cross-sections are presented that correspond with regions and tidal stages with the occurrence of surface convergence fronts (Figure E-1). Landward of the constriction, high velocity occurs on the south part of cross-sections during the flood tide, which corresponds with the strong jet flow from the narrow opening (OB1 and OB2 in Figure E-1). The higher velocity brings higher salinity water landward by differential advection and creates lateral salinity gradients across the lateral shear zones. The lateral salinity gradients can thus create secondary circulation and lead to the V-shaped surface convergence front (see the drone imagery in Figure 6-3 (**a**)), and the detailed mechanisms are explained in the numerical analysis (section 6.3.3). Note that the V-shape can also be inferred by comparing the width of the high-velocity and high-salinity region in OB1 and OB2. The velocity and salinity fields in the model (Figure 6-5) are generally consistent with these observational results.

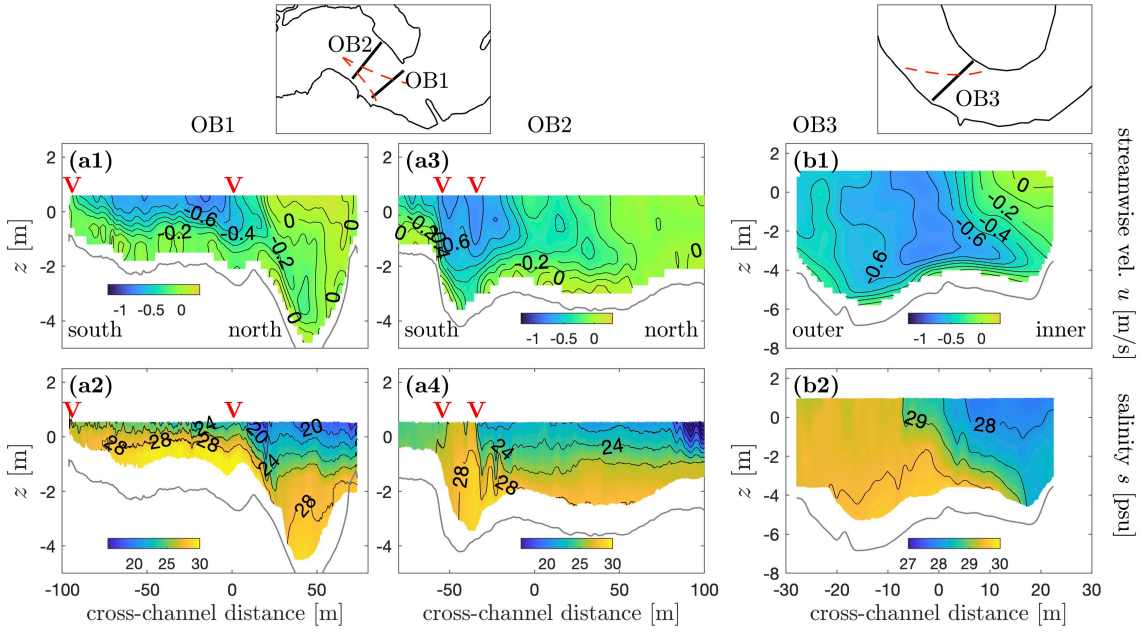

Figure E-1: Shipboard measurements of streamwise velocity and salinity during spring flood tides. **(a1)**-**(a4)**: Two cross-sections landward of the constriction at around 2 km into the estuary (at 10 am on Oct 7, 2021). Negative velocity is landward (flood direction). **(b1)**-**(b2)**: A cross-section in the bend at around 5.5 km into the estuary (at 11 am on Nov 5, 2021). Locations of cross-sections are shown on the small maps, with red lines delineating the surface fronts. Note that the shipboard measurements and drone surveys in Figure 6-3 are conducted at different times but similar tidal conditions and stages.

In the bend at around 5.5 km into the estuary, flow separation occurs during the flood tide at the bend apex and creates the low-velocity zone near the inner bank(OB3 in Figure E-1). The laterally sheared flow differentially advects salinity and thus leads to low salinity in the inner bank. The lateral salinity gradient contributes to the development of secondary circulation that can further interact with the main flow and generate the oblique surface convergence front (see the drone imagery in Figure 6-3 **(b)**; mechanisms examined in the model analysis in section 6.3.3).

Bibliography

Abad, J. D. and Garcia, M. H. (2009). Experiments in a high-amplitude kinoshita meandering channel: 2. implications of bend orientation on bed morphodynamics. *Water Resources Research*, 45(2).

Ahnert, F. (1960). Estuarine meanders in the chesapeake bay area. *Geographical review*, 50(3):390–401.

Apmann, R. P. (1964). A case history in theory and experiment: fluid flow in bends. *Isis*, 55(4):427–434.

Arcement, G. J. and Schneider, V. R. (1989). Guide for selecting manning's roughness coefficients for natural channels and flood plains.

Armi, L. and Farmer, D. (1986). Maximal two-layer exchange through a contraction with barotropic net flow. *Journal of Fluid Mechanics*, 164:27–51.

Aubrey, D. and Speer, P. (1985). A study of non-linear tidal propagation in shallow inlet/estuarine systems part i: Observations. *Estuarine, Coastal and Shelf Science*, 21(2):185–205.

Bagnold, R. A. (1960). *Some aspects of the shape of river meanders*. US Government Printing Office.

Barwis, J. H. (1977). Sedimentology of some south carolina tidal-creek point bars, and a comparison with their fluvial counterparts. *Fluvial Sedimentology*.

Batchelor, C. K. and Batchelor, G. (2000). *An introduction to fluid dynamics*. Cambridge university press.

Becherer, J., Stacey, M. T., Umlauf, L., and Burchard, H. (2015). Lateral circulation generates flood tide stratification and estuarine exchange flow in a curved tidal inlet. *Journal of Physical Oceanography*, 45(3):638–656.

Blanckaert, K. (2010). Topographic steering, flow recirculation, velocity redistribution, and bed topography in sharp meander bends. *Water Resources Research*, 46(9).

Blanckaert, K. (2011). Hydrodynamic processes in sharp meander bends and their morphological implications. *Journal of Geophysical Research*, 116(F1).

Blanckaert, K. (2015). Flow separation at convex banks in open channels. *Journal Of Fluid Mechanics*, 779:432–467.

Blanckaert, K. and De Vriend, H. (2010). Meander dynamics: A nonlinear model without curvature restrictions for flow in open-channel bends. *Journal of Geophysical Research: Earth Surface*, 115(F4).

Blanckaert, K. and de Vriend, H. J. (2003). Nonlinear modeling of mean flow redistribution in curved open channels. *Water Resources Research*, 39(12).

Blanckaert, K. and Graf, W. H. (2004). Momentum transport in sharp open-channel bends. *Journal of Hydraulic Engineering*, 130(3):186–198.

Blanckaert, K., Kleinhans, M. G., McLelland, S. J., Uijttewaal, W. S., Murphy, B. J., van de Kruijs, A., Parsons, D. R., and Chen, Q. (2013). Flow separation at the inner (convex) and outer (concave) banks of constant-width and widening open-channel bends. *Earth Surface Processes and Landforms*, 38(7):696–716.

Bo, T. and Ralston, D. K. (2020). Flow separation and increased drag coefficient in estuarine channels with curvature. *Journal of Geophysical Research: Oceans*, 125(10):e2020JC016267.

Bo, T. and Ralston, D. K. (2022). Frontogenesis, mixing, and stratification in estuarine channels with curvature. *Journal of Physical Oceanography*, 52(7):1333–1350.

Bo, T., Ralston, D. K., and Geyer, W. R. (2023). Sources of drag in estuarine meanders: momentum redistribution, bottom stress enhancement, and bend-scale form drag. *Journal of Physical Oceanography*.

Bo, T., Ralston, D. K., Kranenburg, W. M., Geyer, W. R., and Traykovski, P. (2021). High and variable drag in a sinuous estuary with intermittent stratification. *Journal of Geophysical Research: Oceans*, 126(10):e2021JC017327.

Bowden, K. and Fairbairn, L. (1956). Measurements of turbulent fluctuations and reynolds stresses in a tidal current. *Proceedings of the Royal Society of London. Series A. Mathematical and Physical Sciences*, 237(1210):422–438.

Bricker, J. D., Inagaki, S., and Monismith, S. G. (2005). Bed drag coefficient variability under wind waves in a tidal estuary. *Journal of Hydraulic Engineering*, 131(6):497–508.

Brown, J., Turrell, W., and Simpson, J. (1991). Aerial surveys of axial convergent fronts in uk estuaries and the implications for pollution. *Marine Pollution Bulletin*, 22(8):397–400.

Buijsman, M. and Ridderinkhof, H. (2008). Variability of secondary currents in a weakly stratified tidal inlet with low curvature. *Continental Shelf Research*, 28(14):1711–1723.

Burchard, H., Hetland, R. D., Schulz, E., and Schuttelaars, H. M. (2011). Drivers of residual estuarine circulation in tidally energetic estuaries: Straight and irrotational channels with parabolic cross section. *Journal of Physical Oceanography*, 41(3):548–570.

Burchard, H. and Rennau, H. (2008). Comparative quantification of physically and numerically induced mixing in ocean models. *Ocean Modelling*, 20(3):293–311.

Chang, H. H. (1983). Energy expenditure in curved open channels. *Journal of Hydraulic Engineering*, 109(7):1012–1022.

Chang, H. H. (1984). Variation of flow resistance through curved channels. *Journal of Hydraulic Engineering*, 110(12):1772–1782.

Chant, R. J. (2002). Secondary circulation in a region of flow curvature: Relationship with tidal forcing and river discharge. *Journal of Geophysical Research: Oceans*, 107(C9):14–1.

Chant, R. J. and Wilson, R. E. (1997). Secondary circulation in a highly stratified estuary. *Journal of Geophysical Research: Oceans*, 102(C10):23207–23215.

Chow, V. T. (1959). Open-channel hydraulics. In *Open-channel hydraulics*. McGraw-Hill.

Collignon, A. G. and Stacey, M. T. (2012). Intratidal dynamics of fronts and lateral circulation at the shoal–channel interface in a partially stratified estuary. *Journal of physical oceanography*, 42(5):869–883.

Collignon, A. G. and Stacey, M. T. (2013). Turbulence dynamics at the shoal–channel interface in a partially stratified estuary. *Journal of physical oceanography*, 43(5):970–989.

Constantinescu, G., Kashyap, S., Tokyay, T., Rennie, C., and Townsend, R. (2013). Hydrodynamic processes and sediment erosion mechanisms in an open channel bend of strong curvature with deformed bathymetry. *Journal of Geophysical Research: Earth Surface*, 118(2):480–496.

Dietrich, W. E. and Smith, J. D. (1983). Influence of the point bar on flow through curved channels. *Water Resources Research*, 19(5):1173–1192.

Dietrich, W. E. and Whiting, P. (1989). Boundary shear stress and sediment transport in river meanders of sand and gravel. *River meandering*, 12:1–50.

Dronkers, J. J. (1964). *Tidal computations in rivers and coastal waters*. North-holland publishing company Amsterdam.

Edwards, K. A., MacCready, P., Moum, J. N., Pawlak, G., Klymak, J. M., and Perlin, A. (2004). Form drag and mixing due to tidal flow past a sharp point. *Journal of Physical oceanography*, 34(6):1297–1312.

Einstein, H. and Harder, J. (1954). Velocity distribution and the boundary layer at channel bends. *Eos, Transactions American Geophysical Union*, 35(1):114–120.

Fagherazzi, S., Gabet, E. J., and Furbish, D. J. (2004). The effect of bidirectional flow on tidal channel planforms. *Earth Surface Processes and Landforms: The Journal of the British Geomorphological Research Group*, 29(3):295–309.

Farmer, D. M. and Smith, J. D. (1980). Tidal interaction of stratified flow with a sill in knight inlet. *Deep Sea Research Part A. Oceanographic Research Papers*, 27(3-4):239–254.

Ferguson, R. I., Parsons, D. R., Lane, S. N., and Hardy, R. J. (2003). Flow in meander bends with recirculation at the inner bank. *Water Resources Research*, 39(11):299–13.

Finotello, A., Ghinassi, M., Carniello, L., Belluco, E., Pivato, M., Tommasini, L., and D'Alpaos, A. (2020). Three-dimensional flow structures and morphodynamic evolution of microtidal meandering channels. *Water Resources Research*, 56(7):e2020WR027822.

Fong, D. A., Monismith, S. G., Stacey, M. T., and Burau, J. R. (2009). Turbulent stresses and secondary currents in a tidal-forced channel with significant curvature and asymmetric bed forms. *Journal of Hydraulic Engineering*, 135(3):198–208.

Francis, H. and Traykovski, P. (2021). Development of a highly portable unmanned surface vehicle for surf zone bathymetric surveying. *Journal of Coastal Research*, 37(5):933–945.

Friedrichs, C. T. and Wright, L. (1997). Sensitivity of bottom stress and bottom roughness estimates to density stratification, eckernförde bay, southern baltic sea. *Journal of Geophysical Research: Oceans*, 102(C3):5721–5732.

Frothingham, K. M. and Rhoads, B. L. (2003). Three-dimensional flow structure and channel change in an asymmetrical compound meander loop, embarras river, illinois. *Earth Surface Processes and Landforms: The Journal of the British Geomorphological Research Group*, 28(6):625–644.

Gabet, E. J. (1998). Lateral migration and bank erosion in a saltmarsh tidal channel in san francisco bay, california. *Estuaries*, 21(4):745–753.

Garcia, A. M. P., Geyer, W. R., and Randall, N. (2021). Exchange flows in tributary creeks enhance dispersion by tidal trapping. *Estuaries and Coasts*, pages 1–19.

Garvine, R. W. (1974). Dynamics of small-scale oceanic fronts. *Journal of Physical Oceanography*, 4(4):557–569.

Gawarkiewicz, G. and Chapman, D. C. (1992). The role of stratification in the formation and maintenance of shelf-break fronts. *Journal of Physical Oceanography*, 22(7):753–772.

Geyer, W. R. (1993a). The importance of suppression of turbulence by stratification on the estuarine turbidity maximum. *Estuaries*, 16(1):113–125.

Geyer, W. R. (1993b). Three-dimensional tidal flow around headlands. *Journal of Geophysical Research: Oceans*, 98(C1):955–966.

Geyer, W. R. (2010). Estuarine salinity structure and circulation. *Contemporary issues in estuarine physics*, pages 12–26.

Geyer, W. R. and MacCready, P. (2014). The estuarine circulation. *Annual review of fluid mechanics*, 46:175–197.

Geyer, W. R. and Ralston, D. K. (2011). 2.03 - the dynamics of strongly stratified estuaries. In Wolanski, E. and McLusky, D., editors, *Treatise on Estuarine and Coastal Science*, pages 37–51. Academic Press, Amsterdam.

Geyer, W. R. and Ralston, D. K. (2015). Estuarine frontogenesis. *Journal of Physical Oceanography*, 45(2):546–561.

Geyer, W. R., Ralston, D. K., and Chen, J.-L. (2020). Mechanisms of exchange flow in an estuary with a narrow, deep channel and wide, shallow shoals. *Journal of Geophysical Research: Oceans*, 125(12):e2020JC016092.

Geyer, W. R., Ralston, D. K., and Holleman, R. C. (2017). Hydraulics and mixing in a laterally divergent channel of a highly stratified estuary. *Journal of Geophysical Research: Oceans*, 122(6):4743–4760.

Geyer, W. R., Trowbridge, J. H., and Bowen, M. M. (2000). The dynamics of a partially mixed estuary. *Journal of Physical Oceanography*, 30(8):2035–2048.

Giddings, S. N., Fong, D. A., Monismith, S. G., Chickadel, C. C., Edwards, K. A., Plant, W. J., Wang, B., Fringer, O. B., Horner-Devine, A. R., and Jessup, A. T. (2012). Frontogenesis and frontal progression of a trapping-generated estuarine convergence front and its influence on mixing and stratification. *Estuaries and Coasts*, 35(2):665–681.

Gill, A. E. (1982). *Atmosphere—ocean dynamics*. Academic Press.

Grant, W. D. and Madsen, O. S. (1982). Movable bed roughness in unsteady oscillatory flow. *Journal of Geophysical Research: Oceans*, 87(C1):469–481.

Grant, W. D. and Madsen, O. S. (1986). The continental-shelf bottom boundary layer. *Annual review of fluid mechanics*, 18(1):265–305.

Gross, E. S., Koseff, J. R., and Monismith, S. G. (1999). Three-dimensional salinity simulations of south san francisco bay. *Journal of Hydraulic Engineering*, 125(11):1199–1209.

Haidvogel, D. B., Arango, H., Budgell, W. P., Cornuelle, B. D., Curchitser, E., Di Lorenzo, E., Fennel, K., Geyer, W. R., Hermann, A. J., Lanerolle, L., et al. (2008). Ocean forecasting in terrain-following coordinates: Formulation and skill assessment of the regional ocean modeling system. *Journal of Computational Physics*, 227(7):3595–3624.

Heathershaw, A. and Simpson, J. (1978). The sampling variability of the reynolds stress and its relation to boundary shear stress and drag coefficient measurements. *Estuarine and Coastal Marine Science*, 6(3):263–274.

Howard, L. N. (1961). Note on a paper of john w. miles. *Journal of Fluid Mechanics*, 10(4):509–512.

Huguenard, K., Valle-Levinson, A., Li, M., Chant, R., and Souza, A. (2015). Linkage between lateral circulation and near-surface vertical mixing in a coastal plain estuary. *Journal of Geophysical Research: Oceans*, 120(6):4048–4067.

Ippen, A. T. (1966). Estuary and coastline hydrodynamics. *McGraw-Hill Book Company, IncCatalog Card Number 65-27677, Printed in the United States of America*.

James, C. (1994). Evaluation of methods for predicting bend loss in meandering channels. *Journal of Hydraulic Engineering*, 120(2):245–253.

James, C., Liu, W., and Myers, W. (2001). Conveyance of meandering channels with marginal vegetation. *Proceedings of the Institution of Civil Engineers-Water and Maritime Engineering*, 148(2):97–106.

Jamieson, E. C., Ruta, M. A., Rennie, C. D., and Townsend, R. D. (2013). Monitoring stream barb performance in a semi-alluvial meandering channel: flow field dynamics and morphology. *Ecohydrology*, 6(4):611–626.

Jirka, G. H. and Uijttewaal, W. S. (2004). Shallow flows: a definition. *Shallow flows*, pages 3–11.

Johnson, G. C. and Ohlsen, D. R. (1994). Frictionally modified rotating hydraulic channel exchange and ocean outflows. *Journal of Physical Oceanography*, 24(1):66–78.

Kadlec, R. H. (1990). Overland flow in wetlands: vegetation resistance. *Journal of Hydraulic Engineering*, 116(5):691–706.

Kaimal, J. C., Wyngaard, J., Izumi, Y., and Coté, O. (1972). Spectral characteristics of surface-layer turbulence. *Quarterly Journal of the Royal Meteorological Society*, 98(417):563–589.

Kalkwijk, J. P. T. and Booij, R. (1986). Adaptation of secondary flow in nearly-horizontal flow. *Journal of Hydraulic Research*, 24(1):19–37.

Kalra, T. S., Li, X., Warner, J. C., Geyer, W. R., and Wu, H. (2019). Comparison of physical to numerical mixing with different tracer advection schemes in estuarine environments. *Journal of Marine Science and Engineering*, 7(10):338.

Kashyap, S., Constantinescu, G., Rennie, C. D., Post, G., and Townsend, R. (2012). Influence of channel aspect ratio and curvature on flow, secondary circulation, and bed shear stress in a rectangular channel bend. *Journal of Hydraulic Engineering*, 138(12):1045–1059.

Kimball, P., Bailey, J., Das, S., Geyer, R., Harrison, T., Kunz, C., Manganini, K., Mankoff, K., Samuelson, K., Sayre-McCord, T., et al. (2014). The whoi jetyak: An autonomous surface vehicle for oceanographic research in shallow or dangerous waters. In *2014 IEEE/OES Autonomous Underwater Vehicles (AUV)*, pages 1–7. IEEE.

Kranenburg, W. M., Geyer, W. R., Garcia, A. M. P., and Ralston, D. K. (2019). Reversed lateral circulation in a sharp estuarine bend with weak stratification. *Journal of Physical Oceanography*.

Kunkel, C. M., Hallberg, R. W., and Oppenheimer, M. (2006). Coral reefs reduce tsunami impact in model simulations. *Geophysical research letters*, 33(23).

Lacy, J. R. and Monismith, S. G. (2001). Secondary currents in a curved, stratified, estuarine channel. *Journal of Geophysical Research: Oceans*, 106(C12):31283–31302.

Lacy, J. R., Stacey, M. T., Burau, J. R., and Monismith, S. G. (2003). Interaction of lateral baroclinic forcing and turbulence in an estuary. *Journal of Geophysical Research: Oceans*, 108(C3).

Langbein, W. and Leopold, L. (1966). River meanders-theory of minimum variance. *USGS Prof., Paper 422-H*, 15:1966.

Langbein, W. B. (1963). The hydraulic geometry of a shallow estuary. *Hydrological Sciences Journal*, 8(3):84–94.

Langbein, W. B. and Leopold, L. B. (1970). River meanders and the theory of minimum variance. In *Rivers and river terraces*, pages 238–263. Springer.

Largier, J. L. (1992). Tidal intrusion fronts. *Estuaries*, 15(1):26–39.

Largier, J. L. (1993). Estuarine fronts: how important are they? *Estuaries*, 16(1):1–11.

Leeder, M. R. and Bridges, P. H. (1975). Flow separation in meander bends. *Nature*, 253:1–2.

Lentz, S. J., Davis, K. A., Churchill, J. H., and DeCarlo, T. M. (2017). Coral reef drag coefficients–water depth dependence. *Journal of Physical Oceanography*, 47(5):1061–1075.

Leopold, L. B. (1960). *Flow resistance in sinuous or irregular channels*. US Government Printing Office.

Leopold, L. B., Collins, J. N., and Collins, L. M. (1993). Hydrology of Some Tidal Channels in Estuarine Marshland Near San Francisco . *CATENA VERLAG*, 20:469–493.

Leopold, L. B. and Wolman, M. G. (1960). River meanders. *Geological Society of America Bulletin*, 71(6):769–793.

Leopold, L. B., Wolman, M. G., and Miller, J. P. (1995). *Fluvial processes in geomorphology*. Courier Corporation.

Lerczak, J. A. and Geyer, W. R. (2004). Modeling the lateral circulation in straight, stratified estuaries. *Journal of Physical Oceanography*, 34(6):1410–1428.

Lewis, R. and Lewis, J. (1987). Shear stress variations in an estuary. *Estuarine, Coastal and Shelf Science*, 25(6):621–635.

Li, C., Valle-Levinson, A., Atkinson, L. P., Wong, K. C., and Lwiza, K. M. (2004). Estimation of drag coefficient in james river estuary using tidal velocity data from a vessel-towed adcp. *Journal of Geophysical Research: Oceans*, 109(C3).

Li, M., Cheng, P., Chant, R., Valle-Levinson, A., and Arnott, K. (2014). Analysis of vortex dynamics of lateral circulation in a straight tidal estuary. *Journal of Physical Oceanography*, 44(10):2779–2795.

Li, X., Geyer, W. R., Zhu, J., and Wu, H. (2018). The transformation of salinity variance: A new approach to quantifying the influence of straining and mixing on estuarine stratification. *Journal of Physical Oceanography*, 48(3):607–623.

MacCready, P., Pawlak, G., Edwards, K., and McCabe, R. (2003). Form drag on ocean flows. In *Near Boundary Processes and Their Parameterization: Proc. 13th'Aha Huliko'a Hawaiian Winter Workshop*, pages 119–130.

MacDonald, D. G. and Geyer, W. R. (2005). Hydraulic control of a highly stratified estuarine front. *Journal of physical oceanography*, 35(3):374–387.

Marani, M., Lanzoni, S., Zandolin, D., Seminara, G., and Rinaldo, A. (2002). Tidal meanders. *Water Resources Research*, 38(11):7–1–7–14.

Marmorino, G. and Trump, C. (1996). High-resolution measurements made across a tidal intrusion front. *Journal of Geophysical Research: Oceans*, 101(C11):25661–25674.

Marriott, M. J. (1998). *Hydrodynamics of flow around bends in meandering and compound channels.* PhD thesis, University of Herfordshire.

McCabe, R. M., MacCready, P., and Pawlak, G. (2006). Form drag due to flow separation at a headland. *Journal of physical oceanography*, 36(11):2136–2152.

McWilliams, J. C. (2021). Oceanic frontogenesis. *Annual Review of Marine Science*, 13:227–253.

Miles, J. W. (1961). On the stability of heterogeneous shear flows. *Journal of Fluid Mechanics*, 10(4):496–508.

Millar, R. G. (2000). Influence of bank vegetation on alluvial channel patterns. *Water Resources Research*, 36(4):1109–1118.

Monin, A. and Yaglom, A. (1971). *Statistical fluid mechanics: mechanics of turbulence, volume I*, volume 1. Dover, Mineola, NY.

Monismith, S. G., Hirsh, H., Batista, N., Francis, H., Egan, G., and Dunbar, R. B. (2019). Flow and drag in a seagrass bed. *Journal of Geophysical Research: Oceans*, 124(3):2153–2163.

Mukai, A. Y., Westerink, J. J., Luettich Jr, R. A., and Mark, D. (2002). Eastcoast 2001, a tidal constituent database for western north atlantic, gulf of mexico, and caribbean sea. Technical report, ENGINEER RESEARCH AND DEVELOPMENT CENTER VICKSBURG MS COASTAL AND HYDRAULICSLAB.

Murphy, A. H. (1988). Skill scores based on the mean square error and their relationships to the correlation coefficient. *Monthly weather review*, 116(12):2417–2424.

Nanson, R. A. (2010). Flow fields in tightly curving meander bends of low width-depth ratio. *Earth Surface Processes and Landforms: The Journal of the British Geomorphological Research Group*, 35(2):119–135.

Nepf, H. (1999). Drag, turbulence, and diffusion in flow through emergent vegetation. *Water resources research*, 35(2):479–489.

Nezu, I. (1993). Turbulence in open-channel flows. *IAHR-monograph*.

Nidzieko, N. J., Hench, J. L., and Monismith, S. G. (2009). Lateral Circulation in Well-Mixed and Stratified Estuarine Flows with Curvature. *Journal of Physical Oceanography*, 39(4):831–851.

Nihoul, J. C. and Ronday, F. C. (1975). The influence of the "tidal stress" on the residual circulation. *Tellus*, 27(5):484–490.

Nikuradse, J. (1933). *Strömungsgesetze in rauhen Rohren*. VDI-Verlag.

Nunes, R. and Simpson, J. (1985). Axial convergence in a well-mixed estuary. *Estuarine, Coastal and Shelf Science*, 20(5):637–649.

O'Donnell, J. (1993). Surface fronts in estuaries: a review. *Estuaries*, 16(1):12–39.

O'Donnell, J. (1997). Observations of near-surface currents and hydrography in the connecticut river plume with the surface current and density array. *Journal of Geophysical Research: Oceans*, 102(C11):25021–25033.

Ortals, C., Cordero, O., Valle-Levinson, A., and Angelini, C. (2021). Flows, transport, and effective drag in intertidal salt marsh creeks. *Journal of Geophysical Research: Oceans*, 126(11):e2021JC017357.

Ott, M. W. and Garrett, C. (1998). Frictional estuarine flow in juan de fuca strait, with implications for secondary circulation. *Journal of Geophysical Research: Oceans*, 103(C8):15657–15666.

Ottevanger, W., Blanckaert, K., and Uijttewaal, W. S. (2012). Processes governing the flow redistribution in sharp river bends. *Geomorphology*, 163:45–55.

Parker, B. B. (2007). Tidal analysis and prediction.

Parsons, D. R. (2003). *Flow separation in meander bends.* PhD thesis, University of Sheffield.

Pattiaratchi, C., James, A., and Collins, M. (1987). Island wakes and headland eddies: a comparison between remotely sensed data and laboratory experiments. *Journal of Geophysical Research: Oceans*, 92(C1):783–794.

Pein, J., Valle-Levinson, A., and Stanev, E. V. (2018). Secondary Circulation Asymmetry in a Meandering, Partially Stratified Estuary. *Journal of Geophysical Research: Oceans*, 123(3):1670–1683.

Pingree, R. and Maddock, L. (1980). The effects of bottom friction and earth's rotation on an island's wake. *Journal of the Marine Biological Association of the United Kingdom*, 60(2):499–508.

Prandle, D. (1978). Residual flows and elevations in the southern north sea. *Proceedings of the Royal Society of London. A. Mathematical and Physical Sciences*, 359(1697):189–228.

Pritchard, D. (1952). Estuarine hydrography. In *Advances in geophysics*, volume 1, pages 243–280. Elsevier.

Qian, S., Zhang, J., Wang, D., and Wang, Y. P. (2022). Observational study on drag reduction of continental-shelf bottom boundary layer. *Physics of Fluids*, 34(5):055127.

Ralston, D. K., Cowles, G. W., Geyer, W. R., and Holleman, R. C. (2017). Turbulent and numerical mixing in a salt wedge estuary: Dependence on grid resolution, bottom roughness, and turbulence closure. *Journal of Geophysical Research: Oceans*, 122(1):692–712.

Ralston, D. K. and Stacey, M. T. (2005a). Longitudinal dispersion and lateral circulation in the intertidal zone. *Journal of Geophysical Research: Oceans*, 110(C7).

Ralston, D. K. and Stacey, M. T. (2005b). Stratification and turbulence in subtidal channels through intertidal mudflats. *Journal of Geophysical Research: Oceans*, 110(C8).

Redfield, A. C. (1972). Development of a new england salt marsh. *Ecological monographs*, 42(2):201–237.

Rogers, J. S., Maticka, S. A., Chirayath, V., Woodson, C. B., Alonso, J. J., and Monismith, S. G. (2018). Connecting flow over complex terrain to hydrodynamic roughness on a coral reef. *Journal of Physical Oceanography*, 48(7):1567–1587.

Rozovskii, I. (1957). *Flow of water in bends of open channels*. Academy of Sciences of the Ukrainian SSR.

Schmidt, J. C. (1990). Recirculating flow and sedimentation in the colorado river in grand canyon, arizona. *The Journal of Geology*, 98(5):709–724.

Schnauder, I. and Sukhodolov, A. (2012). Flow in a tightly curving meander bend: effects of seasonal changes in aquatic macrophyte cover. *Earth Surface Processes and Landforms*, 37(11):1142–1157.

Scully, M. E. and Geyer, W. R. (2012). The role of advection, straining, and mixing on the tidal variability of estuarine stratification. *Journal of Physical Oceanography*, 42(5):855–868.

Scully, M. E., Geyer, W. R., and Lerczak, J. A. (2009). The influence of lateral advection on the residual estuarine circulation: A numerical modeling study of the hudson river estuary. *Journal of Physical Oceanography*, 39(1):107–124.

Scully, M. E., Geyer, W. R., and Trowbridge, J. H. (2011). The influence of stratification and nonlocal turbulent production on estuarine turbulence: An assessment of turbulence closure with field observations. *Journal of Physical Oceanography*, 41(1):166–185.

Seim, H., Blanton, J., and Elston, S. (2006). Tidal circulation and energy dissipation in a shallow, sinuous estuary. *Ocean Dynamics*, 56(3-4):360–375.

Seim, H. E., Blanton, J. O., and Gross, T. (2002). Direct stress measurements in a shallow, sinuous estuary. *Continental Shelf Research*, 22(11-13):1565–1578.

Seim, H. E. and Gregg, M. C. (1997). The importance of aspiration and channel curvature in producing strong vertical mixing over a sill. *Journal of Geophysical Research: Oceans*, 102(C2):3451–3472.

Seminara, G. (2006). Meanders. *Journal of fluid mechanics*, 554:271–297.

Shapiro, A. H. and Sonin, A. A. (2018). *Advanced Fluid Mechanics Problems*. (Self-published manuscript).

Shchepetkin, A. F. and McWilliams, J. C. (2005). The regional oceanic modeling system (roms): a split-explicit, free-surface, topography-following-coordinate oceanic model. *Ocean modelling*, 9(4):347–404.

Signell, R. P. and Geyer, W. R. (1991). Transient eddy formation around headlands. *Journal of Geophysical Research: Oceans*, 96(C2):2561–2575.

Simpson, J. and Linden, P. (1989). Frontogenesis in a fluid with horizontal density gradients. *Journal of Fluid Mechanics*, 202:1–16.

Simpson, J. and Nunes, R. (1981). The tidal intrusion front: an estuarine convergence zone. *Estuarine Coastal and Shelf Science*, 13(3):257–IN1.

Simpson, J. and Turrell, W. (1986). Convergent fronts in the circulation of tidal estuaries. In *Estuarine variability*, pages 139–152. Elsevier.

Simpson, J. H., Brown, J., Matthews, J., and Allen, G. (1990). Tidal straining, density currents, and stirring in the control of estuarine stratification. *Estuaries*, 13(2):125–132.

Smith, R. (1982). Where to put a steady discharge in a river. *Journal of Fluid Mechanics*, 115:1–11.

Soulsby, R. (1990). Tidal current boundary layers, the sea, part 1. *Edited by: B. Le Méhauté, University of Miami, USA, John Wiley & Sons Inc., Printed in USA, ISBN: 0 471 63393 3*.

Soulsby, R. (1997). Dynamics of marine sands.

Stacey, M. T., Burau, J. R., and Monismith, S. G. (2001). Creation of residual flows in a partially stratified estuary. *Journal of Geophysical Research: Oceans*, 106(C8):17013–17037.

Stacey, M. T., Monismith, S. G., and Burau, J. R. (1999). Observations of turbulence in a partially stratified estuary. *Journal of Physical Oceanography*, 29(8):1950–1970.

Stacey, M. T. and Ralston, D. K. (2005). The scaling and structure of the estuarine bottom boundary layer. *Journal of Physical Oceanography*, 35(1):55–71.

Stacey, M. T., Rippeth, T., and Nash, J. D. (2011). Turbulence and stratification in estuaries and coastal seas. In Wolanski, E. and McLusky, D. S., editors, *Treatise on Estuarine and Coastal Science*, pages 9–35. Elsevier.

Sternberg, R. (1968). Friction factors in tidal channels with differing bed roughness. *Marine Geology*, 6(3):243–260.

Tennekes, H., Lumley, J. L., Lumley, J. L., et al. (1972). *A first course in turbulence*. MIT press.

Thackston, E. L. and Schnelle, K. B. (1970). Predicting effects of dead zones on stream mixing. *Journal of the Sanitary Engineering Division*, 96(2):319–331.

Thomson, J. (1877). On the origin of windings of rivers in alluvial plains, with remarks on the flow of water round bends in pipes. *Proceedings of the Royal Society of London*, 25(171-178):5–8.

Trowbridge, J. H. and Lentz, S. J. (2018). The bottom boundary layer. *Annual Review of Marine Science*, 10:397–420.

Turner, J. S. and Turner, J. S. (1979). *Buoyancy effects in fluids*. Cambridge university press.

Tyler, M. A., Coats, D. W., and Anderson, D. M. (1982). Encystment in a dynamic environment: deposition of dinoflagellate cysts by a frontal convergence. *Marine Ecology Progress Series*, pages 163–178.

Umlauf, L. and Burchard, H. (2003). A generic length-scale equation for geophysical turbulence models. *Journal of Marine Research*, 61(2):235–265.

Uncles, R. and Jordan, M. (1980). A one-dimensional representation ofresidual currents in the severn estuary and associated observations. *Estuarine and Coastal Marine Science*, 10(1):39–60.

Valle-Levinson, A. (2008). Density-driven exchange flow in terms of the kelvin and ekman numbers. *Journal of Geophysical Research: Oceans*, 113(C4).

Valle-Levinson, A. (2010). *Contemporary issues in estuarine physics*. Cambridge University Press.

Valle-Levinson, A. (2011). 2.07 - large estuaries (effects of rotation). In Wolanski, E. and McLusky, D., editors, *Treatise on Estuarine and Coastal Science*, pages 123–139. Academic Press, Amsterdam.

Valle-Levinson, A., Li, C., Wong, K.-C., and Lwiza, K. M. (2000). Convergence of lateral flow along a coastal plain estuary. *Journal of Geophysical Research: Oceans*, 105(C7):17045–17061.

van Rijn, L. C. (2011). Analytical and numerical analysis of tides and salinities in estuaries; part i: tidal wave propagation in convergent estuaries. *Ocean dynamics*, 61(11):1719–1741.

Vermeulen, B., Hoitink, A., and Labeur, R. (2015). Flow structure caused by a local cross-sectional area increase and curvature in a sharp river bend. *Journal of Geophysical Research: Earth Surface*, 120(9):1771–1783.

Walters, R. A. and Gartner, J. W. (1985). Subtidal sea level and current variations in the northern reach of san francisco bay. *Estuarine, Coastal and Shelf Science*, 21(1):17–32.

Wang, T., Zhao, S., Zhu, L., McWilliams, J. C., Galgani, L., Amin, R. M., Nakajima, R., Jiang, W., and Chen, M. (2022). Accumulation, transformation and transport of microplastics in estuarine fronts. *Nature Reviews Earth & Environment*, 3(11):795–805.

Warner, J. C., Armstrong, B., He, R., and Zambon, J. B. (2010). Development of a coupled ocean–atmosphere–wave–sediment transport (coawst) modeling system. *Ocean modelling*, 35(3):230–244.

Warner, J. C., Geyer, W. R., Ralston, D. K., and Kalra, T. (2020). Using tracer variance decay to quantify variability of salinity mixing in the hudson river estuary. *Journal of Geophysical Research: Oceans*, 125(12):e2020JC016096.

Warner, J. C., Sherwood, C. R., Arango, H. G., and Signell, R. P. (2005). Performance of four turbulence closure models implemented using a generic length scale method. *Ocean Modelling*, 8(1-2):81–113.

Warner, J. C., Sherwood, C. R., Signell, R. P., Harris, C. K., and Arango, H. G. (2008). Development of a three-dimensional, regional, coupled wave, current, and sediment-transport model. *Computers & geosciences*, 34(10):1284–1306.

Warner, S. J. and MacCready, P. (2014). The dynamics of pressure and form drag on a sloping headland: Internal waves versus eddies. *Journal of Geophysical Research: Oceans*, 119(3):1554–1571.

Warner, S. J., MacCready, P., Moum, J. N., and Nash, J. D. (2013). Measurement of tidal form drag using seafloor pressure sensors. *Journal of physical oceanography*, 43(6):1150–1172.

White, B. L. and Helfrich, K. R. (2013). Rapid gravitational adjustment of horizontal shear flows. *Journal of Fluid Mechanics*, 721:86–117.

Wolanski, E. and Hamner, W. M. (1988). Topographically controlled fronts in the ocean and their biological influence. *Science*, pages 177–181.

Wolanski, E., Imberger, J., and Heron, M. L. (1984). Island wakes in shallow coastal waters. *Journal of Geophysical Research: Oceans*, 89(C6):10553–10569.

Zhong, L. and Li, M. (2006). Tidal energy fluxes and dissipation in the chesapeake bay. *Continental Shelf Research*, 26(6):752–770.

Zimmerman, J. (1978). Topographic generation of residual circulation by oscillatory (tidal) currents. *Geophysical & Astrophysical Fluid Dynamics*, 11(1):35–47.

Zimmerman, J. (1979). On the euler-lagrange transformation and the stokes' drift in the presence of oscillatory and residual currents. *Deep Sea Research Part A. Oceanographic Research Papers*, 26(5):505–520.